T · H · E
OHIO STATE UNIVERSITY

NEW MAIN REFLECTOR, SUBREFLECTOR AND DUAL CHAMBER CONCEPTS FOR COMPACT RANGE APPLICATIONS

C.W.I. Pistorius
W.D. Burnside

The Ohio State University

ElectroScience Laboratory

Department of Electrical Engineering
Columbus, Ohio   43212

NOTICES

When Government drawings, specifications, or other data are used for any purpose other than in connection with a definitely related Government procurement operation, the United States Government thereby incurs no responsibility nor any obligation whatsoever, and the fact that the Government may have formulated, furnished, or in any way supplied the said drawings, specifications, or other data, is not to be regarded by implication or otherwise as in any manner licensing the holder or any other person or corporation, or conveying any rights or permission to manufacture, use, or sell any patented invention that may in any way be related thereto.

50272-101

REPORT DOCUMENTATION PAGE	1. REPORT NO.	2.	3. Recipient's Accession No.

4. Title and Subtitle	5. Report Date
NEW MAIN REFLECTOR, SUBREFLECTOR AND DUAL CHAMBER CONCEPTS FOR COMPACT RANGE APPLICATIONS	August 1987
	6.

7. Author(s)	8. Performing Organization Rept. No.
C.W.I. Pistorius and W.D. Burnside	716148-22

9. Performing Organization Name and Address	10. Project/Task/Work Unit No.
The Ohio State University ElectroScience Laboratory 1320 Kinnear Road Columbus, Ohio 43212	
	11. Contract(C) or Grant(G) No
	(C)
	(G) NSG 1613

12. Sponsoring Organization Name and Address	13. Type of Report & Period Covered
National Aeronautics and Space Administration Langley Research Center Hampton, Virginia 23665	Technical
	14.

15. Supplementary Notes

16. Abstract (Limit: 200 words)

A compact range is a facility used for the measurement of antenna radiation and target scattering problems. Most presently available parabolic reflectors do not produce ideal uniform plane waves in the target zone. Design improvements are suggested to reduce the amplitude taper, ripple and cross-polarization errors. The ripple caused by diffractions from the reflector edges can be reduced by adding blended rolled edges and shaping the edge contour. Since the reflected field continues smoothly from the parabola onto the rolled surface, rather than being abruptly terminated, the discontinuity in the reflected field is reduced which results in weaker diffracted fields. This is done by blending the rolled edges from the parabola into an ellipse. An algorithm which enables one to design optimum blended rolled edges was developed that is based on an analysis of the continuity of the surface radius of curvature and its derivatives across the junction. Furthermore, a concave edge contour results in a divergent diffracted ray pattern and hence less stray energy in the target zone. Design equations for three-dimensional reflectors are given. Various examples were analyzed using a new physical optics method which eliminates the effects of the false scattering centers on the incident shadow boundaries. A Gregorian subreflector system, in which both the subreflector and feed axes are tilted, results in a substantial reduction in the

17. Document Analysis   a. Descriptors

b. Identifiers/Open-Ended Terms

c. COSATI Field/Group

18. Availability Statement	19. Security Class (This Report)	21. No. of Pages
Approved for public release; distribution is unlimited.	Unclassified	349
	20. Security Class (This Page) Unclassified	22. Price

(See ANSI–Z39.18)   See Instructions on Reverse

OPTIONAL FORM 272 (4–77)
(Formerly NTIS–35)
Department of Commerce

amplitude taper and cross-polarization errors. A dual chamber configuration is proposed to eliminate the effects of diffraction from the subreflector and spillover from the feed. The main reflector and target zone are located in the upper chamber, and the subreflector and feed in the lower chamber. The chambers are isolated by an absorber fence with a small coupling aperture to transmit signals. The fence attenuates stray signals from the subreflector and feed to an unsignificant level. Diffraction from the coupling aperture can be minimized by terminating the fence in wedges. A computationally efficient technique, based on ray tracing and aperture integration, was developed to analyze the scattering from a lossy dielectric slab with a wedge termination.

TABLE OF CONTENTS

LIST OF FIGURES

ix

xi

LIST OF TABLES

CHAPTER I

INTRODUCTION

Antenna radiation and target scattering parameters, characteristics and patterns are measured on an instrumented facility called a "range"[1]. In the case where the scattering from targets is to be measured, it is required that the scattering body be illuminated by a plane wave of constant amplitude. Plane wave illumination is similarly required to measure the far field radiation parameters of an antenna. The measurement range thus has to be able to produce a uniform plane wave with no cross-polarization errors (or a good approximation thereof) over a specified volume where the target or antenna will be located, referred to as the "target zone". A local plane wave in the target zone can be created in two ways; viz.,

1. Locating the target zone so that it is in the actual far zone of the source antenna[2,3]. In order to meet the requirements for a plane wave approximation one finds that the actual distance separating the source antenna and the target zone becomes very large, so that the measurement range can only be implemented outdoors.

2. Using a collimator to transform the spherical wave radiated by a point source into a plane wave[4]. This conversion can be accomplished in a relatively short space, so that these types of ranges can be accommodated indoors,

1

and are referred to as "compact ranges". Indoor compact ranges are normally housed in so called anechoic chambers, in order to simulate a free space environment[5]. In true free space all energy radiated from a source would propagate to infinity since there is per definition nothing to scatter the energy back. The walls, floor and ceiling of an anechoic chamber are consequently lined with electromagnetic absorbing material, so that (ideally) all electromagnetic energy incident thereon is absorbed rather than scattered. Two types of collimators have been proposed; viz., parabolic reflectors[6] and lenses[4]. The lens concept has not proven to be very succesful, due to the fact that metallic lenses are very frequency dependent and the manufacturing difficulties that are associated with large dielectric lenses. Parabolic reflectors, on the other hand, have been very succesful and are widely used in modern compact ranges. Compact ranges offer many advantages over other types of ranges, and as a result a lot of effort is being directed towards the improvement of their performance. For a general discussion on compact ranges one is referred to references[4], [7]-[10]. A typical focus-fed compact range configuration is shown in Figure 1.

This study proposes several design improvements that can be made to the antenna system of a compact range to enhance the system performance; viz.,

1. Shaping the edge contour of the parabolic main reflector.

2. Adding blended rolled surfaces to the edges of the parabolic main reflector.

3. A dual chamber configuration in which the main reflector and target zone are contained in one chamber and the feed assembly together with a Gregorian
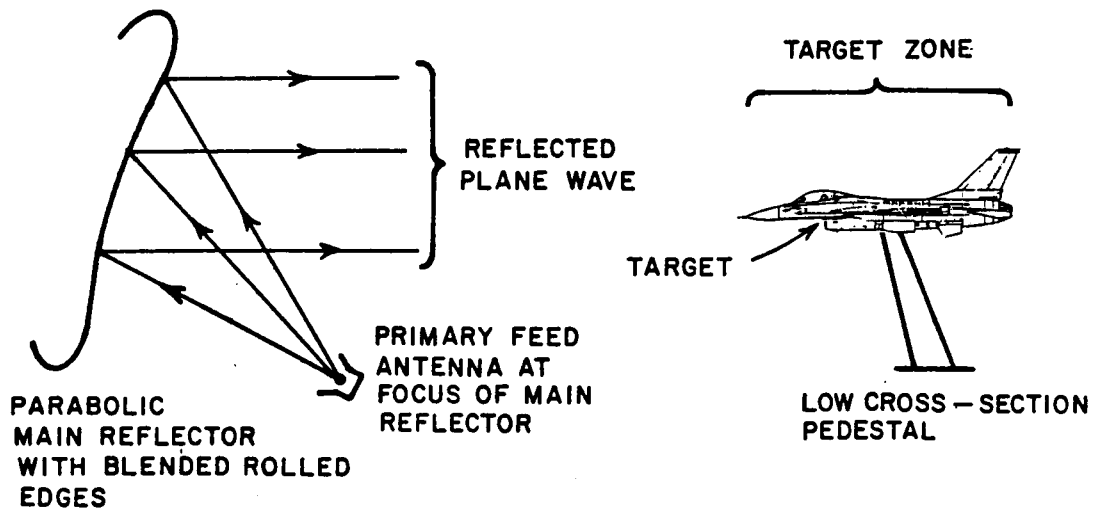
Figure 1: Typical focus-fed compact range configuration.

subreflector in the other. This study is mainly concerned with the absorber fence separating the two chambers.

The first two suggested improvements are aimed at reducing the diffracted fields from the main reflector. These diffracted fields interfere with the plane wave and degrade system performance in that they create a ripple in the reflected plane wave. A dual chamber configuration has several advantages. The use of a tilted Gregorian subreflector reduces the amplitude taper in the reflected field considerably, and virtually eliminates the cross-polarization errors. Since the main reflector and target zone are isolated from the feed assembly and subreflector by the absorber fence, minimal scattering from the subreflector or spillover from the feed illuminate the main reflector or target zone. The suggested design improvements will thus enable one to design a compact range with very small amplitude taper, ripple and cross-polarization errors in the illumination of the target zone.

3

Chapter II discusses the techniques that are used to analyze the antenna and dielectric structures in the rest of this study. A method, whereby the end point contributions resulting from the application of the physical optics method to three-dimensional bodies can be eliminated, is derived. Chapter III discusses the criteria for and creation of plane waves and it is shown how rolled edges in general improve the field quality in the target zone. Elliptical and blended rolled edges are analyzed and compared for two-dimensional cases. The relationship between the order of a blending function and the resulting continuity in the derivatives of the surface radius of curvature across the junction is derived. An algorithm based upon this relationship is proposed for designing optimized blended rolled edges. Design examples are given which clearly show the superiority of blended rolled edges over elliptical rolled edges. Three-dimensional parabolic main reflectors are discussed in Chapter IV. It is shown that a substantial reduction in the edge diffracted fields can be achieved if the edge contour of the parabolic section has a concave shape rather than the conventional convex shape. The design equations for three-dimensional main reflectors with concave edge contours and blended rolled edges are given. Several design examples are discussed to show that these design improvements result in increased performance in the case of three-dimensional reflectors. Chapter V discusses the benefits of a Gregorian subreflector feed system and proposes a dual chamber compact range configuration in which the use of an absorber fence prevents unwanted fields that are diffracted from the subreflector edge and spillover from the feed from reaching the main reflector and target zone. In Chapter VI a technique is described to compute the forward scattered field from a homogeneous lossy dielectric slab with a wedge termination. This type of structure is used in the implementation of the absorber fence in the dual chamber configuration. Chapter VII contains the summary and conclusions that can be made from this study

4

and suggests further topics that can be studied. Two appendices are included, dealing with applications of differential geometry and the derivation of closed form expressions for the aperture integration over a half plane in free space.

CHAPTER II

ANALYTICAL TECHNIQUES

This chapter briefly describes the existing techniques that are used to analyze the reflector and absorber structures in this study, with the exception of the moment method. Since the derivation of these solutions are not the purpose of this section, the equations relating to Geometrical Optics (GO) and the Uniform Theory of Diffraction (UTD) are simply stated without a detailed discussion, and the reader is referred to the references for more details. A new technique to calculate the forward scattering from a homogeneous lossy dielectric slab with a wedge termination is discussed in Chapter VI.

The moment method is based on a field integral equation solution, and is assumed to be exact within the constraints of numerical accuracy and in so far as the scattering body can be accurately modelled. A detailed understanding of the moment method is not required for the analysis of structures discussed in this study, nor for the physical interpretation of results. The reader is referred to references [11,12] for details on the theory and application of the moment method.

Throughout this study an $e^{j\omega t}$ time convention is assumed and suppressed. All reflector surfaces are assumed to be perfectly conducting and smooth. In two-dimensional problems, transverse electric (TE) polarization indicates the case where the electric field vector is perpendicular to the plane of incidence, and transverse magnetic (TM) polarization indicates the case where the magnetic field vector
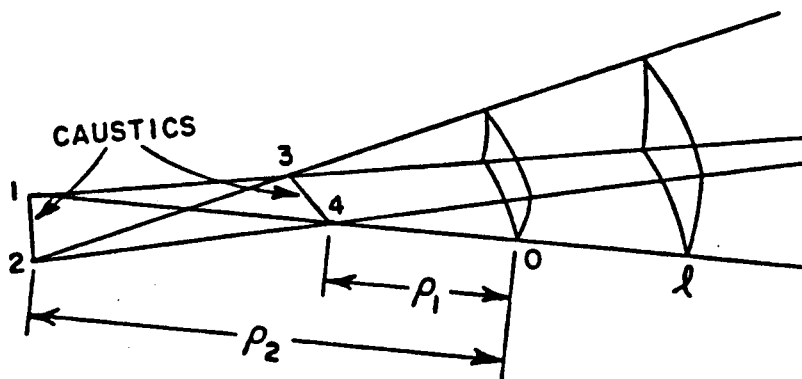
Figure 2: Astigmatic ray tube.

is perpendicular to the plane of incidence. Certain symbols are used throughout, including the free space impedance (Z_0), free space admittance (Y_0), free space wavelength (λ), and free space propagation constant $(k = 2\pi/\lambda)$. Vector quantities are indicated by boldface symbols (eg. $\mathbf{E}$), unit vectors by boldface symbols with hats (eg. $\hat{\mathbf{n}}$) and dyadic quantities by boldface symbols wih an arrow on top (eg. $\vec{\mathbf{R}}$).

2.1 Geometrical Optics

Geometrical Optics is a ray tracing procedure in which the wavelength is allowed to become infinitesimally small, ie., a high frequency limit is assumed. A ray optical field[13] can be described in terms of an astigmatic ray tube as shown in Figure 2. The electric field at l associated with this ray tube is given by

$$\mathbf{E}(l) = \mathbf{E}(0) \, A(\rho_1, \rho_2, l) \, e^{-jkl} \tag{2.1}$$

7

where $\mathbf{E}(0)$ is the field at the reference (0), A is a spread factor and ρ_1, ρ_2 are the radii of curvature of the wavefront. The spread factor is given by

$$A(\rho_1, \rho_2, l) = \sqrt{\frac{\rho_1 \, \rho_2}{(\rho_1 + l)(\rho_2 + l)}} \qquad (2.2)$$

and accounts for the conservation of energy in a ray tube. Note that there is a congruence of the rays at the so called "caustics" (1,2 and 3,4 in Figure 2), so that the caustics can be viewed as virtual sources of the wavefront. Examination of Equation (2.2) shows that the GO field is unbounded at the caustics $(l = -\rho_1, -\rho_2)$. Although Equations (2.1) and (2.2) describe a three-dimensional field, the two-dimensional version can easily be derived by setting the appropriate radius of curvature equal to infinity.

The ray paths follow Fermat's principle[14] which requires that the path transit time be an extremum. It is found that the electric and magnetic fields are perpendicular to each other and the ray path.

In applying Equations (2.1) and (2.2) to the field reflected from a surface, one finds that the reflected field can be expressed as[15]

$$\mathbf{E}^r(\mathbf{r}_{fp}) = \mathbf{E}^i(\mathbf{r}_{rp}) \cdot \vec{\mathbf{R}} \sqrt{\frac{\rho_1^r \, \rho_2^r}{(\rho_1^r + s^r)(\rho_2^r + s^r)}} \; e^{-jks^r} \qquad (2.3)$$

where

$$\mathbf{E}^r(\mathbf{r}_{fp}) = \text{reflected electric field at the field point } (\mathbf{r}_{fp})$$

$$\mathbf{E}^i(\mathbf{r}_{rp}) = \text{incident electric field at the reflection point } (\mathbf{r}_{rp})$$

$$\rho_{1,2}^r = \text{the principal radii of curvature of the reflected}$$
$$\text{wavefront emanating from } \mathbf{r}_{rp}$$

$$s^r = \text{distance from } \mathbf{r}_{rp} \text{ to } \mathbf{r}_{fp}$$

$$\hat{\mathbf{n}} = \text{unit vector normal to the surface at } \mathbf{r}_{rp}$$

$$\hat{\mathbf{s}}' = \text{direction of incident propagation at } \mathbf{r}_{rp}$$

$$\hat{\mathbf{s}} = \text{direction of reflected propagation at } \mathbf{r}_{rp}$$

$$R_{s,h} = \text{acoustic soft/hard reflection coefficients}$$

$$(\text{TE/TM polarization})$$

$$\vec{\mathbf{R}} = \text{dyadic reflection coefficient} = R_s \hat{\mathbf{e}}_\perp \hat{\mathbf{e}}_\perp + R_h \hat{\mathbf{e}}_\parallel^i \hat{\mathbf{e}}^r \quad (2.4)$$

$$\hat{\mathbf{e}}_\perp = \frac{\hat{\mathbf{s}}' \times \hat{\mathbf{n}}}{|\hat{\mathbf{s}}' \times \hat{\mathbf{n}}|} \quad (2.5)$$

$$\hat{\mathbf{e}}_\parallel^i = \hat{\mathbf{s}}' \times \hat{\mathbf{e}}_\perp \text{ , and} \quad (2.6)$$

$$\hat{\mathbf{e}}_\parallel^r = \hat{\mathbf{s}} \times \hat{\mathbf{e}}_\perp \text{ .} \quad (2.7)$$

Note that $R_{s,h} = \mp 1$ in the case of a perfectly conducting surface whose radius of curvature is large in terms of a wavelength. In this case, one finds that

$$\hat{\mathbf{s}} = \hat{\mathbf{s}}' - 2(\hat{\mathbf{n}} \cdot \hat{\mathbf{s}}')\hat{\mathbf{n}} \text{ , and} \quad (2.8)$$

$$\mathbf{E}^i \cdot \vec{\mathbf{R}} = -\mathbf{E}^i + 2(\hat{\mathbf{n}} \cdot \mathbf{E}^i)\hat{\mathbf{n}} \text{ .} \quad (2.9)$$

The incident ray, reflected ray and unit vector normal to the surface at the point of reflection all lie in the same plane (plane of incidence)[15], and the *law of reflection* requires that the incident angle be equal to the reflection angle. A reflected field at $\mathbf{r}_{fp}$ will only exist if a reflection point ($\mathbf{r}_{rp}$) on the surface exists which satisfies these requirements.

2.2 Wedge diffraction

The ray optical GO field discussed in the previous section only exists in those regions where the line of sight between the source and the target point is not obstructed. Consider a wedge with an angle (WA) illuminated by a line source as shown in Figure 3. Three regions can be identified; viz.,

9
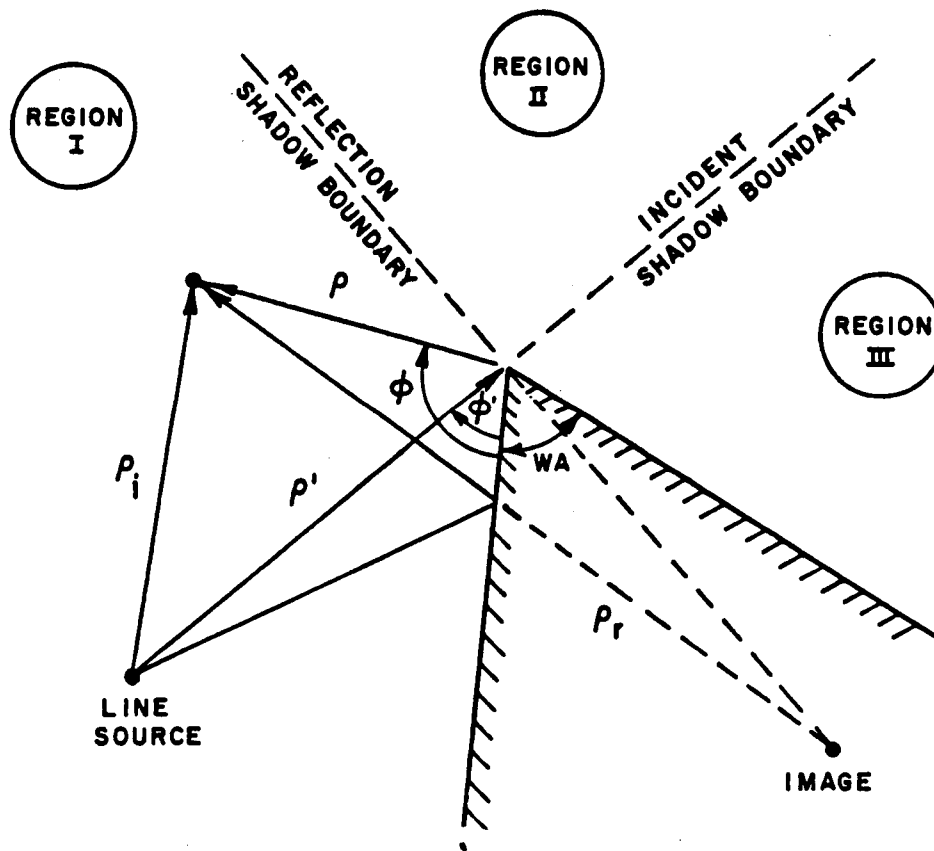
Figure 3: Diffraction from a wedge.

Region 1: Incident and reflected GO fields present.

Region 2: Only incident GO field present.

Region 3: No GO fields present.

These regions are bounded by the so called "incident shadow boundary" (ISB) and "reflection shadow boundary" (RSB). The GO incident and reflected fields exist only within these boundaries, and are zero outside. However, electromagnetic fields must be smooth and continuous everywhere, so that the discontinuities across the shadow boundaries are not allowable. The GO incident and reflected fields are thus not capable of representing the true total field in a region where scattering bodies are present. Keller developed the Geometrical Theory of Diffraction[16] (GTD) to supplement the GO fields and correct these deficiencies. The GTD postulates a diffracted field that emanates from the edge of a scattering body, so that the total field (ie., GO plus diffracted fields) is continuous. However, Keller's diffracted fields are not uniform since they are unbounded along the shadow boundaries. Kouyoumjian and Pathak corrected the GTD when they developed the Uniform Theory of Diffraction[17] (UTD). They found that when Keller's diffraction coefficients are multiplied by a transition function, the total fields are continuous everywhere, including across the shadow boundaries. A brief description of the two-dimensional UTD will now be given.

The high frequency UTD first order diffracted field from a point (Q_E) on the edge of a two-dimensional wedge is given by

$$U_z^d(s) = U_z^i(Q_E) \, D_{s,h} \, \frac{e^{-jks}}{\sqrt{s}} \qquad (2.10)$$

where U_z^d and U_z^i represent the diffracted and incident transverse electric (soft) and magnetic (hard) fields respectively, $D_{s,h}$ are the soft/hard diffraction coefficients, and s is the distance from Q_E to the field point. If a two-dimensional line source

11

generates the incident field, then the two-dimensional diffraction coefficients and associated parameters are given by

$$D_{s,h}(\phi, \phi', L^i, L^{rn}, L^{ro}, R_{s,h}, n) = D_1 + D_2 + R_{s,h}(D_3 + D_4) \qquad (2.11)$$

where

$$D_1 = \frac{-e^{-j\pi/4}}{2n\sqrt{2\pi k}} \cot\left(\frac{\pi + \beta^-}{2n}\right) F[kL^i a^+(\beta^-)] \qquad (2.12)$$

$$D_2 = \frac{-e^{-j\pi/4}}{2n\sqrt{2\pi k}} \cot\left(\frac{\pi - \beta^-}{2n}\right) F[kL^i a^-(\beta^-)] \qquad (2.13)$$

$$D_3 = \frac{-e^{-j\pi/4}}{2n\sqrt{2\pi k}} \cot\left(\frac{\pi + \beta^+}{2n}\right) F[kL^{rn} a^+(\beta^+)] \qquad (2.14)$$

$$D_4 = \frac{-e^{-j\pi/4}}{2n\sqrt{2\pi k}} \cot\left(\frac{\pi - \beta^+}{2n}\right) F[kL^{ro} a^-(\beta^+)] \qquad (2.15)$$

$$\beta^\pm = \phi \pm \phi' \qquad (2.16)$$

$$a^\pm(\beta) = 2\cos^2\left(\frac{2n\pi N^\pm - \beta}{2}\right) \qquad (2.17)$$

$$n = 2 - \frac{WA}{\pi} \text{ , and} \qquad (2.18)$$

$$R_{s,h} = \text{soft/hard reflection coefficient of the surface at } Q_E \text{ .}$$

The parameters and angles are indicated in Figure 4. Note that $N^\pm$ are integers which most nearly satisfy the equations

$$2\pi n N^+ - \beta = \pi \text{ , and} \qquad (2.19)$$

$$2\pi n N^- - \beta = -\pi \text{ .} \qquad (2.20)$$

The transition function is given by

$$F(x) = 2j\sqrt{x}e^{jkx}\int_{\sqrt{x}}^{\infty} e^{-j\tau^2}\, d\tau \qquad (2.21)$$

and is plotted in Figure 5. Note that $|F(x)| < 1$ in the transition region ($x < 2\pi$) and $F(x) \approx 1$ outside the transition region ($x > 2\pi$). If $x < 0$, then one finds that
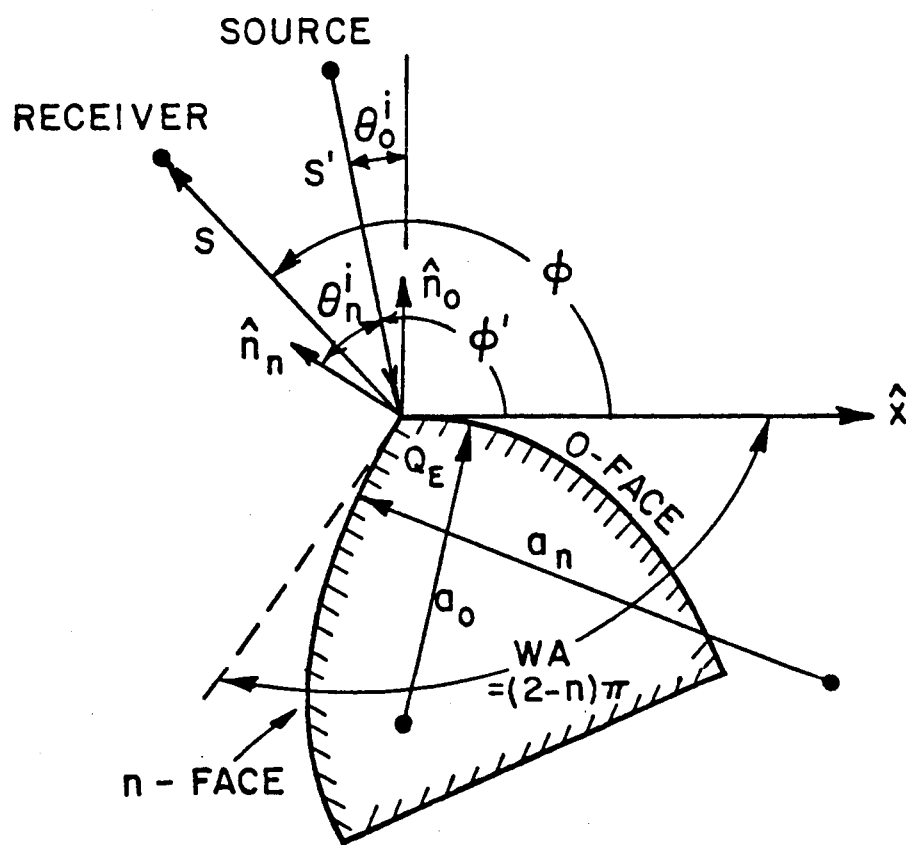
Figure 4: Two-dimensional wedge diffraction geometry.
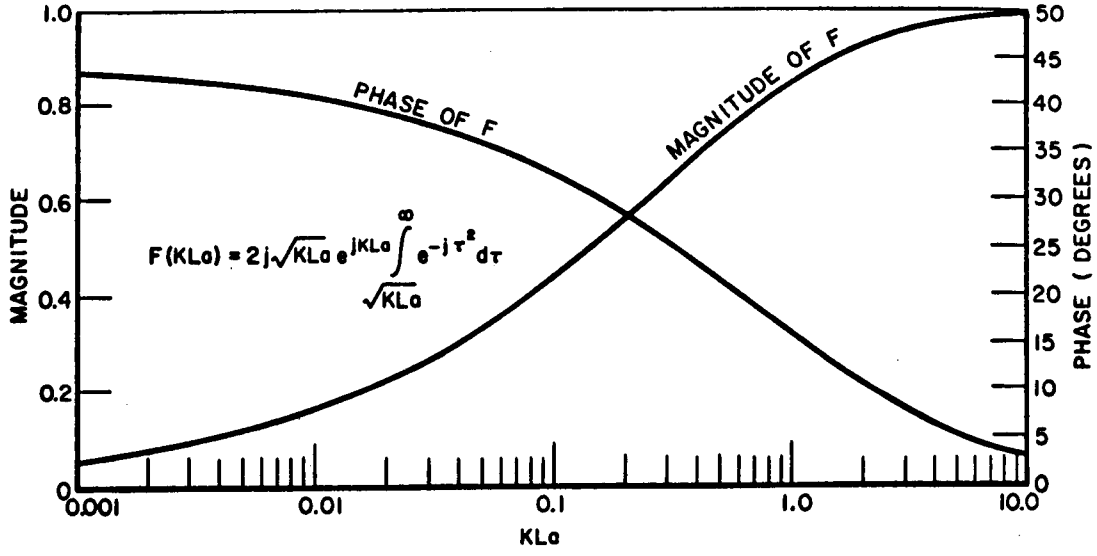
Figure 5: Wedge transition function.

$F(x) = F^*(|x|)$ where $*$ indicates the complex conjugate. The transition function is quite suitable for numerical evaluation[18]. The rest of the relevant parameters are as follows:

$$L^i = \frac{s' \, s}{s' + s} \tag{2.22}$$

$$L^{ro} = \frac{\rho_o^r \, s}{\rho_o^r + s} \tag{2.23}$$

$$\frac{1}{\rho_o^r} = \frac{1}{s'} + \frac{2}{a_o \cos \theta_o^i} \tag{2.24}$$

$$L^{rn} = \frac{\rho_n^r \, s}{\rho_n^r + s} \tag{2.25}$$

$$\frac{1}{\rho_n^r} = \frac{1}{s'} + \frac{2}{a_n \cos \theta_n^i} \tag{2.26}$$

a_o = radius of curvature of the o-face at Q_E

a_n = radius of curvature of the n-face at Q_E

$\rho_{o,n}^r$ = principal radii of curvature of the reflected

wavefront at Q_E in the plane of incidence

from the o and n faces, respectively

14

$$\phi' = \text{the incident angle with respect to the } o\text{-face}$$

$$\phi = \text{the diffraction angle with respect to the } o\text{-face}$$

$$s' = \text{the distance between the source and } Q_E$$

$$s = \text{the distance between the field point and } Q_E$$

$$\theta_o^i = \text{the angle defined by } \hat{\mathbf{n}}_o \cdot \hat{\mathbf{s}}' = -\cos\theta_o^i$$

$$\text{with } \cos\theta_o^i \geq 0 \tag{2.27}$$

$$\theta_n^i = \text{the angle defined by } \hat{\mathbf{n}}_n \cdot \hat{\mathbf{s}}' = -\cos\theta_n^i$$

$$\text{with } \cos\theta_n^i \geq 0 \text{ , and} \tag{2.28}$$

$$\hat{\mathbf{n}}_{o,n} = \text{the unit vectors normal to the}$$

$$o \text{ and } n\text{-faces at } Q_E, \text{ respectively .}$$

The transition regions around the incident and reflected shadow boundaries are shown in Figure 6. Note that these shadow boundaries occur at $\phi \mp \phi' = \pi$, respectively. The diffracted fields have maximum amplitudes along the shadow boundaries, and are strong inside the transition regions. Outside the transition regions the diffracted fields decay rapidly.

As shown in Equation (2.10), the first order diffraction solution is directly dependent on the magnitude of the field incident on the edge of the wedge. This expression may lead one to believe that if a null field is incident on the edge, then the edge diffracted field is zero. This is not the case, however, in that the slope of the incident field will create currents on the wedge surface which result in a slope diffracted field[19,20,21]. This diffraction is known as "slope diffraction", and is given by

$$U_z^d(s) = \frac{1}{jks'} \frac{\partial D_{s,h}}{\partial\phi'} \frac{\partial U_z^i}{\partial\phi'}(Q_E) \frac{e^{-jks}}{\sqrt{s}} \tag{2.29}$$

15
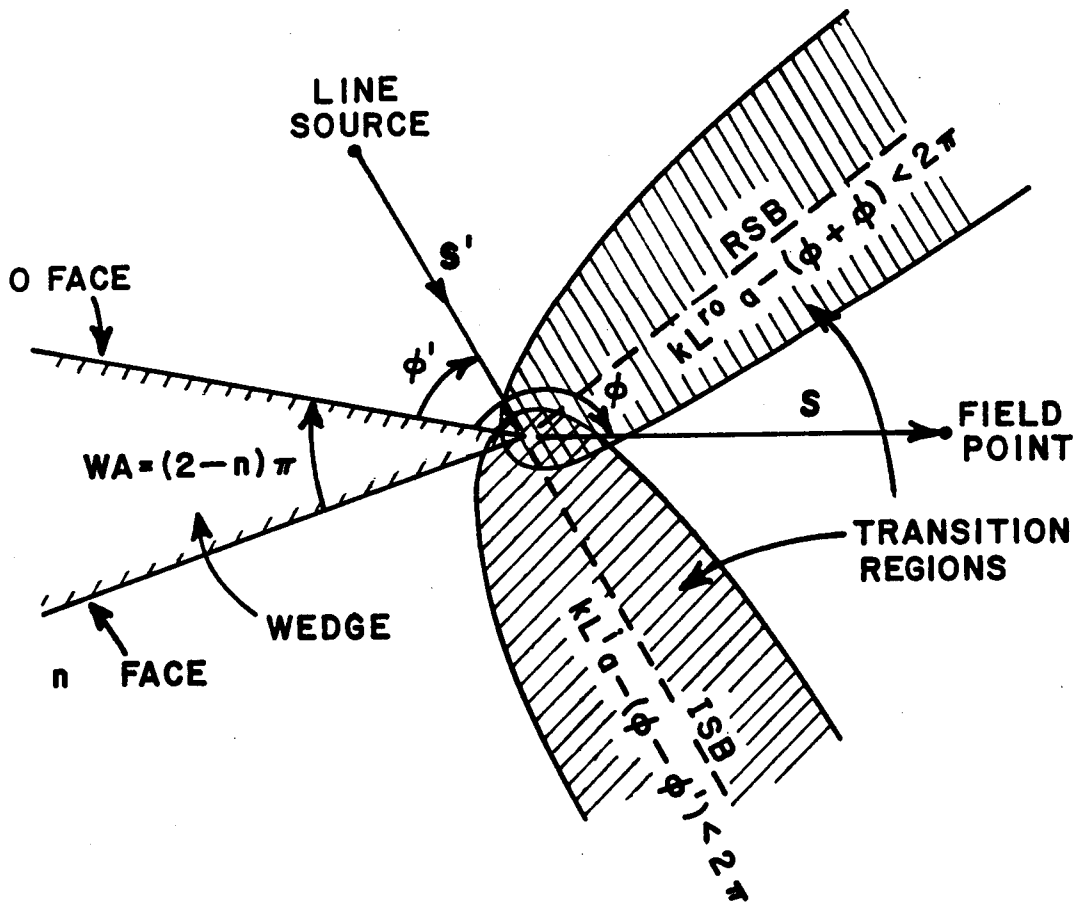
Figure 6: Transition regions around the shadow boundaries.

where $\partial D_{s,h}/\partial\phi'$ are the slope diffraction coefficients for the soft and hard cases, respectively, and $\partial U_z^i/\partial\phi'$ is the derivative of the incident field in the direction of the edge at Q_E as shown in Figure 7. From Equation (2.29) it is clear that the magnitude of the slope diffracted fields are proportional to the slope of the incident fields. The general form of the slope diffraction coefficients are given by

$$
\begin{aligned}
\frac{\partial D_{s,h}}{\partial\phi'} = \frac{-e^{-jk\pi/4}}{4n^2\sqrt{2\pi k}} \Bigg\{ &\Bigg[\csc^2\left(\frac{\pi+\beta^-}{2n}\right) F_s[kL^i a^+(\beta^-)] \\
&- \csc^2\left(\frac{\pi-\beta^-}{2n}\right) F_s[kL^i a^-(\beta^-)] \Bigg] \\
&- R_{s,h}\Bigg[\csc^2\left(\frac{\pi+\beta^+}{2n}\right) F_s[kL^{rn} a^+(\beta^+)] \\
&- \csc^2\left(\frac{\pi-\beta^+}{2n}\right) F_s[kL^{ro} a^-(\beta^+)] \Bigg] \Bigg\}
\end{aligned}
\tag{2.30}
$$

where $\beta^\pm$ and $a^\pm$ are given in Equations (2.16) and (2.17), and

$$
F_s(x) = 2jx[1 - F(x)] .
\tag{2.31}
$$

2.3 Physical Optics

2.3.1 Theory of physical optics

An electromagnetic wave that impinges upon an object induces electric and magnetic currents on that object. These induced currents flow in accordance with Maxwell's equations and the prevailing boundary conditions and in turn act as the sources of a secondary field known as the "scattered field". The Physical Optics (PO) method obtains the scattered field by summing the contributions of all the current elements. For example, the field radiated by a reflector antenna can be calculated by the PO method if the currents induced on the reflector surface by the incident illumination from the feed can be found.

17

LINE SOURCE

$$\frac{\partial}{\partial n} \quad \text{LIES IN } \mathbf{n} \text{ DIRECTION}$$

$$\frac{\partial}{\partial n} = \frac{1}{s'} \frac{\partial}{\partial \phi'}$$
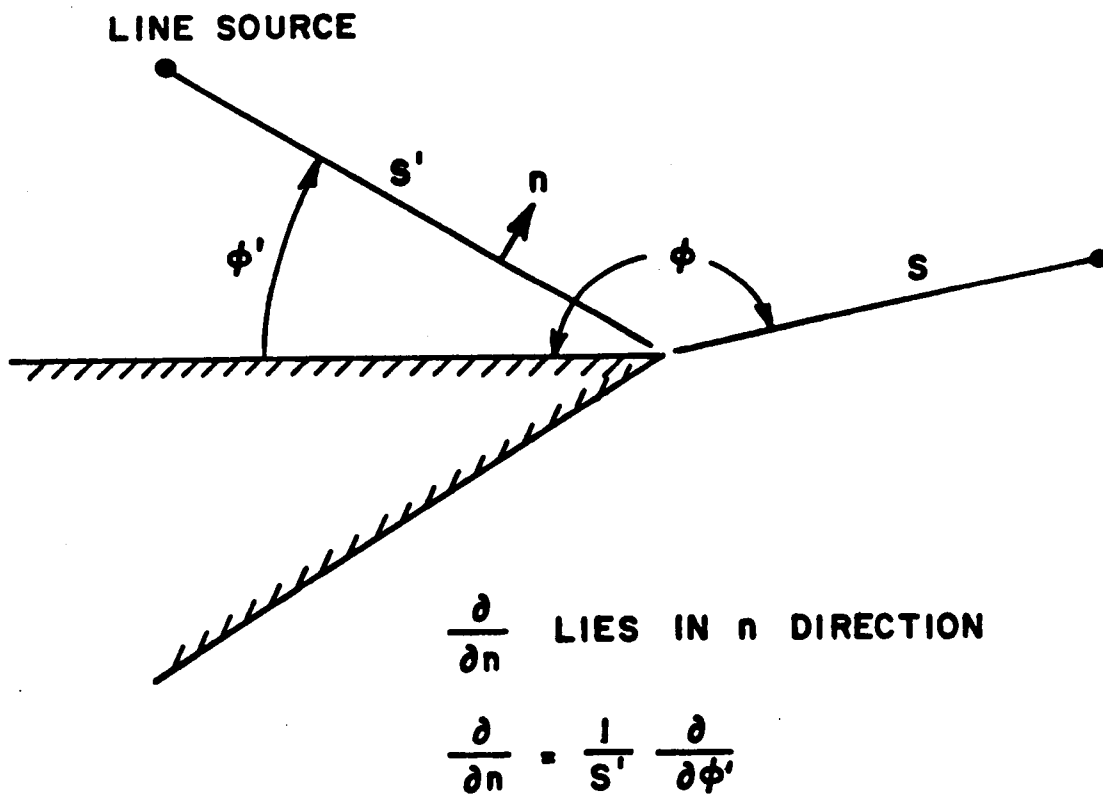
Figure 7: Geometry for slope diffracted fields.

18

Consider now the magnetic field resulting from the vector potential ($\mathbf{A}$), which is given by [22]

$$\mathbf{H} = \nabla \times \mathbf{A} \qquad (2.32)$$

where

$$\mathbf{A}(\mathbf{r}_{fp}) = \iint \frac{\mathbf{J}_s(\mathbf{r}')}{4\pi|\mathbf{r}_{fp} - \mathbf{r}'|} e^{-jk|\mathbf{r}_{fp}-\mathbf{r}'|} \, dS' \qquad (2.33)$$

$$\mathbf{J}_s \;\; = \;\; \text{induced surface current , and}$$

$$\mathbf{r}_{fp} \;\; = \;\; \text{field point .}$$

In the PO format, the integration is carried out only over the illuminated portion of the surface. The far zone scattered electric field is then given by [23]

$$\mathbf{E}^s(\mathbf{r}_{fp}) \approx -j\,kZ_0\,\mathbf{A}^t \qquad (2.34)$$

where the far zone transverse vector potential $\mathbf{A}^t$ is the component of $\mathbf{A}$ which is transverse to the direction of propagation; ie.,

$$\mathbf{A}^t \;\; = \;\; \mathbf{A} - (\mathbf{A} \cdot \hat{\mathbf{r}}^s)\hat{\mathbf{r}}^s \;\; , \text{ and} \qquad (2.35)$$

$$\hat{\mathbf{r}}^s \;\; = \;\; \text{direction of scattered propagation .}$$

Note that this definition for the electric field requires that the field point be in the far field of the source current.

In general, the current induced on the surface is given by

$$\mathbf{J}_s = \hat{\mathbf{n}} \times \mathbf{H}^t \qquad (2.36)$$

where

$$\hat{\mathbf{n}} \;\; = \;\; \text{unit vector normal to surface , and}$$

$$\mathbf{H}^t \;\; = \;\; \text{total magnetic field on the surface .}$$

19

The total magnetic field on the surface can be approximated by making a tangent plane approximation; ie., the surface fields are assigned the values that they would have if the body had been perfectly smooth and flat at the surface patch of integration. This tangential approximation restricts the application of the PO method to cases where the surface radius of curvature is large compared to the wavelength; ie., there is a lower frequency limit. Since it is assumed that the reflector surface is perfectly conducting, it follows from the application of the boundary conditions at the surface and image theory that the following conditions hold on the surface:

$$\hat{n} \times \mathbf{E}^t = 0 \tag{2.37}$$

$$\hat{n} \times \mathbf{H}^r = \hat{n} \times \mathbf{H}^i \tag{2.38}$$

where

$$\mathbf{E}^t = \text{total electric field on the surface}$$

$$\mathbf{H}^i = \text{incident magnetic field on the surface , and}$$

$$\mathbf{H}^r = \text{reflected magnetic field on the surface}$$

so that

$$\mathbf{J}_s = \begin{cases} 2\,\hat{n} \times \mathbf{H}^i & \text{in the illuminated region} \\ 0 & \text{in the shadow region .} \end{cases} \tag{2.39}$$

This is known as the "physical optics approximation", and is valid when the radius of curvature of the surface is large compared to a wavelength. The incident magnetic field on the surface is taken to be the geometrical optics field.

Consider now an illuminated body as shown in Figure 8. Let the magnetic field incident on the body be a plane wave which is given by

$$\mathbf{H}^i(\mathbf{r}) = \mathbf{H}_0\, e^{-jk\hat{k}\cdot\mathbf{r}} \tag{2.40}$$

20
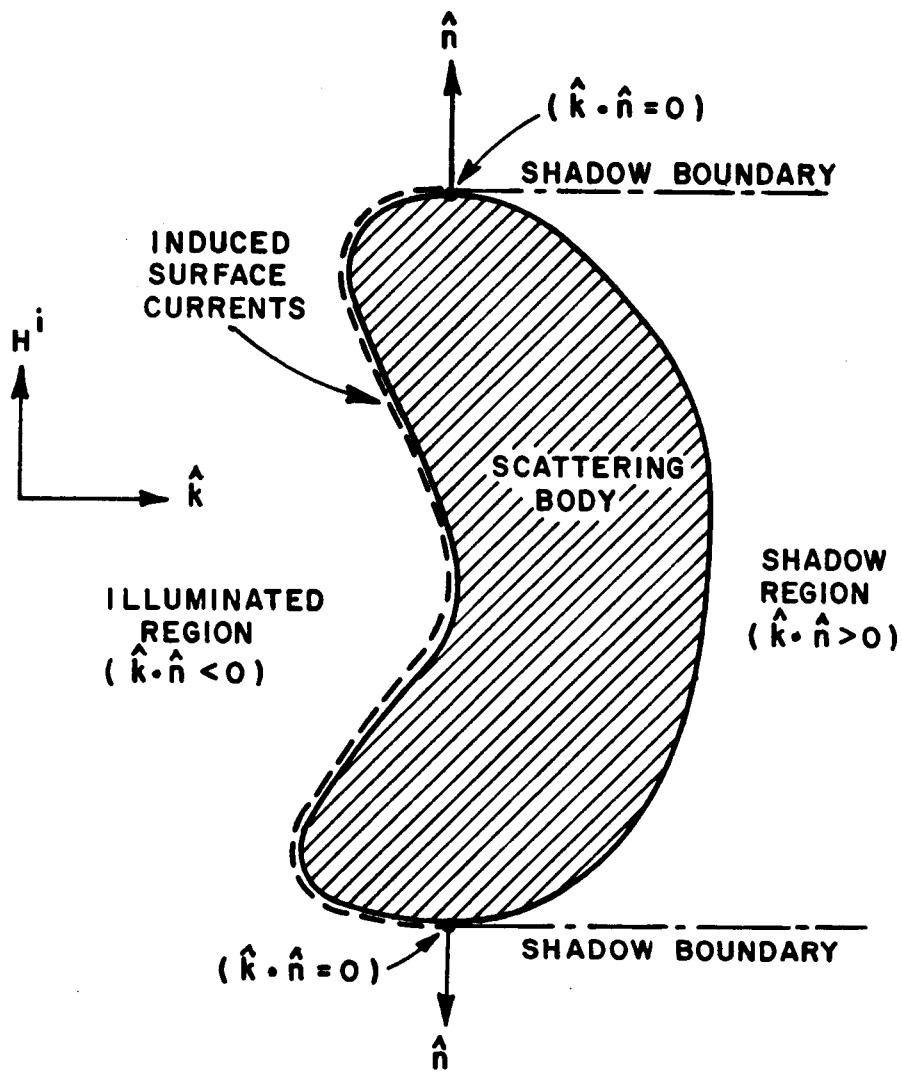
Figure 8: Illuminated portion of scattering body used for PO calculation.

where **r** is a position vector and $\hat{k}$ the direction of propagation of the incident field. The illuminated and shadow regions on the surface are determined by

$$\hat{n} \cdot \hat{k} \begin{cases} < 0 & \text{in the illuminated region} \\ = 0 & \text{on the shadow boundary , and} \\ > 0 & \text{in the shadow region .} \end{cases} \qquad (2.41)$$

Note that the PO approximation assumes that $\mathbf{J}_s$ is zero in the shadow region; ie., there is an abrupt discontinuity in the assumed value of $\mathbf{J}_s$ across the shadow boundary, although the true current is smooth and continuous across this boundary. This discrepancy introduces an error in the result obtained from the PO method which creates false scattering centers at the incident shadow boundaries. A way to compensate for this error will be discussed in Section 2.3.3. A similar problem occurs in bodies with edges, in that the PO assumption for $\mathbf{J}_s$ near the edges is not correct. The Physical Theory of Diffraction (PTD) [24] has been developed to compensate for this error.

2.3.2 Scattered field from a surface patch

In order to calculate the scattered fields of a reflector antenna using a PO approach, one normally models the surface of the antenna by small planar patches. Triangular patches are useful, since the three corners of such a patch lie in a flat plane, and a unique vector normal to the patch can thus be constructed. This is not always possible with patches that have more than three corners. The patches are considered to be very small in terms of a wavelength, so that it can be assumed that each patch is illuminated by a local plane wave, and that the field point is in the far zone of the patch. The total field at a field point is then obtained by summing the contributions of all the illuminated patches on the reflector surface.

22

Let a patch be located in its own local coordinate system as shown in Figure 9, with $\mathbf{r}'$ the position vector of a point on the surface of the patch in local coordinates. Consider now a triangular patch in the far zone of a point source. The incident field on the patch is considered to be a *local* plane wave, so that it can be expressed as

$$\mathbf{E}^i(\mathbf{r}') = \frac{\mathbf{e}^i(\theta, \phi)}{R^i} e^{-jk(R^i + \hat{\mathbf{r}}^i \cdot \mathbf{r}')} \tag{2.42}$$

where

$$R^i \;\; = \;\; \text{distance from the feed to the local origin on the patch}$$

$$\hat{\mathbf{r}}^i \;\; = \;\; \text{unit vector in the direction from the feed to the local patch origin}$$

$$\mathbf{e}^i(\theta, \phi) \;\; = \;\; \text{polarization and magnitude of the incident electric field}$$

$$\text{independent of } R^i \text{, and}$$

$$\theta, \phi \;\; = \;\; \text{angular dependence of the incident electric field .}$$

Since the incident electric field is assumed to be a local plane wave, the incident magnetic field on the patch is given by

$$\mathbf{H}^i(\mathbf{r}') = Y_0 \, \hat{\mathbf{r}}^i \times \mathbf{E}^i(\mathbf{r}') = \frac{Y_0}{R^i} e^{-jk(R^i + \hat{\mathbf{r}}^i \cdot \mathbf{r}')} \mathbf{h}^i \tag{2.43}$$

where

$$\mathbf{h}^i = \hat{\mathbf{r}}^i \times \mathbf{e}^i . \tag{2.44}$$

Making the PO approximation, the induced surface current on the patch is given by

$$\mathbf{J}_s(\mathbf{r}') = 2 \, \hat{\mathbf{n}}(\mathbf{r}') \times \mathbf{H}^i(\mathbf{r}') = \frac{2Y_0}{R^i} e^{-jk(R^i + \hat{\mathbf{r}}^i \cdot \mathbf{r}')} \hat{\mathbf{n}} \times \mathbf{h}^i . \tag{2.45}$$

The vector potential at the field point is then given by

$$\mathbf{A}(\mathbf{r}_{fp}) = \iint \frac{\mathbf{J}_s(\mathbf{r}')}{4\pi R^s} e^{-jk(R^s - \hat{\mathbf{r}}^s \cdot \mathbf{r}')} \, dS' \tag{2.46}$$

23
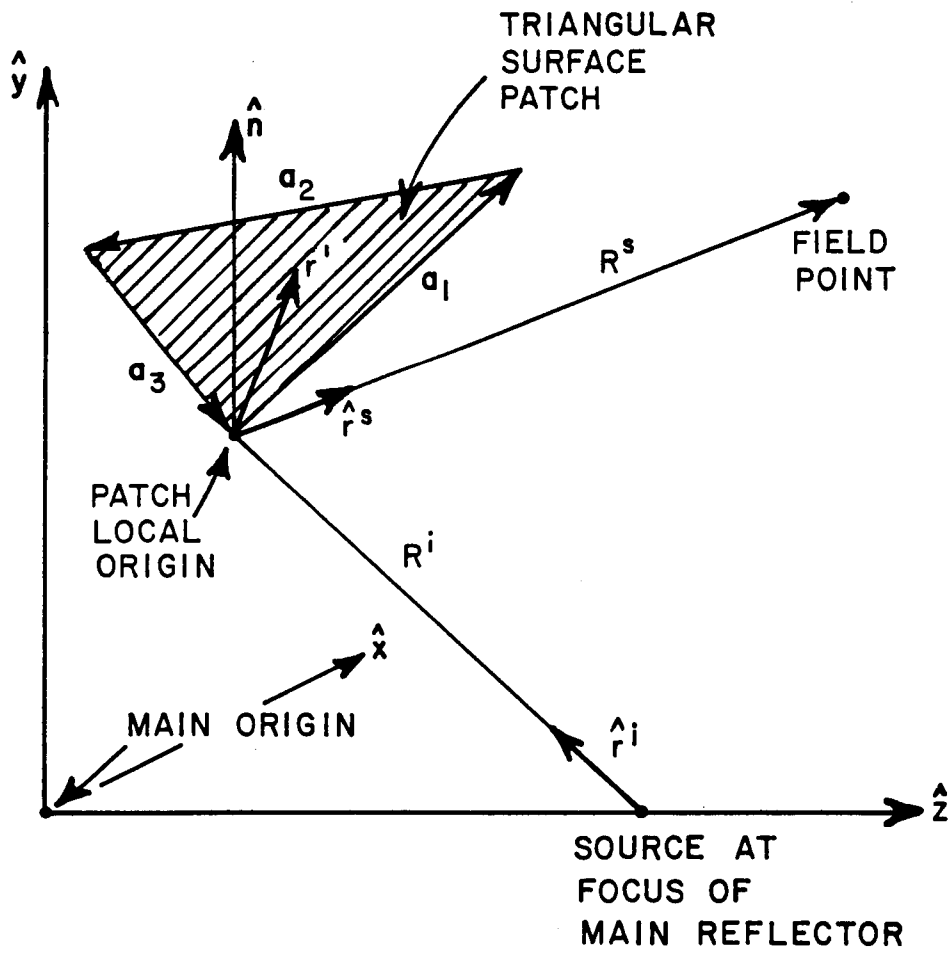
Figure 9: Surface patch coordinate system.

where the integration is performed over the entire surface of the patch, and

$$R^s = \text{distance from the local origin to the field point , and}$$

$$\hat{\mathbf{r}}^s = \text{unit vector in the direction from the}$$

local origin to the field point .

Substituting for $\mathbf{J}_s$, one finds that

$$\mathbf{A}(\mathbf{r}_{fp}) = \frac{Y_0\, I}{2\pi R^i R^s} e^{-jk(R^i + R^s)} \hat{\mathbf{n}} \times \mathbf{h}^i \qquad (2.47)$$

where

$$I = \iint_{patch} e^{jk(\hat{\mathbf{r}}^s - \hat{\mathbf{r}}^i)} dS' \; . \qquad (2.48)$$

By invoking Stokes' theorem, I can be converted from a surface integral to a line integral[4,25], so that

$$I = \begin{cases} -(j/kT)\sum_{m=1}^{3}(\hat{\mathbf{p}} \cdot \mathbf{a}_m) e^{jk\mathbf{r}_m \cdot \mathbf{w}} \; \text{sinc}(\tfrac{k}{2}\mathbf{a}_m \cdot \mathbf{w}) & \text{if } T \neq 0 \text{ , and} \\[2em] |\mathbf{a}_1 \times \mathbf{a}_2|/2 & \text{if } T = 0 \end{cases} \qquad (2.49)$$

where

$$\mathbf{a}_m = \text{vector describing the length and orientation of}$$

the m-th edge of the patch, arranged tip to tail

in a counter-clockwise direction

$$\mathbf{r}_m = \text{position vector of the midpoint of the } m\text{-th edge}$$

$$\mathbf{w} = \hat{\mathbf{r}}^s - \hat{\mathbf{r}}^i \qquad (2.50)$$

$$\hat{\mathbf{p}} = \frac{\hat{\mathbf{n}} \times \mathbf{w}}{|\hat{\mathbf{n}} \times \mathbf{w}|} \qquad (2.51)$$

$$\hat{\mathbf{n}} = \text{unit vector normal to the plate} = \frac{\mathbf{a}_1 \times \mathbf{a}_2}{|\mathbf{a}_1 \times \mathbf{a}_2|} \qquad (2.52)$$

$$T = \text{length of the projection of } \mathbf{w} \text{ onto the}$$

$$\text{plane of the patch} = |\mathbf{w} - (\mathbf{w} \cdot \hat{n})\hat{n}| \text{ , and} \qquad (2.53)$$

$$\mathrm{sinc}(x) \;=\; \frac{\sin x}{x} \; . \qquad (2.54)$$

Note that the closed form expression above can be used for a flat plate with an arbitrary number of edges, as long it is illuminated by a plane wave and the field point is in the far zone of the patch.

The far zone transverse vector potential is thus given by

$$\mathbf{A}^{t}(\mathbf{r}_{fp}) = \frac{Y_0 I}{2\pi R^i R^s} e^{-jk(R^i + R^s)} [\hat{n} \times \mathbf{h}^i - (\hat{n} \times \mathbf{h}^i \cdot \hat{\mathbf{r}}^s)\hat{\mathbf{r}}^s] \qquad (2.55)$$

so that the resulting scattered electric field at the field point can be expressed as

$$\mathbf{E}^{s}_{patch}(\mathbf{r}_{fp}) = \frac{-jkI}{2\pi R^i R^s} e^{-jk(R^i + R^s)} \mathbf{e}^{s} \qquad (2.56)$$

where

$$\mathbf{e}^{s} = \hat{n} \times \mathbf{h}^i - (\hat{n} \times \mathbf{h}^i \cdot \hat{\mathbf{r}}^s)\hat{\mathbf{r}}^s \; . \qquad (2.57)$$

The total scattered electric field at the field point is then given by the contributions from all the surface patches making up the illuminated part of the surface; ie.,

$$\mathbf{E}^{s}_{total}(\mathbf{r}_{fp}) = \sum_{reflector\ surface} \mathbf{E}^{s}_{patch}(\mathbf{r}_{fp}) \; . \qquad (2.58)$$

2.3.3 Subtraction of the end point contributions

The abrupt termination of the induced surface currents at the incident shadow boundary causes the creation of false scattering centers which will corrupt the true pattern of the scattered field. The end point contributions have been known to exist for some time. However, most authors have assumed that the end point contributions from curved surfaces are insignificant in that the PO integrand goes to zero for grazing incidence and scatter. Gupta and Burnside[26] have shown that this is not the case, however. In order to demonstrate how this error can be

26

corrected, consider a 3-dimensional circular cylinder with radius (a) and length (l) as shown in Figure 10. Let the cylinder be illuminated by a plane wave. The electric field incident on the cylinder ($\mathbf{E}^i$) is then given by

$$\mathbf{E}^i(\mathbf{n}) = e^{-jk(R^i + \hat{\mathbf{r}}^i \cdot \mathbf{n})} \mathbf{e}^i(\mathbf{n}) \tag{2.59}$$

where

$$
\begin{aligned}
\mathbf{e}^i(\mathbf{n}) &= \text{polarization and amplitude of } \mathbf{E}^i \text{ at } \mathbf{n} \\
R^i &= \text{distance from the far zone source phase reference to the origin} \\
\mathbf{n}(\phi_n, z_n) &= \text{position on the cylinder, or} \\
\mathbf{n}(\phi_n, z_n) &= a\cos\phi_n\hat{\mathbf{x}} + a\sin\phi_n\hat{\mathbf{y}} + z_n\hat{\mathbf{z}} \text{ , and} \\
\hat{\mathbf{r}}^i(\theta_i, \phi_i) &= \text{incident field propagation direction, or} \\
\hat{\mathbf{r}}^i(\theta_i, \phi_i) &= -(\sin\theta_i\cos\phi_i\hat{\mathbf{x}} + \sin\theta_i\sin\phi_i\hat{\mathbf{y}} + \cos\theta_i\hat{\mathbf{z}}) \text{ .}
\end{aligned}
$$

$$(2.60)$$

$$(2.61)$$

The incident electric and magnetic fields are related by

$$\mathbf{H}^i = Y_0\, \hat{\mathbf{r}}^i \times \mathbf{E}^i \tag{2.62}$$

such that the magnetic field incident on the cylinder can be expressed as

$$\mathbf{H}^i(\mathbf{n}) = Y_0\, e^{-jkR^i} e^{jk[a\sin\theta_i\cos(\phi_i - \phi_n) + z_n\cos\theta_i]} (\hat{\mathbf{r}}^i \times \mathbf{e}^i) \text{ .} \tag{2.63}$$

The current induced on the surface of the cylinder ($\mathbf{J}_s$) is given by the PO approximation as

$$\mathbf{J}_s(\mathbf{n}) = 2\,\hat{\mathbf{n}}(\phi_n) \times \mathbf{H}^i(\mathbf{n}) \tag{2.64}$$

or

$$\mathbf{J}_s(\mathbf{n}) = 2Y_0 e^{-jkR^i} \hat{\mathbf{n}}(\phi_n) \times (\hat{\mathbf{r}}^i \times \mathbf{e}^i) e^{jk[a\sin\theta_i\cos(\phi_i - \phi_n) + z_n\cos\theta_i]} \tag{2.65}$$
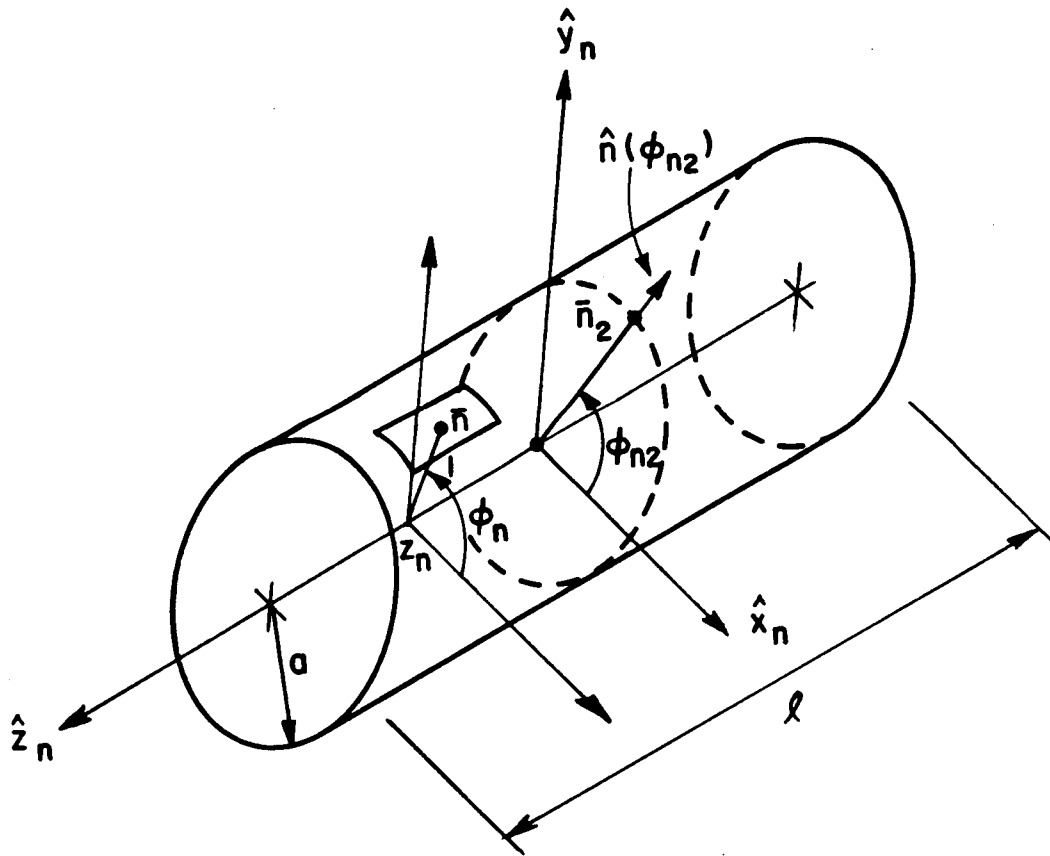
Figure 10: Finite circular cylinder geometry.

where the unit vector normal to the surface of the cylinder ($\hat{\mathbf{n}}$) is given by

$$\hat{\mathbf{n}}(\phi_n) = \cos\phi_n\hat{\mathbf{x}} + \sin\phi_n\hat{\mathbf{y}} \ . \tag{2.66}$$

Notice that $\hat{\mathbf{n}}(\phi_n) \times (\hat{\mathbf{r}}^i \times \mathbf{e}^i)$ is independent of z_n.

The vector potential at the far zone field point is given by Equation (2.33), so that

$$\mathbf{A}(\hat{\mathbf{r}}^s, R^s) = \iint \frac{\mathbf{J}_s(\mathbf{n})}{4\pi R^s} e^{-jk[R^s - \hat{\mathbf{r}}^s \cdot \mathbf{n}]} dS_n \tag{2.67}$$

where the integral is taken over the illuminated part of the cylinder, and

$$R^s \quad = \quad \text{distance from the origin to the far zone field point}$$

$$\hat{\mathbf{r}}^s(\theta_s, \phi_s) \quad = \quad \text{scattered field propagation direction, or}$$

$$\hat{\mathbf{r}}^s(\theta_s, \phi_s) \quad = \quad \sin\theta_s\cos\phi_s\hat{\mathbf{x}} + \sin\theta_s\sin\phi_s\hat{\mathbf{y}} + \cos\theta_s\hat{\mathbf{z}} \ , \text{ and} \tag{2.68}$$

$$dS_n \quad = \quad a\, d\phi_n\, dz_n \ . \tag{2.69}$$

Thus, the vector potential is given by

$$\mathbf{A} = \frac{aY_0}{2\pi R^s} e^{-jk(R^i + R^s)} I_z\, \mathbf{I}_\phi^a \tag{2.70}$$

where

$$I_z \quad = \quad \int_{-l/2}^{l/2} e^{jkz_n(\cos\theta_i + \cos\theta_s)}\, dz_n = l\, \text{sinc}(k\psi) \tag{2.71}$$

$$\psi(\theta_i, \theta_s) \quad = \quad \frac{l}{2}(\cos\theta_i + \cos\theta_s) \tag{2.72}$$

$$\mathbf{I}_\phi^a \quad = \quad \int_{\phi_{n1}}^{\phi_{n2}} \hat{\mathbf{n}}(\phi_n) \times \mathbf{h}^i e^{jka\beta}\, d\phi_n \ , \text{ and} \tag{2.73}$$

$$\beta \quad = \quad [\sin\theta_s\cos(\phi_s - \phi_n) + \sin\theta_i\cos(\phi_i - \phi_n)] \ . \tag{2.74}$$

The angles (ϕ_{n1}, ϕ_{n2}) define the illuminated part of the cylinder. Note that in some cases, eg., axial backscatter from a body of revolution, it is advantageous to treat the finite cylinder as an infinitesimal cylinder and then evaluate I_z in the appropriate coordinate system.

The scattered electric field in the far zone is given by Equation (2.34) such that

$$\mathbf{E}^s \approx -j\, kZ_0\, \mathbf{A}^t \ . \tag{2.75}$$

Let $\mathbf{e}^s(\phi_n)$ be the component of $\hat{\mathbf{n}}(\phi_n) \times (\hat{\mathbf{r}}^i \times \mathbf{e}^i)$ that is transverse to $\hat{\mathbf{r}}^s$; ie.,

$$\mathbf{e}^s(\phi_n) = \hat{\mathbf{n}}(\phi_n) \times (\hat{\mathbf{r}}^i \times \mathbf{e}^i) - [\hat{\mathbf{n}}(\phi_n) \times (\hat{\mathbf{r}}^i \times \mathbf{e}^i) \cdot \hat{\mathbf{r}}^s]\hat{\mathbf{r}}^s \ . \tag{2.76}$$

The scattered electric field is then given by

$$\mathbf{E}^s = \frac{-jka e^{-jk(R^i+R^s)}\mathbf{I}_\phi I_z}{2\pi R^s} \tag{2.77}$$

where

$$\mathbf{I}_\phi = \int_{\phi_{n1}}^{\phi_{n2}} \mathbf{e}^s(\phi_n) e^{jka[\sin\theta_s \cos(\phi_s-\phi_n)+\sin\theta_i \cos(\phi_i-\phi_n)]} d\phi_n \ . \tag{2.78}$$

The integral ($\mathbf{I}_\phi$) can be evaluated by the method of stationary phase [27], which can briefly be described as follows. Consider the integral given by

$$I_\phi(k) = \int_{\phi_{n1}}^{\phi_{n2}} F_0(\phi_n) e^{jk\Phi(\phi_n)} d\phi_n \tag{2.79}$$

where

$$\phi_n \quad = \quad \text{real variable}$$

$$k \quad = \quad \text{real, positive and large}$$

$$F_0(\phi_n) \quad = \quad \text{slowly varying amplitude function that is}$$

well behaved in the range of integration , and

$$\Phi(\phi_n) \quad = \quad \text{phase term that is real and continuous with}$$

continuous derivatives in the range of integration .

For large k, $I_\phi(k)$ can be asymptotically approximated by

$$I_\phi \sim I_{sp} + I_e(\phi_{n2}) + I_e(\phi_{n1}) \tag{2.80}$$

30

where

$$I_{sp} = \text{stationary point contribution , and}$$

$$I_e(\phi_{n1,n2}) = \text{end point contributions .}$$

The stationary point contribution is given by

$$I_{sp} = F_0(\phi_{ns})\sqrt{\frac{2\pi}{k \mid \Phi''(\phi_{ns}) \mid}} e^{j[k\Phi(\phi_{ns})+\frac{\pi}{4}\text{sgn}\Phi''(\phi_{ns})]} \tag{2.81}$$

where the stationary point (at ϕ_{ns}) satisfies

$$\frac{d\Phi(\phi_{ns})}{d\phi_n} = \Phi'(\phi_{ns}) = 0 . \tag{2.82}$$

The end point contributions are given by Gupta and Burnside[26] as

$$I_e(k) = \sum_{m=0}^{\infty} \left[\frac{(-1)^m F_m(\phi_n) e^{jk\Phi(\phi_n)}}{jk\Phi'(\phi_n)} \right]_{\phi_{n1}}^{\phi_{n2}} \tag{2.83}$$

where

$$F_m(\phi_n) = \frac{d}{d\phi_n}\left[\frac{F_{m-1}(\phi_n)}{jk\Phi'(\phi_n)}\right], \text{ for } m \geq 1 . \tag{2.84}$$

Applying the expressions above to $\mathbf{I}_\phi$, one finds that

$$\mathbf{F}_0(\phi_n) = \mathbf{e}^s(\phi_n) \tag{2.85}$$

$$\Phi(\phi_n) = a[\sin\theta_s\cos(\phi_s - \phi_n) + \sin\theta_i\cos(\phi_i - \phi_n)] \tag{2.86}$$

$$\Phi'(\phi_n) = a[\sin\theta_s\sin(\phi_s - \phi_n) + \sin\theta_i\sin(\phi_i - \phi_n)] , \text{ and} \tag{2.87}$$

$$\Phi''(\phi_n) = -\Phi(\phi_n) . \tag{2.88}$$

Note that the vector notation merely serves to combine three scalar equations into one vector equation.

The numerical computation of the PO integral as described in Section 2.3.2 yields $\mathbf{I}_\phi$ as expressed in Equation (2.80). The "true" scattered field is represented

31

by the stationary point contribution and can be obtained by subtracting the end point contributions from $\mathbf{I}_\phi$, since the end point contributions represent the false scattering centers at the incident shadow boundaries. For the purpose of this derivation it is assumed that the shadow boundary of interest occurs at ϕ_{n2}. The first two terms of the end point contributions ($\mathbf{I}_e^0$ and $\mathbf{I}_e^1$) are determined next.

a) First term (m=0)

The first term of the end point contribution is given by

$$\mathbf{I}_e^0(\phi_{n2}) = \frac{\mathbf{F}_0(\phi_{n2})e^{jk\Phi(\phi_{n2})}}{jk\Phi'(\phi_{n2})} \tag{2.89}$$

or

$$\mathbf{I}_e^0(\phi_{n2}) = \frac{\mathbf{e}^s(\phi_{n2})e^{jka[\sin\theta_s\cos(\phi_s-\phi_{n2})+\sin\theta_i\cos(\phi_i-\phi_{n2})]}}{jka[\sin\theta_s\sin(\phi_s-\phi_{n2})+\sin\theta_i\sin(\phi_i-\phi_{n2})]} \; . \tag{2.90}$$

The first term of the end point contribution at ϕ_{n2} to the far zone scattered electric field ($\mathbf{E}_0^s$) is thus given by

$$\mathbf{E}_0^s(\mathbf{n}_2) = e^{-jks'}\mathbf{D}_0^e(\phi_{n2})\frac{e^{-jks}}{s} \tag{2.91}$$

where

$$\mathbf{D}_0^e = I_z\mathbf{d}_0^e \tag{2.92}$$

and

$$\mathbf{d}_0^e(\phi_{n2}) \;=\; \frac{-\mathbf{e}^s(\phi_{n2})}{2\pi[\sin\theta_s\sin(\phi_s-\phi_{n2})+\sin\theta_i\sin(\phi_i-\phi_{n2})]} \tag{2.93}$$

$$\mathbf{n}_2 \;=\; \mathbf{n}(\phi_{n2},0) = a\cos\phi_{n2}\hat{\mathbf{x}} + a\sin\phi_{n2}\hat{\mathbf{y}} \tag{2.94}$$

$$s' \;=\; \text{distance from the far zone source phase reference to } \mathbf{n}_2, \text{ or}$$

$$s' \;=\; R^i - a\sin\theta_i\cos(\phi_i-\phi_{n2}) \; , \text{ and} \tag{2.95}$$

$$s \;=\; \text{distance from } \mathbf{n}_2 \text{ to the far zone field point, or}$$

$$s \;=\; R^s - a\sin\theta_s\cos(\phi_s-\phi_{n2}) \; . \tag{2.96}$$

The term $\mathbf{d}^e$ will be referred to as the "modified scattering coefficient". In the case of a finite scattering cylinder, one thus finds that

$$\mathbf{D}_0^e(\phi_{n2}) = \frac{-l \ \text{sinc}[\frac{kl}{2}(\cos\theta_s + \cos\theta_i)]\mathbf{e}^s(\phi_{n2})}{2\pi[\sin\theta_s \sin(\phi_s - \phi_{n2}) + \sin\theta_i \sin(\phi_i - \phi_{n2})]} \ . \qquad (2.97)$$

Note that this notation casts the end point contribution of the scattered electric field in terms of an end point scattering coefficient $(\mathbf{D}_0^e)$, evaluated on the surface of the cylinder, at the shadow boundary in the $x_n y_n$–plane . The scalar components of the end point contribution of the scattered electric field are given by

$$E_{0p}^s(\mathbf{n}_2) = \mathbf{E}_0^s(\mathbf{n}_2) \cdot \hat{\mathbf{p}} = e^{-jks'} \ \mathbf{D}_0^e(\phi_{ns}) \cdot \hat{\mathbf{p}} \ \frac{e^{-jks}}{s} \qquad (2.98)$$

where $\hat{\mathbf{p}}$ represents each of the coordinate unit vectors; ie., $\hat{\mathbf{x}}$, $\hat{\mathbf{y}}$, and $\hat{\mathbf{z}}$. It is evident from Equations (2.91) and (2.97) that $\mathbf{D}_0^e$ (and therefore $\mathbf{E}_0^s$) is independent of the cylinder radius (a).

In general, let the axis of the cylinder be orientated along a unit vector $(\hat{\mathbf{e}})$. The previous equations can then be expressed in vector notation by using the following relationships:

$$\cos\theta_i \ = \ -\hat{\mathbf{r}}^i \cdot \hat{\mathbf{e}} \ , \text{ and} \qquad (2.99)$$

$$\cos\theta_s \ = \ \hat{\mathbf{r}}^s \cdot \hat{\mathbf{e}} \qquad (2.100)$$

so that

$$\cos\theta_s + \cos\theta_i = \hat{\mathbf{e}} \cdot (\hat{\mathbf{r}}^s - \hat{\mathbf{r}}^i) \ . \qquad (2.101)$$

Furthermore, since $0 \le \theta_{i,s} \le 180^o$, one finds that

$$\sin\theta_i \ = \ | \ \hat{\mathbf{r}}^i \times \hat{\mathbf{e}} \ | \ , \text{ and} \qquad (2.102)$$

$$\sin\theta_s \ = \ | \ \hat{\mathbf{r}}^s \times \hat{\mathbf{e}} \ | \ . \qquad (2.103)$$

Let the component of $\hat{\mathbf{r}}^i$ that is perpendicular to $\hat{\mathbf{e}}$ and directed away from $\hat{\mathbf{e}}$ be given by

$$\mathbf{r}_\perp^i = -(\hat{\mathbf{r}}^i - (\hat{\mathbf{r}}^i \cdot \hat{\mathbf{e}})\hat{\mathbf{e}}) \tag{2.104}$$

or

$$\hat{\mathbf{r}}_\perp^i = -\frac{\hat{\mathbf{r}}^i - (\hat{\mathbf{r}}^i \cdot \hat{\mathbf{e}})\hat{\mathbf{e}}}{|\hat{\mathbf{r}}^i - (\hat{\mathbf{r}}^i \cdot \hat{\mathbf{e}})\hat{\mathbf{e}}|} . \tag{2.105}$$

Similarly, let the component of $\hat{\mathbf{r}}^s$ that is perpendicular to $\hat{\mathbf{e}}$ and directed away from $\hat{\mathbf{e}}$ be given by

$$\mathbf{r}_\perp^s = \hat{\mathbf{r}}^s - (\hat{\mathbf{r}}^s \cdot \hat{\mathbf{e}})\hat{\mathbf{e}} \tag{2.106}$$

or

$$\hat{\mathbf{r}}_\perp^s = \frac{\hat{\mathbf{r}}^s - (\hat{\mathbf{r}}^s \cdot \hat{\mathbf{e}})\hat{\mathbf{e}}}{|\hat{\mathbf{r}}^s - (\hat{\mathbf{r}}^s \cdot \hat{\mathbf{e}})\hat{\mathbf{e}}|} \tag{2.107}$$

where the unit vectors $\hat{\mathbf{r}}_\perp^i$ and $\hat{\mathbf{r}}_\perp^s$ are shown in Figure 11. Furthermore, one finds that

$$\sin(\phi_s - \phi_{n2}) = (\hat{\mathbf{n}}(\phi_{n2}) \times \hat{\mathbf{r}}_\perp^s) \cdot \hat{\mathbf{e}} \tag{2.108}$$

$$\sin(\phi_i - \phi_{n2}) = (\hat{\mathbf{n}}(\phi_{n2}) \times \hat{\mathbf{r}}_\perp^i) \cdot \hat{\mathbf{e}} \tag{2.109}$$

$$\cos(\phi_s - \phi_{n2}) = \hat{\mathbf{r}}_\perp^s \cdot \hat{\mathbf{n}}(\phi_{n2}) , \text{ and} \tag{2.110}$$

$$\cos(\phi_i - \phi_{n2}) = \hat{\mathbf{r}}_\perp^i \cdot \hat{\mathbf{n}}(\phi_{n2}) . \tag{2.111}$$

The end point scattering coefficient can thus, in general, be expressed as

$$\mathbf{D}_0^e = I_z \mathbf{d}_0^e \tag{2.112}$$

where

$$\mathbf{d}_0^e(\phi_{n2}) = \frac{-\mathbf{e}^s(\phi_{n2})}{2\pi(|\hat{\mathbf{r}}^i \times \hat{\mathbf{e}}|(\hat{\mathbf{n}}(\phi_{n2}) \times \hat{\mathbf{r}}_\perp^i) \cdot \hat{\mathbf{e}} + |\hat{\mathbf{r}}^s \times \hat{\mathbf{e}}|(\hat{\mathbf{n}}(\phi_{n2}) \times \hat{\mathbf{r}}_\perp^s) \cdot \hat{\mathbf{e}})} . \tag{2.113}$$

In the case of a finite scattering cylinder, one thus finds that

$$\mathbf{D}_0^e(\phi_{n2}) = \frac{-l \ \mathrm{sinc}[\frac{kl}{2}\hat{\mathbf{e}} \cdot (\hat{\mathbf{r}}^s - \hat{\mathbf{r}}^i)]\mathbf{e}^s(\phi_{n2})}{2\pi(|\hat{\mathbf{r}}^i \times \hat{\mathbf{e}}|(\hat{\mathbf{n}}(\phi_{n2}) \times \hat{\mathbf{r}}_\perp^i) \cdot \hat{\mathbf{e}} + |\hat{\mathbf{r}}^s \times \hat{\mathbf{e}}|(\hat{\mathbf{n}}(\phi_{n2}) \times \hat{\mathbf{r}}_\perp^s) \cdot \hat{\mathbf{e}})} . \tag{2.114}$$
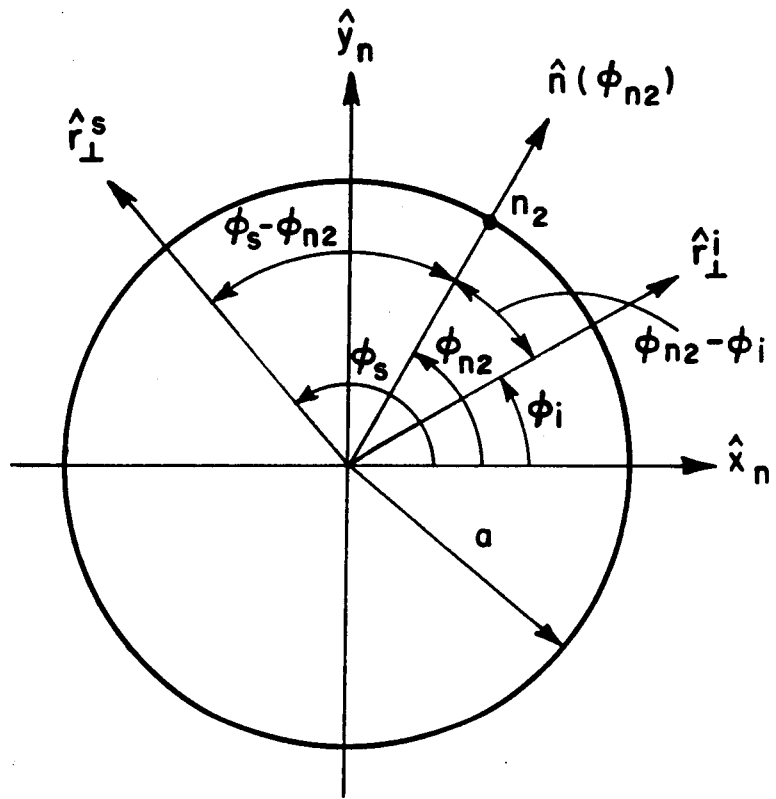
Figure 11: The $x_n y_n$-projection of the scattering cylinder.

The vector representation of Equation (2.114) is very convenient from a computational viewpoint, since the vectors need not necessarily be known in the cylinder's local coordinates.

Note that the incident field on the cylinder is considered to be a plane wave. If, however, the far zone source is a point source (as in Section 2.2) and the incident field on the cylinder is considered to be a local plane wave, then $\mathbf{e}^i$ can be replaced by

$$\mathbf{e}^i = \frac{\mathbf{e}_a^i}{R^i} \tag{2.115}$$

where $\mathbf{e}_a^i$ is the angular dependent part of $\mathbf{e}^i$. In this case, the far zone source phase reference will be the location of the point source.

b) Second term (m=1)

The second term of the end point contribution is given by

$$\mathbf{I}_e^1(\phi_{n2}) = \frac{-\mathbf{F}_1(\phi_{n2})e^{jk\Phi(\phi_{n2})}}{jk\Phi'(\phi_{n2})} \tag{2.116}$$

where

$$\mathbf{F}_1(\phi_{n2}) = \frac{d}{d\phi_n}\left[\frac{F_0(\phi_n)}{jk\Phi'(\phi_n)}\right]^{\phi_{n2}} \tag{2.117}$$

such that

$$\mathbf{I}_e^1(\phi_{n2}) = \left[\frac{(\Phi'\frac{de^s}{d\phi_n} + \Phi''e^s)e^{jk\Phi}}{k^2(\Phi')^3}\right]^{\phi_{n2}} . \tag{2.118}$$

The second term of the end point contribution at ϕ_{n2} to the far zone scattered electric field ($\mathbf{E}_1^s$), is thus given by

$$\mathbf{E}_1^s(\mathbf{n}_2) = e^{-jks'}\mathbf{D}_1^e(\phi_{n2})\frac{e^{-jks}}{s} \tag{2.119}$$

where

$$\mathbf{D}_1^e = I_z\mathbf{d}_1^e \tag{2.120}$$

36

and

$$\mathbf{d}_1^e(\phi_{n2}) = \frac{-j[\mathbf{B}'(\phi_{n2}) + \mathbf{B}(\phi_{n2})]}{2\pi ka[\sin\theta_s \sin(\phi_s - \phi_{n2}) + \sin\theta_i \sin(\phi_i - \phi_{n2})]^3} \ . \tag{2.121}$$

In the case of a finite scattering cylinder, one finds that

$$\mathbf{D}_1^e(\phi_{n2}) = \frac{-jl \ \text{sinc}[\frac{kl}{2}(\cos\theta_s + \cos\theta_i)][\mathbf{B}'(\phi_{n2}) + \mathbf{B}(\phi_{n2})]}{2\pi ka[\sin\theta_s \sin(\phi_s - \phi_{n2}) + \sin\theta_i \sin(\phi_i - \phi_{n2})]^3} \tag{2.122}$$

where

$$\mathbf{B}'(\phi_{n2}) = [\sin\theta_s \sin(\phi_s - \phi_{n2}) + \sin\theta_i \sin(\phi_i - \phi_{n2})]\frac{d\mathbf{e}^s(\phi_{n2})}{d\phi_n} \tag{2.123}$$

and

$$\mathbf{B}(\phi_{n2}) = [\sin\theta_s \cos(\phi_s - \phi_{n2}) + \sin\theta_i \cos(\phi_i - \phi_{n2})]\mathbf{e}^s(\phi_{n2}) \ . \tag{2.124}$$

In terms of a general cylinder with its axis orientated along a unit vector $\hat{\mathbf{e}}$, the scattering coefficient can be expressed as

$$\mathbf{D}_1^e = I_z \mathbf{d}_1^e \tag{2.125}$$

where

$$\mathbf{d}_1^e(\phi_{n2}) = \frac{-j[\mathbf{B}'(\phi_{n2}) + \mathbf{B}(\phi_{n2})]}{2\pi ka(|\ \hat{\mathbf{r}}^i \times \hat{\mathbf{e}}\ | \ (\hat{\mathbf{n}}(\phi_{n2}) \times \hat{\mathbf{r}}_\perp^i) \cdot \hat{\mathbf{e}} + |\ \hat{\mathbf{r}}^s \times \hat{\mathbf{e}}\ | \ (\hat{\mathbf{n}}(\phi_{n2}) \times \hat{\mathbf{r}}_\perp^s) \cdot \hat{\mathbf{e}})^3} \ . \tag{2.126}$$

In the case of a finite scattering cylinder one thus finds that

$$\mathbf{D}_1^e(\phi_{n2}) = \frac{-jl \ \text{sinc}[\frac{kl}{2}\hat{\mathbf{e}} \cdot (\hat{\mathbf{r}}^s - \hat{\mathbf{r}}^i)][\mathbf{B}'(\phi_{n2}) + \mathbf{B}(\phi_{n2})]}{2\pi ka(|\ \hat{\mathbf{r}}^i \times \hat{\mathbf{e}}\ | \ (\hat{\mathbf{n}}(\phi_{n2}) \times \hat{\mathbf{r}}_\perp^i) \cdot \hat{\mathbf{e}} + |\ \hat{\mathbf{r}}^s \times \hat{\mathbf{e}}\ | \ (\hat{\mathbf{n}}(\phi_{n2}) \times \hat{\mathbf{r}}_\perp^s) \cdot \hat{\mathbf{e}})^3} \tag{2.127}$$

where

$$\mathbf{B}'(\phi_{n2}) = (|\ \hat{\mathbf{r}}^i \times \hat{\mathbf{e}}\ | \ (\hat{\mathbf{n}}(\phi_{n2}) \times \hat{\mathbf{r}}_\perp^i) \cdot \hat{\mathbf{e}} + |\ \hat{\mathbf{r}}^s \times \hat{\mathbf{e}}\ | \ (\hat{\mathbf{n}}(\phi_{n2}) \times \hat{\mathbf{r}}_\perp^s) \cdot \hat{\mathbf{e}})\frac{d\mathbf{e}^s(\phi_{n2})}{d\phi_n} \tag{2.128}$$

and

$$\mathbf{B}(\phi_{n2}) = (|\ \hat{\mathbf{r}}^i \times \hat{\mathbf{e}}\ |\ (\hat{\mathbf{n}}(\phi_{n2}) \cdot \hat{\mathbf{r}}_{\perp}^i) + |\ \hat{\mathbf{r}}^s \times \hat{\mathbf{e}}\ |\ (\hat{\mathbf{n}}(\phi_{n2}) \cdot \hat{\mathbf{r}}_{\perp}^s))\mathbf{e}^s(\phi_{n2})\ . \quad (2.129)$$

If $\mathbf{P}(\phi)$ and $\mathbf{Q}(\phi)$ are vectors, then

$$\frac{d}{d\phi}(\mathbf{P} \cdot \mathbf{Q}) = \frac{d\mathbf{P}}{d\phi} \cdot \mathbf{Q} + \mathbf{P} \cdot \frac{d\mathbf{Q}}{d\phi}\ , \text{ and} \quad (2.130)$$

$$\frac{d}{d\phi}(\mathbf{P} \times \mathbf{Q}) = \frac{d\mathbf{P}}{d\phi} \times \mathbf{Q} + \mathbf{P} \times \frac{d\mathbf{Q}}{d\phi}\ . \quad (2.131)$$

It thus follows from Equation (2.76) that

$$\frac{d\mathbf{e}^s}{d\phi_n} = \frac{d\hat{\mathbf{n}}}{d\phi_n} \times (\hat{\mathbf{r}}^i \times \mathbf{e}^i) - \left(\frac{d\hat{\mathbf{n}}}{d\phi_n} \times (\hat{\mathbf{r}}^i \times \mathbf{e}^i) \cdot \hat{\mathbf{r}}^s\right)\hat{\mathbf{r}}^s \quad (2.132)$$

since $\hat{\mathbf{r}}^i \times \mathbf{e}^i$ is independent of ϕ_n. Differentiating Equation (2.66) yields

$$\frac{d\hat{\mathbf{n}}}{d\phi_n} = -\sin\phi_n\hat{\mathbf{x}} + \cos\phi_n\hat{\mathbf{y}}\ . \quad (2.133)$$

In terms of the general cylinder with its axis orientated along a unit vector $\hat{\mathbf{e}}$, this term can be expressed as

$$\frac{d\hat{\mathbf{n}}}{d\phi_n} = \hat{\mathbf{e}} \times \hat{\mathbf{n}}(\phi_n)\ . \quad (2.134)$$

The vector $d\hat{\mathbf{n}}/d\phi_n$ is a unit vector, since $\hat{\mathbf{e}}$ and $\hat{\mathbf{n}}$ are perpendicular to each other. Note that $\mathbf{D}_1^c$, and thus $\mathbf{E}_1^s$, are functions of the radius of curvature of the cylinder (a). The larger the radius of curvature becomes, the smaller the contribution from the second term will be. In fact, one finds that the higher order terms in the series given in Equation (2.83) are functions of $(1/ka)^n$. Since k is a large number, higher order terms in the series thus become less significant.

In the case of axial backscattering from bodies of revolution, it was found that the first term of the end point contribution ($\mathbf{D}_0^c$) goes to zero, but that the second term ($\mathbf{D}_1^c$) gives the correct expression for the false scattering from the incident shadow boundary[28].

The total end point contribution at the incident shadow boundary contour on a reflector illuminated by a point source at the focus ($\mathbf{E}^{endpoint}$) can be found by evaluating

$$\mathbf{E}^{endpoint} = \oint_C \mathbf{d}^e \, e^{jkc\hat{e}\cdot(\hat{r}^s - \hat{r}^i)} \frac{e^{-jk(s+s')}}{s} \, dc \qquad (2.135)$$

in a counter-clockwise direction, where

$$C \;\; = \;\; \text{incident shadow boundary contour on the surface}$$

$$\mathbf{d}^e \;\; = \;\; \text{modified end point scattering coefficient}$$

$$\hat{r}^i \;\; = \;\; \text{direction of incident propagation on C at the element } (dc)$$

$$\hat{r}^s \;\; = \;\; \text{direction of scattered propagation from C at the element } (dc)$$

$$s \;\; = \;\; \text{distance from the element } (dc) \text{ on C to far zone field point , and}$$

$$s' \;\; = \;\; \text{distance from the far zone source phase reference}$$

$$\text{to the element } (dc) \text{ on C .}$$

In the case of a numerical computation where the three-dimensional surface is modelled by triangular patches, the finite scattering cylinders are fitted onto the sides of the patches making up the incident shadow boundary contour. Figure 12 shows how the finite scattering cylinders are fitted onto the incident shadow boundary contour of the rolled edge of compact range main reflector. $\mathbf{E}^{endpoint}$ is then found by evaluating

$$\mathbf{E}^{endpoint} = \sum_C (\mathbf{D}_0^e + \mathbf{D}_1^e) \frac{e^{-jk(s+s')}}{s} \qquad (2.136)$$

where

$$\mathbf{D}^e \;\; = \;\; \text{end point scattering coefficient}$$

$$s \;\; = \;\; \text{distance from the shadow boundary on the cylinder}$$

$$\text{to the far zone field point (see Equation (2.96)) , and}$$

s' = distance from the far zone source phase reference

to the shadow boundary on the cylinder (see Equation (2.95)) .

The PO solution in which the end point contributions have been eliminated will forthwith be referred to as the "corrected PO method".

This analysis of the PO method has been presented in a three-dimensional coordinate system. A similar analysis can be done in two dimensions, in which case the two-dimensional Green's function is used in the PO integration, and the fields have a $1/\sqrt{R}$ amplitude dependence[26].

FINITE SCATTERING
CYLINDER

SHADOW BOUNDARY CONTOUR

a

a

ROLLED SURFACE
TERMINATION

TRIANGULAR
SURFACE PATCH

(a) Detail.

FINITE SCATTERING
CYLINDERS

SHADOW
BOUNDARY
CONTOUR (C)

PARABOLIC REFLECTOR
WITH ROLLED EDGES
(FRONT VIEW)

(b) Finite scattering cylinders along the entire
shadow boundary contour of a blended rolled edge.
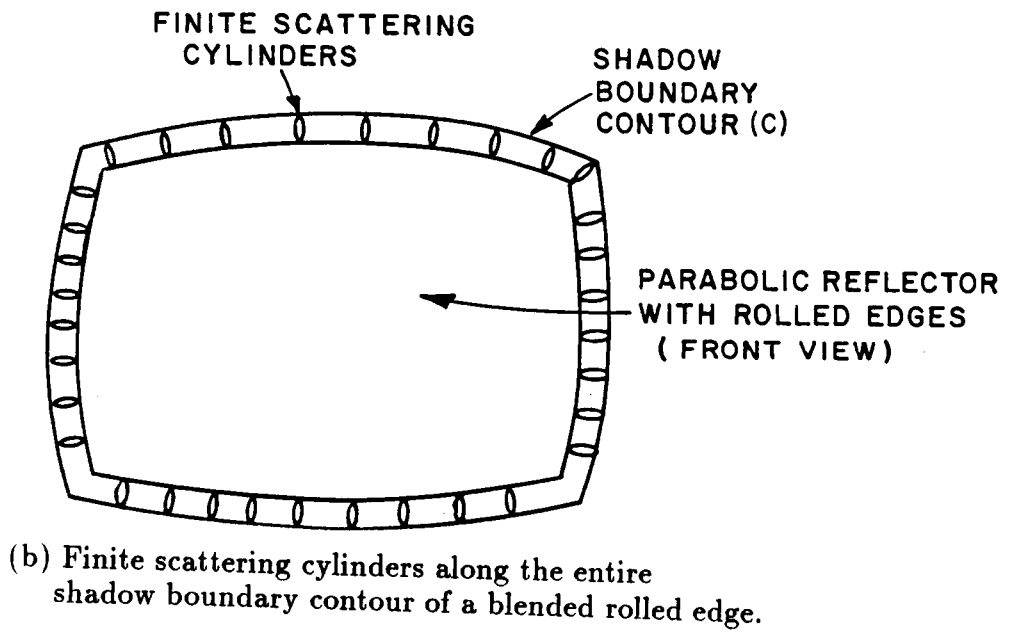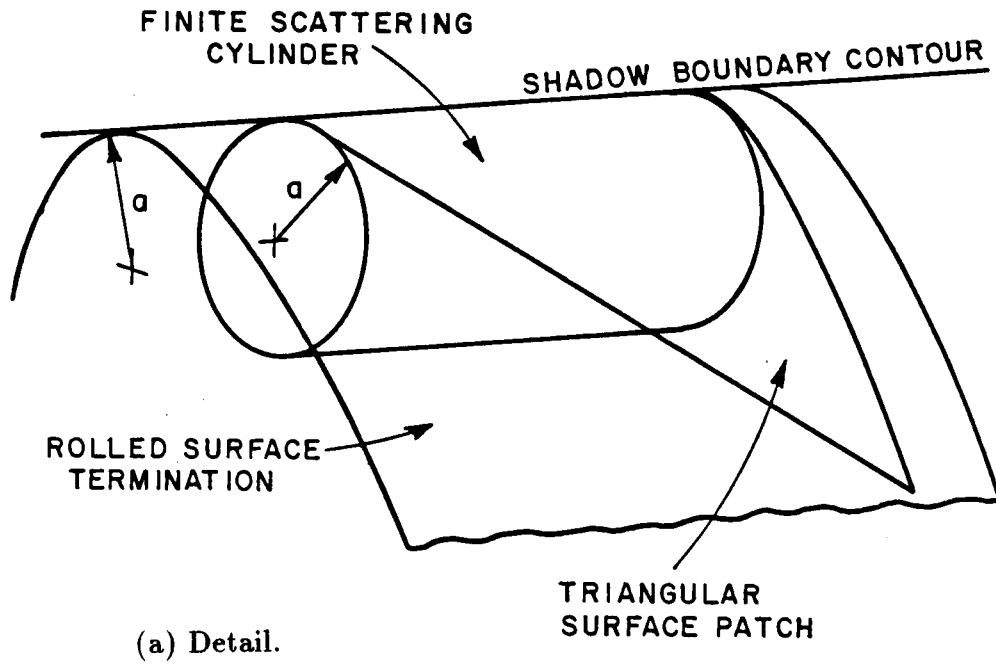
Figure 12: Location of the finite scattering cylinders at the incident shadow
boundary of a rolled edge of a parabolic reflector.

CHAPTER III

EDGE TREATMENT FOR THE MAIN REFLECTOR

3.1 Plane wave criteria

Due to the nature of their operation, one is usually interested in the far zone characteristics of radar and communications antennas, although in some special cases the near zone characteristics are of interest. Since there are only transverse field components present in the far zone, it is mathematically convenient to approximate the far zone fields by a plane wave; ie., the spherical phase front radiated by an antenna is approximated locally by a planar phase front. This can only be a local approximation, since true plane waves require infinite energy and can therefore not exist in reality. If all the field components in the planar phase front have the same amplitude, then the plane wave is known as a "uniform plane wave".

Consider an Antenna-Under-Test (AUT) being operated in the receive mode. Measurements relating to the far zone characteristics of the AUT are based on the assumption that it is illuminated by a uniform plane wave of given polarization. The definition of radar cross-section (RCS) also assumes that the target is illuminated by a uniform plane wave. Although true plane waves do not exist, it is nevertheless convenient to use them as a measurement standard. In practice, a portion of a spherical or cylindrical wavefront is considered to be a local plane wave if the phase and amplitude deviations over that portion of the wavefront do not exceed specified limits.
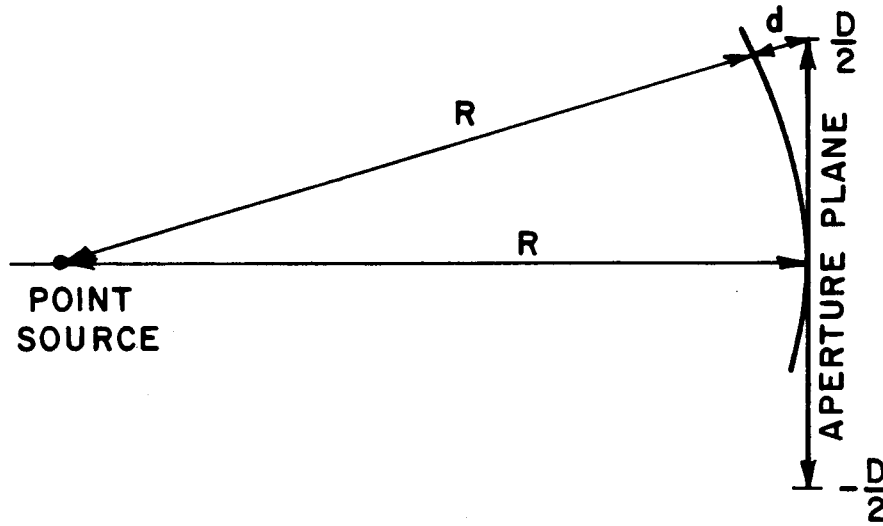
Figure 13: Plane wave approximation over an aperture.

Consider now a point source radiating a spherical wave as shown in Figure 13. A plane wave is required over an aperture of width (D), that is removed a distance (R) from the point source. Let this plane wave be approximated by the spherical wave, such that the maximum phase deviation over the aperture does not exceed $\triangle \Phi_{max}$. It is required to find the minimum separation (R_{min}) where this will occur. The phase of the spherical wave (Φ) at a distance (r) from the point source is given by

$$\Phi(r) = kr \tag{3.1}$$

so that the phase at the center of the aperture is given by

$$\Phi(R) = kR \tag{3.2}$$

and the phase at the extreme end of the aperture is given by

$$\Phi(R + d) = k(R + d) \ . \tag{3.3}$$

43

Note that d is the radial distance discrepancy between the spherical and planar phase fronts at the extreme end of the aperture as shown in Figure 13 and is given by

$$R + d = \sqrt{R^2 + (D/2)^2} \qquad (3.4)$$

so that

$$d = R(\sqrt{1 + (D/2R)^2} - 1) \qquad (3.5)$$

or

$$d \approx \frac{D^2}{8R} \quad \text{for } D \ll R . \qquad (3.6)$$

The maximum phase deviation over the aperture is thus given by

$$\triangle \Phi_{max} = kd \qquad (3.7)$$

so that

$$R_{min} = \frac{\pi D^2}{4 \lambda \triangle \Phi_{max}} . \qquad (3.8)$$

Due to the quadratic nature of Equation (3.6), the resulting phase error is sometimes referred to as a "quadratic error". Clearly, the larger R is, the smaller $\triangle \Phi_{max}$ will be, yielding a better plane wave approximation. Table 1 shows various values of R_{min} versus $\triangle \Phi_{max}$ obtained from Equation (3.8). Note that in the case of RCS measurements, the phase error is included in both the incident and scattered paths, so that

$$R_{min} = \frac{\pi D^2}{2 \lambda \triangle \Phi_{max}} . \qquad (3.9)$$

Traditionally an amplitude deviation of 1 dB and a phase deviation of

$$\triangle \Phi_{max} = \frac{\pi}{8} \ (=22.5^o) \qquad (3.10)$$

in a phase front have been considered as an acceptable approximation for a plane wave[29], resulting in

$$R_{min} = \frac{2D^2}{\lambda} . \qquad (3.11)$$

44

Table 1: R_{min} versus $\triangle\Phi_{max}$.

$\triangle\Phi_{max}$	R_{min}
45^0	D^2/λ
22.5^0	$2D^2/\lambda$
11.25^0	$4D^2/\lambda$
10^0	$4.5D^2/\lambda$
9^0	$5D^2/\lambda$
7.5^0	$6D^2/\lambda$
5^0	$9D^2/\lambda$
4.5^0	$10D^2/\lambda$

Recent studies[30] have shown, however, that although these criteria may be acceptable for measuring the patterns of antennas with −25 dB sidelobes, the measurement of low RCS targets and antennas with low sidelobes (−30 dB and lower) require that measurements be made at distances much larger than that given in Equation (3.11), indicating a phase deviation much smaller than 22.5^o. The quadratic errors result in the following discrepancies[31]:

- Reduced main lobe amplitude.

- Increased sidelobe levels.

- Filling in of nulls.

In order to accurately measure low RCS targets and the patterns of antennas with low sidelobes, it is thus *imperative that the amplitude and phase deviations of*

the plane wave in the target zone of a compact range be as small as possible. The design improvements proposed in this study are aimed at reducing these deviations.

3.2 Creation of a plane wave by a compact range

A plane wave can be created in the target zone of a compact range by illuminating a parabolic reflector with a point source located at the focus. This is a result of the following geometrical characteristics of a paraboloid:

1. The two caustic distances for the reflected fields are both equal to infinity[32], so that all the reflected rays are parallel to the axis of symmetry. This implies that there is no amplitude decay after reflection.

2. The path lengths of all rays that originate at the focus and are reflected by the parabolic surface to a plane that is perpendicular to the axis of symmetry are equal. This plane can thus be viewed as the phase front of a plane wave. Since all the reflected rays are parallel, this planar phase front will propagate into the target zone. It will be shown that for a plane located at $z_t > f_c$ (where f_c is the focal length of the parabolic reflector), the path length is equal to the constant $z_t + f_c$.

Notice, however, that due to the spatial attenuation associated with the point source at the focus, the rays illuminating the reflector have a $1/R$ amplitude dependence before reflection. Since all points on the surface are not an equal distance away from the focus, this spatial decay results in an amplitude taper in the reflected field. Although the reflected field is a plane wave, it is thus not a uniform plane wave. This effect is shown in Figure 14(a). Compact ranges usually employ offset main reflectors in order to reduce aperture blockage by the feed. The pri-

46

mary feed antenna at the focus is then tilted to decrease the amplitude taper in the reflected field[33,34].

The reflected field exists as a plane wave only over the surface of the parabola, and stops abruptly at the surface termination. Since electromagnetic waves must be smooth and continuous everywhere, there will be a diffracted field emanating from the terminating edge to compensate for the discontinuity in the reflected field and make the total field (ie., reflected plus diffracted fields) smooth and continuous. This diffracted field interferes constructively and destructively with the plane wave, causing unwanted amplitude and phase ripples in the total field in the target zone. The edge diffracted fields are shown in Figure 14(b). In fact, the antenna and/or target sizes that can be measured in presently available compact ranges are directly related to the edge treatment of the main reflector. Burnside and Peters[35] have recently shown that in order to measure low backscatter targets, a ripple of less than 0.1 dB is required; whereas, a taper of less than 1 dB is satisfactory. Phase deviations of 5° or less have also been suggested[36].

In order to relate the magnitude of the ripple in the total field to the level of the diffracted field, consider Figure 15. Let e_t, e_{go} and e_d denote the total, GO and diffracted fields, respectively. The maximum deviations of e_t from e_{go} will occur when e_{go} and e_d are either completely in phase or completely out of phase.

Case 1: e_{go} and e_d are in phase

The ripple amplitude is given by

$$R_1 = (20 \log e_t - 20 \log e_{go}) \text{ dB} \qquad (3.12)$$

or

$$R_1 = 20 \log(1 + 10^{(E_d - E_{go})/20}) \text{ dB} \qquad (3.13)$$

47
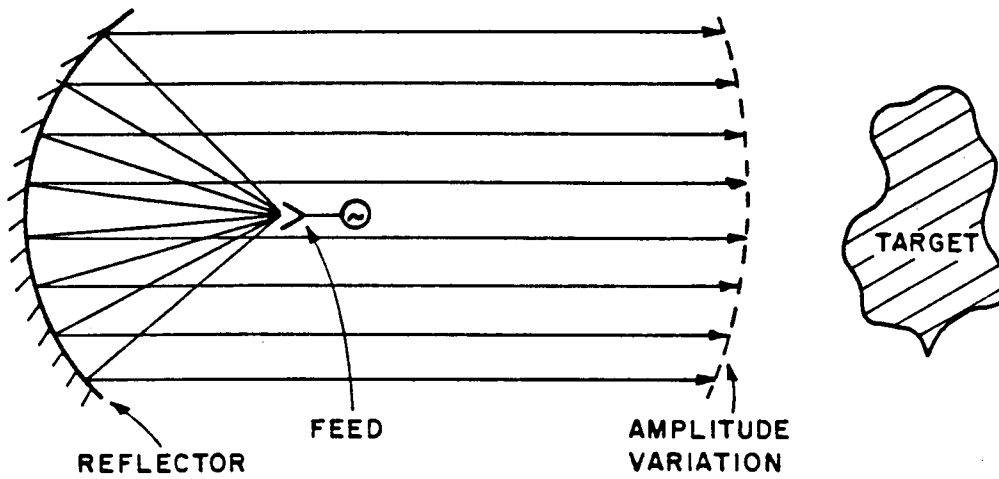
(a) Taper due to spatial decay of feed radiation.
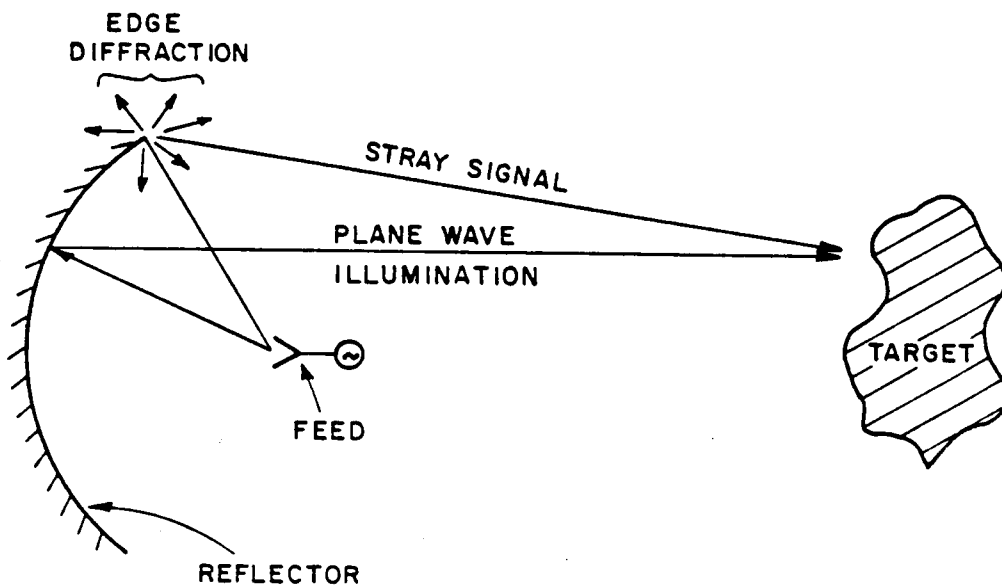
(b) Stray signal due to edge diffraction.

Figure 14: Top view of a compact range, showing the reflected plane wave and diffractions from the edge terminations.
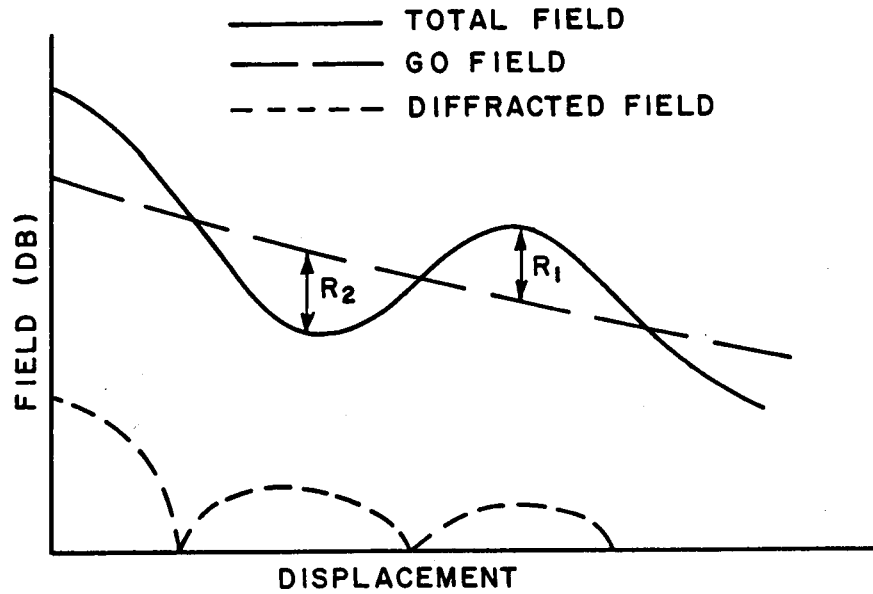
Figure 15: Ripple amplitude related to the diffracted field level.

where

$$E_d \quad = \quad \text{amplitude of the diffracted field (dB) , and}$$

$$E_{go} \quad = \quad \text{amplitude of the GO field (dB) .}$$

Case 2: e_{go} and e_d are out of phase

The ripple amplitude is given by

$$R_2 = -20\log(1 - 10^{(E_d - E_{go})/20}) \text{ dB .} \qquad (3.14)$$

Since $R_2 > R_1$ for a given value of $E_d - E_{go}$, the ripple amplitude (R) will be defined as

$$R = -20\log(1 - 10^{(E_d - E_{go})/20}) \quad \text{dB .} \qquad (3.15)$$

Notice that this definition implies that

$$E_{go} - R \leq E_t \leq E_{go} + R \qquad (3.16)$$

49

Table 2: Ripple amplitude (R) versus ($E_d - E_{go}$).

$E_d - E_{go}$ (dB)	R (dB)
-10	3.30
-20	0.83
-30	0.27
-40	0.09
-50	0.03
-60	0.01

where

$$E_t \quad = \quad \text{amplitude of the total field (dB) .}$$

Several values for R versus ($E_d - E_{go}$) are shown in Table 2.

In order to eliminate the edge diffracted fields completely, one would have to use an infinite paraboloid. However, since this is not practical, some form of termination of the parabolic section has to be found such that edge diffractions into the target zone are minimized. Various options to reduce the energy that is scattered from the edge termination of the main reflector into the target zone have been investigated in the past, including the use of absorber material as well as serrated and rolled edges[33,37]. Serrated edges serve to disrupt the caustic effect of a convex edge, and are being used on various compact range main reflectors[38,39,40]. It was found, however, that the addition of a large curved surface to the termination, as shown in Figure 16, can increase the performance of the main reflector considerably[41]. The addition of such a curved surface to the parabolic reflector reduces the energy diffracted from the termination of the parabolic section,
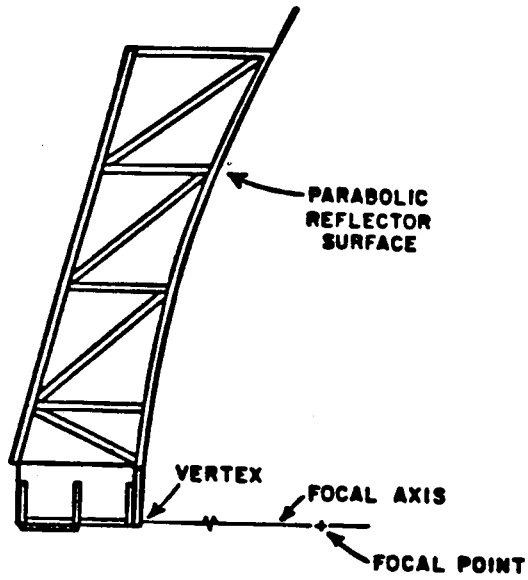
(a) Standard reflector.
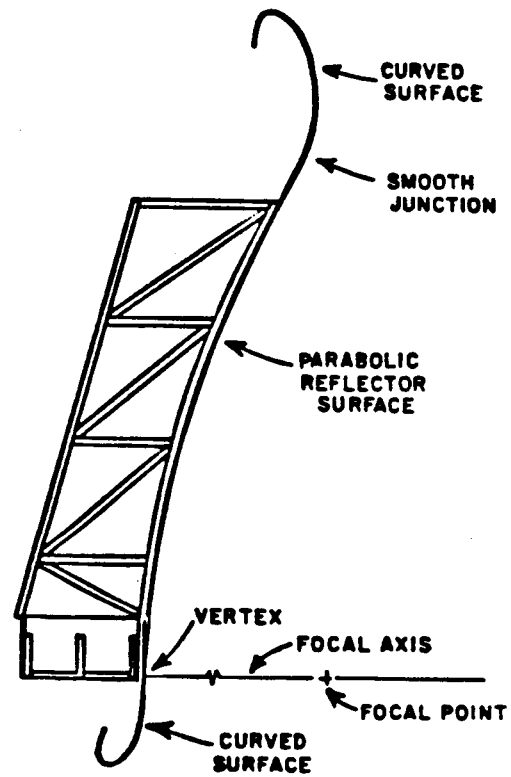
(b) Rolled edge modified reflector.

Figure 16: Addition of large rolled surface edge terminations to a parabolic reflector.
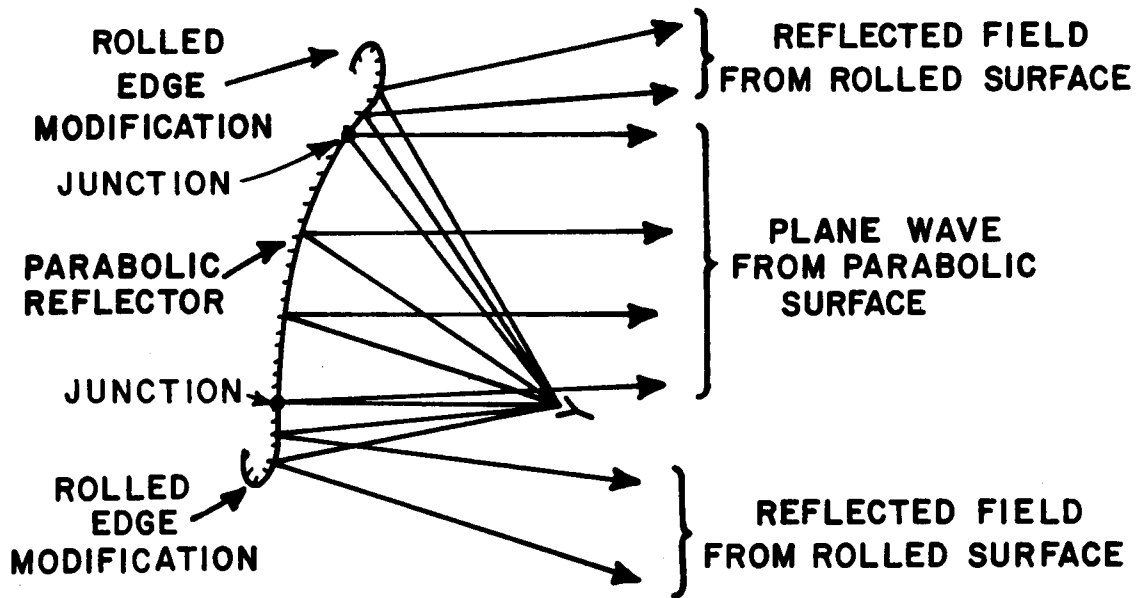
Figure 17: Continuity of reflected field using rolled edges.

since the rolled edge creates a reflected field which goes more smoothly from the parabolic surface to the rolled surface (as shown in Figure 17) than in the case of an abrupt termination with no edge treatment. Since the surfaces on either side of the edge junction are not the same, there will still be a discontinuity in the reflected field across the junction. However, the discontinuity in the reflected field is smaller, and the diffracted field weaker, than in the case with no edge treatment. The rolled surface is added in such a way that the surface slope is continuous across the junction. Furthermore, the rolled edge continuously curves away from the focus and continues into the shadow region. This ensures that the GO rays that are reflected from the rolled edge do not enter the target zone.

An elliptic rolled edge was added to the reflector at the Ohio State University ElectroScience Laboratory, resulting in greatly improved performance[41,42]. In gaining experience with rolled surfaces, the following rules of thumb were

developed[32]:

1. The radius of curvature of the rolled surface at the junction between the parabolic reflector and the rolled surface should be greater than a focal length.

2. The minimum radius of curvature of the rolled surface should never be less than a quarter of a wavelength at the lowest frequency of operation ($\lambda_{max}/4$).

The lowest frequency of operation of a compact range main reflector is thus related to the minimum radius of curvature of the rolled edge. The upper frequency limit is generally dictated by the surface tolerance of the reflector[43].

In addition to the adding of rolled surface terminations, it can be shown that shaping the edge contour separating the parabolic section from the rolled surface terminations will also enhance the performance of the main reflector. Such a shaping has also been proposed by Kelleher[44] in conjunction with the control of sidelobes from parabolic antennas.

3.3 Elliptic rolled surface terminations

3.3.1 Reduction of diffracted fields using elliptic rolled edges

In order to examine the effect of elliptic and blended rolled surface terminations on the total field in the target zone, the two-dimensional case will be discussed in the rest of this chapter.

Consider an elliptic rolled edge attached to a parabolic reflector at $P_j(y_j, z_j)$ as shown in Figure 18. Let the focal length of the reflector be f_c. The ellipse has semi-major and semi-minor axes of lengths (a_e) and (b_e), respectively. The ellipse is attached in such a way that the surface slope at the junction is continuous. The

parabolic surface can be described by

$$z = \frac{y^2}{4f_c} \tag{3.17}$$

where the z-axis is the axis of symmetry. In anticipation of the three-dimensional case that will follow, the y-axis is chosen as the vertical axis. The coordinates of the junctions located at the top and bottom of the parabolic section of the reflector, respectively, are then given by

$$z_j = \frac{y_j^2}{4f_c} \tag{3.18}$$

where

$$y_j = y_{top} \text{ indicates the top junction , and}$$

$$y_j = y_{bot} \text{ indicates the bottom junction .}$$

In the case of the offset reflectors considered in this study, it is assumed that y_{bot} and y_{top} are both greater than zero.

It is convenient to define a local coordinate system for the ellipse such that its major axis is aligned with the x_e-direction, and its minor axis with the y_e-direction. Let the origin of this coordinate system be at the junction (P_j). In order to make the slope of the surface continuous across the junction, the tangential vectors to the parabola and ellipse at the junction should be parallel. Let the y_e-axis thus be defined by

$$\hat{\mathbf{y}}_e = -\hat{\mathbf{n}}_{junction} \tag{3.19}$$

where $\hat{\mathbf{n}}_{junction}$ is the unit vector normal to the parabola at the junction, as given in Appendix A. The ellipse coordinate axes are then given by

$$\hat{\mathbf{x}}_e = x_{p2}\hat{\mathbf{y}} + x_{p3}\hat{\mathbf{z}} \text{ , and} \tag{3.20}$$

$$\hat{\mathbf{y}}_e = y_{p2}\hat{\mathbf{y}} + y_{p3}\hat{\mathbf{z}} \tag{3.21}$$

54
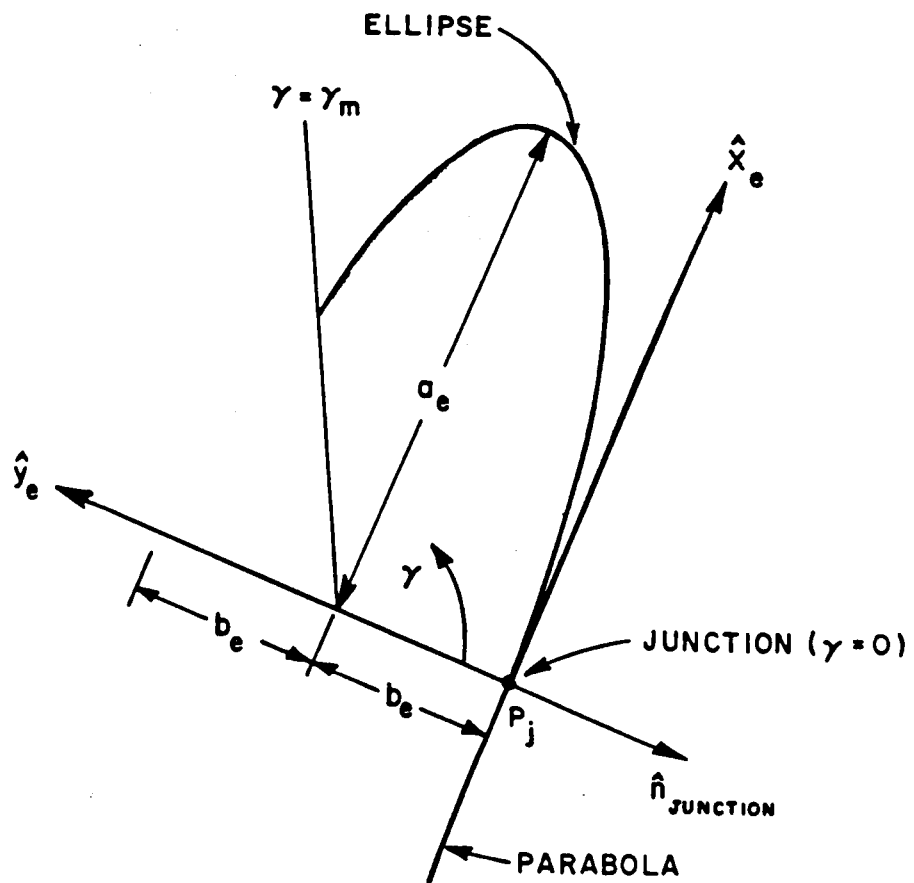
Figure 18: The $x_e y_e$-coordinate system for an elliptic rolled surface termination.

where the direction cosines are given by

$$y_{p2} = \frac{y_j}{\sqrt{y_j^2 + 4f_c^2}} \tag{3.22}$$

$$y_{p3} = \frac{-2f_c}{\sqrt{y_j^2 + 4f_c^2}} \tag{3.23}$$

$$x_{p2}(y_{top,bot}) = \mp y_{p3} \text{ , and} \tag{3.24}$$

$$x_{p3}(y_{top,bot}) = \pm y_{p2} \text{ .} \tag{3.25}$$

This will ensure that $\hat{\mathbf{x}}_e$ is parallel to the vector that is tangential to the parabola at the junction. The transformation from the $x_e y_e$-system to the yz-system is used to specify a point on the rolled surface in the yz-system. It is given by

$$\begin{pmatrix} y(\gamma) \\ z(\gamma) \end{pmatrix} = \begin{pmatrix} x_{p2} & y_{p2} \\ x_{p3} & y_{p3} \end{pmatrix} \begin{pmatrix} x_e(\gamma) \\ y_e(\gamma) \end{pmatrix} + \begin{pmatrix} y_j \\ z_j \end{pmatrix} \tag{3.26}$$

where the parametric angle γ of the rolled surface is valid in the region

$$0 \leq \gamma \leq \gamma_m \tag{3.27}$$

such that

$$\gamma = 0 \text{ at the junction , and} \tag{3.28}$$

$$\gamma = \gamma_m \text{ at the extreme end of the rolled surface .} \tag{3.29}$$

The ellipse can be described in the $x_e y_e$-system by the following curve:

$$\mathbf{r}_e(\gamma) = x_e(\gamma)\hat{\mathbf{x}}_e + y_e(\gamma)\hat{\mathbf{y}}_e = (a_e \sin\gamma)\hat{\mathbf{x}}_e + b_e(1 - \cos\gamma)\hat{\mathbf{y}}_e \text{ .} \tag{3.30}$$

In terms of the yz-system, the elliptic rolled surface can thus be expressed as

$$\mathbf{r}_{ellipse}(\gamma) = y_{ellipse}(\gamma)\hat{\mathbf{y}} + z_{ellipse}(\gamma)\hat{\mathbf{z}} \tag{3.31}$$

56

where

$$y_{ellipse}(\gamma) = (a_e \sin\gamma)x_{p2} + b_e(1 - \cos\gamma)y_{p2} + y_j \text{ , and} \qquad (3.32)$$

$$z_{ellipse}(\gamma) = (a_e \sin\gamma)x_{p3} + b_e(1 - \cos\gamma)y_{p3} + z_j \text{ .} \qquad (3.33)$$

There is no need for a z_e-component, since the ellipse lies in a flat plane.

It is shown in Appendix A that the radius of curvature of the parabola at the junction is given by

$$R_c^{parabola}(y_j) = 2f_c \left[1 + \left(\frac{y_j}{2f_c}\right)^2\right]^{\frac{3}{2}} \qquad (3.34)$$

and that the radius of curvature of the ellipse at the junction is given by

$$R_c^{ellipse}(y_j) = \frac{a_e^2}{b_e} \text{ .} \qquad (3.35)$$

It is thus apparent that, although the slope of the surface is continuous across the junction, the radius of curvature there is discontinuous. In fact, the parabola is a concave surface (when viewed from the focus); whereas, the ellipse is a convex surface. The radii of curvature on either side of the junction can thus be interpreted as having different signs in addition to being discontinuous in magnitude. Consequently, the reflected fields from the two surfaces are not equal, and a diffracted field is created at the junction which compensates for this discontinuity. The expression for this diffracted field is given by Chu[45]. As mentioned before, this diffracted field is much smaller than the one resulting from an untreated edge and accounts for the increase in performance obtained by using rolled edges.

3.3.2 Design example (focus feed)

Consider now the parabolic reflector with $f_c = 12'$ and elliptic rolled surface terminations shown in Figure 19. The values of a_e and b_e were chosen such that

$$\frac{a_e^2}{b_e} = f_c \text{ , and} \qquad (3.36)$$

57

Table 3: Surface characteristics for S2.1.

No Blending			RADIUS OF CURVATURE (ROLLED EDGE)					
f_c	12'		Junction		Minimum		Shadow Boundary	
a_e	3'		bottom	top	bottom	top	bottom	top
b_e	0.75'							
y_{bot}	5'	γ	0°	0°	90°	90°	89°	81°
y_{top}	11'	R_c	12'	12'	0.188'	0.188'	0.188'	0.308'
z_{pat}	24'							

Table 4: Radii of curvature at the junctions of a parabola with $f_c = 12'$.

RADIUS OF CURVATURE (PARABOLA)		
	bottom($y_{bot} = 5'$)	top($y_{top} = 11'$)
R_c	25.579'	31.947'

$$\frac{b_e^2}{a_e} = \frac{\lambda_{max}}{4} \tag{3.37}$$

where λ_{max} corresponds to the wavelength at the lowest frequency of operation, in this case 1 GHz. The surface is designated as S2.1 with characteristics given in Table 3. The radii of curvature at y_{top} and y_{bot} of a parabola with $f_c = 12'$ are given in Table 4. Comparison of Tables 3 and 4 shows the discontinuity in the radius of curvature of the reflector across the junctions. The radii of curvature of the elliptic rolled surfaces can be calculated using the expressions derived in Appendix A and are shown in Figures 20 and 21 as a function of y.

The total field in the target zone was calculated using the corrected PO
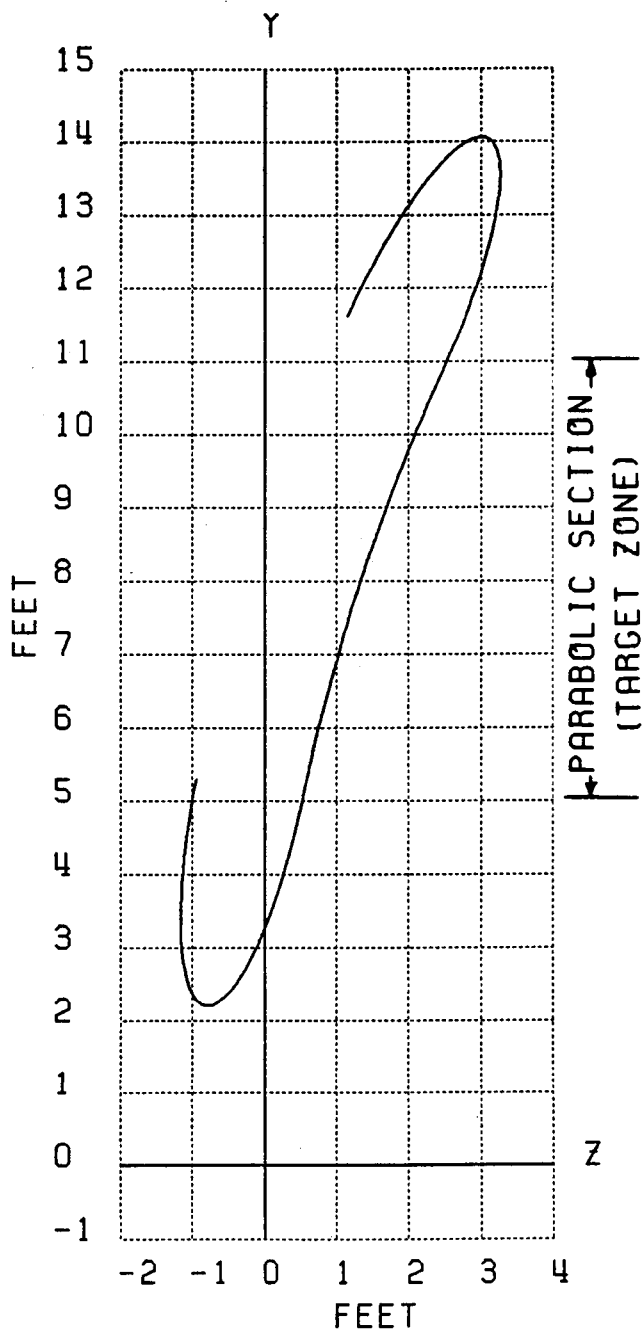
Figure 19: Two-dimensional parabolic reflector with elliptic rolled edges (S2.1).
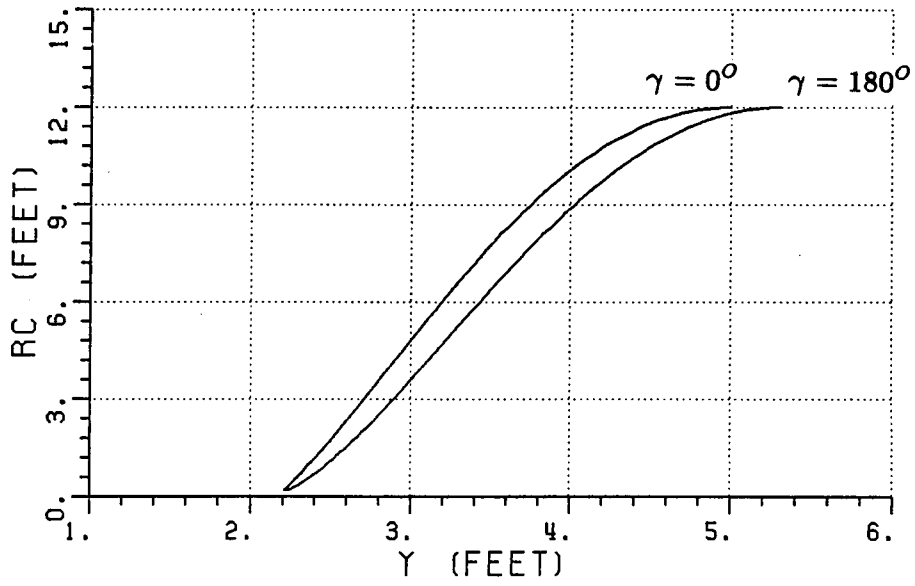
Figure 20: Radius of curvature of the bottom elliptic rolled surface of S2.1.
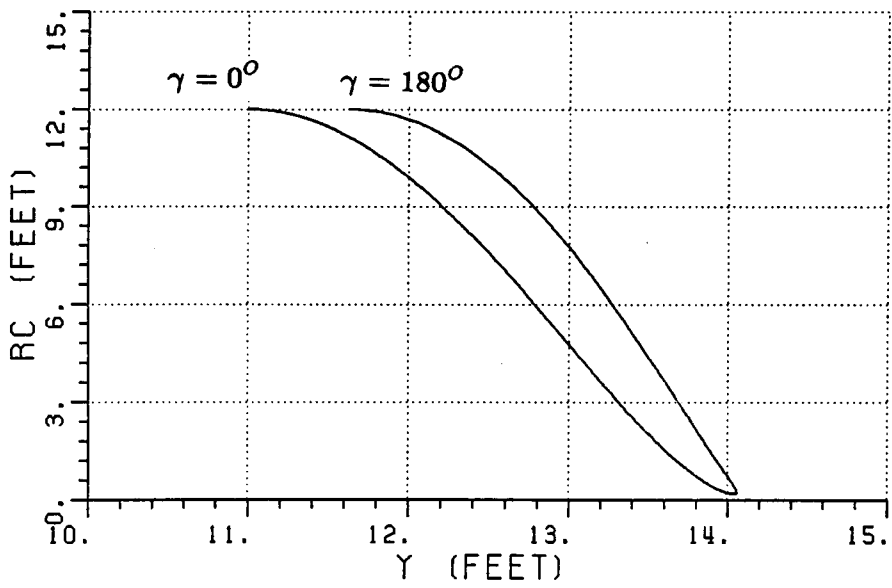
Figure 21: Radius of curvature of the top elliptic rolled surface of S2.1.

method, with the end point contributions at the incident shadow boundaries of the rolled surfaces subtracted. The parabolic section stretches from y_{bot} to y_{top}, as does the target zone. The reflector is illuminated by a transverse magnetic (TM) line source with a uniform pattern located at the focus. The target zone is considered to be located at a distance (z_{pat}) of 24' away from the main origin along the z-axis. Although Section 2.3.3 describes the three-dimensional case of the PO end point subtraction, the principle can also be applied to the two-dimensional case. Investigation of reflectors with rolled edges has shown that results obtained with the two-dimensional corrected PO method compares very favourably with those obtained by the moment method[26]. In the case of two-dimensional surfaces, the PO integral is evaluated numerically by applying Simpson's rule. Samples are taken at intervals of 0.03λ along the surface. For the purpose of this calculation it is assumed that there is no direct illumination from the source into the target zone.

Once the total field is known, the GO reflected field can be calculated and then subtracted from the total field. The residual field will by default be the fields diffracted from the junctions at y_{bot} and y_{top}, since no other significant scattering mechanisms contribute to the total field in the target zone.

The two-dimensional GO reflected field (E^r) at a point (y_t, z_t) in the target zone, is given by

$$E^r(y_t, z_t) = R_{s,h} \frac{e^{-jk(s'+s)}}{\sqrt{s'}}$$
(3.38)

where

$$R_{s,h} = \mp 1$$
(3.39)

$$s' = \frac{y_t^2}{4f_c} + f_c \text{ , and}$$
(3.40)

61
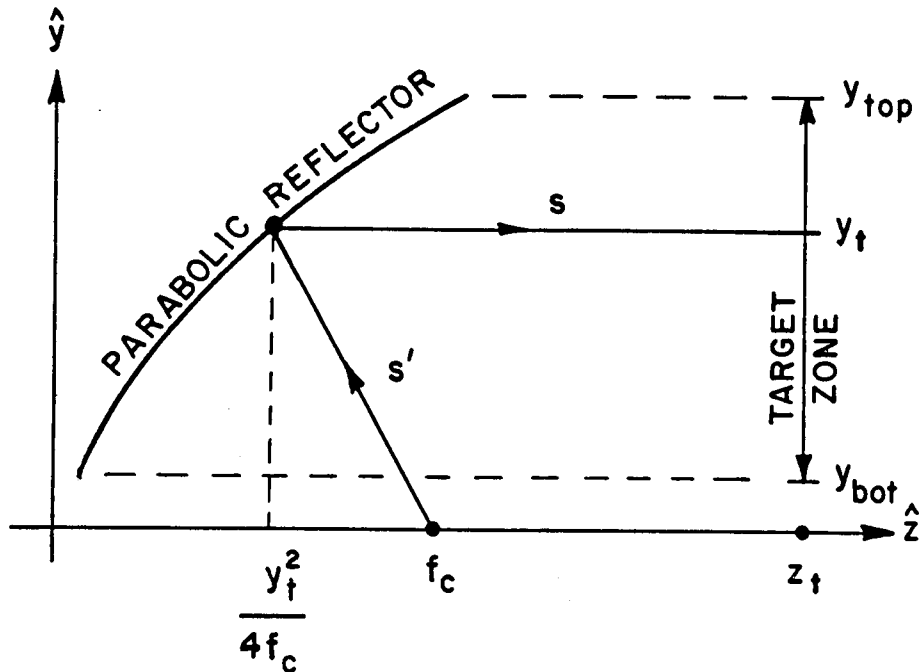
Figure 22: Two-dimensional GO reflected field from a parabolic reflector.

$$s \ = \ z_t - \frac{y_t^2}{4f_c} \tag{3.41}$$

so that

$$s' + s = f_c + z_t \ . \tag{3.42}$$

The fact that $s' + s$ is a constant indicates that the reflected field is indeed a plane wave, since all the reflected field components in the target plane at z_t will have the same phase. Note that the sign of the reflection coefficient $(R_{s,h})$ is associated with the incident polarization. The geometry associated with Equation (3.38) is shown in Figure 22.

The normalized magnitude and phase of the total field in the target zone, calculated at 3 GHz, are shown in Figures 23 and 24. Figure 25 shows the magnitude of the reflected field and the diffracted fields from the junctions. The corresponding magnitudes and phases calculated at 6 GHz and 10 GHz are shown in Figures 26–31.
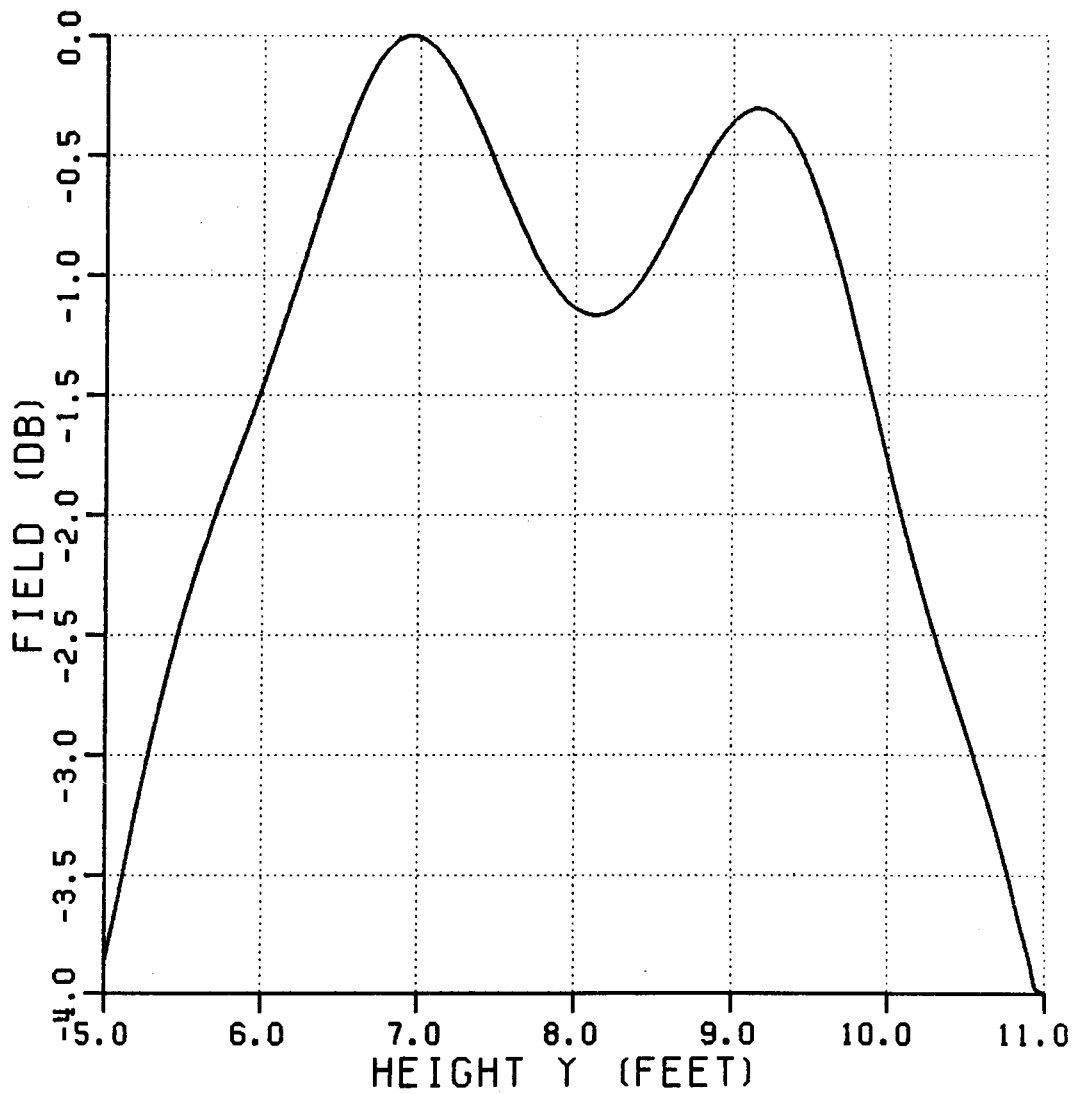
Figure 23: Normalized magnitude of the total field from S2.1 (3 GHz).
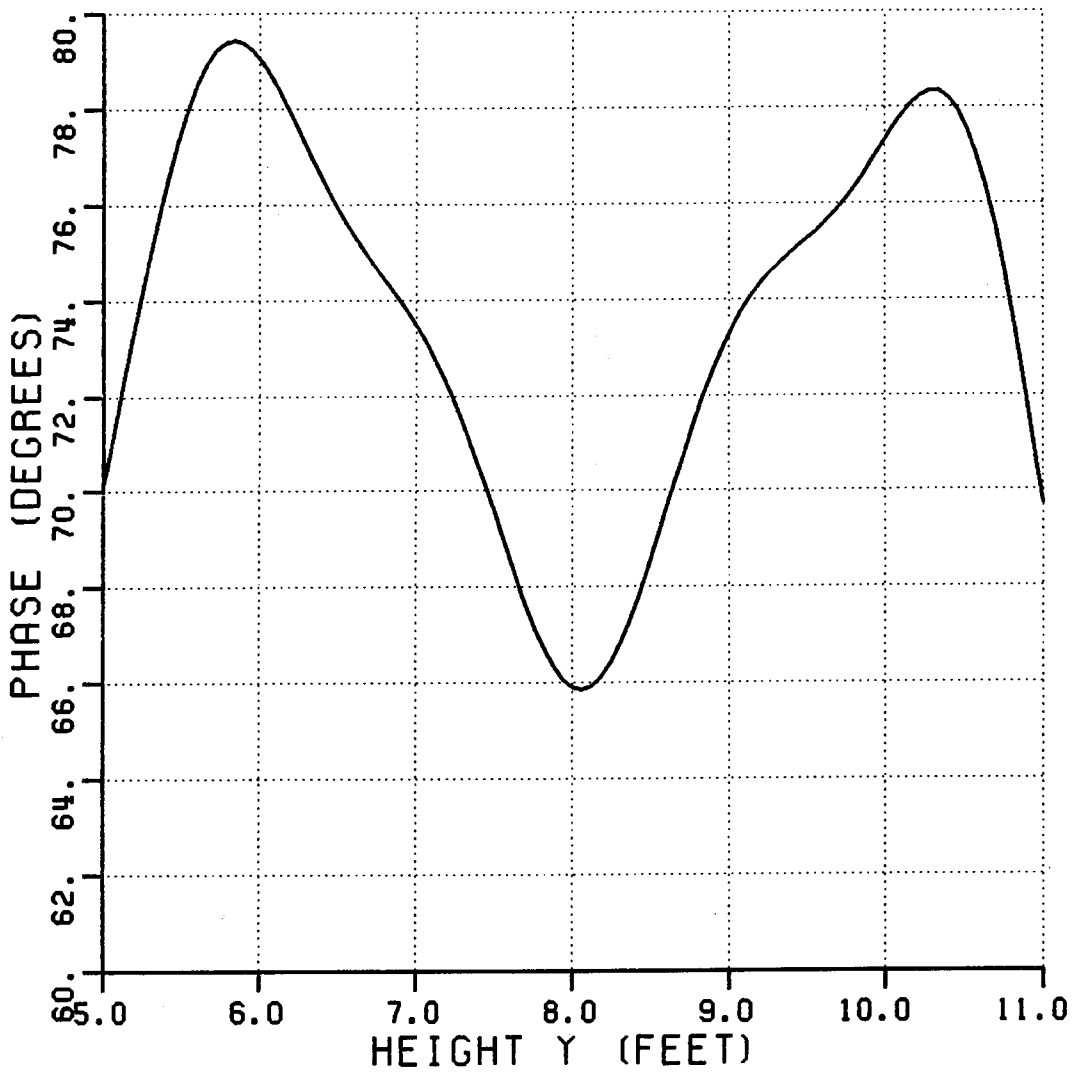
Figure 24: Phase of the total field from S2.1 (3 GHz).
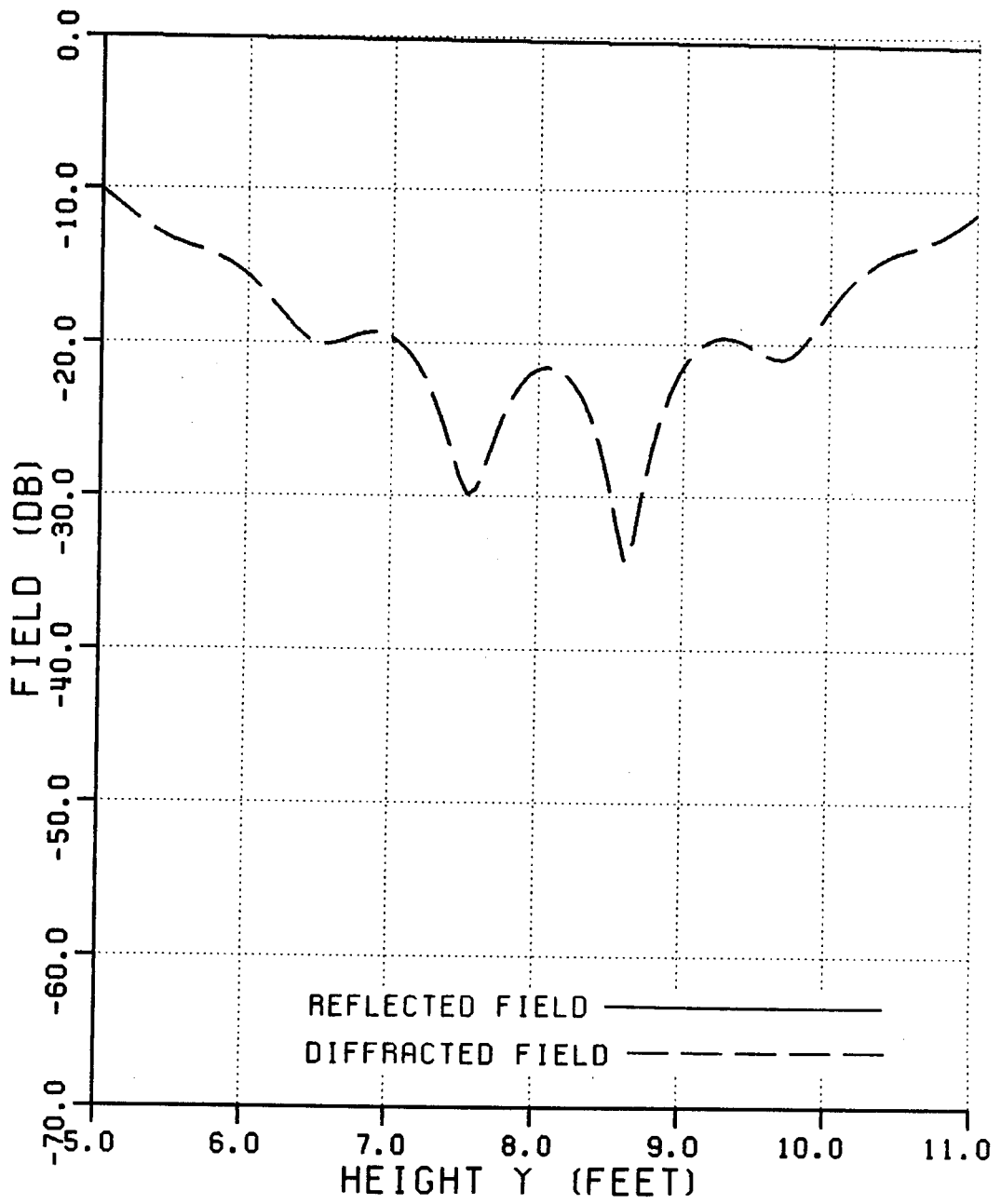
Figure 25: Normalized magnitude of the reflected and diffracted fields from S2.1 (3 GHz).

65
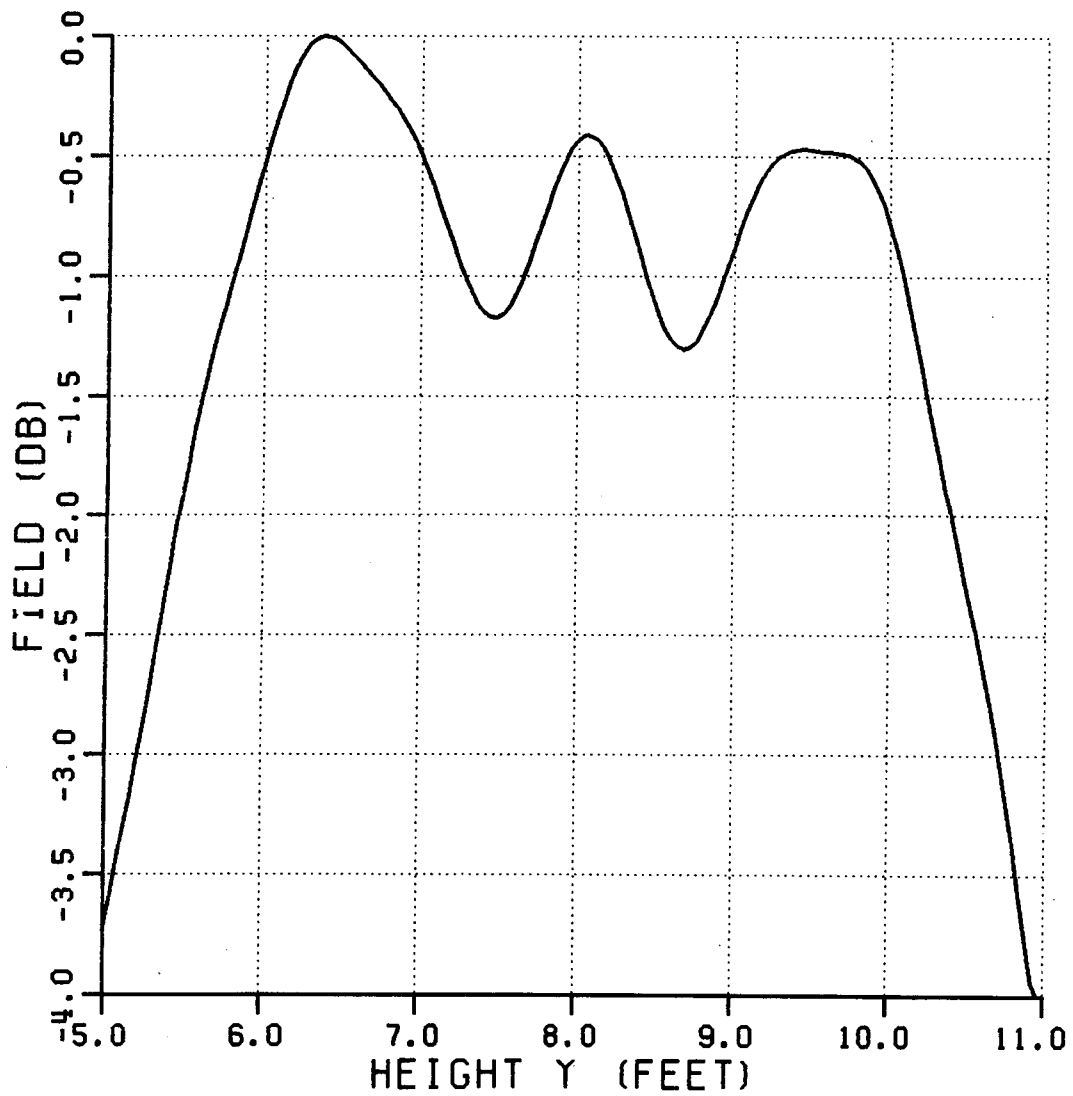
Figure 26: Normalized magnitude of the total field from S2.1 (6 GHz).
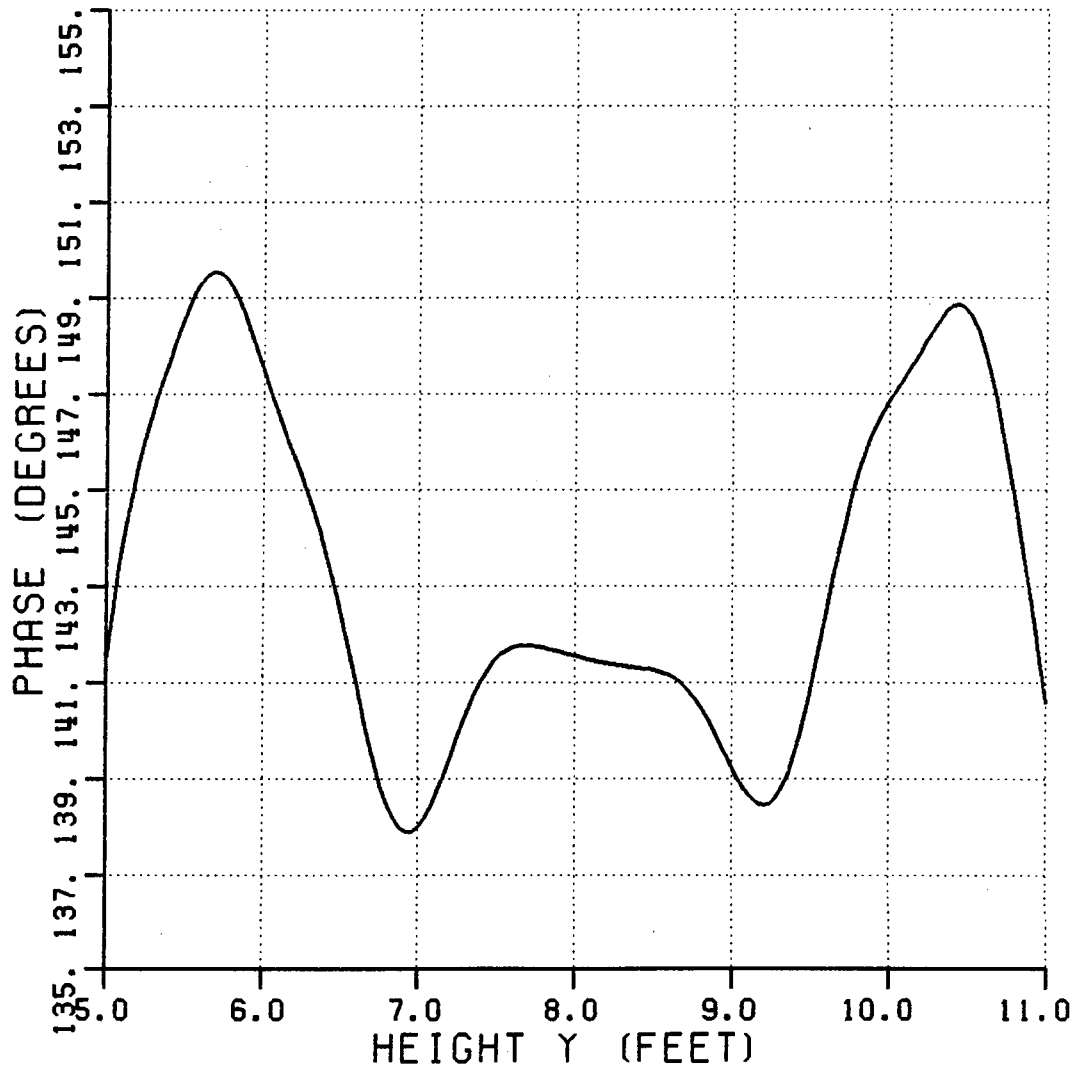
Figure 27: Phase of the total field from S2.1 (6 GHz).

67
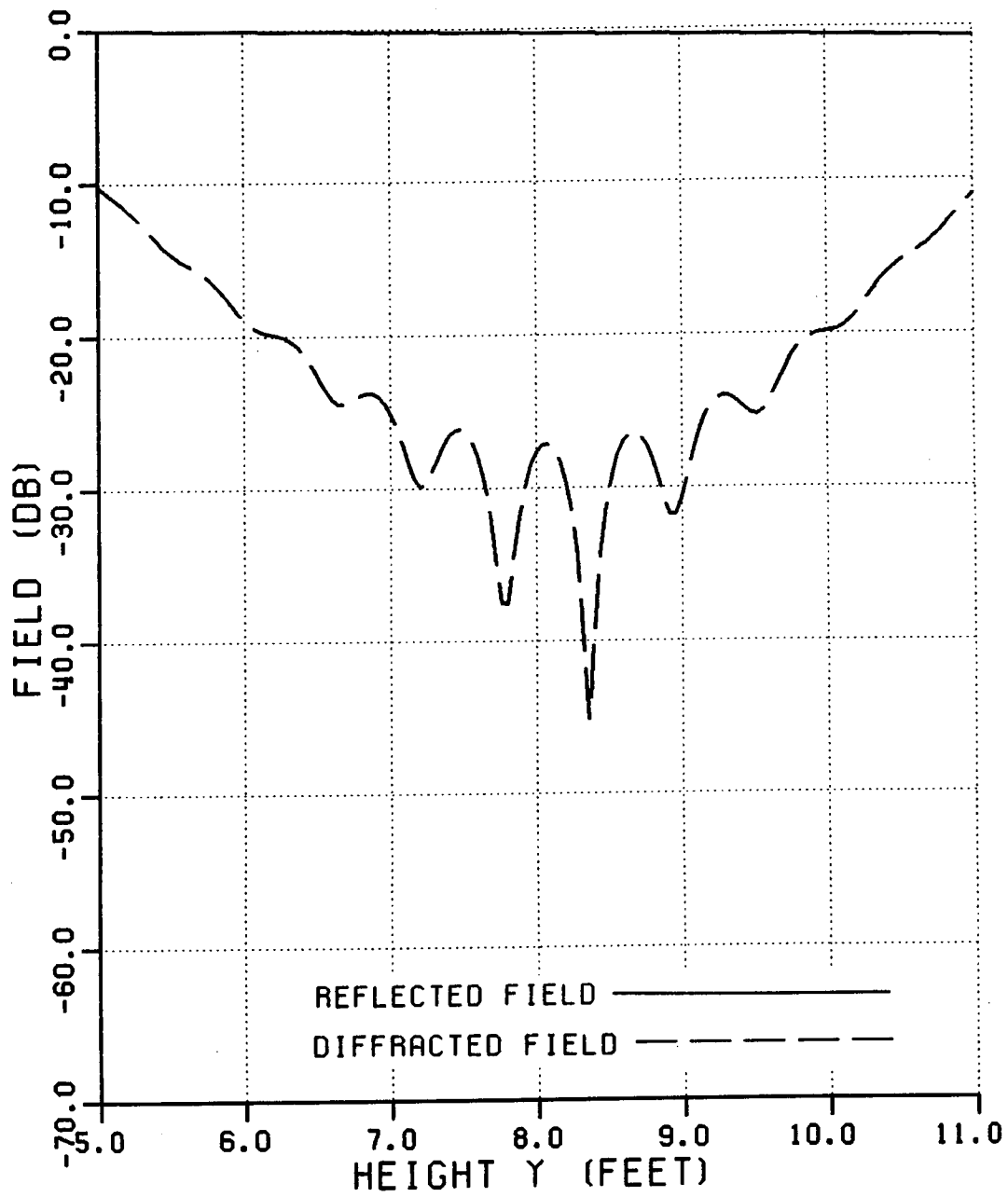
Figure 28: Normalized magnitude of the reflected and diffracted fields from S2.1 (6 GHz).
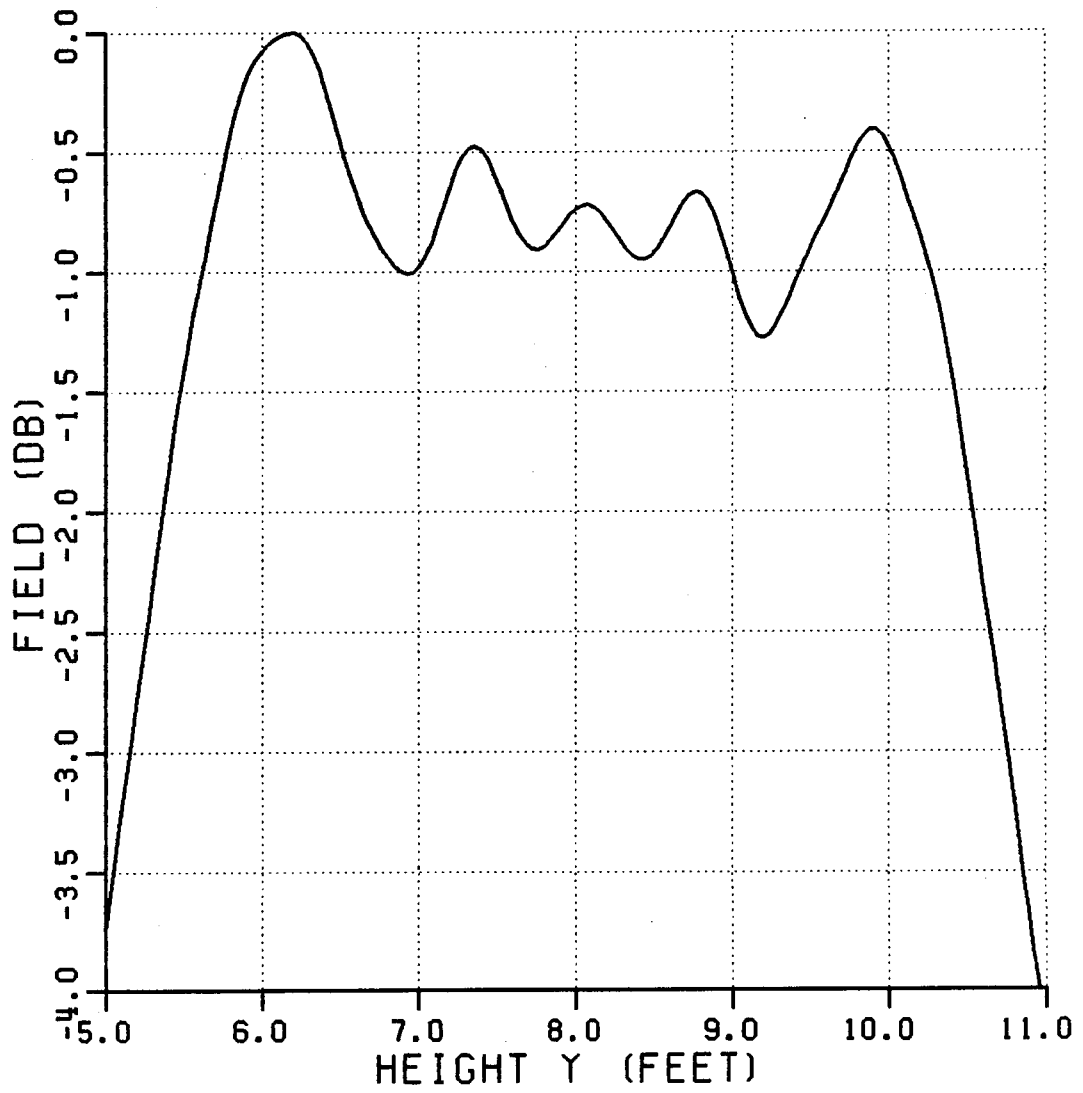
Figure 29: Normalized magnitude of the total field from S2.1 (10 GHz).
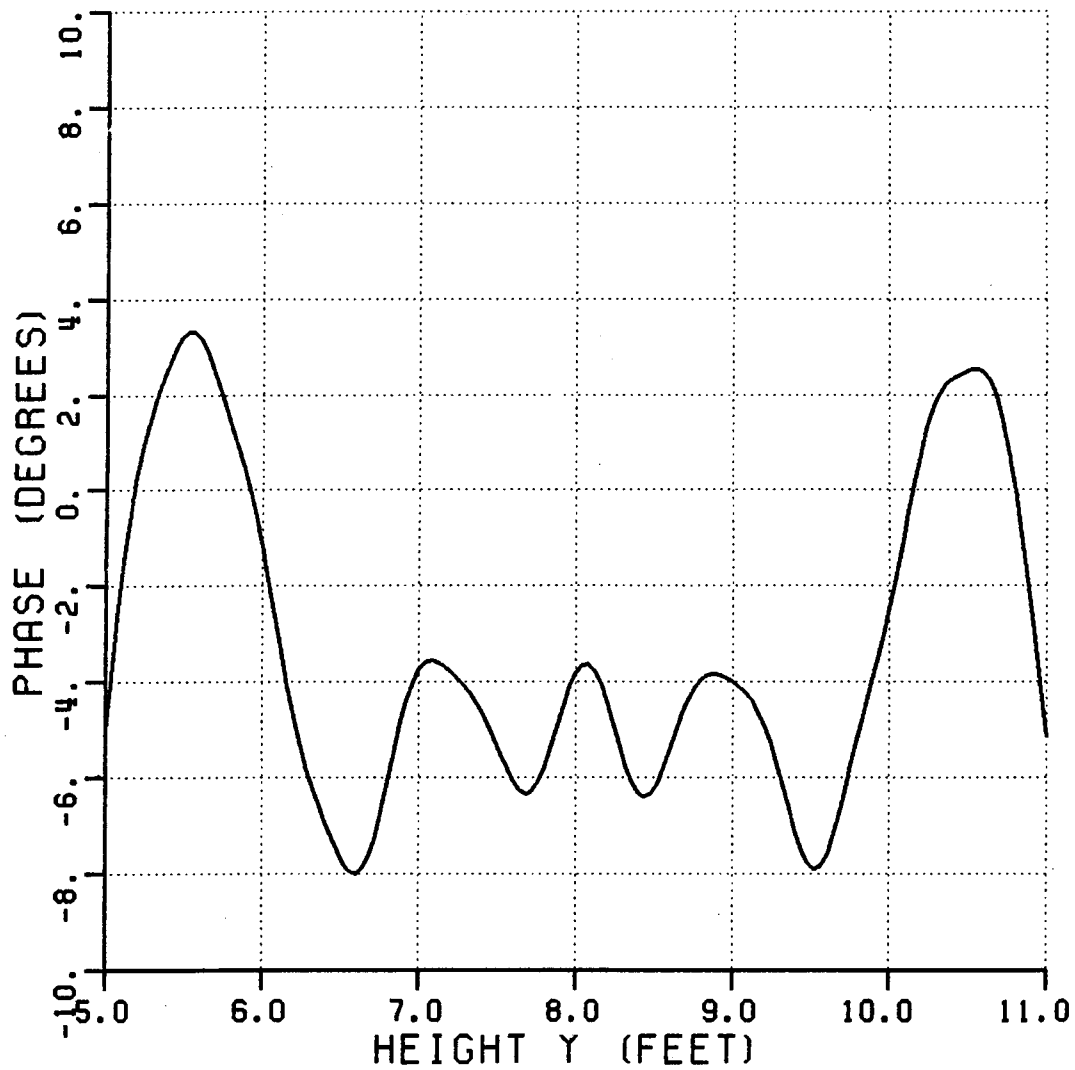
Figure 30: Phase of the total field from S2.1 (10 GHz).
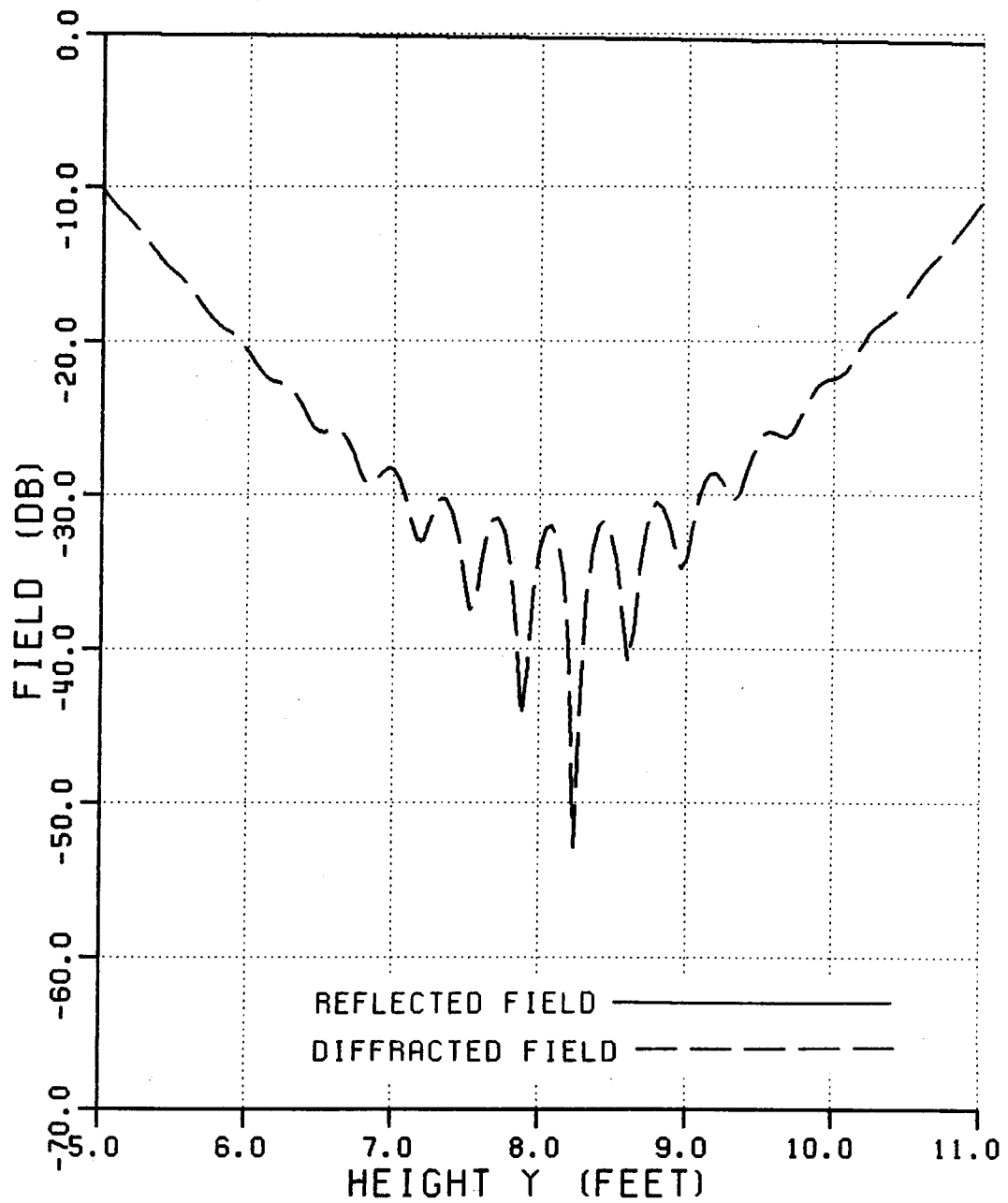
Figure 31: Normalized magnitude of the reflected and diffracted fields from S2.1 (10 GHz).

71

In the case of pure elliptic rolled surface terminations, the UTD can also be used to calculate the scattered fields in the target zone. However, the UTD diffraction coefficients for the higher order blended junctions discussed in the next section are not yet available, so that an alternative method, like PO, has to be used.

It is evident from the results that the performance of this reflector is not up to standard. There is a peak-to-peak phase deviation of 14° at 3 GHz (11° at 10 GHz). The diffracted field is barely 20 dB below the GO level over a $2'$ area of the target zone at 3 GHz, and 20 dB below the GO level over a $4'$ area of the target zone at 10 GHz. The ripple amplitude level is thus in the order of 0.8 dB. From these results it is also evident that the performance of the reflector improves with increasing frequency. By examining the low frequency case one can thus perform a worst case analysis.

3.4   Blended rolled surface terminations

3.4.1   Reduction of diffracted fields using blended rolled edges

The discontinuity of the radius of curvature across the junction of the elliptic rolled surface causes a discontinuity in the reflected fields across the junction which gives rise to an unwanted diffracted field. The creation of a more continuous reflected field across the junction, and hence a smaller edge diffracted field, can be accomplished by smoothly blending the surface of the rolled edge from a parabola into an ellipse. The rolled surface is thus transformed from a pure ellipse into a blended surface according to the expression[32,46]:

$$f_{blend}(\gamma) = f_{parabola}(\gamma)[1 - b(\gamma)] + f_{ellipse}(\gamma)b(\gamma) \qquad (3.43)$$

where γ is a parametric angle (see Equation (3.27)) and $b(\gamma)$ is a blending function which in general varies between zero (at the junction) and one (at the extreme end

of the rolled surface); ie.,

$$b(0) \quad = \quad 0 \text{ , and} \tag{3.44}$$

$$b(\gamma_m) \quad = \quad 1 \text{ .} \tag{3.45}$$

The term $f_{parabola}$ implies the extension of the parabola beyond the junction. The extended parabola is shown in Figure 32. Note that the blended surface is attached to the parabola at P_j in the same way as the ellipse, so that the slope of the surface is smooth across the junction. Equations (3.19)–(3.25) define the local coordinate system of the rolled edge.

It is shown in Appendix A that the use of a blending function as described, will ensure that the surface radius of curvature is continuous across the junction; ie., the radius of curvature of the blended surface at the junction is equal to that of the parabola at the junction in both magnitude and sign. It will be shown later in this section that the following conditions will also hold at the junction:

$$R_c^{(n-1)} \text{ is continuous if } b^{(m)}(0) = 0, \quad m = 1, 2, \ldots, n - 1 \tag{3.46}$$

where $R_c^{(n-1)}$ is the $(n-1)$-th derivative of the radius of curvature with respect to y, and $b^{(m)}$ is the m-th derivative of the blending function with respect to γ. The selection of a blending function that has $b^{(m)}(0) = 0$, will create junctions with increasing degrees of smoothness in terms of the radius of curvature as m increases. A smoother junction will, in turn, tend to minimize the diffracted fields in the target zone. There is, however, a point of diminishing returns where this is no longer true. This point will be discussed again in the next section. A blending function with

$$b^{(n)}(0) \quad \neq \quad 0 \text{ , and} \tag{3.47}$$

$$b^{(m)}(0) \quad = \quad 0, \quad m = 1, 2, \ldots, n - 1 \tag{3.48}$$

73
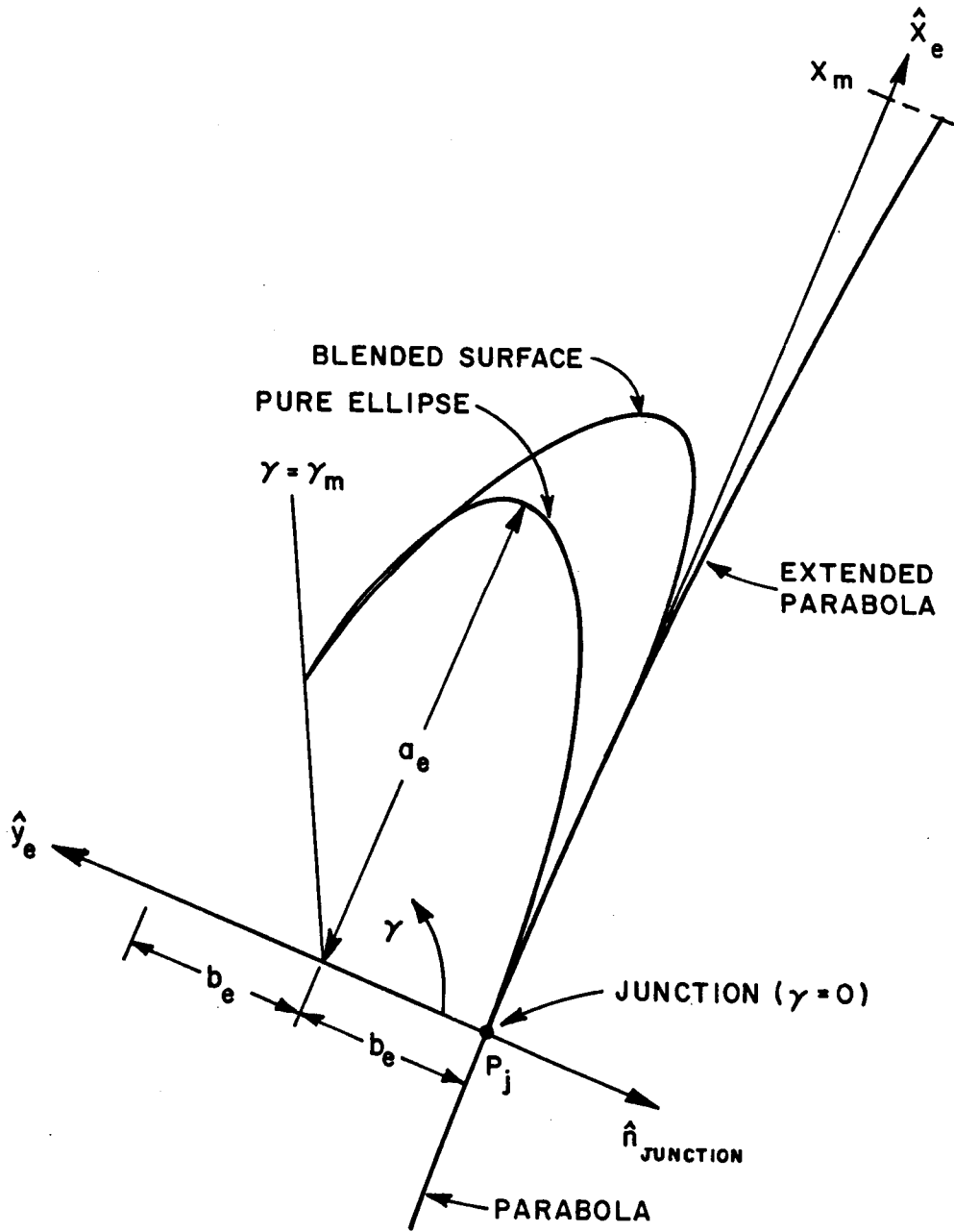
Figure 32: The $x_e y_e$-coordinate system for a blended rolled surface termination.

will be referred to as an n-th order blending function. Reference to Equation (3.46) shows that the n-th derivative of the radius of curvature of a blended surface incorporating an n-th order blending function is discontinuous across the junction, while the m-th order derivatives $(m = 1, 2, \ldots, n-1)$ will all be continuous across the junction.

The following blending functions have been considered:

1) Linear blending:

$$b(\gamma) = \frac{\gamma}{\gamma_m} \tag{3.49}$$

$$b'(\gamma) = \frac{1}{\gamma_m} \text{ , and} \tag{3.50}$$

$$b^{(n)}(\gamma) = 0 \text{ for } n \geq 2 \text{ .} \tag{3.51}$$

2) Square blending:

$$b(\gamma) = \left(\frac{\gamma}{\gamma_m}\right)^2 \tag{3.52}$$

$$b'(\gamma) = \frac{2\gamma}{\gamma_m^2} \tag{3.53}$$

$$b''(\gamma) = \frac{2}{\gamma_m^2} \text{ , and} \tag{3.54}$$

$$b^{(n)}(\gamma) = 0 \text{ for } n \geq 3 \text{ .} \tag{3.55}$$

3) Cosine blending:

$$b(\gamma) = \frac{1}{2}\left(1 - \cos\frac{\pi\gamma}{\gamma_m}\right) \tag{3.56}$$

$$b'(\gamma) = \frac{1}{2}\left(\frac{\pi}{\gamma_m}\right)\sin\frac{\pi\gamma}{\gamma_m} \tag{3.57}$$

75

$$b''(\gamma) = \frac{1}{2}\left(\frac{\pi}{\gamma_m}\right)^2 \cos\frac{\pi\gamma}{\gamma_m} \tag{3.58}$$

$$b'''(\gamma) = -\frac{1}{2}\left(\frac{\pi}{\gamma_m}\right)^3 \sin\frac{\pi\gamma}{\gamma_m} \tag{3.59}$$

$$b^{iv}(\gamma) = -\frac{1}{2}\left(\frac{\pi}{\gamma_m}\right)^4 \cos\frac{\pi\gamma}{\gamma_m} \tag{3.60}$$

$$b^{v}(\gamma) = \frac{1}{2}\left(\frac{\pi}{\gamma_m}\right)^5 \sin\frac{\pi\gamma}{\gamma_m} \text{ , and} \tag{3.61}$$

$$b^{vi}(\gamma) = \frac{1}{2}\left(\frac{\pi}{\gamma_m}\right)^6 \cos\frac{\pi\gamma}{\gamma_m} \text{ .} \tag{3.62}$$

4) Cosine squared blending:

$$b(\gamma) = \frac{1}{4}\left(1 - \cos\frac{\pi\gamma}{\gamma_m}\right)^2 \tag{3.63}$$

$$b'(\gamma) = \frac{1}{2}\left(\frac{\pi}{\gamma_m}\right)\left(\sin\frac{\pi\gamma}{\gamma_m} - \frac{1}{2}\sin\frac{2\pi\gamma}{\gamma_m}\right) \tag{3.64}$$

$$b''(\gamma) = \frac{1}{2}\left(\frac{\pi}{\gamma_m}\right)^2\left(\cos\frac{\pi\gamma}{\gamma_m} - \cos\frac{2\pi\gamma}{\gamma_m}\right) \tag{3.65}$$

$$b'''(\gamma) = \frac{1}{2}\left(\frac{\pi}{\gamma_m}\right)^3\left(2\sin\frac{2\pi\gamma}{\gamma_m} - \sin\frac{\pi\gamma}{\gamma_m}\right) \tag{3.66}$$

$$b^{iv}(\gamma) = \frac{1}{2}\left(\frac{\pi}{\gamma_m}\right)^4\left(4\cos\frac{2\pi\gamma}{\gamma_m} - \cos\frac{\pi\gamma}{\gamma_m}\right) \tag{3.67}$$

$$b^{v}(\gamma) = \frac{1}{2}\left(\frac{\pi}{\gamma_m}\right)^5\left(\sin\frac{\pi\gamma}{\gamma_m} - 8\sin\frac{2\pi\gamma}{\gamma_m}\right) \text{ , and} \tag{3.68}$$

$$b^{vi}(\gamma) = \frac{1}{2}\left(\frac{\pi}{\gamma_m}\right)^6\left(\cos\frac{2\pi\gamma}{\gamma_m} - 16\cos\frac{\pi\gamma}{\gamma_m}\right) \text{ .} \tag{3.69}$$

The case where $b(\gamma) = 1$ implies that no blending occurs, so that the blended surface remains a pure ellipse. The elliptic curve has already been described as a function of γ in Equations (3.32) and (3.33). However, in order to describe the general blended surface, it is necessary to define the extended parabola resulting from $b(\gamma) = 0$ as a function of γ as well. Since the blending algorithm has to be

76

applied ultimately to the design of a three-dimensional concave edged reflector as well as to the two-dimensional case considered here, the extended parabola will be defined as follows:

Let x_m be a maximum distance measured along the positive x_e-axis, starting at the junction. Let the parametric angle (γ) be transformed into a linear displacement along this axis, such that

$$x_e(\gamma) = \gamma \frac{x_m}{\gamma_m} \quad \text{for } 0 \le \gamma \le \gamma_m .\tag{3.70}$$

Using Equations (3.18), (3.26) and (3.70), the extended parabola can then be defined by

$$y_{parabola}(\gamma) = \gamma\left(\frac{x_m}{\gamma_m}\right)x_{p2} + y_j , \text{ and} \tag{3.71}$$

$$z_{parabola}(\gamma) = \frac{y_{parabola}^2(\gamma)}{4f_c} . \tag{3.72}$$

The general two-dimensional blended rolled surface can thus now be expressed in the yz-system as

$$\mathbf{r}_{blend}(\gamma) = y_{blend}(\gamma)\hat{\mathbf{y}} + z_{blend}(\gamma)\hat{\mathbf{z}} \tag{3.73}$$

where

$$y_{blend}(\gamma) = \left[\gamma\left(\frac{x_m}{\gamma_m}\right)x_{p2} + y_j\right][1 - b(\gamma)]$$
$$+ [(a_e \sin\gamma)x_{p2} + b_e(1 - \cos\gamma)y_{p2} + y_j]b(\gamma) \tag{3.74}$$

and

$$z_{blend}(\gamma) = \left(\frac{[\gamma(x_m/\gamma_m)x_{p2} + y_j]^2}{4f_c}\right)[1 - b(\gamma)]$$
$$+ [(a_e \sin\gamma)x_{p3} + b_e(1 - \cos\gamma)y_{p3} + z_j]b(\gamma) . \tag{3.75}$$

The direction cosines ($x_{p2}, x_{p3}, y_{p2}, y_{p3}$) are given in Equations (3.22)–(3.25).

77

The radii of curvature of the blended surface and parabola as well as their derivatives with respect to y are derived in Appendix A. In order to investigate the discontinuities in the derivatives of the radius of curvature across the junction, the expressions for the derivatives of the radius of curvature of the blended surface and the parabola will now be compared at the top junction (except for the first order case where both top and bottom junctions are considered). Consider a first order blending function; ie., $b'(0) \neq 0$. At $\gamma = 0$, one finds that

$$\left(\frac{dR_c}{dy}\right)^{blend} = \left(\frac{dR_c}{dy}\right)^{parabola} + b'(0)\epsilon_1 \qquad (3.76)$$

where

$$\epsilon_1 = \frac{\pm 12 f_c \left[1 + (y_j/2f_c)^2\right]^2}{(x_m/\gamma_m)} \left(\frac{a_e}{(x_m/\gamma_m)} + \frac{f_c b_e \sqrt[3]{1 + (y_j/2f_c)^2}}{(x_m/\gamma_m)^2} - \frac{1}{2}\right) \qquad (3.77)$$

and y_j is the y-coordinate of the junction. The ($\pm$) sign corresponds to the top and bottom junctions, respectively. In the special case of linear blending, $b'(0) = 1/\gamma_m$, so that

$$b'(0)\epsilon_1 = \frac{\pm 12 f_c \left[1 + (y_j/2f_c)^2\right]^2}{x_m} \left(\frac{a_e}{(x_m/\gamma_m)} + \frac{f_c b_e \sqrt[3]{1 + (y_j/2f_c)^2}}{(x_m/\gamma_m)^2} - \frac{1}{2}\right) .$$
$$(3.78)$$

Consider now a second order blending function; ie., $b'(0) = 0$ and $b''(0) \neq 0$. At $\gamma = 0$, one finds that

$$\left(\frac{d^2 R_c}{dy^2}\right)^{blend} = \left(\frac{d^2 R_c}{dy^2}\right)^{parabola} + b''(0)\epsilon_2 \qquad (3.79)$$

where

$$\epsilon_2 = \frac{24 f_c \left[1 + (y_{top}/2f_c)^2\right]^{\frac{5}{2}}}{(x_m/\gamma_m)^2} \left(\frac{a_e}{(x_m/\gamma_m)} + \frac{f_c b_e \sqrt[3]{1 + (y_{top}/2f_c)^2}}{(x_m/\gamma_m)^2} - \frac{1}{2}\right) . \qquad (3.80)$$

In the special case of square blending, $b''(0) = 2/\gamma_m^2$, so that

$$b''(0)\epsilon_2 = \frac{48f_c \left[1 + (y_{top}/2f_c)^2\right]^{\frac{5}{2}}}{x_m^2} \left(\frac{a_e}{(x_m/\gamma_m)} + \frac{f_c b_e \sqrt[3]{1 + (y_{top}/2f_c)^2}}{(x_m/\gamma_m)^2} - \frac{1}{2}\right) .$$

(3.81)

In the special case of cosine blending, $b''(0) = \pi^2/2\gamma_m^2$, so that

$$b''(0)\epsilon_2 = \frac{118.44f_c \left[1 + (y_{top}/2f_c)^2\right]^{\frac{5}{2}}}{x_m^2} \left(\frac{a_e}{(x_m/\gamma_m)} + \frac{f_c b_e \sqrt[3]{1 + (y_{top}/2f_c)^2}}{(x_m/\gamma_m)^2} - \frac{1}{2}\right) .$$

(3.82)

Although square blending and cosine blending are both second order blending functions, square blending yields a smoother junction in terms of the continuity of the second derivative of the radius of curvature at the junction, since the value of the second derivative of the square blending function at the junction is smaller than that of the cosine blending function for a given set of blending parameters $(a_e, b_e, x_m, \gamma_m)$. However, these parameters will not necessarily yield a blended surface that adheres to all the design criteria, so that one cannot say that a square blend will be better than a cosine blend in general. Consider now a fourth order blending function; ie., $b'(0) = 0, b''(0) = 0, b'''(0) = 0$ and $b^{iv}(0) \neq 0$. At $\gamma = 0$, one finds that

$$\left(\frac{d^4R_c}{dy^4}\right)^{blend} = \left(\frac{d^4R_c}{dy^4}\right)^{parabola} + b^{iv}(0)\epsilon_4$$

(3.83)

where

$$\epsilon_4 = \frac{60f_c \left[1 + (y_{top}/2f_c)^2\right]^{\frac{7}{2}}}{(x_m/\gamma_m)^4} \left(\frac{a_e}{(x_m/\gamma_m)} + \frac{f_c b_e \sqrt[3]{1 + (y_{top}/2f_c)^2}}{(x_m/\gamma_m)^2} - \frac{1}{2}\right)$$

(3.84)

In the special case of cosine square blending, $b^{iv}(0) = 3\pi^4/2\gamma_m^4$, so that

$$b^{iv}(0)\epsilon_4 = \frac{8767f_c \left[1 + (y_{top}/2f_c)^2\right]^{\frac{7}{2}}}{x_m^4} \left(\frac{a_e}{(x_m/\gamma_m)} + \frac{f_c b_e \sqrt[3]{1 + (y_{top}/2f_c)^2}}{(x_m/\gamma_m)^2} - \frac{1}{2}\right) .$$

(3.85)

C - 2

Based upon the expressions above, one now can make the following generalizations:

1. In the case of an n-th order blending function, the following will hold at the junction ($\gamma = 0, y = y_{top}$):

$$\left(\frac{d^n R_c}{dy^n}\right)^{blend} = \left(\frac{d^n R_c}{dy^n}\right)^{parabola} + b^{(n)}(0)\epsilon_n \text{ , and} \qquad (3.86)$$

$$\left(\frac{d^m R_c}{dy^m}\right)^{blend} = \left(\frac{d^m R_c}{dy^m}\right)^{parabola} , \quad m = 1, 2, \ldots, n-1 \qquad (3.87)$$

where

$$\epsilon_n = \frac{\alpha_n f_c [1 + (y_j/2f_c)^2]^{(n+3)/2}}{(x_m/\gamma_m)^n} \left(\frac{a_e}{(x_m/\gamma_m)} + \frac{f_c b_e \sqrt[3]{1 + (y_j/2f_c)^2}}{(x_m/\gamma_m)^2} - \frac{1}{2}\right)$$
$$(3.88)$$

and α_n is a constant.

2. The error term (ϵ_n) will be zero if

$$\left(\frac{x_m}{\gamma_m}\right) = a_e + \sqrt{a_e^2 + 2f_c b_e \sqrt[3]{1 + (y_j/2f_c)^2}} . \qquad (3.89)$$

where γ_m is evaluated in radians. This will lead to continuity in the n-th derivative of the radius of curvature across the junction. For the design cases considered, however, it was found that blending parameters that satisfy this equation do not yield blended surfaces that adhere to the design requirements.

Table 5 indicates the orders of various blending functions with their derivatives at the junction.

3.4.2 Design of blended rolled edges

This section describes a design algorithm for blended rolled edges. As of yet there are no closed form design equations available that will yield optimum blended

80

Table 5: Orders of various blending functions and their derivatives at the junction.

	First order	Second order		Fourth order
	Linear	Square	Cosine	Cosine squared
$b'(0)$	$1/\gamma_m$	0	0	0
$b''(0)$	0	$2/\gamma_m^2$	$\pi^2/2\gamma_m^2$	0
$b'''(0)$	0	0	0	0
$b^{iv}(0)$	0	0	$-\pi^4/2\gamma_m^4$	$3\pi^4/2\gamma_m^4$

edges, so that the design is an iterative process which involves the calculation of the scattered fields for every given set of blending parameters $(a_e, b_e, x_m, \gamma_m)$. The blending parameters are changed from one iteration to the next according to whether the diffracted fields become smaller or not. The final design will then be based on that set of parameters that yields the smallest edge diffracted field in the target zone. This cut-and-try approach is very unsatisfactory since one can never be sure that the design is actually an optimum. Furthermore, the calculation of the scattered field is a very cumbersome process, especially as a step in an iterative process.

A new design algorithm was developed in the course of this study which is based upon an analysis of the continuity of the higher order derivatives of the radius of curvature of the surface across the junction. It allows the user to see how the surface characteristics that influence the diffracted field change as a function of the blending parameters. This enables one to select a set of blending parameters that will yield an optimum design. Once the optimum blending parameters have been selected, the scattered fields are calculated to verify the design.
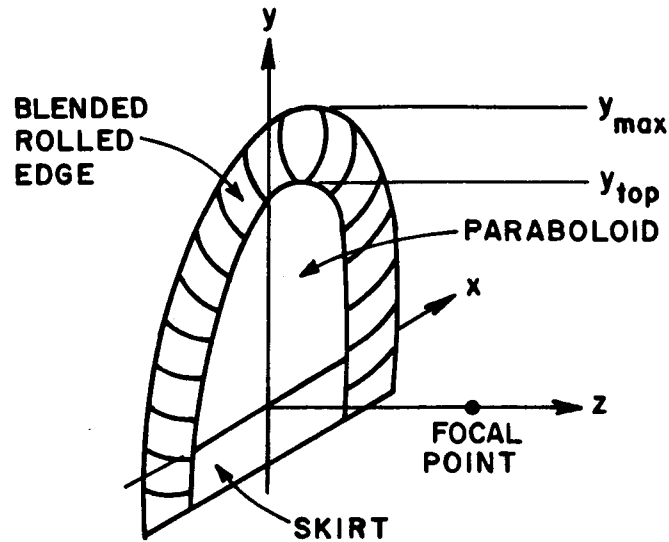
Figure 33: Axially symmetric reflector with a blended rolled edge.

This discussion centers around the design of a blended rolled edge for an axially symmetric reflector as shown in Figure 33[47,48]. The yz-plane can thus be considered without loss of generality. It is assumed that the focal length (f_c) and the height of the junction between the parabola and the blended edge (y_{top}) are given. The size of the parabolic section is usually equal to or larger than ten wavelengths at the lowest frequency of operation ($10\lambda_{max}$)[49]. The blended edge is to be designed such that the minimum radius of curvature in the lit region of the rolled edge (R_c^{min}) is equal to a quarter of a wavelength at the lowest frequency of operation ($\lambda_{max}/4$) and the maximum height of the reflector, measured from the axis of symmetry of the paraboloid to the top of the rolled edge, is equal to y_{max}. Note that the skirt shown in Figure 33 is not included in the definition of y_{max}. The design problem is to find that set of blending parameters (a_e, b_e, x_m, γ_m) that will satisfy these requirements and results in the smallest diffracted field from the junction into the target zone.

The first step in the design is to select a blending function. It is desirable to

82

select a blending function with as high an order as possible, since this will ensure that the higher order derivatives of the radius of curvature are continuous across the junction. However, an arbitrarily high order of blending function may make it impossible to satisfy the requirements placed on R_c^{min} and y_{max} since a higher order blending function requires more space ($y_{max} - y_{top}$) in order to obtain a smooth junction. Furthermore, there is a point of diminishing returns where the continuity of higher derivatives of the radius of curvature across the surface no longer yield smaller diffracted fields over the entire target zone. This is due to the fact that the transition region spreads out as the junction becomes smoother, as shown in Figure 34. Since the diffracted field is strongest in the transition region, a higher order blending function consequently results in a weaker diffracted field which is prevalent over a larger area of the target zone. In the course of this study it was found that a cosine blending function is a good choice when

$$y_{max} - y_{top} < 5\, \lambda_{max} \qquad (3.90)$$

and that a cosine squared blending function should be used when

$$y_{max} - y_{top} > 5\, \lambda_{max} \; . \qquad (3.91)$$

If

$$y_{max} - y_{top} \approx 5\, \lambda_{max} \qquad (3.92)$$

it is worthwhile to consider both cosine and cosine squared blending functions and then to select the one that results in the smallest edge diffracted fields in the target zone. Equations (3.90)–(3.92) can be used as a rule–of–thumb when selecting a blending function. Since higher order blending functions inherently result in smoother junctions, the manufacturing difficulties will also be a consideration.

In order to facilitate the iterative design process a computer program was developed that determines the following values in table format:
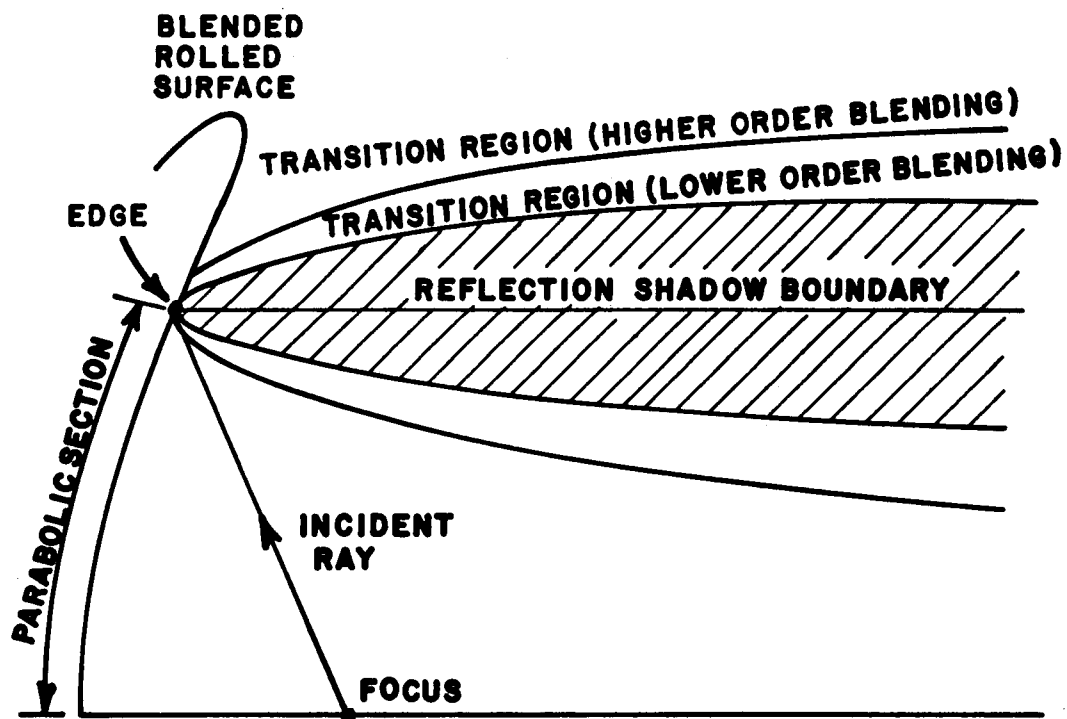
83

Figure 34: The influence of the blending function on the transition region around the reflection shadow boundary.

1. Radius of curvature and the first four derivatives with respect to y on either side of the junction. Analytic expressions are used to evaluate these quantities (see Appendix A).

2. Radius of curvature and corresponding γ-value at the incident shadow boundary. The location of the shadow boundary is found by making use of Equation (2.41).

3. Minimum radius of curvature and corresponding γ-value along the entire blended edge (lit and shadow regions).

4. Maximum height of the reflector (including parabolic section and blended edge, ie. y_{max}) and maximum z-dimension.

The values above are determined for a range of x_m and γ_m parameters when a_e and b_e are fixed. A set of tables are then generated for various combinations of a_e and b_e. From these tables the sets of blending parameters that satify the constraints (R_c^{min}, y_{max} and y_{top}) can be determined. A typical output using a cosine squared blending function is shown in Table 6.

There are usually several sets of blending parameters that will satisfy the design constraints. However for an n-th order blending function, the first $n - 1$ derivatives of the surface radius of curvature are continuous across the junction but the n-th derivative is not. The optimum set of blending parameters will be the set that satisfies the design constraints and minimizes the discontinuity in the n-th derivative of the radius of curvature across the junction. Examination of Equation (3.88) indicates that large values of x_m, small values of γ_m (ie. a large x_m/γ_m ratio), and small values of a_e and b_e will generally yield better results, since they will tend to minimize the error term (ϵ_n). Note that the absolute minimum

85

Table 6: Typical output of the optimization program for the design of blended rolled edges.

COSINE SQUARED BLENDING DESIGN REQUIREMENTS:						FOCUS=24′ RCMIN = 0.246′ (1 GHz)			YTOP=15′ YMAX = 20′		
XM	GM	RC	RC1	RC2 (10X)	RC3 (100X)	RC4 (100X)	RSH	GSH	RMIN	GMIN	YMAX
_ae = 2.60′_					_be = 2.40′_				(OPTIMUM)		
11.00	110.	55.20	0.982	0.713	0.113	3925.	0.235	60.	0.235	60.	19.76
11.00	116.	55.20	0.982	0.713	0.113	4425.	0.275	63.	0.275	63.	19.80
11.00	120.	55.20	0.982	0.713	0.113	4771.	0.301	65.	0.301	65.	19.83
11.62	110.	55.20	0.982	0.713	0.113	2778.	0.211	60.	0.209	60.	19.96
11.62 *	116.	55.20	0.982	0.713	0.113	3140.	0.246	63.	0.246	63.	20.00
11.62	120.	55.20	0.982	0.713	0.113	3390.	0.271	65.	0.271	65.	20.03
12.00	110.	55.20	0.982	0.713	0.113	2265.	0.196	60.	0.195	60.	20.08
12.00	116.	55.20	0.982	0.713	0.113	2564.	0.232	63.	0.230	63.	20.12
12.00	120.	55.20	0.982	0.713	0.113	2771.	0.255	65.	0.254	65.	20.15
Parabola		55.20	0.982	0.713	0.113	0.006					
_ae = 2.70′_					_be = 2.40′_				(INCREASED _ae_)		
11.62	110.	55.20	0.982	0.713	0.113	2805.	0.222	60.	0.220	60.	19.99
11.62	116.	55.20	0.982	0.713	0.113	3168.	0.258	63.	0.258	63.	20.04
11.62	120.	55.20	0.982	0.713	0.113	3419.	0.283	65.	0.283	66.	20.07
_ae = 2.50′_					_be = 2.40′_				(DECREASED _ae_)		
11.62	110.	55.20	0.982	0.713	0.113	2752.	0.201	59.	0.199	60.	19.92
11.62	116.	55.20	0.982	0.713	0.113	3112.	0.235	63.	0.234	63.	19.96
11.62	120.	55.20	0.982	0.713	0.113	3362.	0.258	65.	0.258	65.	19.99
_ae = 2.60′_					_be = 2.50′_				(INCREASED _be_)		
11.62	110.	55.20	0.982	0.713	0.113	2899.	0.225	60.	0.224	60.	19.96
11.62	116.	55.20	0.982	0.713	0.113	3274.	0.264	63.	0.263	63.	20.01
11.62	120.	55.20	0.982	0.713	0.113	3534.	0.289	65.	0.289	65.	20.04
_ae = 2.60′_					_be = 2.30′_				(DECREASED _be_)		
11.62	110.	55.20	0.982	0.713	0.113	2658.	0.196	60.	0.195	60.	19.95
11.62	116.	55.20	0.982	0.713	0.113	3006.	0.231	63.	0.229	63.	19.99
11.62	120.	55.20	0.982	0.713	0.113	3247.	0.254	65.	0.253	65.	20.02

* = optimum design
FOCUS = focal length of parabolic reflector
YTOP = height of junction between parabolic section and blended rolled edge
RCMIN = minimum radius of curvature along the lit part of the blended rolled edge
YMAX = maximum height of surface
XM = maximum linear blending distance (x_m)
GM = maximum parametric blending angle (γ_m)
RC = radius of curvature at the junction
RCn = n-th derivative of the radius of curvature at the junction
RSH = radius of curvature at the shadow boundary
GSH = angle at which shadow boundary occurs
RMIN = minimum radius of curvature along the surface
GMIN = angle at which minimum radius of curvature occurs
Lengths in feet, angles in degrees

86

radius of curvature along the entire blended surface usually occurs in the shadow region, so that the radius of curvature at the shadow boundary is the minimum radius of curvature in the lit region (R_c^{min}). However, the absolute minimum radius of curvature along the entire blended surface can also occur in the lit region, in which case that value will then be R_c^{min}. The actual minimum radius of curvature in the lit region of the blended surface that is obtained for a given set of blending parameters should not be smaller than R_c^{min}, since that implies a higher, lowest frequency of operation. On the other hand, an actual minimum radius of curvature in the lit region that is larger than R_c^{min} indicates an over-design and consequently not an optimum. An actual maximum height that is smaller than y_{max} similarly is not an optimum design, since it was found that, in general, smoother junctions can be obtained if more height is available to fit the blended rolled edge in.

The iterative design process thus involves the following steps:

1. Determine the focal length of the parabola and the height of the junction between the parabolic section and the blended edge (y_{top}).

2. Select a maximum total height (y_{max}).

3. Select the lowest frequency of operation and let $R_c^{min} = \lambda_{max}/4$.

4. Select a blending function of order n. The rules–of–thumb given in Equations (3.90)–(3.92) are useful guidelines in this choice.

5. Generate data tables for a wide range of blending parameters (a_e, b_e, x_m, γ_m) to gain a general idea of the orders of magnitude of the blending parameters that will satisfy the design constraints (R_c^{min}, y_{top} and y_{max}).

6. Generate data tables using the blending parameter values in all the regions around those found in Step 5 until blending parameters are found that satisfy

the design constraints. Select that set of blending parameters that has the smallest discontinuity in the n-th derivative of the radius of curvature of the surface across the junction This step is repeated until an optimum is found.

7. Calculate the scattered fields.

Although it has not been done at this time, the algorithm is suitable for automation, so that the complete iteration can be done by a computer.

As an example, consider the data in Table 6. The design requirements were as follows:

$$f_c = 24' \tag{3.93}$$

$$y_{top} = 15' \text{ , and} \tag{3.94}$$

$$y_{max} = 20' . \tag{3.95}$$

The lowest frequency of operation is 1 GHz, which corresponds to a free space wavelength of $\lambda_{max} = 0.984'$. Since the minimum radius of curvature of the blended edge in the lit region has to be equal to $\lambda_{max}/4$, the design requirement is $R_c^{min} = 0.246'$. Table 6 indicates that an optimum design, using a cosine squared blending function, was obtained for the following blending parameters:

$$a_e = 2.60' \tag{3.96}$$

$$b_e = 2.40' \tag{3.97}$$

$$x_m = 11.62' \text{ , and} \tag{3.98}$$

$$\gamma_m = 116^o . \tag{3.99}$$

The design is an optimum since the blending parameters in Equations (3.96)–(3.99) result in a blended edge that satisfies the design constraints in Equations (3.93)–(3.95), and a small change in the parameters result in a larger discontinuity in

88

R_c^{iv} across the junction. Note that for these parameters, the minimum radius of curvature along the entire blended surface occurs at the shadow boundary. Since cosine squared blending was used, the first three derivatives of the radius of curvature are continuous across the junction, but the fourth derivative is not.

The effect of the error term defined in Equation (3.86) is clearly demonstrated in Table 6; viz.,

1. For a_e, b_e and x_m fixed, $(R_c^{iv})^{blend}$ approaches $(R_c^{iv})^{parabola}$ as γ_m decreases.

2. For a_e, b_e and γ_m fixed, $(R_c^{iv})^{blend}$ approaches $(R_c^{iv})^{parabola}$ as x_m increases.

3. Increasing and decreasing the values of a_e and b_e (with x_m and γ_m fixed) results in enlarging and reducing the discontinuity between $(R_c^{iv})^{blend}$ and $(R_c^{iv})^{parabola}$ at the junction, respectively.

Note that this algorithm is used to optimize the blended rolled edge in the yz-plane, and is applicable to the three-dimensional reflector in Figure 33 because it is axially symmetric. In order to expand the method to optimize edges in planes other than the yz-plane, the equations for the derivatives of the radius of curvature in Appendix A would have to be derived in three dimensions.

3.4.3 Design example (focus feed)

Consider now the parabolic reflector described in Section 3.3 (S2.1), but with a cosine blended edge and blending parameters $x_m = 7'$ and $\gamma_m = 120^o$. Note that this blended surface is not optimized. The design illustrates the improvement that can be obtained by blending when the dimensions of the ellipse axes (a_e and b_e) are kept constant. This surface is designated as S2.2 and shown in Figure 35. The surface characteristics are given in Table 7. The radii of curvature at the junctions y_{bot} and y_{top} of a parabola with $f_c = 12'$ are given in Table 8. The quantities R_c'
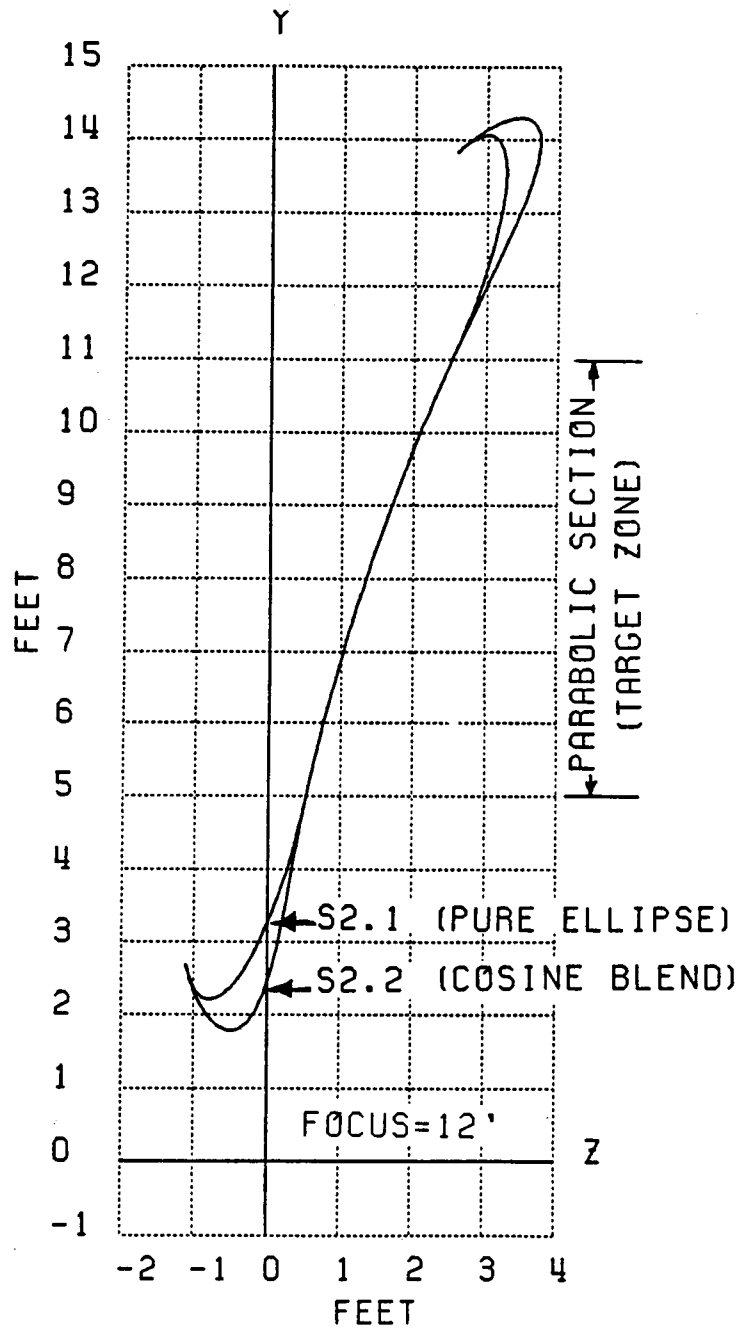
Figure 35: Two-dimensional parabolic reflector with cosine blended rolled edges (S2.2).

90

Table 7: Surface characteristics for S2.2.

Cosine Blending								
f_c	12′	\multicolumn						
a_e	3′							
b_e	0.75′							

Cosine Blending		RADIUS OF CURVATURE (ROLLED EDGE)					
			Junction		Minimum		Shadow Boundary
f_c	12′		bottom	top	bottom	top	bottom	top
a_e	3′							
b_e	0.75′							
x_m	7′	γ	0°	0°	78°	78°	81°	73°
γ_m	120°	R_c	25.579′	31.947′	0.234′	0.209′	0.248′	0.256′
y_{bot}	5′	R_c'	0.638	1.513				
y_{top}	11′	R_c''	40.655	68.451				
z_{pat}	24′							

and R_c'' denote differentiation with respect to y. Comparison of Tables 7 and 8 shows that in the case of the cosine blended edge, R_c and R_c' are continuous across the junction, but R_c'' is not. Based on Equation (3.46), this result is to be expected since cosine blending is a second order blending function. The radii of curvature of the blended rolled surfaces are shown in Figures 36 and 37. Note that the rolled surface is concave at the junction but convex at the extreme end, so that there is an inflection point somewhere along the surface where the surface changes from concave to convex. The radius of curvature of the surface goes to infinity at this point as shown in Figures 36 and 37. Consequently, there is no discontinuity in the reflected field in the area of this inflection point such that no diffracted field results.

The reflector is illuminated by a TM line source with a uniform pattern located at the focus. The target zone is considered to be located at a distance (z_{pat}) of

91

Table 8: Radii of curvature at the junctions of a parabola with $f_c = 12'$.

RADIUS OF CURVATURE (PARABOLA)		
	bottom($y_{bot} = 5'$)	top($y_{top} = 11'$)
R_c	25.579'	31.947'
R_c'	0.638	1.513
R_c''	0.133	0.161
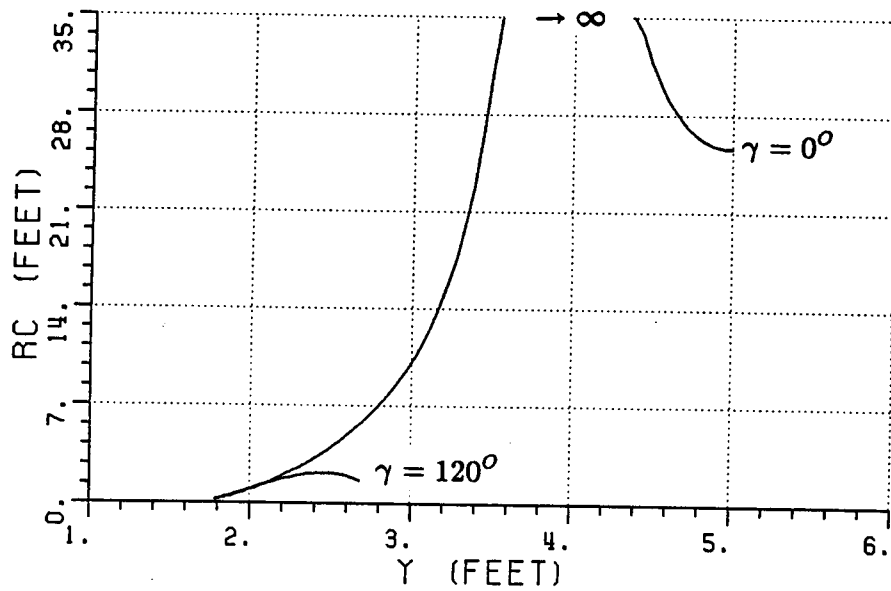
Figure 36: Radius of curvature of the bottom blended surface of S2.2.
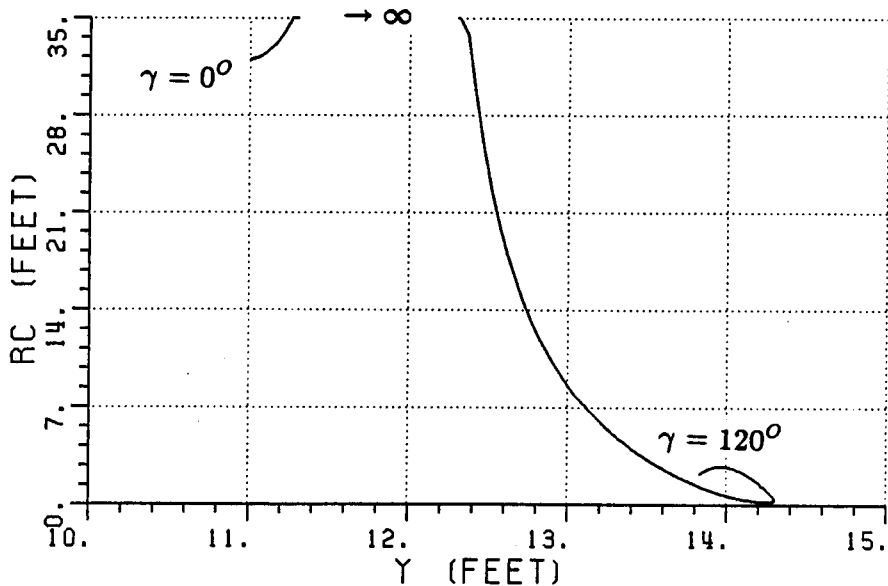
Figure 37: Radius of curvature of the top blended surface of S2.2.

$24'$ away from the main origin along the z-axis. For the purpose of this analysis it is assumed that there is no direct illumination from the source in the target zone. The total field in the target zone can be calculated using the corrected PO method, with the end point contributions at the shadow boundaries of the rolled surfaces subtracted to yield the "true" total field. The GO reflected field can then be subtracted from the total field to determine the fields diffracted from the junctions.

The normalized magnitude and phase of the total field in the target zone, together with plots comparing the reflected fields with the fields diffracted from the junctions are shown in Figures 38–46, calculated at frequencies of 3 GHz, 6 GHz and 10 GHz, respectively. Comparison of Figures 38–46 with Figures 23–31 show the improvement in performance of the cosine blended rolled surface (S2.2) over

the pure elliptic rolled surface (S2.1). Note that the blended rolled edges of S2.2 are based on an ellipse that has the same dimensions as the rolled edge of S2.1, so the only difference between S2.1 and S2.2 is the blending of S2.2. It is thus clear from these results that the blended rolled edges have increased the performance of S2.2 substantially compared to that of S2.1. At 3 GHz the diffracted fields from S2.2 are 20 dB below the GO field over the entire target zone and 30 dB below over a $3'$ area of the target zone. The ripple amplitude of S2.2 is thus 0.27 dB over a $3'$ area of the target zone compared to 0.83 dB over a $2'$ area for S2.1. The peak-to-peak phase variation of S2.2 is 6° over the entire target zone compared to 14° for S2.1. At 10 GHz the performance improvement of S2.2 over S2.1 is even better. The diffracted fields of S2.2 are 26 dB below the GO field over the entire target zone, 40 dB below over a $4.5'$ area of the target zone, 50 dB below over a $3'$ area and 60 dB below over a $2'$ area. These levels correspond to ripple amplitudes of 0.45 dB, 0.09 dB, 0.03 dB and 0.01 dB respectively.

3.4.4 Design example (subreflector feed)

Consider now the case of a parabolic reflector with $f_c = 7.25'$ and a cosine squared blended edge with blending parameters $a_e = 3.4'$, $b_e = 0.75'$, $x_m = 6.8'$ and $\gamma_m = 120^o$. This surface is designated as S2.3, and is shown in Figure 47. Note that the surface has not been completely optimized, since the optimization algorithm was developed after pattern calculations corresponding to a three-dimensional version of S2.3 were done. Nevertheless, the example serves to illustrate the improvements that can be obtained with higher order blending functions. The surface characteristics are given in Table 9, and the radii of curvature at y_{top} and y_{bot} of a parabola with $f_c = 7.25'$ are given in Table 10. The quantities R'_c, R''_c, R'''_c and R^{iv}_c in Tables 9 and 10 denote differentiation with respect to y. Compar-
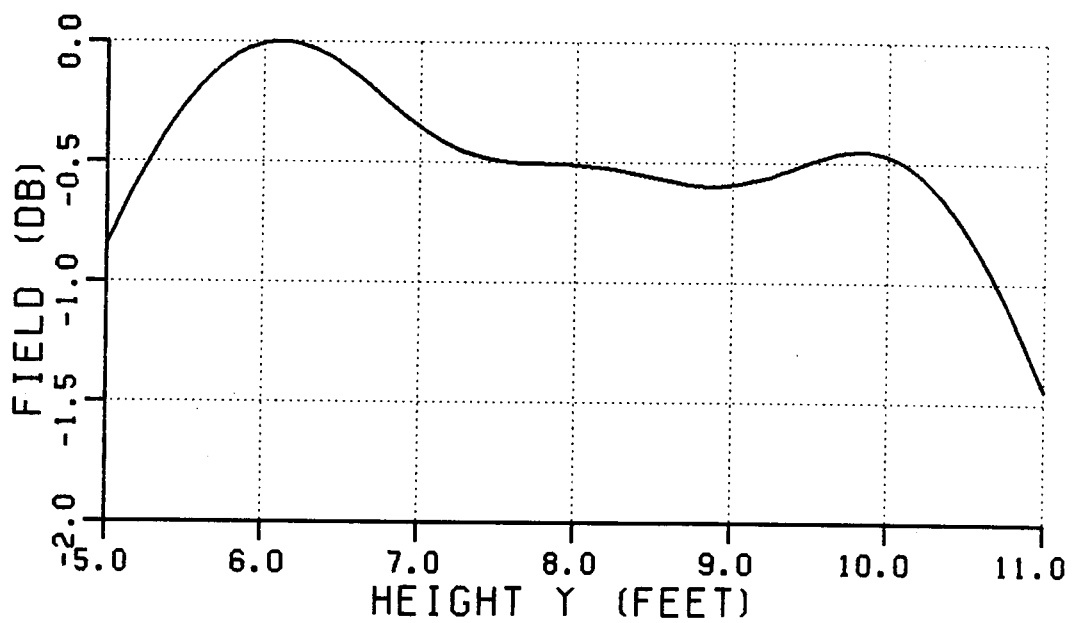
Figure 38: Normalized magnitude of the total field from S2.2 (3 GHz).
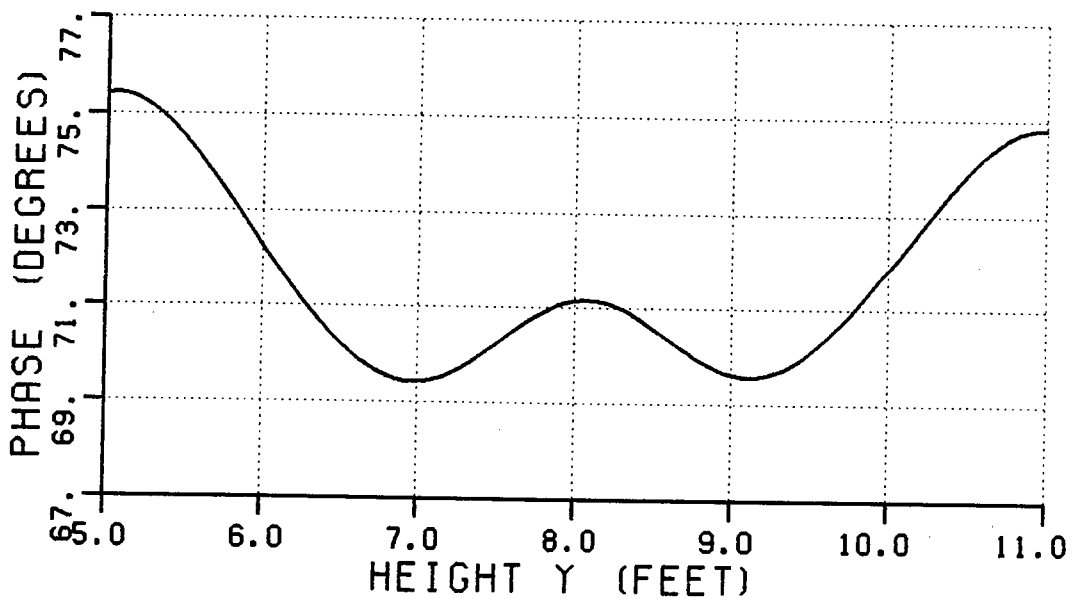
Figure 39: Phase of the total field from S2.2 (3 GHz).
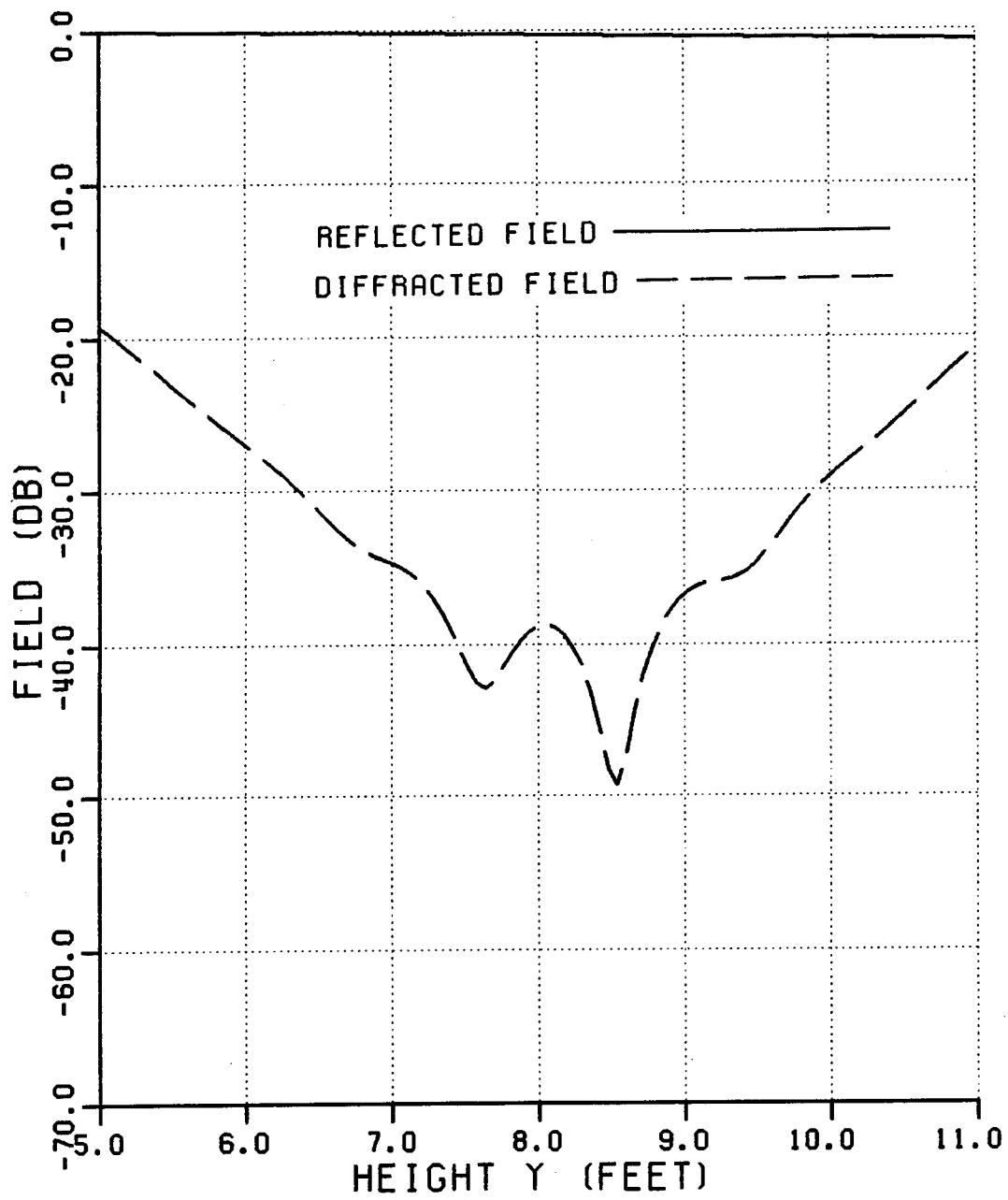
Figure 40: Normalized magnitude of the reflected and diffracted fields from S2.2 (3 GHz).
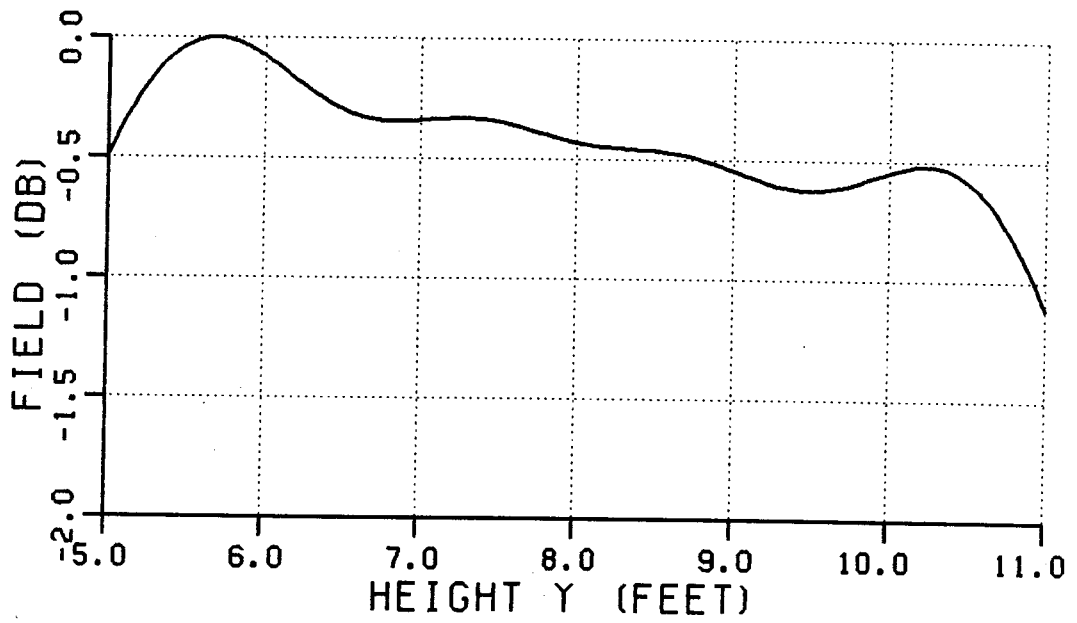
Figure 41: Normalized magnitude of the total field from S2.2 (6 GHz).
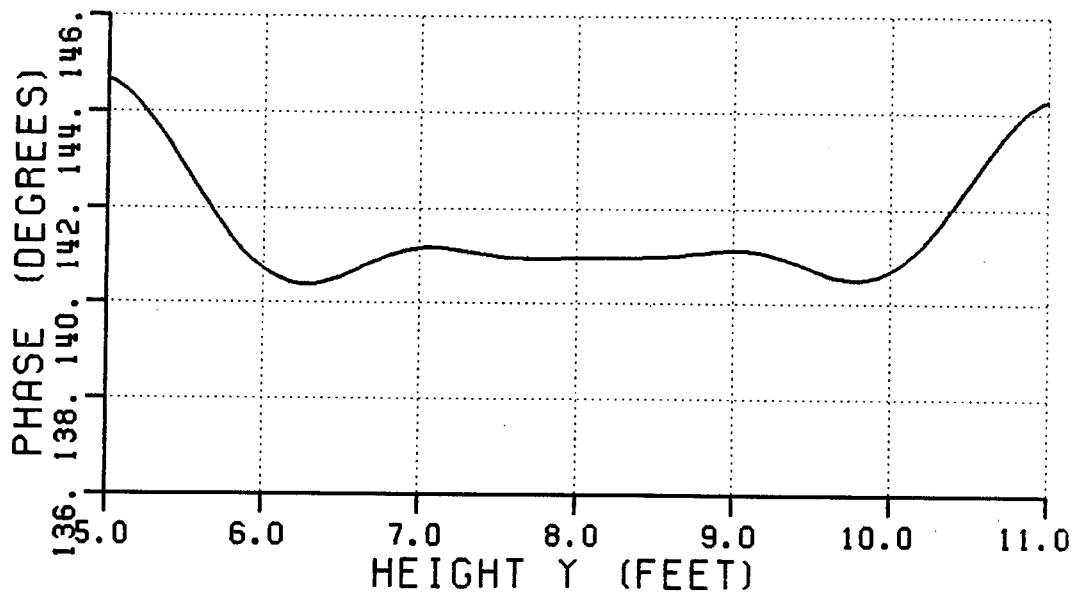
Figure 42: Phase of the total field from S2.2 (6 GHz).
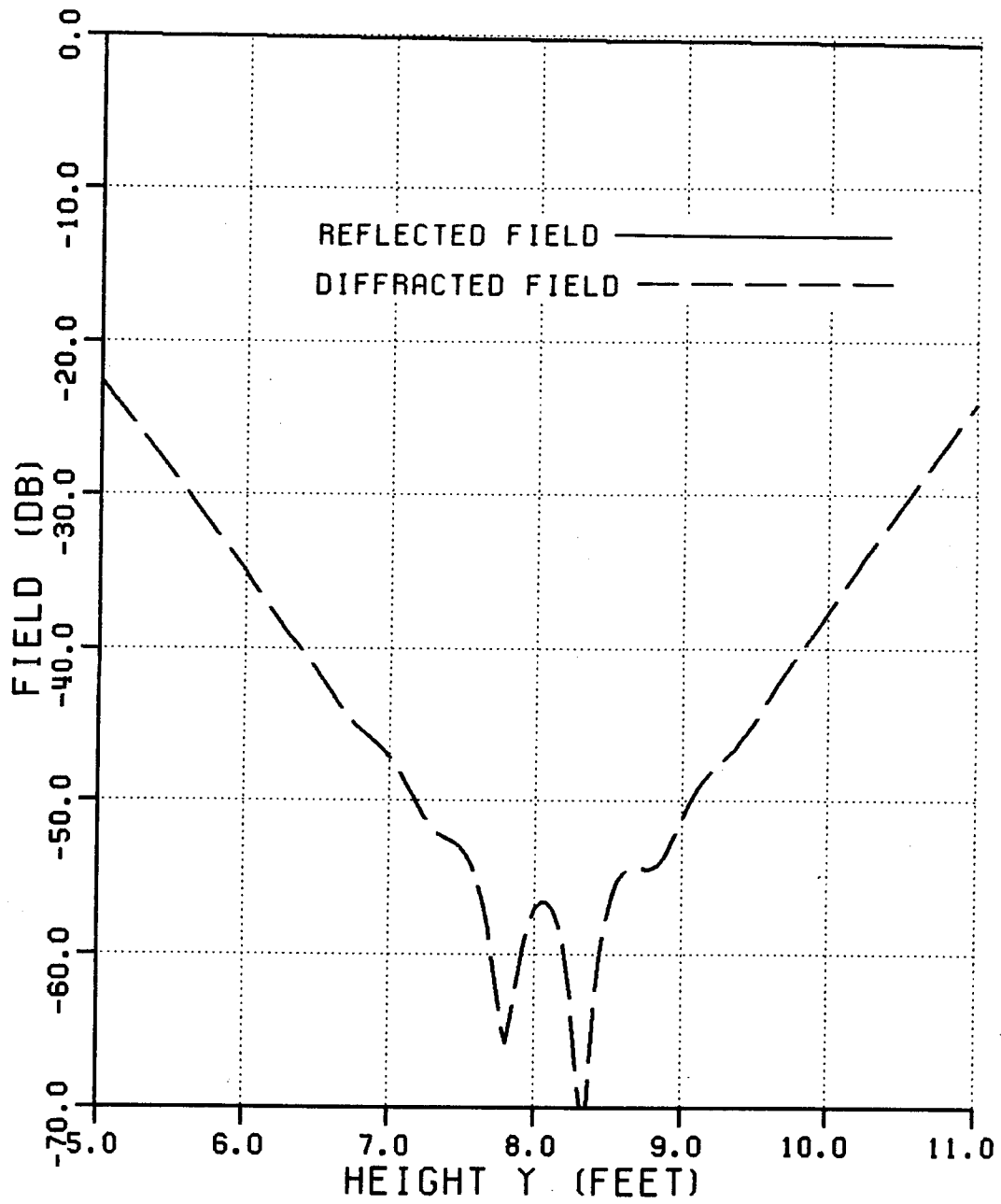
Figure 43: Normalized magnitude of the reflected and diffracted fields from S2.2 (6 GHz).
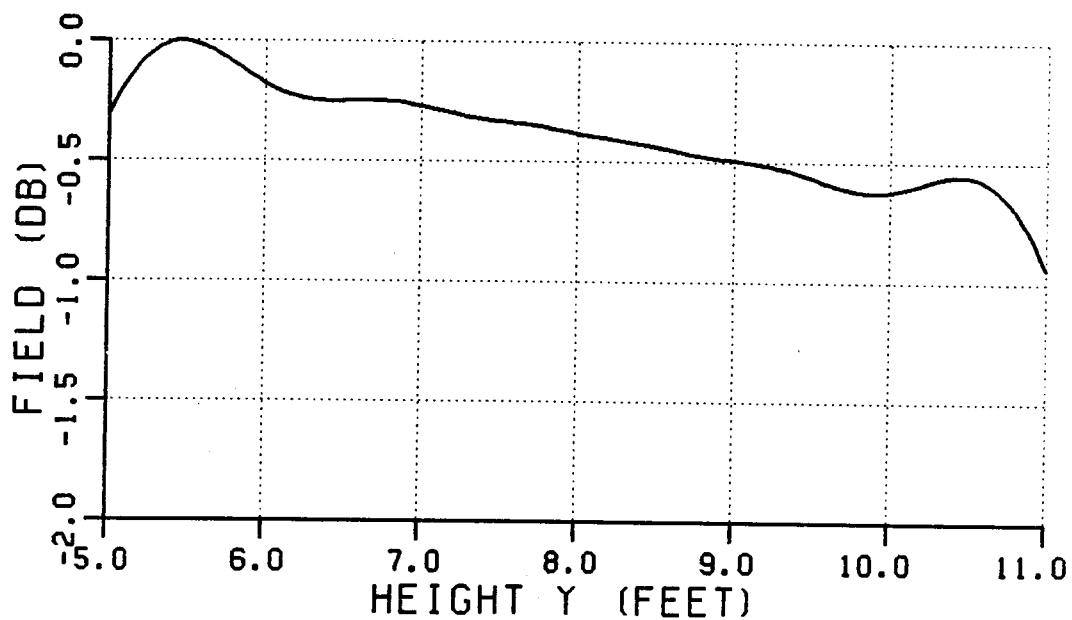
Figure 44: Normalized magnitude of the total field from S2.2 (10 GHz).
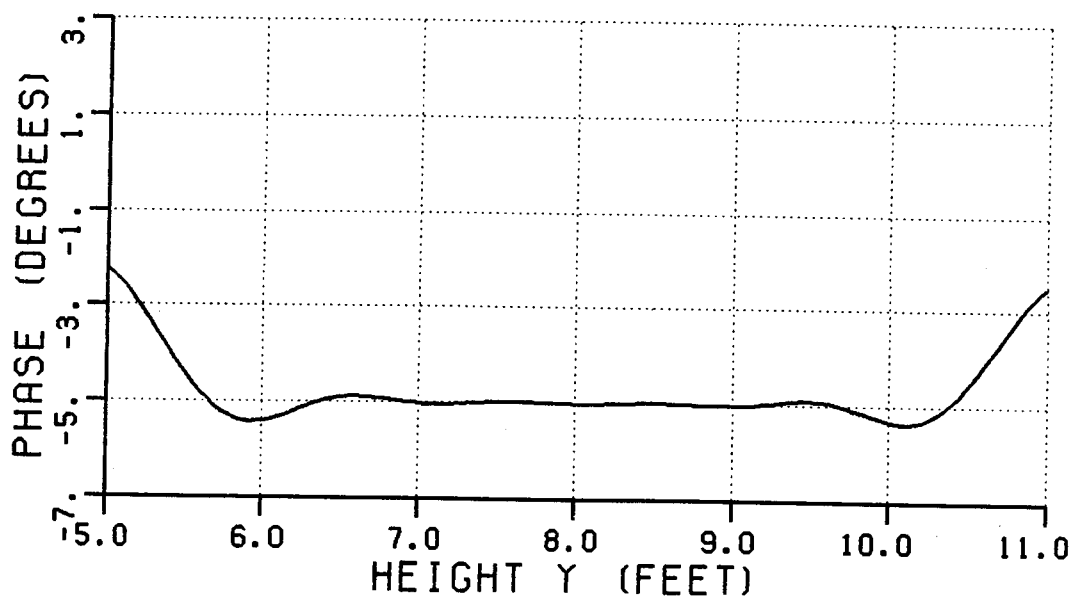
Figure 45: Phase of the total field from S2.2 (10 GHz).
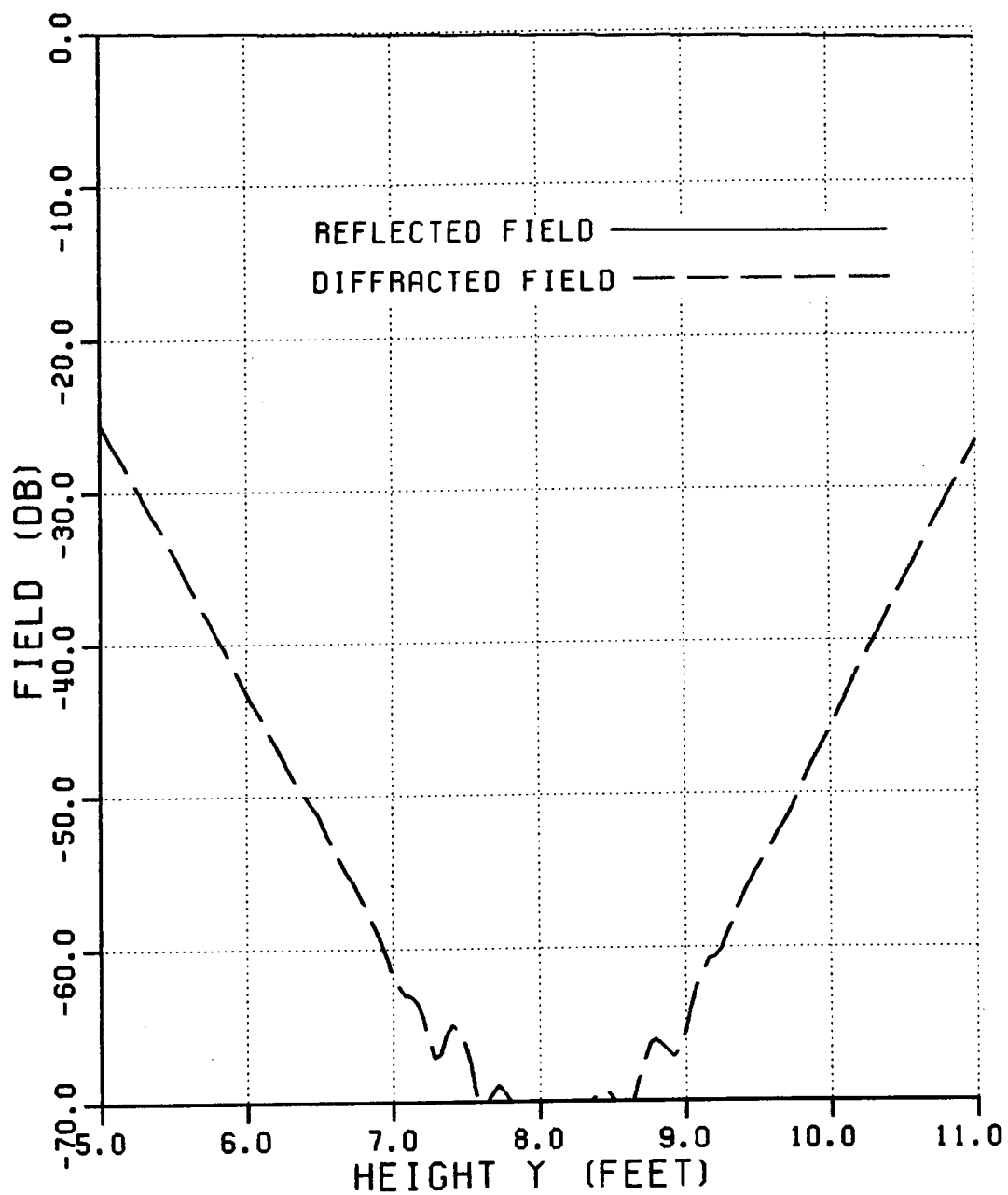
Figure 46: Normalized magnitude of the reflected and diffracted fields from S2.2 (10 GHz).

100
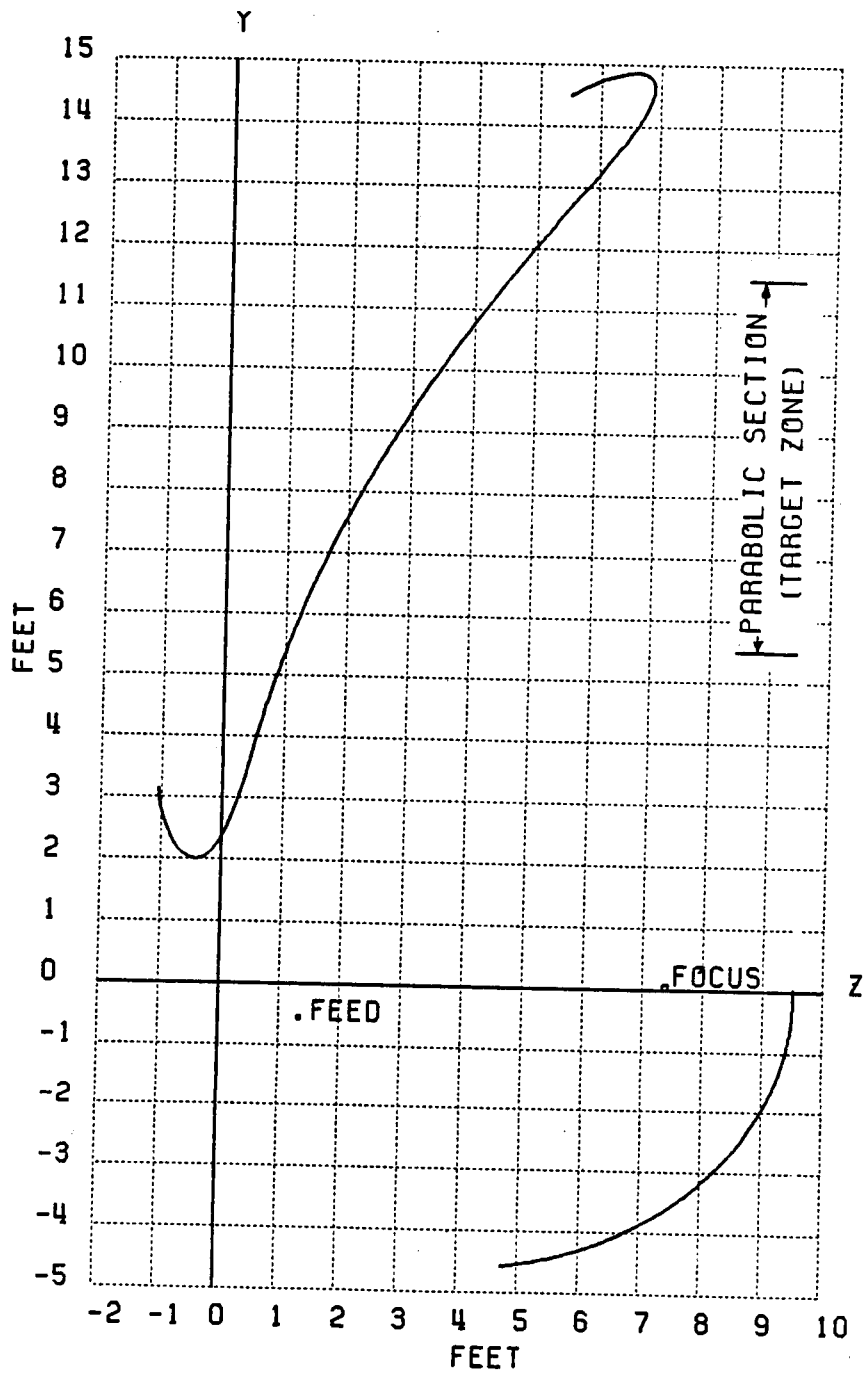
Figure 47: Two-dimensional parabolic reflector with cosine squared blended rolled edges (S2.3) and a Gregorian subreflector.

ison of Tables 9 and 10 shows that in the case of the cosine squared blended edge, R_c, R_c', R_c'' and R_c''' are all continuous across the junctions, but R_c^{iv} is not. Based on Equation (3.46), this result is to be expected, since cosine squared blending is a fourth order blending function.

In this case, the main reflector is illuminated by a Gregorian subreflector system, which in turn is illuminated by a magnetic line source with a uniform pattern. A discussion of the equations governing the illumination of the main reflector by the subreflector is given in Section 4.5 for the three-dimensional case. The two-dimensional case discussed here is analogous to the yz-plane of the three-dimensional case, with the provision that the fields in the two-dimensional case have a $1/\sqrt{R}$ amplitude dependence.

The target zone is considered to be located at a distance (z_{pat}) of 20' away from the main origin along the z-axis. In calculating the scattered field in the target zone it is assumed that there is no direct illumination from the feed or diffraction from the subreflector into the target zone and that the reflector is illuminated only by the GO field reflected from the subreflector. Fields diffracted from the edges of the subreflector are deliberately ignored in order to establish the performance of the main reflector when illuminated by an ideal subreflector system. The motivation for this assumption will be given in Chapter V.

The total field in the target zone can be calculated using the corrected PO method, with the end point contributions at the shadow boundaries of the rolled surfaces subtracted to give the "true" total field. Subtraction of the GO reflected field from the total field will give the fields diffracted from the junctions. The normalized magnitude and phase of the total field in the target zone together with plots comparing the reflected fields with the fields diffracted from the junctions, calculated at 3 GHz, are shown in Figures 48–56 for the cases where no

102

Table 9: Surface characteristics for S2.3.

Cosine Squared Blending	
f_c	7.25'
a_e	3.4'
b_e	0.75'
x_m	6.8'
γ_m	120°
y_{bot}	5.5'
y_{top}	11.5'
a_{sr}	5.25'
b_{sr}	4.308'
f_{sr}	3'
β	5.5°
α	20°
z_{pat}	20'

	RADIUS OF CURVATURE (ROLLED EDGE)					
	Junction		Minimum		Shadow Boundary	
	bottom	top	bottom	top	bottom	top
γ	0°	0°	81°	81°	84°	75°
R_c	17.739'	30.148'	0.267'	0.188'	0.293'	0.332'
R_c'	1.217	3.037				
R_c''	0.249	0.356				
R_c'''	0.0145	0.0232				
R_c^{iv}	56.069	265.649				

103

Table 10: Radii of curvature at the junctions of a parabola with $f_c = 7.25'$.

RADIUS OF CURVATURE (PARABOLA)		
	bottom($y_{bot} = 5.5'$)	top($y_{top} = 11.5'$)
R_c	17.739'	30.148'
R_c'	1.217	3.037
R_c''	0.249	0.366
R_c'''	0.0145	0.0232
R_c^{iv}	0.00211	0.00087

end point contributions are subtracted, only first order end point contributions are subtracted, and finally, first and second order end point contributions are subtracted. The effect of the erroneous scattering terms that are imbedded in the results obtained from the numerical PO integration are clearly visible when the magnitude and phase of the total field *without* the subtraction of the end point contributions (see Figures 48 and 49) are compared to the magnitude and phase of the total field *with* the end point contributions subtracted (see Figures 54 and 55). The high frequency ripples in Figures 48 and 49 are created by the false scattering centers at the incident shadow boundaries on the blended rolled edges. Note that the frequency of the ripple is much lower when these terms are subtracted (see Figures 54 and 55). This indicates that the resulting diffractions are originating at the junctions between the parabola and the blended edges. Since these junctions have a smaller spatial separation than the false scattering centers at the incident shadow boundaries on the blended edges, the frequency of the ripple is lower. The plot of diffracted fields with the end point contributions subtracted in Figure 56 clearly shows that the diffracted fields from the parabola/rolled edge junctions

have maxima on the reflection shadow boundaries. The normalized magnitude and phase of the total field in the target zone together with plots comparing the reflected fields with the fields diffracted from the junctions, calculated at 1 GHz and 10 GHz, are shown in Figures 57–62. Comparison of Figures 54–56 and 60–62 corresponding to S2.3 with Figures 23–25 and 29–31 corresponding to S2.1, and Figures 38–40 and 44–46 corresponding to S2.2 show the improved performance achieved by the reflector with a cosine squared blended edge and subreflector feed over the other designs. The subreflector feed of S2.3 resulted in a dramatic decrease in the taper of the reflected field. This concept will be explored further in Chapter V. Even though the focal lengths of S2.1 and S2.2 are longer than that of S2.3, it is clear that the performance of S2.3 is significantly better than that of the other two. This is mainly the result of the higher order blending function that has been employed in the rolled edges of S2.3. At 3 GHz the diffracted fields from S2.3 are 30 dB below the level of the GO reflected field over almost the entire target zone and 40 dB below over a 3.5' area of the target zone. These levels correspond to ripple amplitudes of 0.27 dB and 0.09 dB, respectively. The peak-to-peak phase variation is less than 4° over the entire target zone compared to 6° for S2.2 and 14° for S2.1. At 10 GHz the diffracted fields of S2.3 are 42 dB below the GO level over the entire target zone and 60 dB below over a 4.5' area. These levels correspond to ripple amplitudes of 0.09 dB and 0.01 dB.

From Table 9 it is seen that the minimum radius of curvature of the rolled edge in the lit region is 0.188'. Using the $\lambda_{max}/4$ rule-of-thumb, this corresponds to a minimum operating frequency of about 1 GHz. Figures 57–59 indicate that at 1 GHz the diffracted fields are 20 dB below the GO level over the entire target area and 28 dB below over a 2' area. These levels correspond to ripple amplitudes of 0.83 dB and 0.35 dB respectively. The peak-to-peak phase variation is 9° over the

105

entire target zone. Even though this reflector thus does not satify the 0.1 dB ripple amplitude requirement at 1 GHz, it will be shown in Section 4.6 that optimizing the design of the blended rolled edges allows one to achieve the desired performance.

Based on the numerical results and the experience gained while calculating them, one is justified in saying that the use of blended rolled edges enables one to design a reflector which meets the ripple amplitude requirement at higher frequencies without too much difficulty, as shown in Figure 62. It is, however, much more difficult to obtain an acceptable performance over a useful area of the target zone at lower frequencies. This is due in part to the fact that the transition region around the reflection shadow boundary spreads out as the frequency decreases, so that a larger part of the target zone will be intercepted by the transition region as shown in Figure 63. Since the diffracted fields are strongest in the transition region, this creates a larger ripple in the plane wave. It is for this same reason that it is advantageous to have the target zone as close as possible to the main reflector.
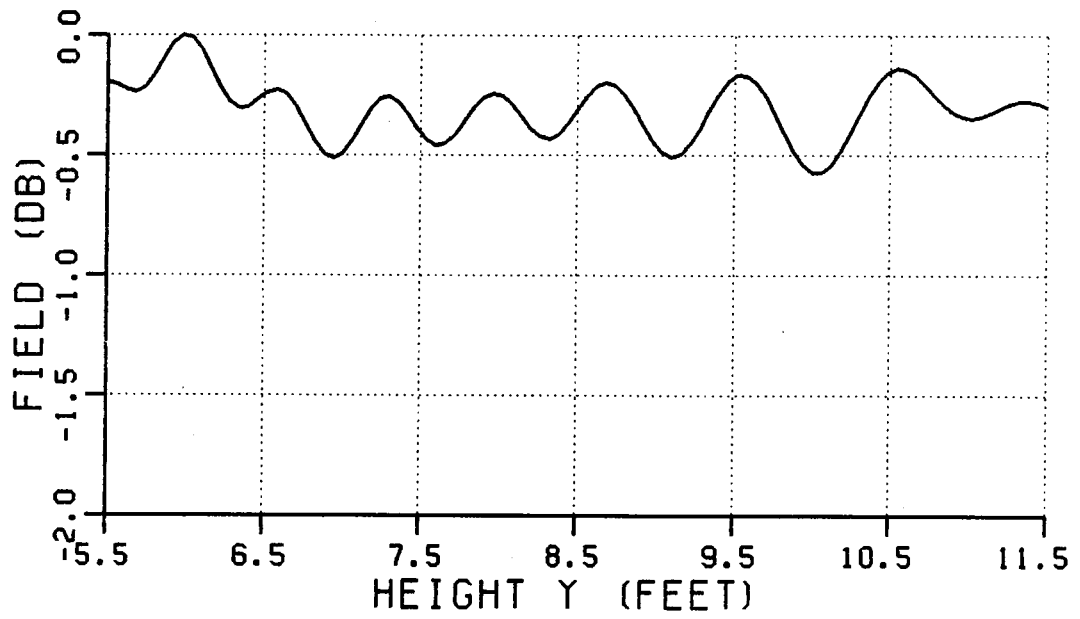
Figure 48: Normalized magnitude of the total field from S2.3 (3 GHz). No end point contributions subtracted.
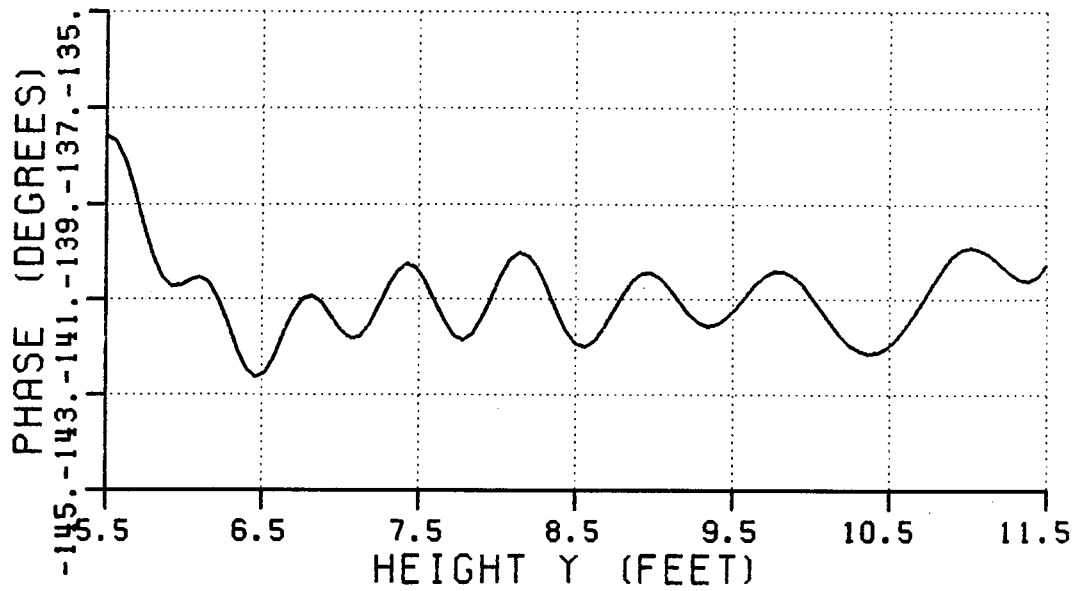
Figure 49: Phase of the total field from S2.3 (3 GHz). No end point contributions subtracted.

107
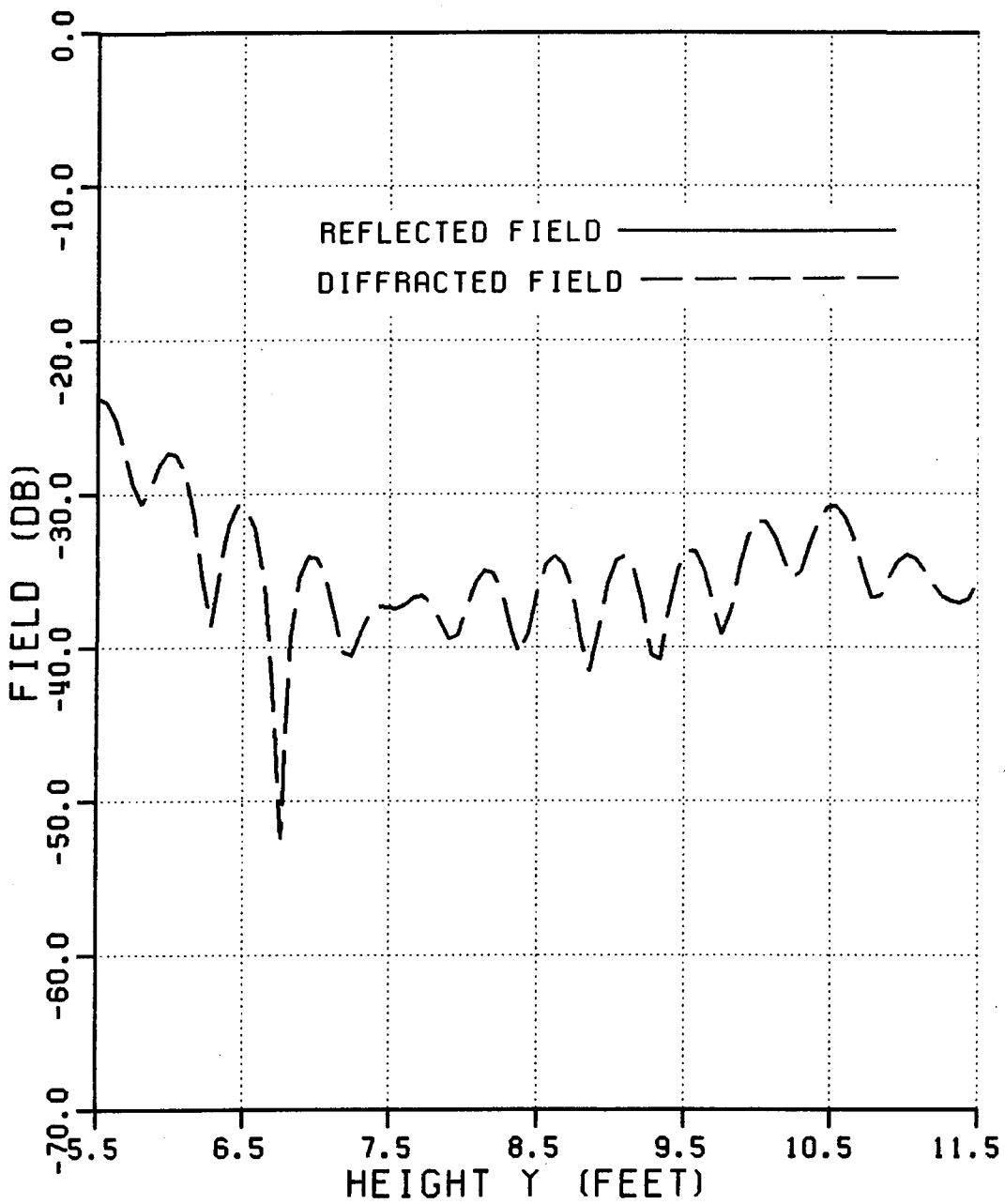
Figure 50: Normalized magnitude of the reflected and diffracted fields from S2.3 (3 GHz). No end point contributions subtracted.
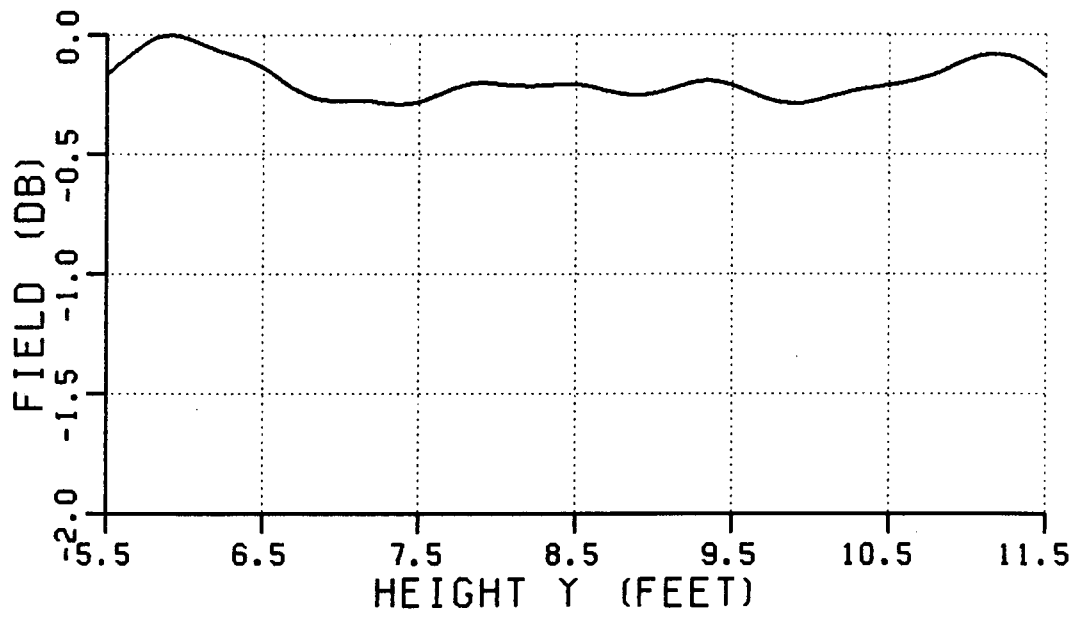
Figure 51: Normalized magnitude of the total field from S2.3 (3 GHz). First order end point contributions subtracted.
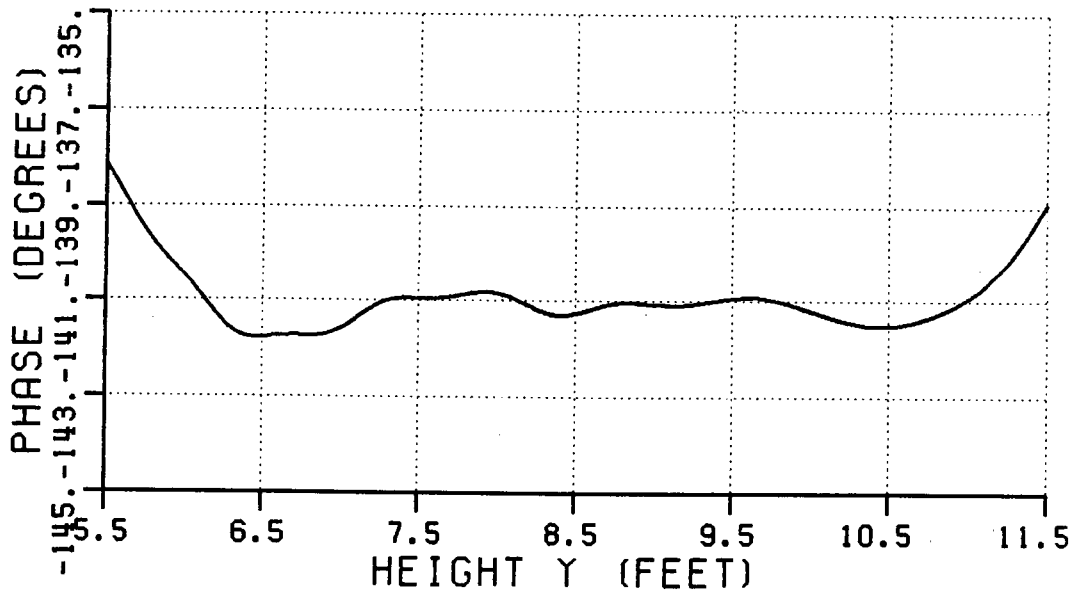
Figure 52: Phase of the total field from S2.3 (3 GHz). First order end point contributions subtracted.

109
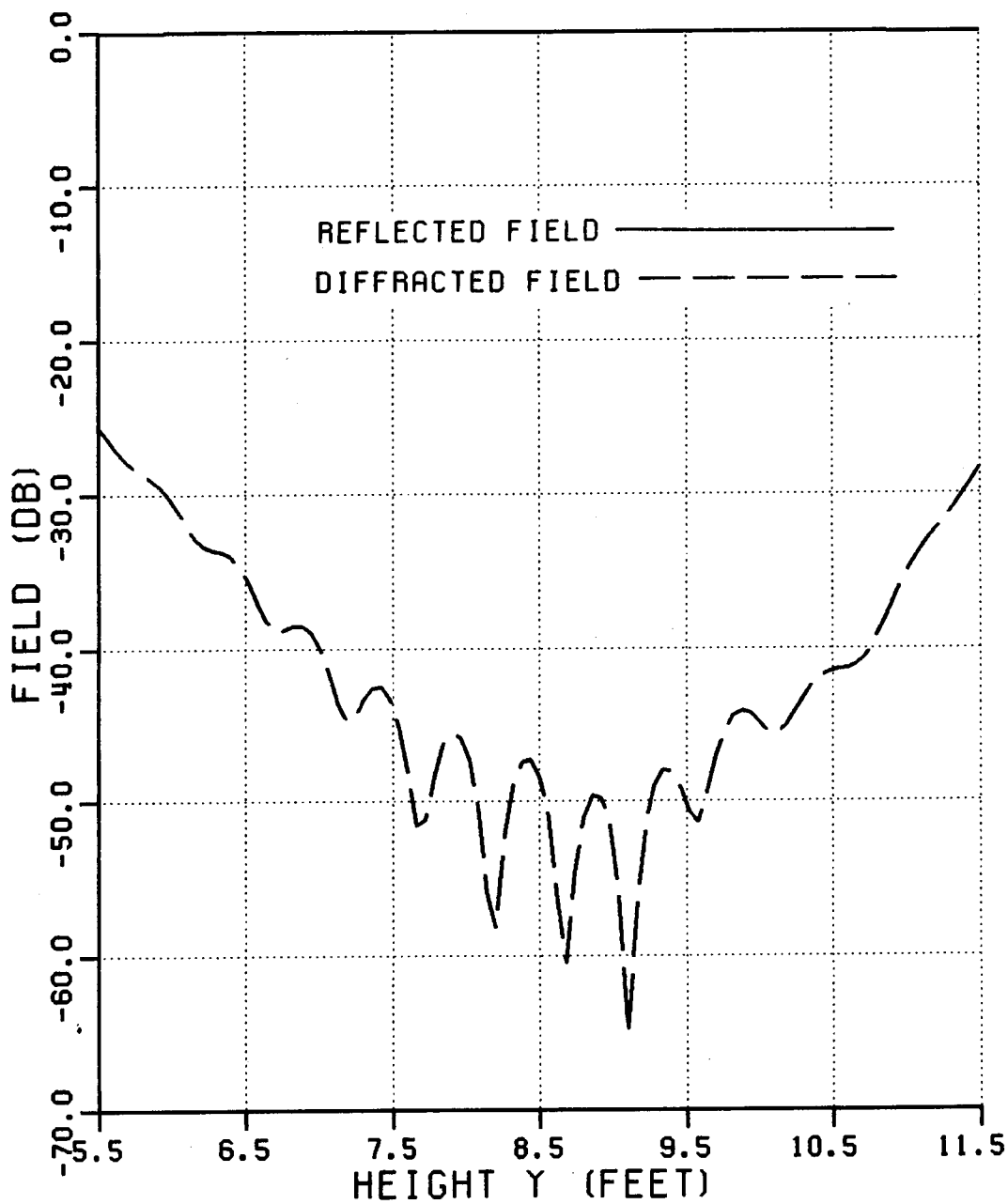
Figure 53: Normalized magnitude of the reflected and diffracted fields from S2.3 (3 GHz). First order end point contributions subtracted.
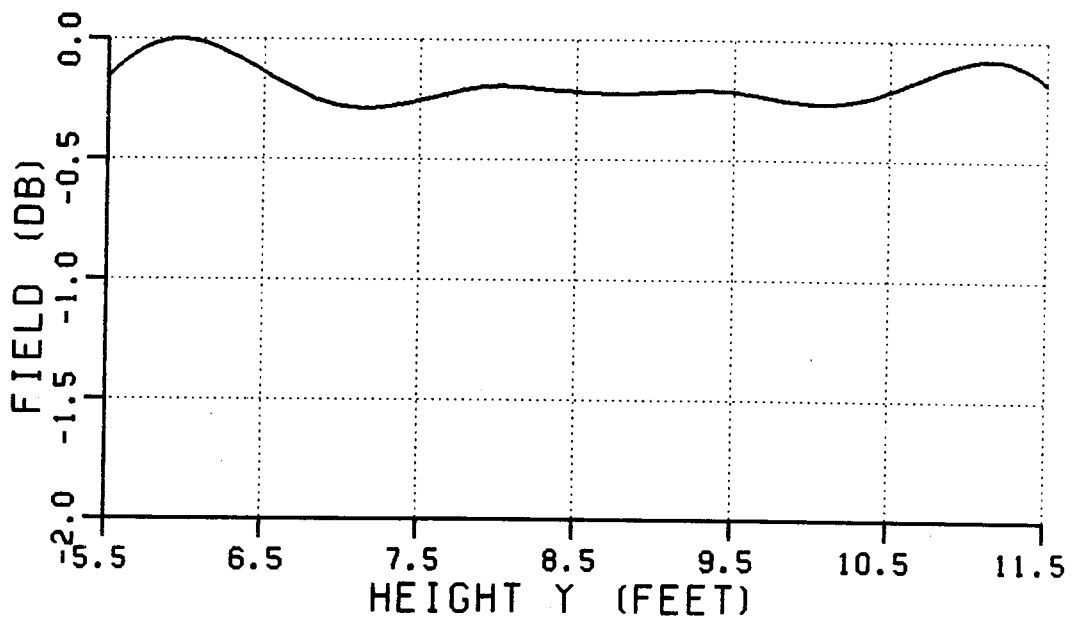
Figure 54: Normalized magnitude of the total field from S2.3 (3 GHz). First and second order end point contributions subtracted.
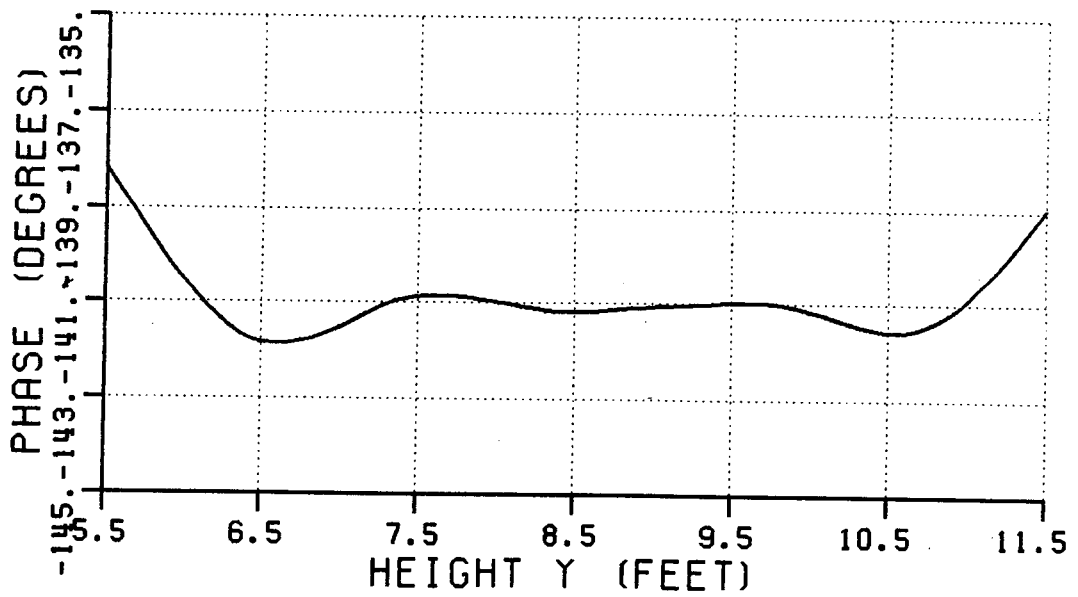
Figure 55: Phase of the total field from S2.3 (3 GHz). First and second order end point contributions subtracted.

111
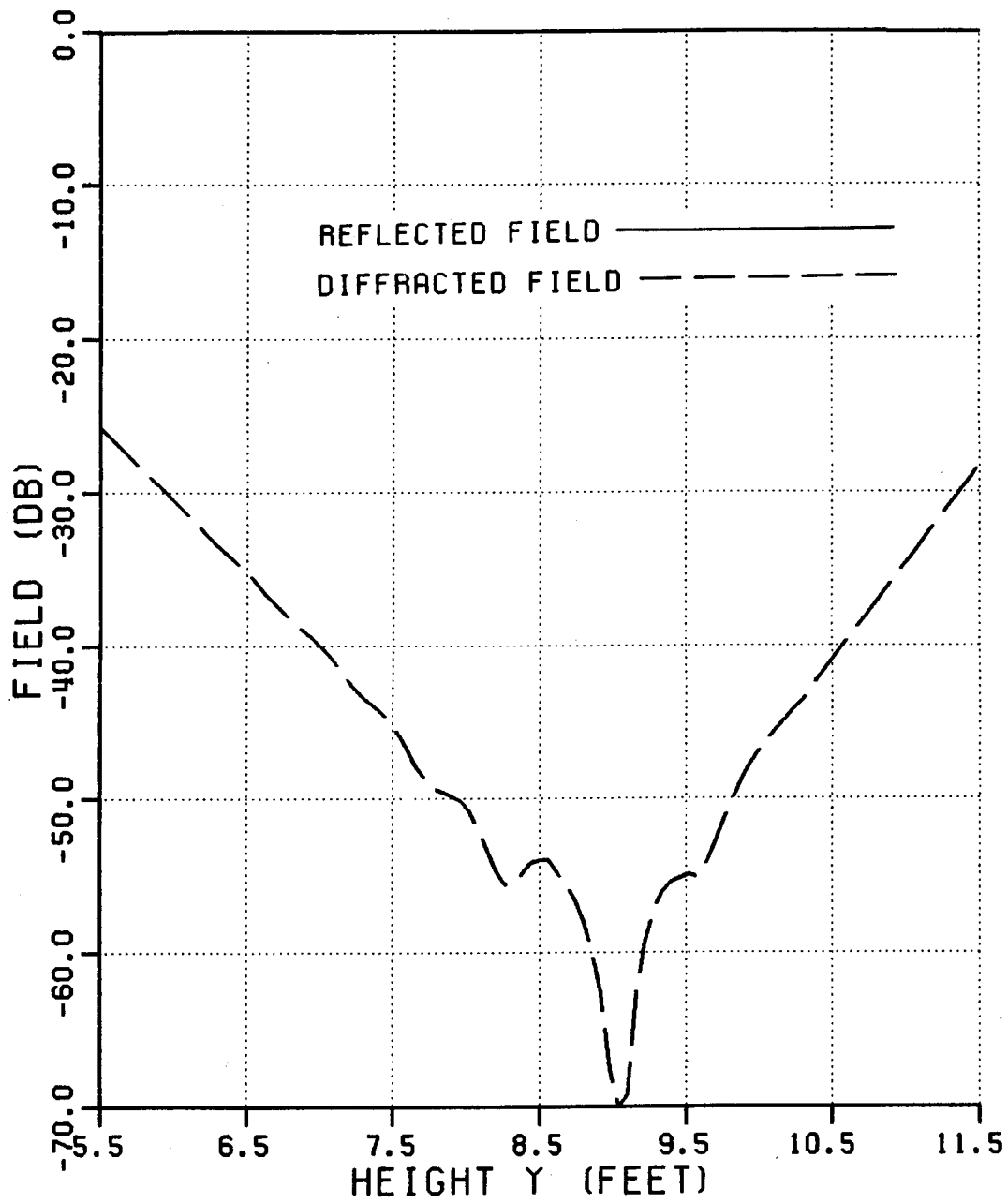
Figure 56: Normalized magnitude of the reflected and diffracted fields from S2.3 (3 GHz). First and second order end point contributions subtracted.

112
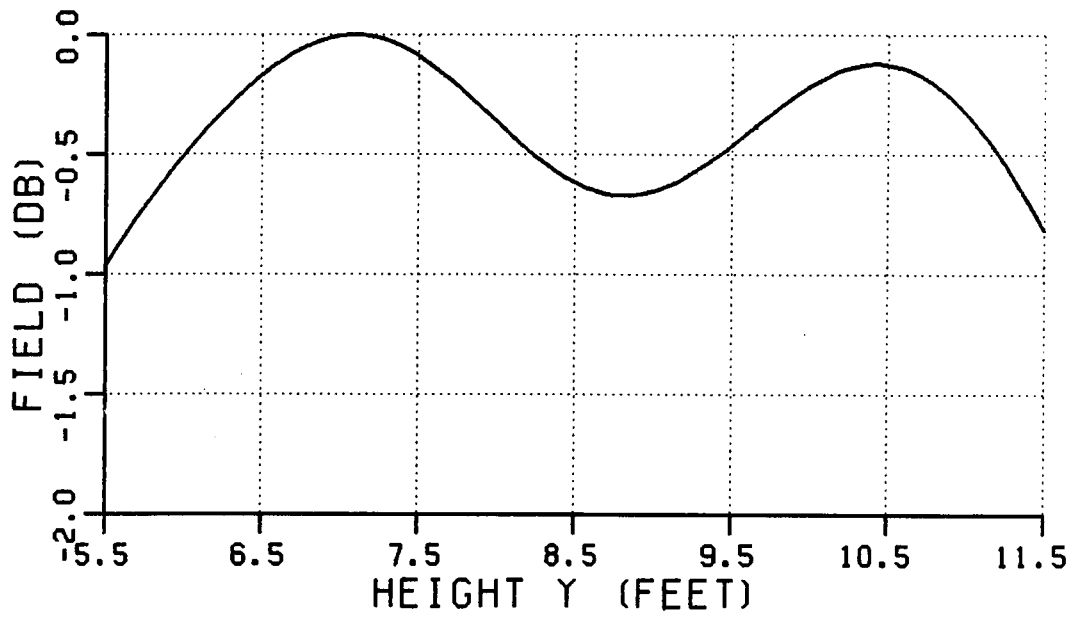
Figure 57: Normalized magnitude of the total field from S2.3 (1 GHz).
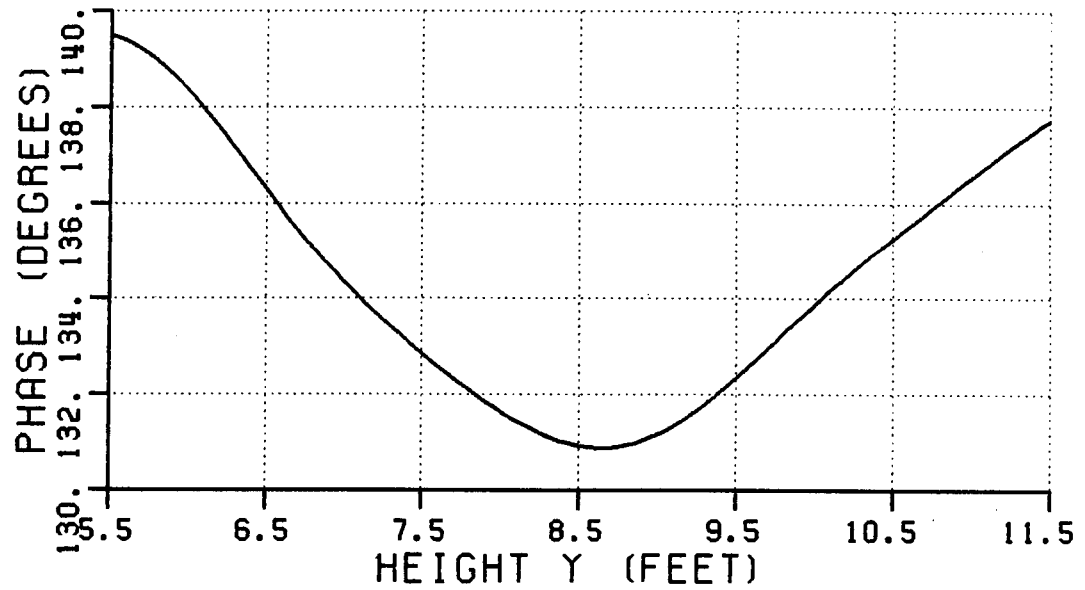
Figure 58: Phase of the total field from S2.3 (1 GHz).

113
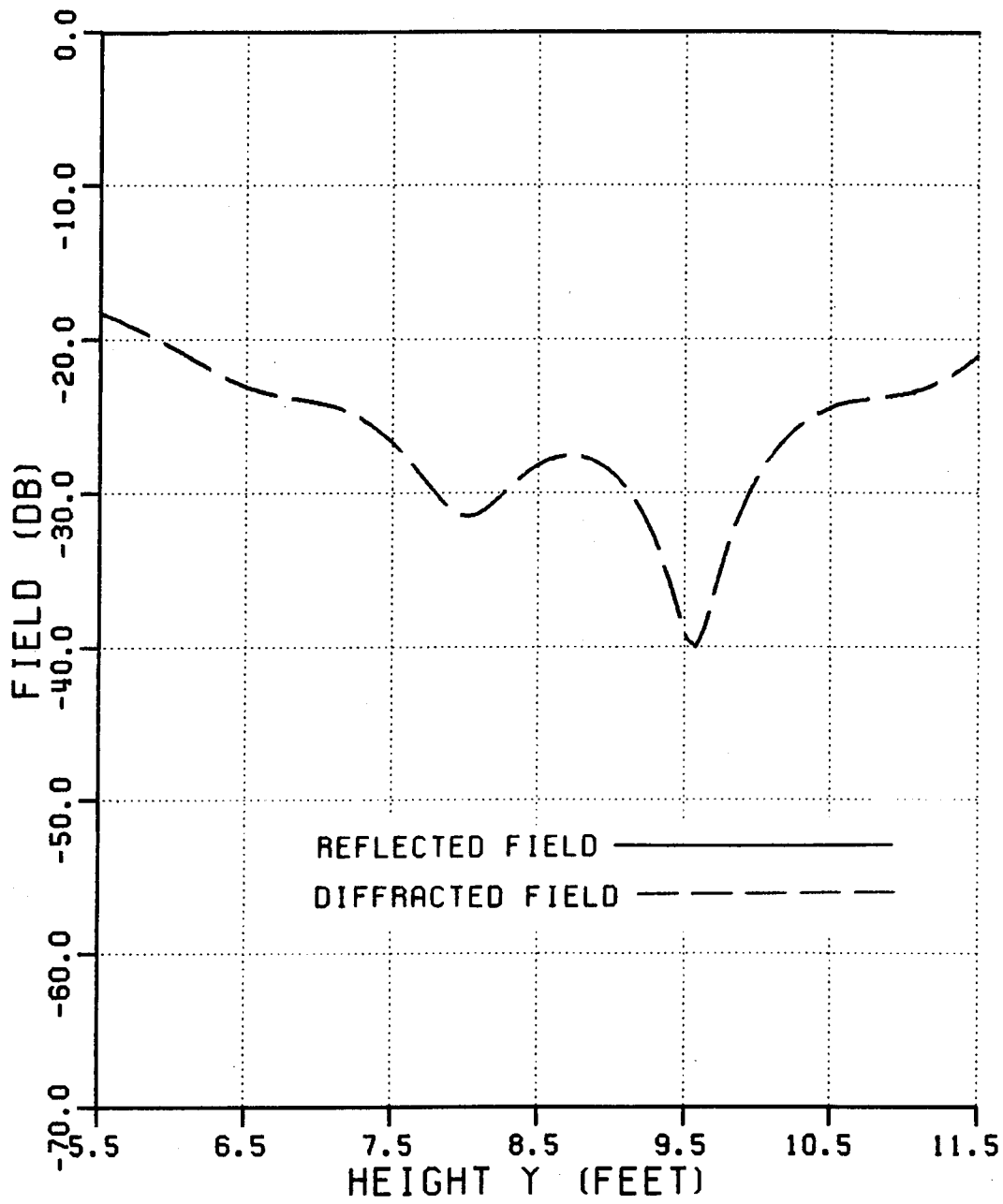
Figure 59: Normalized magnitude of the reflected and diffracted fields from S2.3 (1 GHz).

114
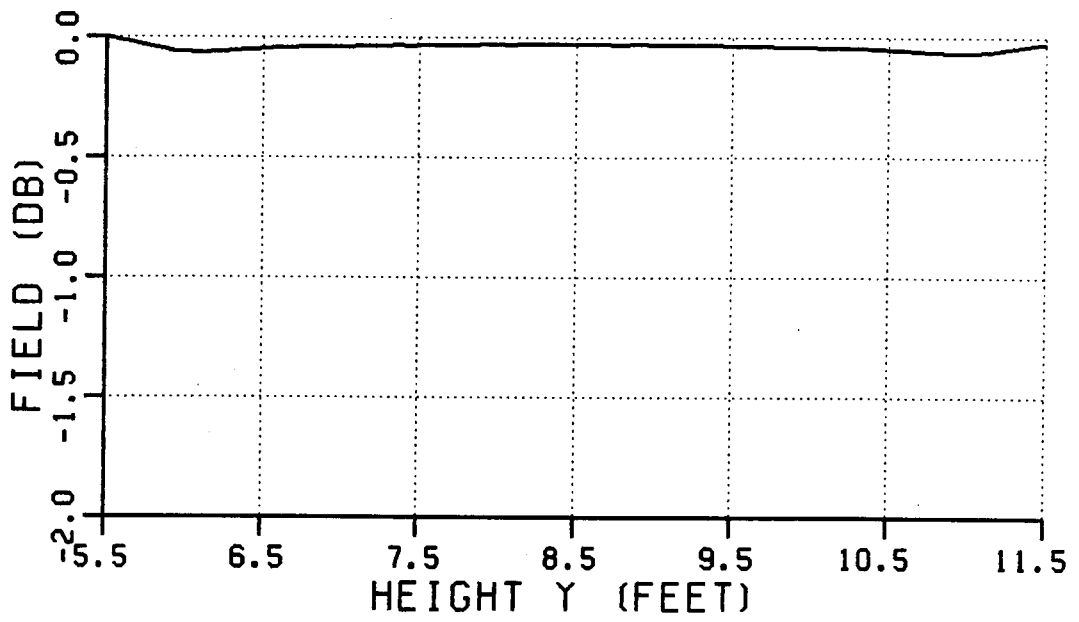
Figure 60: Normalized magnitude of the total field from S2.3 (10 GHz).
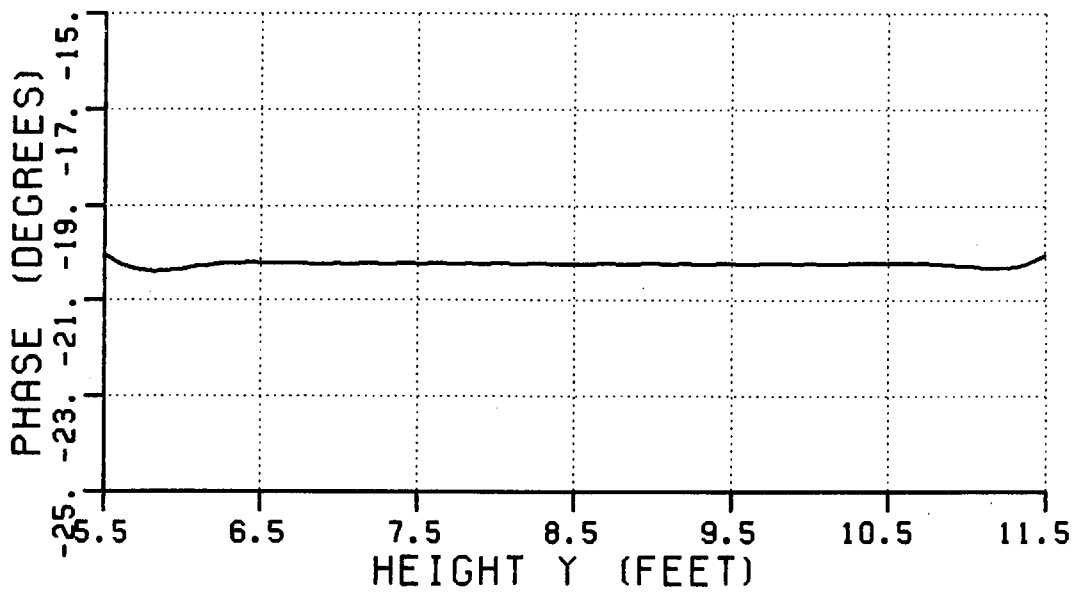
Figure 61: Phase of the total field from S2.3 (10 GHz).

115
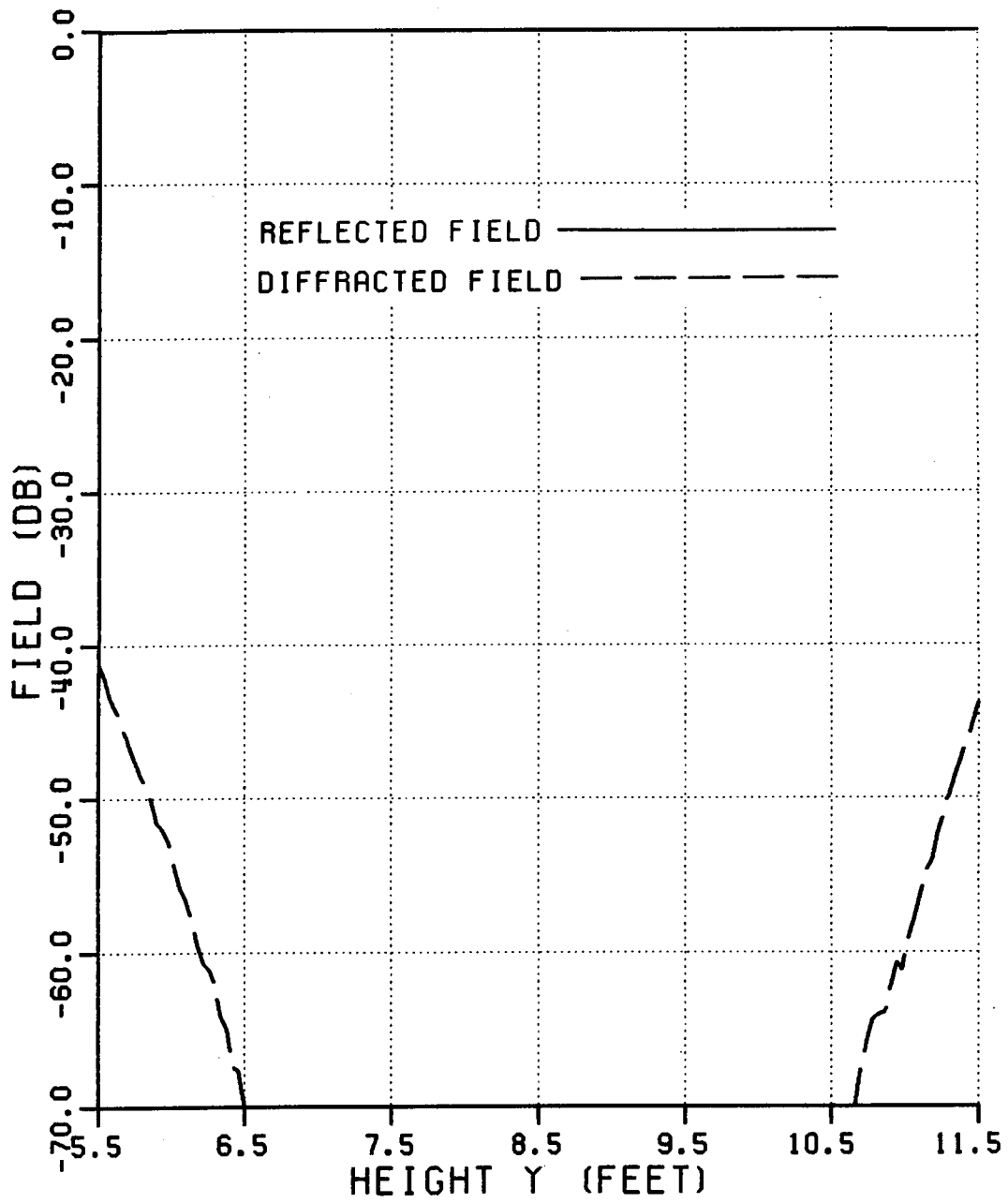
Figure 62: Normalized magnitude of the reflected and diffracted fields from S2.3 (10 GHz).
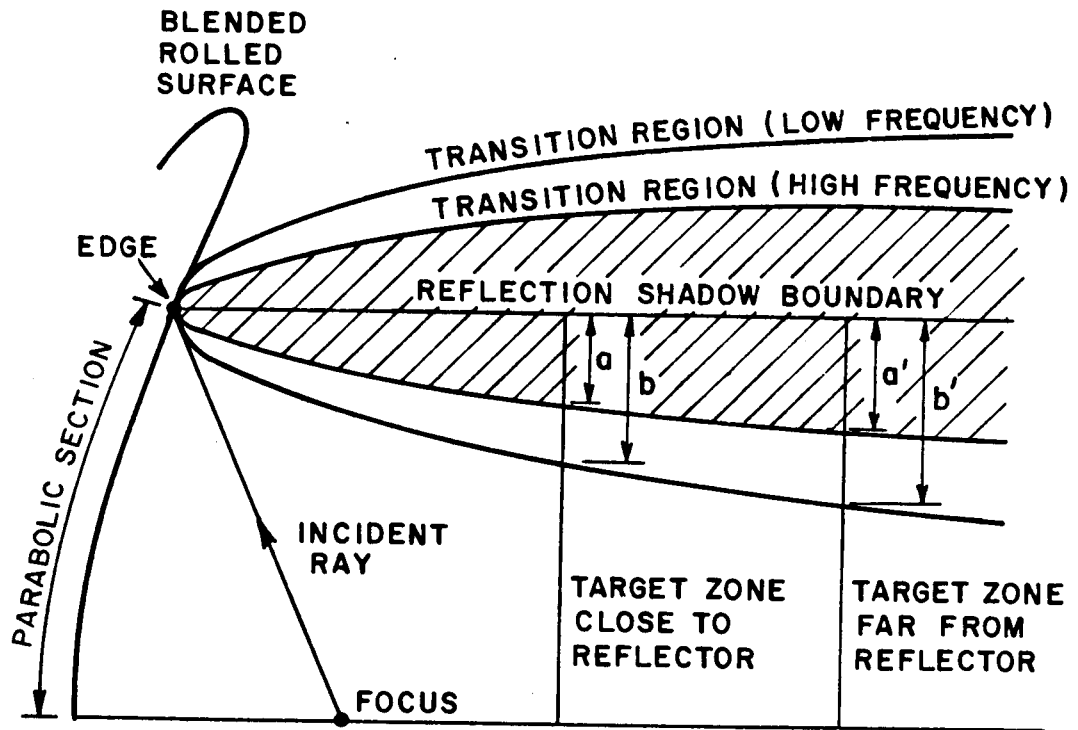
a, a': Section of the target zone intercepted by the transition
region when the target zone is near/far from the reflector
at high frequencies ($a' > a$).

b, b': Section of the target zone intercepted by the transition
region when the target zone is near/far from the reflector
at low frequencies ($b' > b$).

Figure 63: The frequency dependence of the transition region around the
reflection shadow boundary.

CHAPTER IV

A CONCAVE EDGED REFLECTOR WITH BLENDED ROLLED SURFACE TERMINATIONS

4.1 Introduction

The blended rolled surface terminations can now be applied towards the design of a three-dimensional main reflector. The main reflector surface is a paraboloid with focal length (f_c), and it can be described by

$$z = \frac{x^2 + y^2}{4f_c} \tag{4.1}$$

where the z-axis is considered to be the axis of symmetry. The reflector is assumed to be symmetric around the yz-plane, and offset in the positive y-direction. The blended rolled surface terminations are based on a blend between the paraboloid and ellipses with semi-major and semi-minor axes of lengths of a_e and b_e, respectively. In the three-dimensional case, one finds that additional performance enhancement can be obtained by shaping the the edge contour separating the paraboloid and blended rolled surface terminations.

4.2 Shaping the edge contour

The creation of the edge contour at the termination of the parabolic section can be visualized by considering the edge contour to be the intersection of a paraboloid by a flat plane as shown in Figure 64(a). It is found that the orientation

118

of this plane has a great influence on the shape of the edge contour and the resulting edge diffracted fields. A plane parallel to the xy-plane will create a convex edge contour as shown in Figure 64(a), with the corresponding xy-projection of the reflector shape shown in Figure 64(b). The case of an intersecting plane parallel to the xz-plane is illustrated in Figure 65(a). Planes parallel to the xz-plane and the yz-plane create "straight" edges; ie., the edges are perceived to be straight when projected onto the xy-plane, as shown in Figure 65(b). The edge contours are actually curved (see Figure 65(a)), but for focal lengths and reflector sizes typically associated with compact range main reflectors, the curvature will be slight. This edge contour will forthwith be referred to as "rectangular". Concave edge contours are created when the planes parallel to the xz-plane and the yz-plane are tilted as shown in Figure 66(a). The concave edge contours of this reflector shape are clearly visible in the xy-projection of the edge contour as shown in Figure 66(b). The unit vector normal to the edge contour ($\hat{n}_e$) at a point Q_E (in the yz-plane) directed away from the center of curvature but in the plane of the curvature is also shown in Figures 64(a), 65(a) and 66(a). It will be shown that the direction of $\hat{n}_e$ and the radius of curvature of the edge contour at Q_E have a profound effect on the magnitude of the edge diffracted fields.

The xy-projection of the edge contours of conventional compact range reflectors have been circular (convex) or rectangular in shape. Edge diffraction analysis indicates, however, that convex or rectangular edge contours may not be the best choice. A concave contour in fact, results in smaller edge diffracted fields in the target zone.

To substantiate the above claim, consider the UTD expression for the electric

119
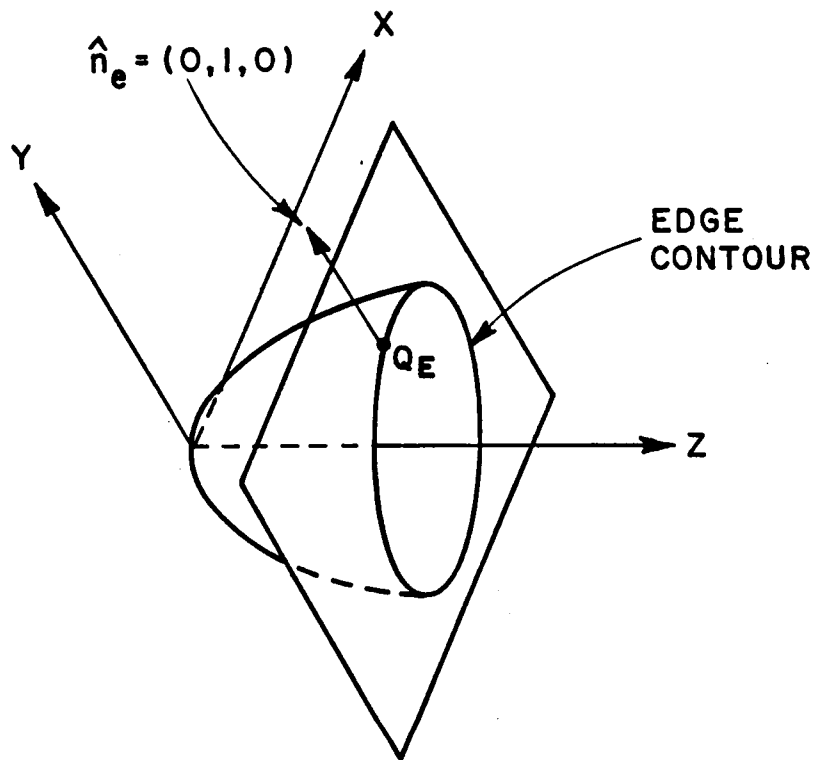
(a) Creation of a convex edge contour.
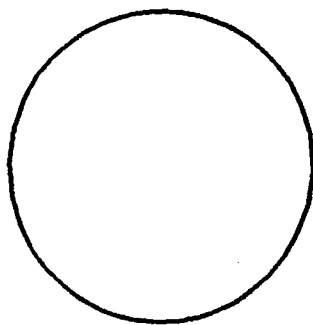
(b) XY-projection of a convex edge contour.

Figure 64: Convex edge contour.
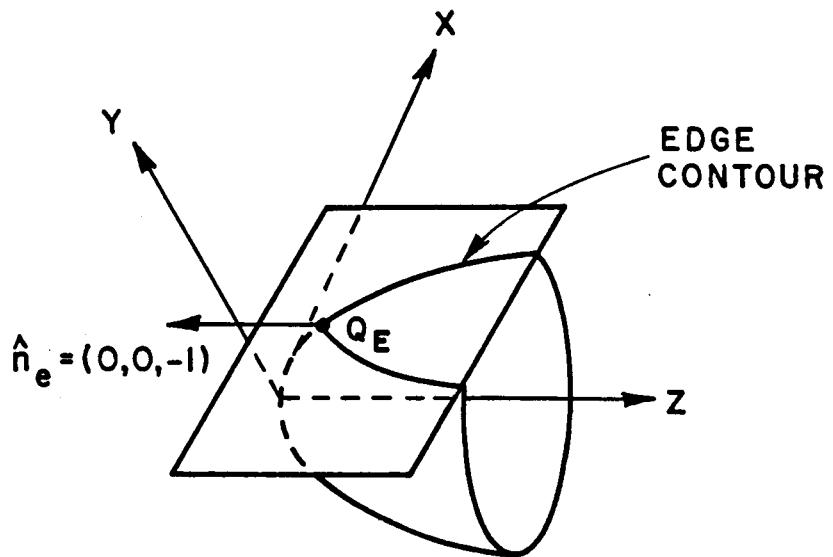
(a) Creation of a rectangular edge contour.
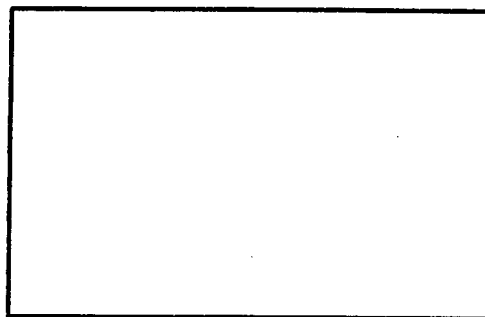
(b) XY-projection of a rectangular edge contour.

Figure 65: Rectangular edge contour.
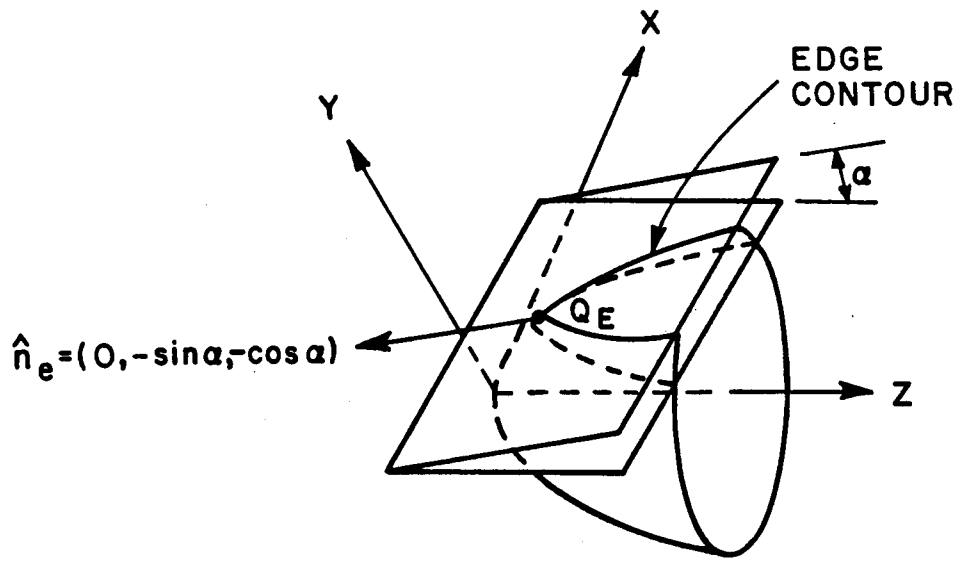
(a) Creation of a concave edge contour.
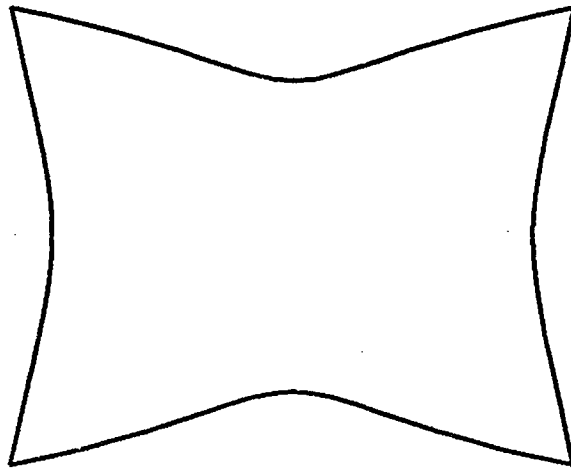
(b) XY-projection of a concave edge contour.

Figure 66: Concave edge contour.

fields diffracted from a point (Q_E) along an edge[17]; ie.,

$$\mathbf{E}^d(s) = \mathbf{E}^i(Q_E) \cdot \vec{\mathbf{D}} \; A \; e^{-jks} \tag{4.2}$$

where the spread factor (A) is given by

$$A = \sqrt{\frac{\rho_c}{s(\rho_c + s)}} \; . \tag{4.3}$$

Note that the edge caustic distance (ρ_c) is given by

$$\frac{1}{\rho_c} = \frac{1}{\rho_e} - \frac{\hat{n}_e \cdot (\hat{s}' - \hat{s})}{\rho_g \sin^2 \beta_0'} \tag{4.4}$$

where

$\hat{n}_e$ = unit vector normal to the edge contour

at Q_E directed away from the center of

curvature, but in the plane of the curvature

s = distance from Q_E to the field point

$\mathbf{E}^d(s)$ = diffracted electric field at the field point

$\mathbf{E}^i(Q_E)$ = incident electric field at Q_E

$\vec{\mathbf{D}}$ = dyadic diffraction coefficient

ρ_e = radius of curvature of the incident wavefront in the edge-fixed

plane of incidence

ρ_g = radius of curvature of the edge at Q_E

$\hat{s}'$ = unit vector in the direction of the incident propagation

$\hat{s}$ = unit vector in the direction of the diffracted propagation , and

β_0' = angle between $\hat{s}'$ and the tangent to the edge at Q_E .

The parameters in Equations (4.2)–(4.4) are shown in Figure 67. Let Q_E

123
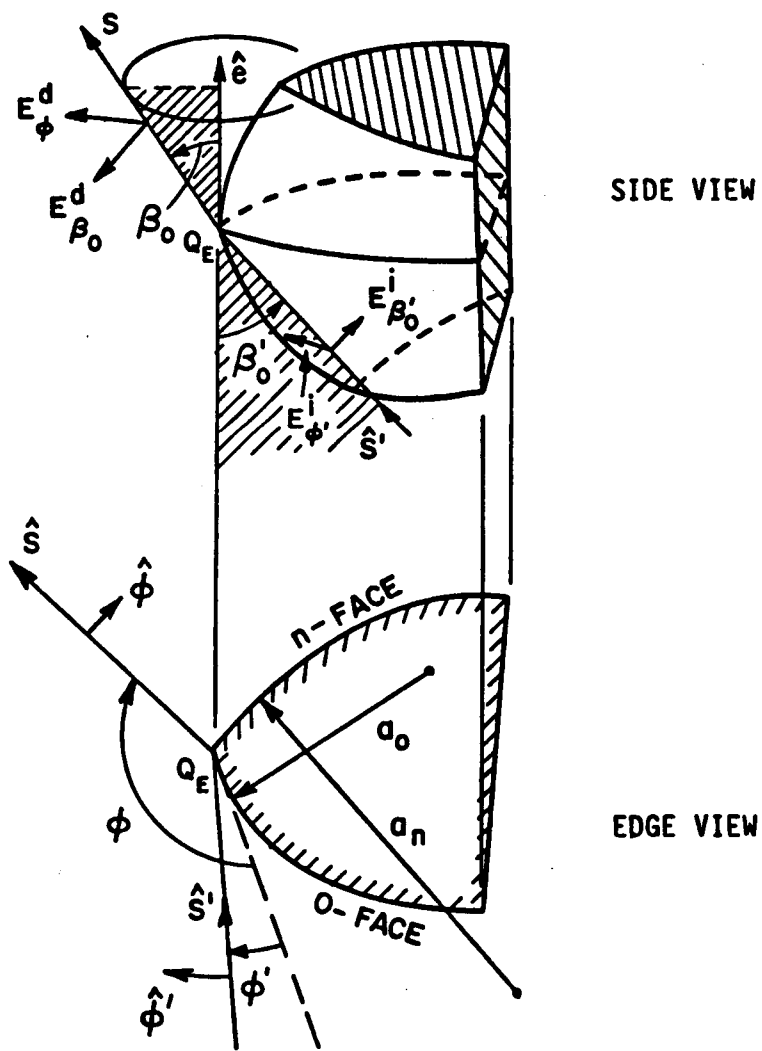
Figure 67: Three-dimensional wedge diffraction geometry.

124

be fixed at a point in space through which the edge will pass. It is then found that all parameters in the spread factor, except ρ_g and $\hat{n}_e$, are also fixed if the source and field points remain fixed. These two parameters determine the shape of the edge contour in that they control the radius of curvature of the edge contour and the orientation of the plane in which the edge contour lies. It is clear from Figures 64(a), 65(a) and 66(a) that the different edge contours result in different directions of $\hat{n}_e$ and magnitudes of ρ_g. By choosing an appropriate edge contour through Q_E, one can thus manipulate ρ_g and $\hat{n}_e$ to minimize the spread factor and thereby reduce the energy diffracted from Q_E into the target zone. The reason for this can be found by examining the physical significance of the spread factor as given in Equation (4.3). This factor accounts for the conservation of energy along a ray tube by enforcing the condition that all the energy entering the ray tube at one end be transmitted to the other end. By changing the size of the edge caustic (ρ_c), rays diffracted from adjacent positions on an edge can be made to be more divergent. This will alter the shape of the ray tube and decrease the value of the spread factor.

Consider now a convex, straight and concave edge in the xy-plane, all of which are illuminated by the same point source located along the z-axis. The diffracted rays from the edges are shown in Figures 68–70. It is seen that the horizontally diffracted rays from two adjacent points (Q_1 and Q_2) are parallel in the case of the convex edge. By reciprocity, when the edge is illuminated by a plane wave from the target zone, rays diffracted from the entire edge contour will intersect at every point on the z-axis as shown in Figure 68, so that the edge is a caustic. In contrast to the convex edge, the straight edge will have a divergent ray pattern as shown in Figure 69. The rays diffracted from the concave edge will diverge even more than those from the rectangular edge (see Figure 70). The change from the divergent

125
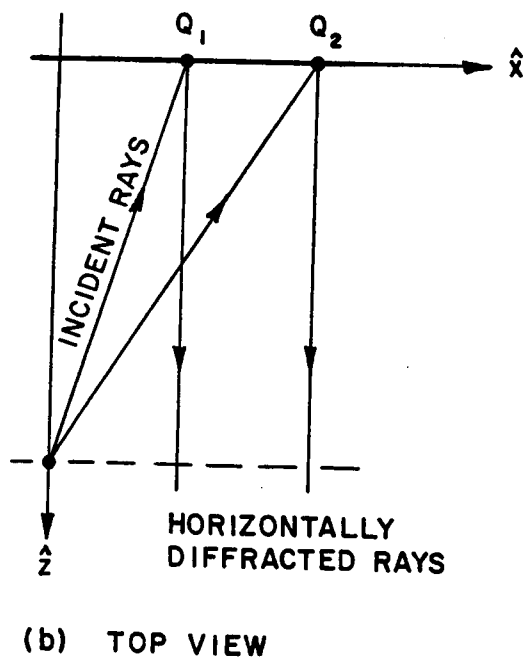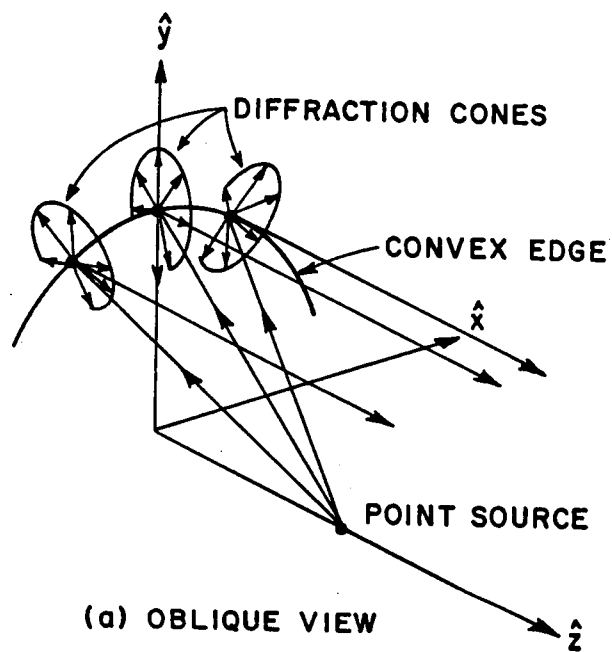
Figure 68: Diffraction from a convex edge.

126

DIFFRACTION CONES

STRAIGHT EDGE

$\hat{y}$

$\hat{x}$

POINT SOURCE

$\hat{z}$

(a) OBLIQUE VIEW

Q_1 Q_2 $\hat{x}$

INCIDENT RAYS

HORIZONTALLY DIFFRACTED RAYS

$\hat{z}$
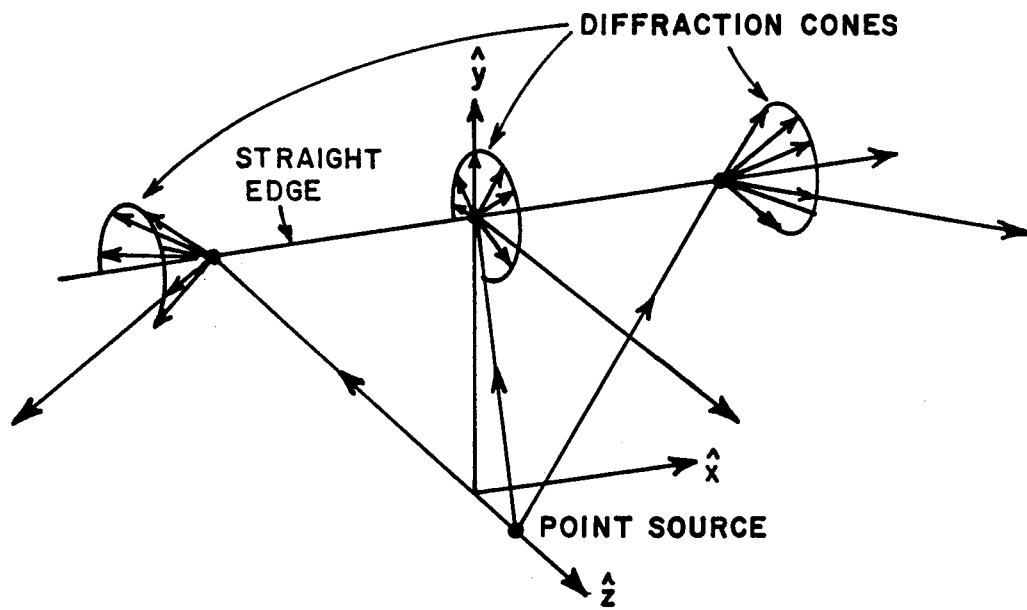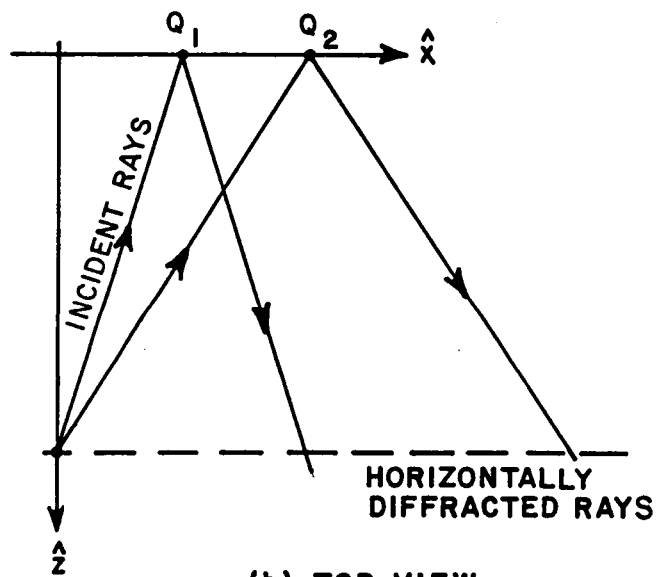
(b) TOP VIEW

Figure 69: Diffraction from a straight edge.

127
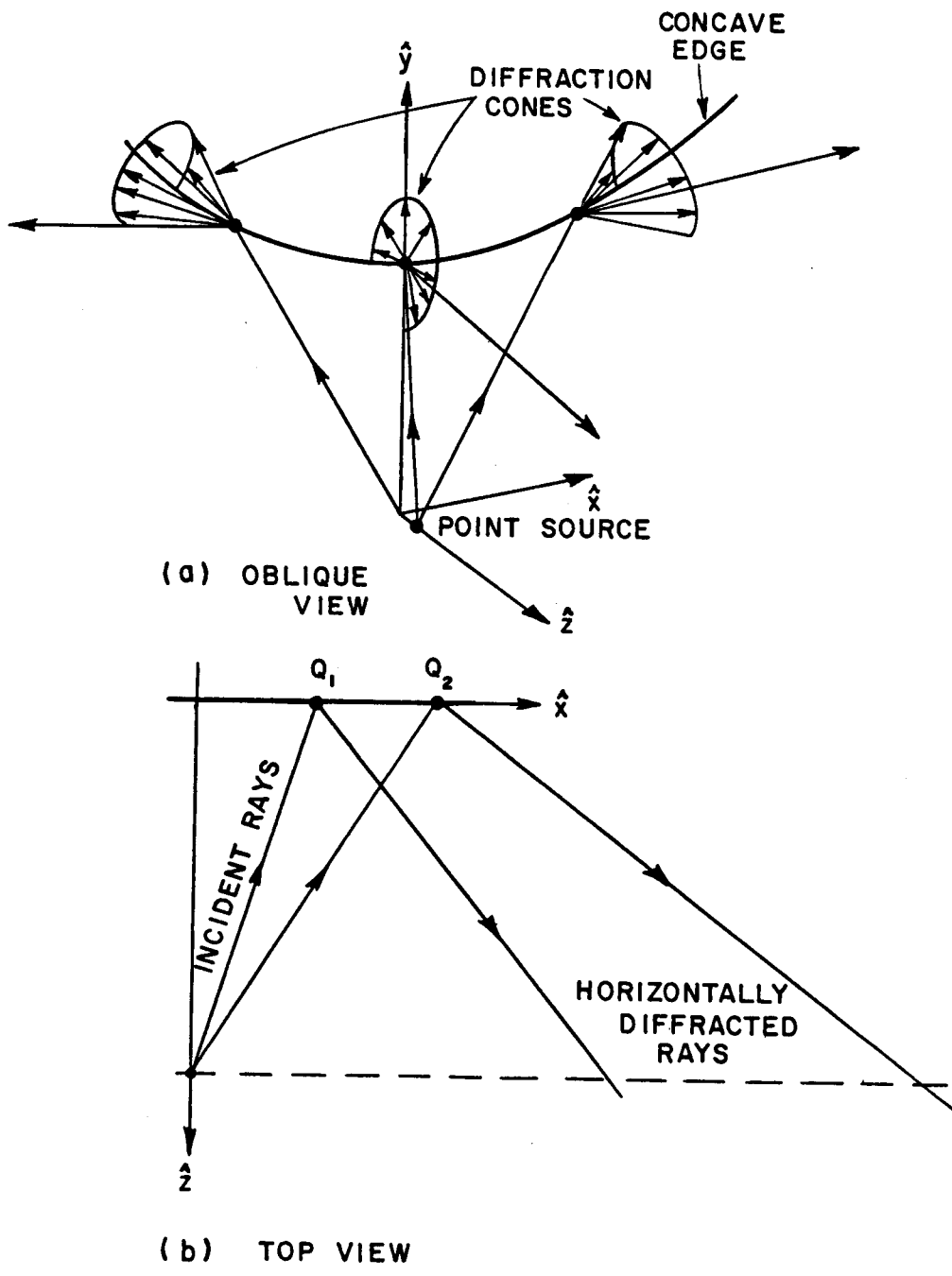
Figure 70: Diffraction from a concave edge.

128

rays in the case of the concave edge to the highly convergent rays in the case of the convex edge, is caused by the change in direction of the unit vector tangent to the edge as the edge contour is traced from Q_1 to Q_2. It is clear from these figures that a more divergent ray pattern can be obtained by using a concave edge contour. It is seen from Equation (4.2) that this will result in a reduction of the diffracted field magnitude.

In order to compare the spread factor and diffracted fields for the three types of edges discussed, consider a paraboloid with focal length equal to $12'$, and an offset target zone of width $8'$ in the x-dimension and height $6'$ in the y-dimension. Let the center of the target zone be $8'$ high, and located at a distance $24'$ away from the origin along the z-axis, as shown in Figure 71. Let the shapes of the three offset reflectors be that of the rectangular target zone projected onto the paraboloid, and enclosed by the convex, rectangular and concave edge contours, respectively. In the case of the convex edge, the target zone is modified to be $6'$ wide in the x-dimension due to the symmetry required by the circular shape of the edge contour. The xy-projection of the three reflector shapes are shown in Figure 72. Note that the xy-projection of the rectangular edge contour coincides with the xy-projection of the target zone, and that these reflectors have no rolled edge terminations.

The concave edge contour is formed by considering a rectangle in the xy-plane, hereafter referred to as the "defining rectangle", of dimensions (x_{min}, x_{max}) and (y_{min}, y_{max}) around the xy-projection of the target zone. The xy-projection of the target zone is considered to have dimensions (x_{left}, x_{right}) and (y_{bot}, y_{top}). The center of the defining rectangle coincides with the center of the xy-projection of the target zone. Radial lines are drawn from the center of the defining rectangle to its border. The concave edge is then formed by the locii of points on the radial
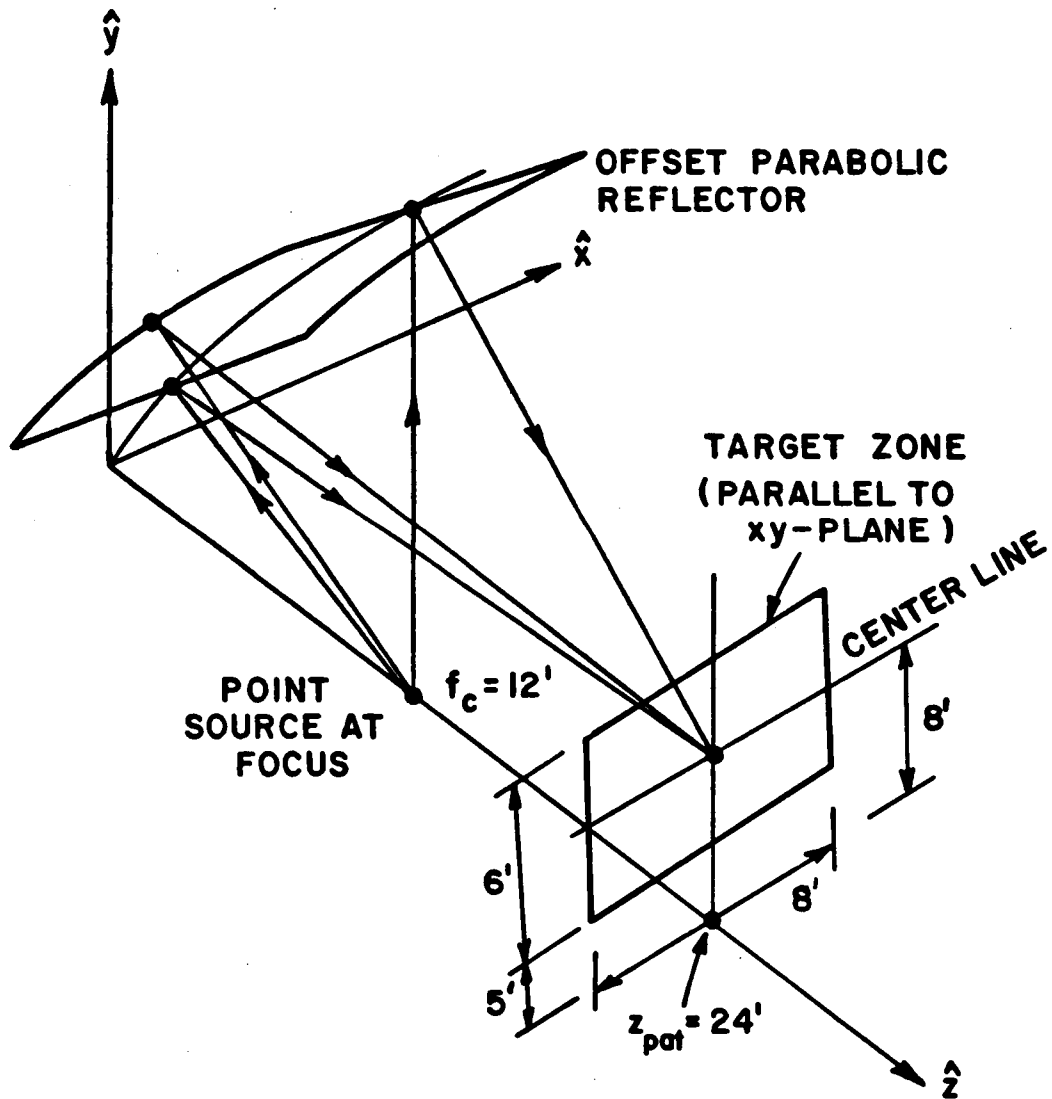
Figure 71: Offset reflector and target zone used for the comparison of the edge contours.
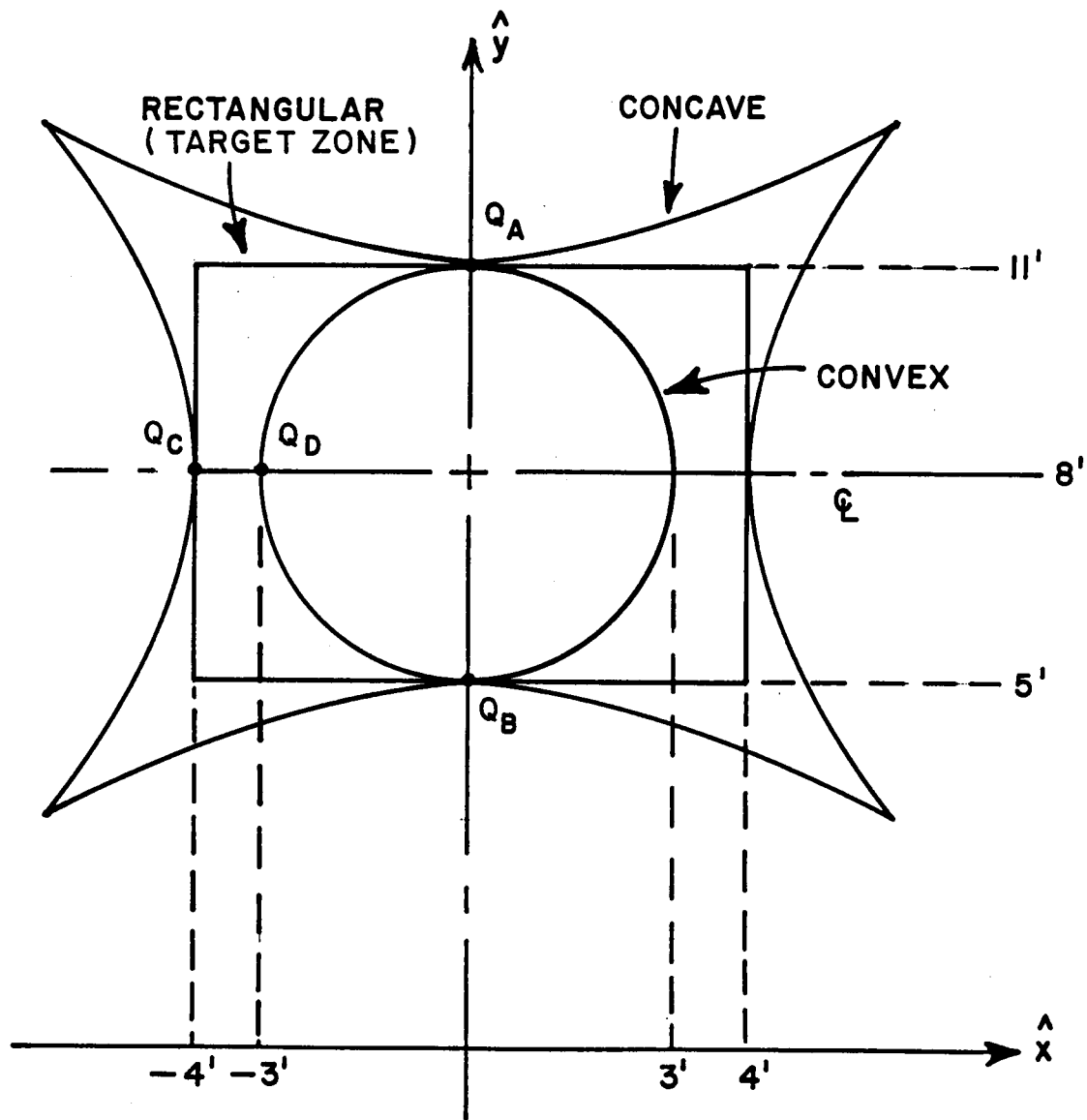
Figure 72: XY-projection of the offset reflector shapes with different edge contours.

131

lines that are a fixed distance (a_e) from the border of the rectangle as shown in Figure 73. The relation between the dimensions of the defining rectangle and the xy-projection of the target zone are thus given by

$$x_{max} = x_{right} + a_e \tag{4.5}$$

$$x_{min} = x_{left} - a_e \tag{4.6}$$

$$y_{max} = y_{top} + a_e \text{ , and} \tag{4.7}$$

$$y_{min} = y_{bot} - a_e \text{ .} \tag{4.8}$$

Note that the parameters (y_{min}) and (y_{max}) that are used in this context are not the same as those in Section 3.4.2. The center of the xy-projection of the target zone, and thus the center of the defining rectangle, is located at $(0, y_{avg})$, where y_{avg} is given by

$$y_{avg} = \frac{y_{max} + y_{min}}{2} = \frac{y_{top} + y_{bot}}{2} \text{ .} \tag{4.9}$$

Let (x_{ax}, y_{ax}) be a point on the perimeter of the defining rectangle as shown in Figure 73. The corresponding point on the concave edge contour of the paraboloid $[P_j(x_j, y_j, z_j)]$, is given by

$$x_j = x_{ax} - \frac{a_e x_{ax}}{\sqrt{x_{ax}^2 + (y_{ax} - y_{avg})^2}} \tag{4.10}$$

$$y_j = y_{ax} - \frac{a_e(y_{ax} - y_{avg})}{\sqrt{x_{ax}^2 + (y_{ax} - y_{avg})^2}} \text{ , and} \tag{4.11}$$

$$z_j = \frac{x_j^2 + y_j^2}{4f_c} \text{ .} \tag{4.12}$$

The entire concave edge contour of the paraboloid can be generated by tracing (x_{ax}, y_{ax}) around the perimeter of the defining rectangle. Note that the actual maximum and minimum dimensions of the reflector will not necessarily be equal to the values of $x_{min}, x_{max}, y_{min}$ and y_{max}. The parameters defining the concave edge used in this comparison are given in Table 11.

132
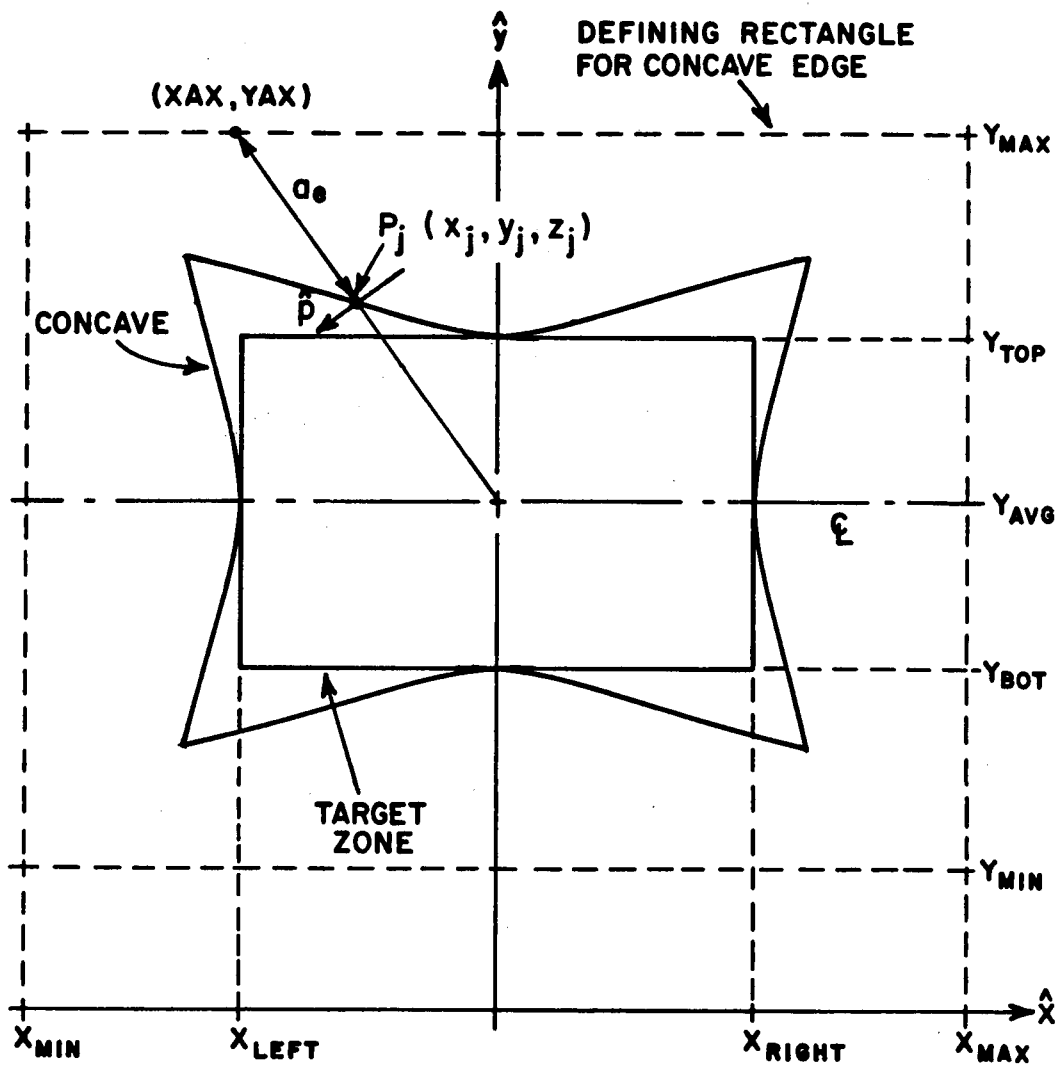
Figure 73: Defining rectangle for a concave edge contour.

Table 11: Parameters for the concave edge used in the comparison of the edge contours.

x_{min}	$-7'$
x_{max}	$7'$
y_{min}	$2'$
y_{max}	$14'$
f_c	$12'$
a_e	$3'$

The NEC Reflector Antenna Code[50] was used to analyze the three reflectors, using the UTD. Numerical values of a modified spread factor, which is given by

$$A^s = \left| \sqrt{\frac{\rho_c}{\rho_c + s}} \right|$$ (4.13)

were calculated for rays diffracted into the target zone from points common to all three edges. Since s is a constant when Q_E is fixed, A^s is a good measure of ρ_c. The common diffraction points are shown in Figure 72, and are defined as follows:

Q_A = top of the target zone projection, in the yz-plane

Q_B = bottom of the target zone projection, in the yz-plane

Q_C = left of the target zone projection, at the height of the centerline (concave and rectangular edge contours) , and

Q_D = left of the target zone projection, at the height of centerline (convex edge contour) .

The spread factor magnitudes are given in Tables 12 and 13 for vertical cuts through the center of the target zone and in Table 14 for a horizontal pattern cut

134

through the center of the target zone, for the various edge contours. The magnitude of the y-polarized fields diffracted from the three reflectors into the target zone are shown in Figure 74. The patterns were taken along a vertical cut through the center of the target zone at 10 GHz and also calculated with the NEC Code. The following observations and conclusions can be made from these results:

- The caustic effect of the convex edge is clearly demonstrated by the sharply increasing values of A^s towards the center of the target zone. This is especially true in the case of the horizontal pattern cut. Figure 74 shows the strong diffracted field from the convex edge in the center of the target zone. This is a very undesirable characteristic.

- The numerical values of the modified spread factor for the "rectangular edge" tend to stay close to 1. Since the edge is almost straight one finds that

$$\rho_g \to \infty \tag{4.14}$$

so that it follows from Equation (4.13) that

$$A^s \approx 1 . \tag{4.15}$$

- In the case of the concave edge, A^s is seen to decrease significantly across the target zone, with the highest values along the reflection shadow boundaries.

- Figure 74 clearly shows that the fields diffracted from the concave edged reflector into the target zone are smaller than those diffracted from both the rectangular and convex edged reflectors. This is due to the fact that the concave edge has a smaller spread factor than the other two edges as indicated in Tables 12–14.

135

Table 12: Modified spread factor for diffraction from Q_A.

VERTICAL PATTERN CUT					
Diffraction point: Q_A=(0.00,11.00,2.52)					
Pattern position			Modified spread factor (A^s)		
xpat	ypat	zpat	concave	rectangular	convex
0.00	5.00	24.00	0.563	0.983	0.960
0.00	5.50	24.00	0.581	0.986	1.052
0.00	6.00	24.00	0.601	0.988	1.175
0.00	6.50	24.00	0.623	0.990	1.353
0.00	7.00	24.00	0.645	0.992	1.646
0.00	7.50	24.00	0.673	0.994	2.275
0.00	8.00	24.00	0.701	0.996	7.353*
0.00	8.50	24.00	0.734	0.997	2.540
0.00	9.00	24.00	0.772	0.998	1.748
0.00	9.50	24.00	0.815	0.999	1.417
0.00	10.00	24.00	0.865	0.999	1.224
0.00	10.50	24.00	0.925	1.000	1.094
0.00	11.00	24.00	0.999[†]	1.000[†]	0.998[†]
Dimensions in feet					

*Edge diffraction caustic

[†]Reflection shadow boundary

Table 13: Modified spread factor for diffraction from Q_B.

VERTICAL PATTERN CUT					
Diffraction point: Q_B=(0.00,5.00,0.52)					
Pattern position			Modified spread factor (A^s)		
xpat	ypat	zpat	concave	rectangular	convex
0.00	5.00	24.00	1.000[†]	1.000[†]	0.998[†]
0.00	5.50	24.00	0.926	1.000	1.092
0.00	6.00	24.00	0.867	0.999	1.218
0.00	6.50	24.00	0.818	0.999	1.400
0.00	7.00	24.00	0.776	0.998	1.697
0.00	7.50	24.00	0.740	0.997	2.318
0.00	8.00	24.00	0.709	0.996	6.211*
0.00	8.50	24.00	0.682	0.995	2.741
0.00	9.00	24.00	0.657	0.993	1.854
0.00	9.50	24.00	0.635	0.991	1.494
0.00	10.00	24.00	0.615	0.989	1.287
0.00	10.50	24.00	0.597	0.987	1.148
0.00	11.00	24.00	0.581	0.985	1.047
Dimensions in feet					

*Edge diffraction caustic

†Reflection shadow boundary

Table 14: Modified spread factor for diffraction from Q_C and Q_D.

HORIZONTAL PATTERN CUT					
Diffraction point: Q_C=(-4.00,8.00,1.67)					
Diffraction point: Q_D=(-3.00,8.00,1.52)					
Pattern position			Modified spread factor (A^s)		
xpat	ypat	zpat	concave (Q_C)	rectangular (Q_C)	convex (Q_D)
-4.00	8.00	24.00	1.001[†]	1.000[†]	
-3.00	8.00	24.00	0.921	0.999	0.998[†]
-2.00	8.00	24.00	0.854	0.998	1.206
-1.00	8.00	24.00	0.807	0.996	1.639
-0.50	8.00	24.00	0.783	0.995	2.165
0.00	8.00	24.00	0.762	0.993	LARGE*
0.50	8.00	24.00	0.736	0.991	2.954
1.00	8.00	24.00	0.718	0.989	1.948
2.00	8.00	24.00	0.688	0.985	1.309
3.00	8.00	24.00	0.659	0.979	1.052
4.00	8.00	24.00	0.631	0.974	
Dimensions in feet					

*Edge diffraction caustic

[†]Reflection shadow boundary

- The performance of the concave edged reflector is thus clearly superior to the other two, and one can ascertain that the use of such an edge contour will, in general, lead to smaller edge diffractions in the target zone.

4.3 Three-dimensional rolled surface terminations

The ellipses forming the basis of the blended rolled surface terminations lie in flat planes as described in Sections 3.3 and 3.4.1. In particular, the ellipse attached at P_j is defined in a local $x_e y_e$-coordinate system, with P_j as its origin. In order for the ellipse attached at $P_j(x_j, y_j, z_j)$ to be aligned with the parabolic surface it is required that

$$\hat{\mathbf{y}}_e = -\hat{\mathbf{n}}_{junction} \tag{4.16}$$

where $\hat{\mathbf{n}}_{junction}$ is the unit vector normal to the paraboloid at the junction (P_j). The expression for $\hat{\mathbf{n}}_{junction}$ is derived in Appendix A. Thus, one finds that

$$\hat{\mathbf{y}}_e(P_j) = y_{p1}\hat{\mathbf{x}} + y_{p2}\hat{\mathbf{y}} + y_{p3}\hat{\mathbf{z}} \tag{4.17}$$

where the direction cosines are given by

$$y_{p1} = \frac{x_j}{\sqrt{x_j^2 + y_j^2 + 4f_c^2}} \tag{4.18}$$

$$y_{p2} = \frac{y_j}{\sqrt{x_j^2 + y_j^2 + 4f_c^2}} \text{, and} \tag{4.19}$$

$$y_{p3} = \frac{-2f_c}{\sqrt{x_j^2 + y_j^2 + 4f_c^2}} \text{.} \tag{4.20}$$

Let $\hat{\mathbf{p}}$ be a unit vector in the xy-plane at the projection of P_j onto the xy-plane such that $\hat{\mathbf{p}}$ is perpendicular to the radial line connecting the projection of P_j and the center of the defining rectangle as shown in Figure 73; ie.,

$$\hat{\mathbf{p}} = \frac{-(y_{ax} - y_{avg})}{\sqrt{x_{ax}^2 + (y_{ax} - y_{avg})^2}}\hat{\mathbf{x}} + \frac{x_{ax}}{\sqrt{x_{ax}^2 + (y_{ax} - y_{avg})^2}}\hat{\mathbf{y}} = p_1\hat{\mathbf{x}} + p_2\hat{\mathbf{y}} \text{.} \tag{4.21}$$
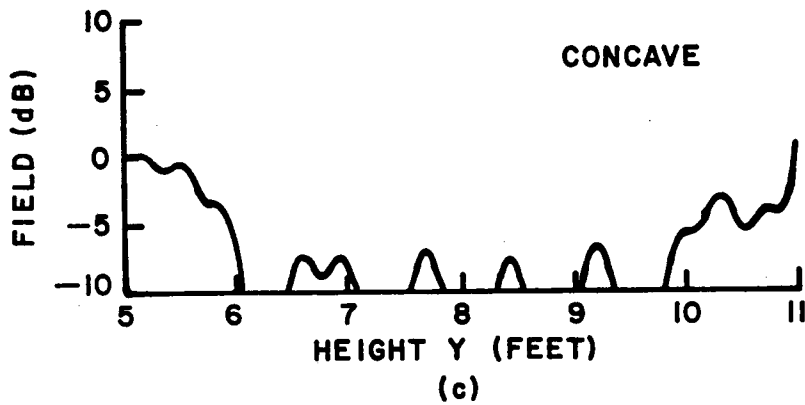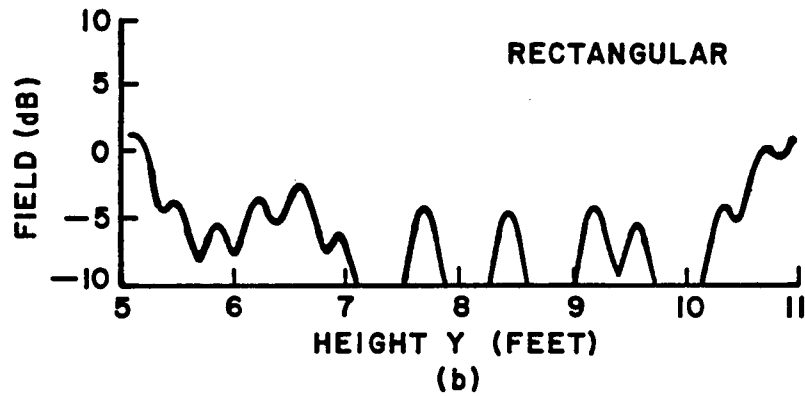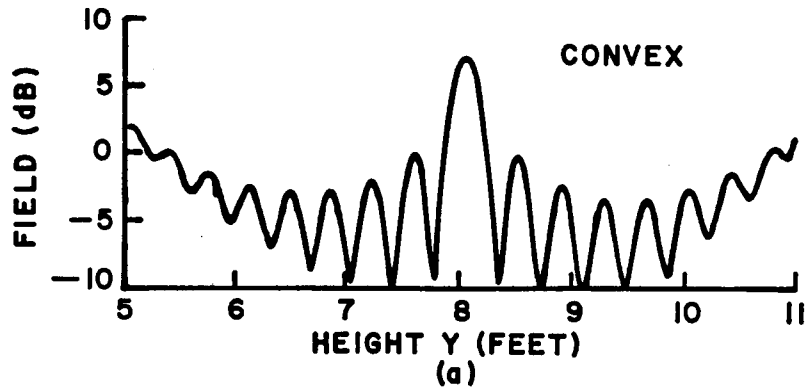
Figure 74: Magnitude of the diffracted fields from the reflectors used in the edge comparison (10 GHz).

140

The unit vector $\hat{\mathbf{x}}_e$ can then be defined as

$$\hat{\mathbf{x}}_e = \frac{\hat{\mathbf{y}}_e \times \hat{\mathbf{p}}}{|\hat{\mathbf{y}}_e \times \hat{\mathbf{p}}|} = x_{p1}\hat{\mathbf{x}} + x_{p2}\hat{\mathbf{y}} + x_{p3}\hat{\mathbf{z}} \qquad (4.22)$$

where the direction cosines are given by

$$x_{p1} = \frac{-y_{p3}p_2}{y_{pg}} \qquad (4.23)$$

$$x_{p2} = \frac{y_{p3}p_1}{y_{pg}} \qquad (4.24)$$

$$x_{p3} = \frac{y_{p1}p_2 - y_{p2}p_1}{y_{pg}} \text{, and} \qquad (4.25)$$

$$y_{pg} = \sqrt{(y_{p3}p_2)^2 + (y_{p3}p_1)^2 + (y_{p1}p_2 - y_{p2}p_1)^2} \text{.} \qquad (4.26)$$

Consider now a projection in the xy-plane. The surface normal ($\hat{n}_{junction}$) points toward the axis of symmetry of the paraboloid and in particular to the point $(0, 0, 2f_c)$. In the case where the target zone is symmetric around the axis of symmetry of the paraboloid, the center of the defining rectangle lies on the axis of symmetry of the paraboloid, so that all the $x_e y_e$-planes will be perpendicular to the xy-plane as shown in Figure 75(a). In the case of an offset target zone, however, only the two $x_e y_e$-planes attached to $P_j(0, y_j, z_j)$ will be perpendicular to the xy-plane as shown in Figure 75(b). This is due to the fact that the radial lines of the defining rectangle are parallel to $\hat{n}_{junction}$ in the case of the symmetric target zone, and in the case of the offset target zone, they are not. The two cases are illustrated in Figure 76. The dark line in the interior of the reflectors shown in Figure 75 indicate the junction between the parabolic section and the rolled surface terminations. Note that the grid lines on the surfaces of the reflectors in these figures are not contour lines in that contour lines generally indicate some parameter being constant.

In order to specify the rolled surface attached at $P_j(x_j, y_j, z_j)$ in the xyz-system, it is necessary to use the transformation from the $x_e y_e$-system to the

141
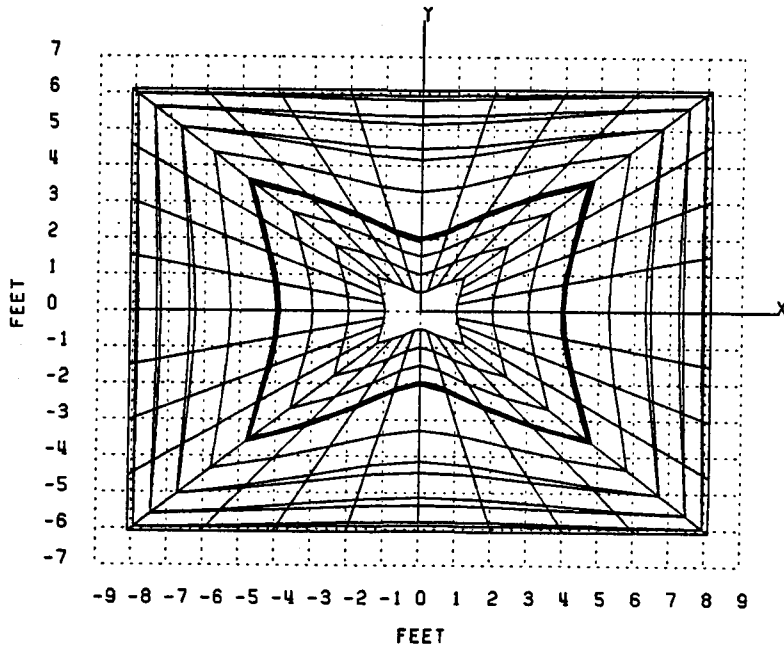
(a) Symmetric target zone.
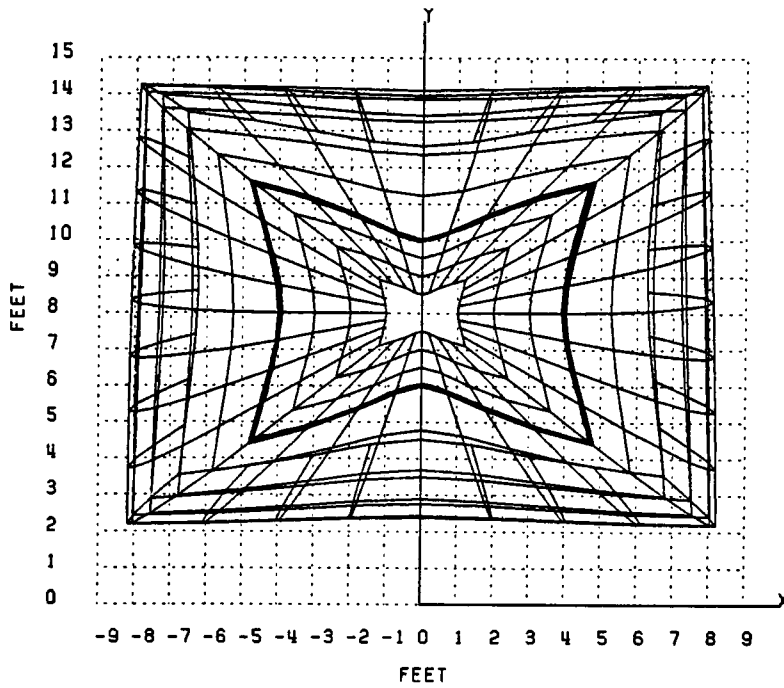
(b) Offset target zone.

Figure 75: The $x_e y_e$-planes for symmetric an offset target zones.

142

(a) SYMMETRIC TARGET ZONE

(b) OFFSET TARGET ZONE

Figure 76: Radial lines for symmetric and offset target zones.

143

xyz-system which is given by

$$
\begin{pmatrix} x(\gamma) \\ y(\gamma) \\ z(\gamma) \end{pmatrix} = \begin{pmatrix} x_{p1} & y_{p1} \\ x_{p2} & y_{p2} \\ x_{p3} & y_{p3} \end{pmatrix} \begin{pmatrix} x_e(\gamma) \\ y_e(\gamma) \end{pmatrix} + \begin{pmatrix} x_j \\ y_j \\ z_j \end{pmatrix} . \tag{4.27}
$$

Following the discussion in Section 3.4, it is seen that in the case where $b(\gamma) = 1$, the pure elliptic rolled surface attached at P_j is given by

$$
x(\gamma) = (a_e \sin\gamma)x_{p1} + b_e(1 - \cos\gamma)y_{p1} + x_j \tag{4.28}
$$

$$
y(\gamma) = (a_e \sin\gamma)x_{p2} + b_e(1 - \cos\gamma)y_{p2} + y_j , \text{ and} \tag{4.29}
$$

$$
z(\gamma) = (a_e \sin\gamma)x_{p3} + b_e(1 - \cos\gamma)y_{p3} + z_j . \tag{4.30}
$$

Similarly, in the case where $b(\gamma) = 0$, the resulting extended parabola attached at P_j is given by

$$
x(\gamma) = \gamma \left(\frac{x_m}{\gamma_m} \right) x_{p1} + x_j \tag{4.31}
$$

$$
y(\gamma) = \gamma \left(\frac{x_m}{\gamma_m} \right) x_{p2} + y_j , \text{ and} \tag{4.32}
$$

$$
z(\gamma) = \frac{x^2 + y^2}{4f_c} . \tag{4.33}
$$

In the case of the general blending function, the blended rolled surface attached at $P_j(x_j, y_j, z_j)$ can thus be described by

$$
\begin{aligned}
x(\gamma) = {} & \left[\gamma \left(\frac{x_m}{\gamma_m} \right) x_{p1} + x_j \right] [1 - b(\gamma)] \\
& + [(a_e \sin\gamma)x_{p1} + b_e(1 - \cos\gamma)y_{p1} + x_j]b(\gamma)
\end{aligned} \tag{4.34}
$$

$$
\begin{aligned}
y(\gamma) = {} & \left[\gamma \left(\frac{x_m}{\gamma_m} \right) x_{p2} + y_j \right] [1 - b(\gamma)] \\
& + [(a_e \sin\gamma)x_{p2} + b_e(1 - \cos\gamma)y_{p2} + y_j]b(\gamma) , \text{ and}
\end{aligned} \tag{4.35}
$$

144

$$z(\gamma) = \left[\frac{[\gamma(x_m/\gamma_m)x_{p1} + x_j]^2 + [\gamma(x_m/\gamma_m)x_{p2} + y_j]^2}{4f_c}\right][1 - b(\gamma)]$$
$$+[(a_e \sin\gamma)x_{p3} + b_e(1 - \cos\gamma)y_{p3} + z_j]b(\gamma) . \tag{4.36}$$

The method described here by which the blended rolled surfaces are attached to the parabolic section is not restricted to concave edge contours, but can be applied to other edge contours as well. Figure 77 shows a parabolic reflector with a rectangular edge contour and blended rolled edges. A parabolic reflector with a convex edge contour and blended rolled edges will be described in Section 4.6.

4.4 Main reflector design with focus feed

Two three-dimensional reflectors with $f_c = 12'$ and concave edge contours will now be considered. They are designated as S3.1 and S3.2, and correspond to the two-dimensional surfaces S2.1 and S2.2 in that S2.1 and S2.2 are the yz-plane cuts of S3.1 and S3.2, respectively. The surface characteristics of S3.1 and S3.2 are given in Table 15.

The target zone is considered to be $8'$ wide and $6'$ high, with the center of the target zone $8'$ above the axis of symmetry of the paraboloid and situated at a distance (z_{pat}) of $24'$ away from the main origin along the z-axis, as shown in Figure 72. In calculating the scattered fields from the reflectors it is assumed that there is no direct illumination from the feed into the target zone.

The reflectors are illuminated by a Huygens source located at the focal point. The Huygens source approximation is based on the assumption that it best represents the radiation and polarization properties of a horn feed antenna. A more complete motivation for the use of a Huygens source will be given in Chapter V.

Consider the feed antenna to be located in its own $x_f y_f z_f$-coordinate system, with origin located at the focal point of the main reflector so that $\hat{x}_f = -\hat{x}$ as

145
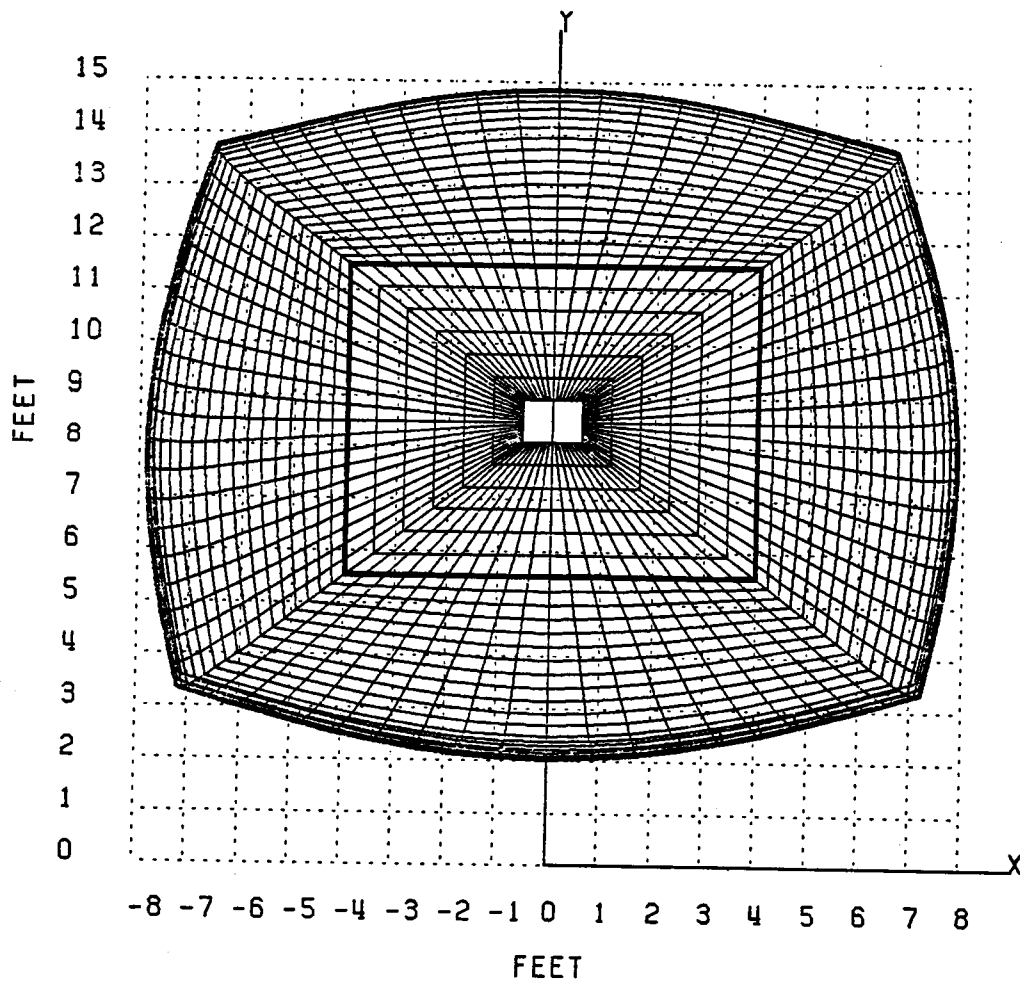
Figure 77: Parabolic reflector with a rectangular edge contour and blended rolled edges (Front view).

146

Table 15: Surface characteristics for S3.1 and S3.2.

	S3.1	S3.2
Blending	None	Cosine
f_c	$12'$	$12'$
a_e	$3'$	$3'$
b_e	$0.75'$	$0.75'$
x_m		$7'$
γ_m		120°
y_{bot}	$5'$	$5'$
y_{avg}	$8'$	$8'$
y_{top}	$11'$	$11'$
x_{left}	$-4'$	$-4'$
x_{right}	$4'$	$4'$
α	36.87^o	36.87^o
z_{pat}	$24'$	$24'$

147
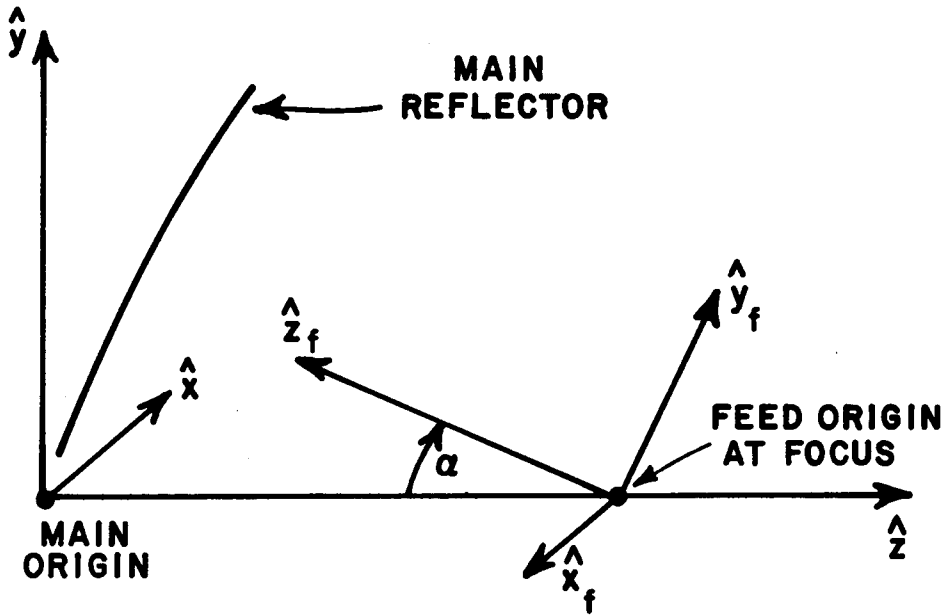
Figure 78: Focus feed coordinate system.

shown in Figure 78. Let the z_f-axis be the axis of symmetry of the feed. The z_f-axis is tilted at an angle (α) relative to the $-z$-axis. In this case the angle (α) is chosen so that the z_f-axis points towards the center of the projection of the target zone on the main reflector; ie.,

$$\tan\alpha = \frac{y_{avg}}{f_c - y_{avg}^2/4f_c} \ . \tag{4.37}$$

The transformation from the xyz-system to the $x_f y_f z_f$-system is given by

$$\begin{pmatrix} x_f \\ y_f \\ z_f \end{pmatrix} = \begin{pmatrix} -1 & 0 & 0 \\ 0 & \cos\alpha & \sin\alpha \\ 0 & \sin\alpha & -\cos\alpha \end{pmatrix} \begin{pmatrix} x \\ y \\ z \end{pmatrix} + \begin{pmatrix} 0 \\ -f_c\sin\alpha \\ f_c\cos\alpha \end{pmatrix} . \tag{4.38}$$

It is assumed that the Huygens source is y_f-polarized, so that the radiated far zone electric field is given (in feed coordinates) by

$$\mathbf{E}_f(R,\theta_f,\phi_f) = \mathbf{e}^i(\theta_f,\phi_f)\frac{e^{-jkR}}{R} \tag{4.39}$$

148

where

$$\mathbf{e}^i(\theta_f, \phi_f) = F_\theta(\theta_f, \phi_f)\hat{\theta}_f(\theta_f, \phi_f) + F_\phi(\theta_f, \phi_f)\hat{\phi}_f(\theta_f, \phi_f) \tag{4.40}$$

$$F_\theta(\theta_f, \phi_f) = \left(\sin\phi_f \cos^2\frac{\theta_f}{2}\right) F_\theta^a(\theta_f, \phi_f) \text{ , and} \tag{4.41}$$

$$F_\phi(\theta_f, \phi_f) = \left(\cos\phi_f \cos^2\frac{\theta_f}{2}\right) F_\phi^a(\theta_f, \phi_f) \text{ .} \tag{4.42}$$

In this case, it is assumed that $F_\theta^a = 1$ and $F_\phi^a = 1$. The spherical unit vectors are given by

$$\begin{pmatrix} \hat{\theta}_f \\ \hat{\phi}_f \end{pmatrix} = \begin{pmatrix} \cos\theta_f\cos\phi_f & \cos\theta_f\sin\phi_f & -\sin\theta_f \\ -\sin\phi_f & \cos\phi_f & 0 \end{pmatrix} \begin{pmatrix} \hat{\mathbf{x}}_f \\ \hat{\mathbf{y}}_f \\ \hat{\mathbf{z}}_f \end{pmatrix} \tag{4.43}$$

so that

$$\begin{pmatrix} \hat{\theta}_f \\ \hat{\phi}_f \end{pmatrix} = \begin{pmatrix} \cos\theta_f\cos\phi_f & \begin{array}{c}\cos\theta_f\sin\phi_f\cos\alpha \\ -\sin\theta_f\sin\alpha\end{array} & \begin{array}{c}\cos\theta_f\sin\phi_f\sin\alpha \\ +\sin\theta_f\cos\alpha\end{array} \\ \sin\phi_f & \cos\alpha\cos\phi_f & \sin\alpha\cos\phi_f \end{pmatrix} \begin{pmatrix} \hat{\mathbf{x}} \\ \hat{\mathbf{y}} \\ \hat{\mathbf{z}} \end{pmatrix} \text{ .} \tag{4.44}$$

Given a point $\mathbf{P}_p(x_p, y_p, z_p)$ on the surface of the main reflector, Equation (4.38) can be used to transform it to $\mathbf{P}_p(x_f, y_f, z_f)$ in feed coordinates. The unit vector from the feed origin to the point on the surface of the main reflector is thus given in feed coordinates by

$$\hat{\mathbf{P}}_p = \frac{\mathbf{P}_p}{|\mathbf{P}_p|} = (x_{fn}, y_{fn}, z_{fn}) \text{ .} \tag{4.45}$$

One further finds that

$$R = \sqrt{x_f^2 + y_f^2 + z_f^2} \tag{4.46}$$

$$\theta_f = \arccos(z_{fn}) \text{ , and} \tag{4.47}$$

149

$$\phi_f \;=\; \begin{cases} \arctan(y_{fn}/x_{fn}) & \text{if } x_{fn} \neq 0 \\[2mm] 90^o & \text{if } x_{fn}=0, y_{fn} \geq 0 \text{ , and} \\[2mm] -90^o & \text{if } x_{fn}=0, y_{fn} < 0 \text{ .} \end{cases} \qquad (4.48)$$

Once θ_f and ϕ_f are determined, the field incident on $\mathbf{P}_p$ can be calculated in terms of $\hat{\mathbf{x}}$, $\hat{\mathbf{y}}$ and $\hat{\mathbf{z}}$, by substituting Equation (4.44) into Equation (4.39).

4.4.1 Design example (elliptic rolled edges)

Consider now S3.1 with pure elliptic rolled surface terminations, as shown in Figures 79 and 80 for two different viewing angles.

The patterns of the three-dimensional reflectors can be computed using the corrected PO method. As mentioned before, this method is used since the UTD diffraction coefficients for higher order blended junctions are not yet available. The numerical PO integration is performed by dividing the entire reflector surface into small triangular patches as described in Section 2.3.2, so that the maximum dimension of a patch does not exceed 0.1λ. Each of the trapezoidal patches shown in Figures 79 and 80 are divided into two triangular surface patches. Since the patches are very small, it can be assumed that each patch is in the far zone of the source, and that each pattern point in the target zone is in the far zone of a patch. This implies that the incident field on a patch can be considered to be a local plane wave, and that the field scattered from a patch can be calculated using the far zone approximation of the PO integral. The total field at a pattern point is obtained by summing the contributions of all the illuminated patches on the reflector surface and then subtracting the end point contributions around the incident shadow boundary contour on the blended rolled surface terminations as described in Section 2.3.3. Note however that the second term of the end point scattering coefficient depends on the radius of curvature of the surface at

150
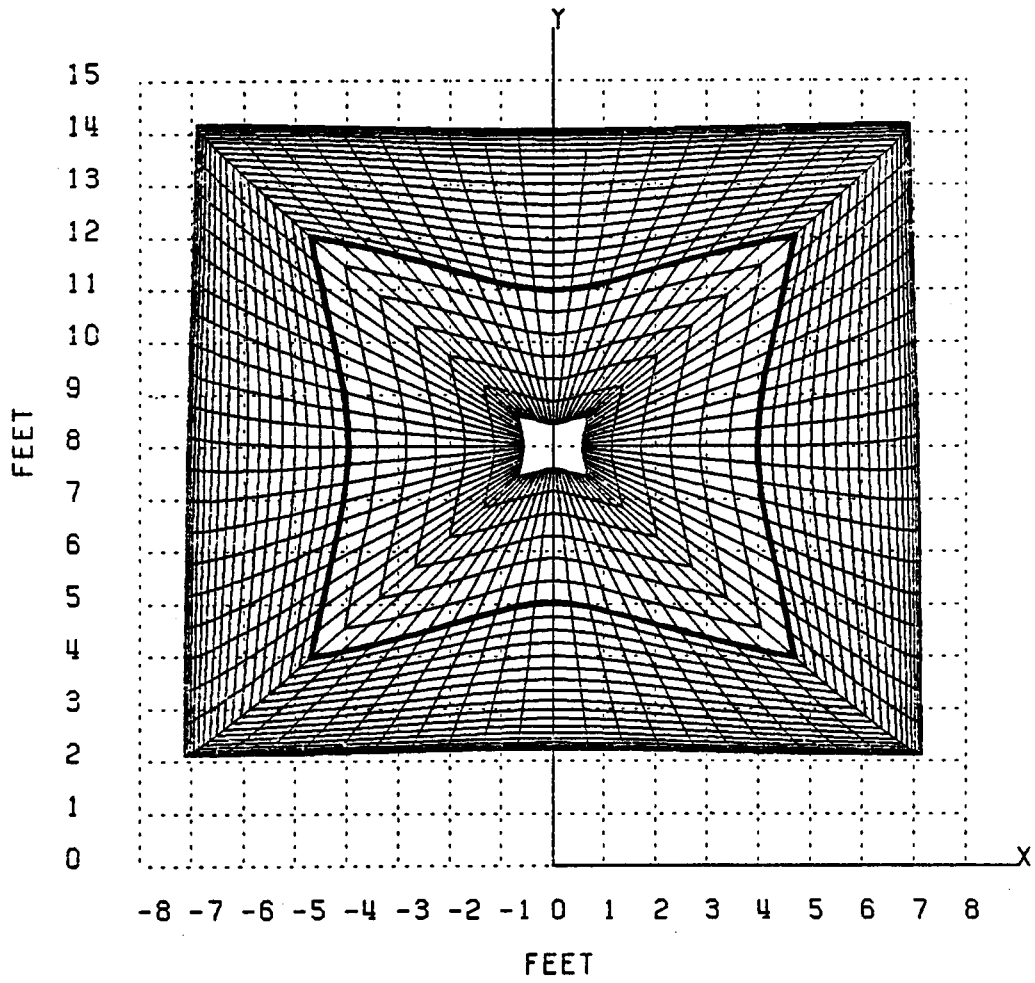
Figure 79: Three-dimensional parabolic reflector with elliptic rolled edges (S3.1)(Front view).

151
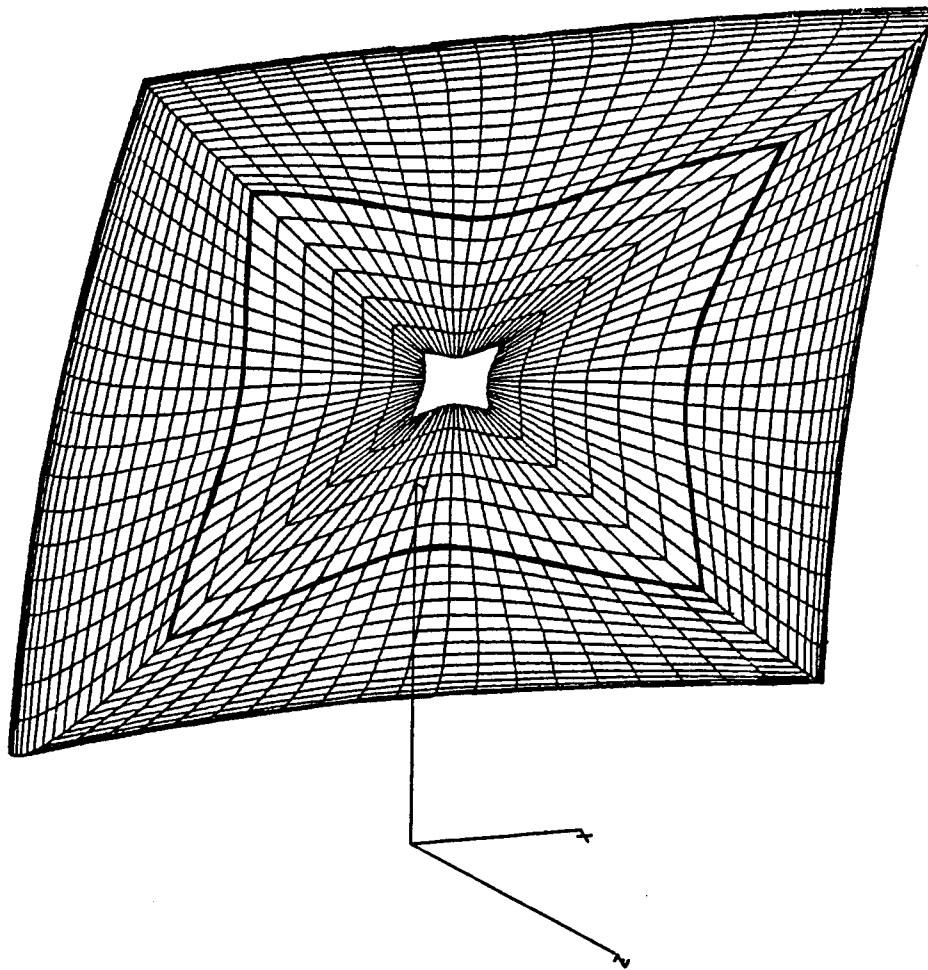
Figure 80: Three-dimensional parabolic reflector with elliptic rolled edges (S3.1)
(View angle: $\theta = 30^o, \phi = 150^o$).

the incident shadow boundary. Due to the twisted planes in which the rolled surface ellipses are located (see Figure 75(b)), this is a very tedious calculation; consequently, the radii of curvature at the top and bottom shadow boundaries are approximated by their values in the yz-plane. These values are obtained as part of the optimization algorithm described in Section 3.4.2. The second order PO correction terms have not been applied for the left and right rolled surface shadow boundaries. Since the actual numerical computation of a PO pattern for a three-dimensional antenna was found to be almost prohibitively expensive in terms of computer time, patterns were calculated at 3 GHz only.

Once the total field is known, the GO reflected field can be calculated and subtracted from the total field. The residual field will by default be the field diffracted from the concave edge junction between the parabolic and rolled surfaces, since no other significant scattering mechanisms contribute to the total field in the target zone.

Keeping in mind that the caustic distances for the reflected field from a paraboloid due to illumination from a point source at the focus are both equal to infinity, one finds that the GO field ($\mathbf{E}^r$) reflected from a point Q_R on the parabolic surface to the target zone is given by

$$\mathbf{E}^r(s) = [-\mathbf{E}^i + 2(\hat{\mathbf{n}} \cdot \mathbf{E}^i)\hat{\mathbf{n}}]e^{-jks} \qquad (4.49)$$

where

$\mathbf{E}^i$ = incident electric field at Q_R

$\hat{\mathbf{n}}$ = unit vector normal to the surface at Q_R (See Appendix A) , and

s = distance from Q_R to the field point .

Patterns were calculated along a cut through the yz-plane, located at a distance (z_{pat}) of 24' away from the main origin along the z-axis. The normalized

153

magnitude and phase of the total field together with plots comparing the reflected fields with fields diffracted from the concave junctions are shown in Figures 81–89 for the cases where no end point contributions are subtracted, only first order end point contributions are subtracted, and, finally, first and second order end point contributions are subtracted. The tickmarks on the plots indicate the sampling points in the target zone used in the numerical calculations. By comparing Figures 83 and 89 it is seen that, in this case of pure elliptic rolled surfaces, the difference in diffracted fields for the cases where no end point contributions are subtracted and first as well as second end point contributions are subtracted, is small. This implies that the end point contributions are overshadowed by the relatively large diffractions coming from the edge junction between the paraboloid and the rolled edge. Comparison of Figures 87–89 with Figures 23–25 indicate the good agreement between the patterns for the three-dimensional (S3.1) and two-dimensional (S2.1) reflectors.

4.4.2 Design example (cosine blended edge)

Consider now S3.2 with cosine blended rolled surface terminations as shown in Figures 90 and 91 for two different viewing angles. The scattered fields from this reflector were calculated along a cut through the yz-plane, located at a distance (z_{pat}) of 24′ away from the main origin along the z-axis. The normalized magnitude and phase of the total field in the yz-plane of the target zone together with plots comparing the reflected fields with fields diffracted from the concave junctions are shown in Figures 92–100 for the cases where no end point contributions are subtracted, only first order end point contributions are subtracted and, finally, first and second order end point contributions are subtracted. Comparison of Figures 98–100 with Figures 38–40 indicate the good agreement between the

154

Figure 81: Normalized magnitude of the total field from S3.1(3 GHz). No end point contributions subtracted.
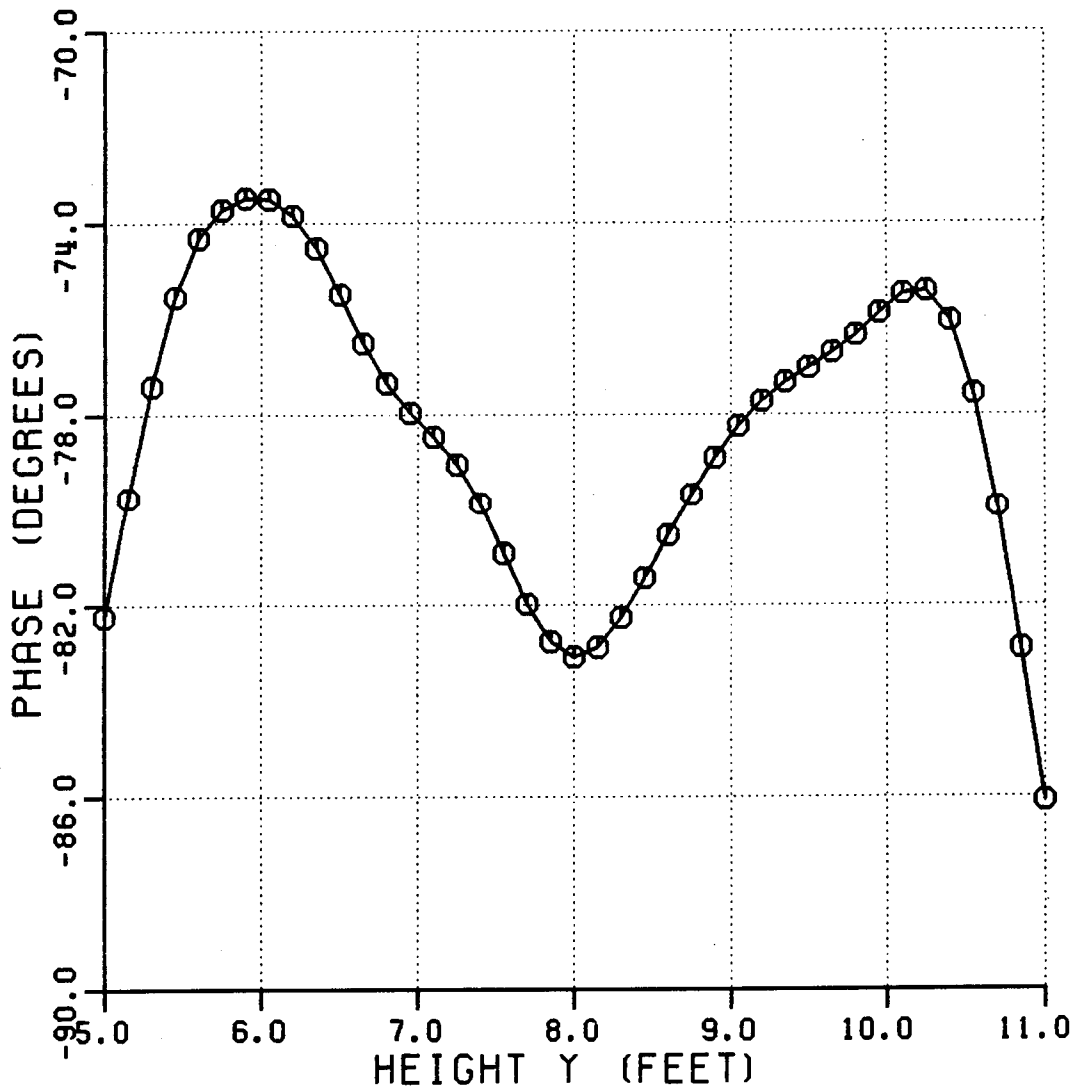
Figure 82: Phase of the total field from S3.1(3 GHz). No end point contributions subtracted.

156
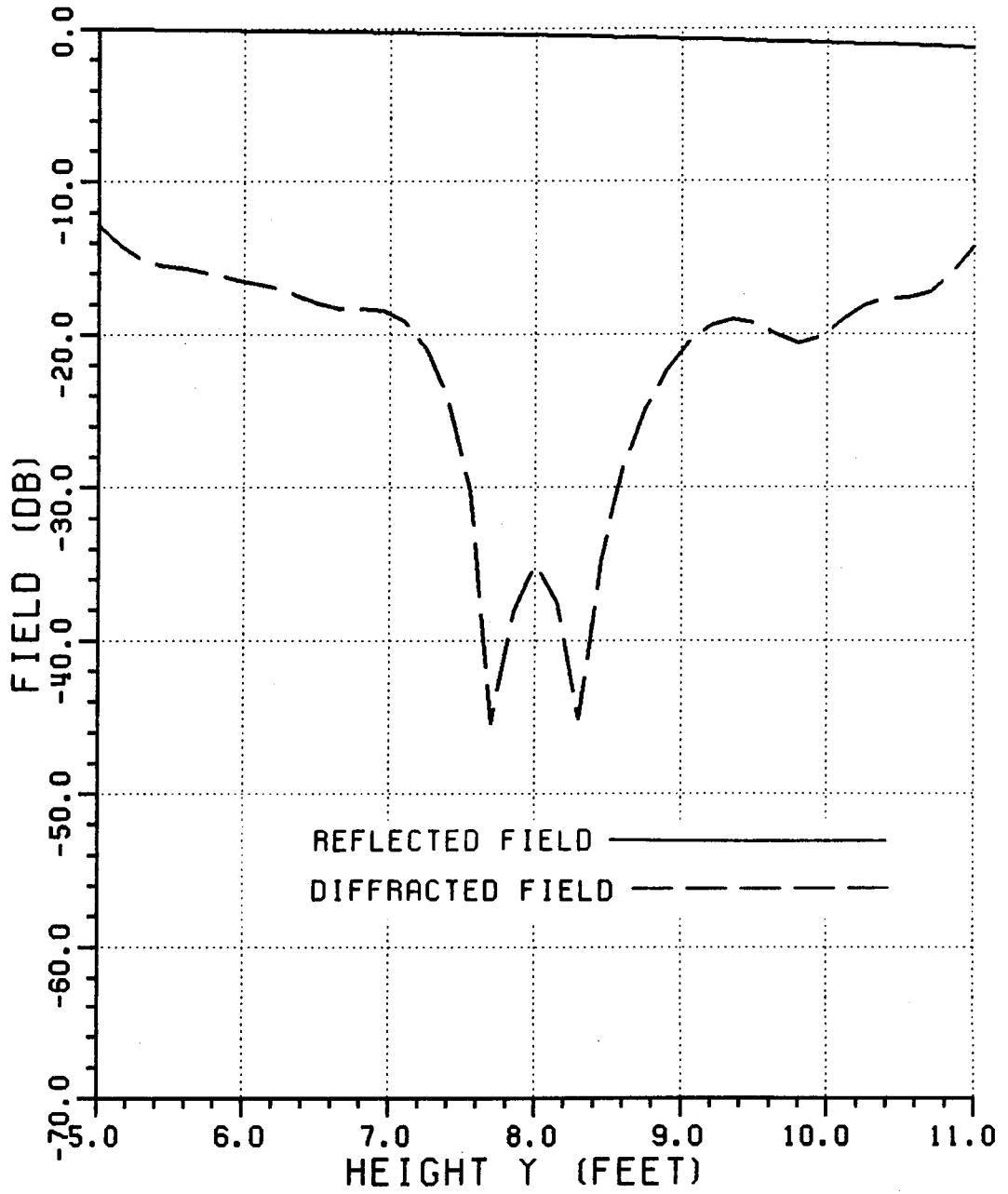
Figure 83: Normalized magnitude of the reflected and diffracted fields from S3.1(3 GHz). No end point contributions subtracted.

157

Figure 84: Normalized magnitude of the total field from S3.1(3 GHz). First order
end point contributions subtracted.

158
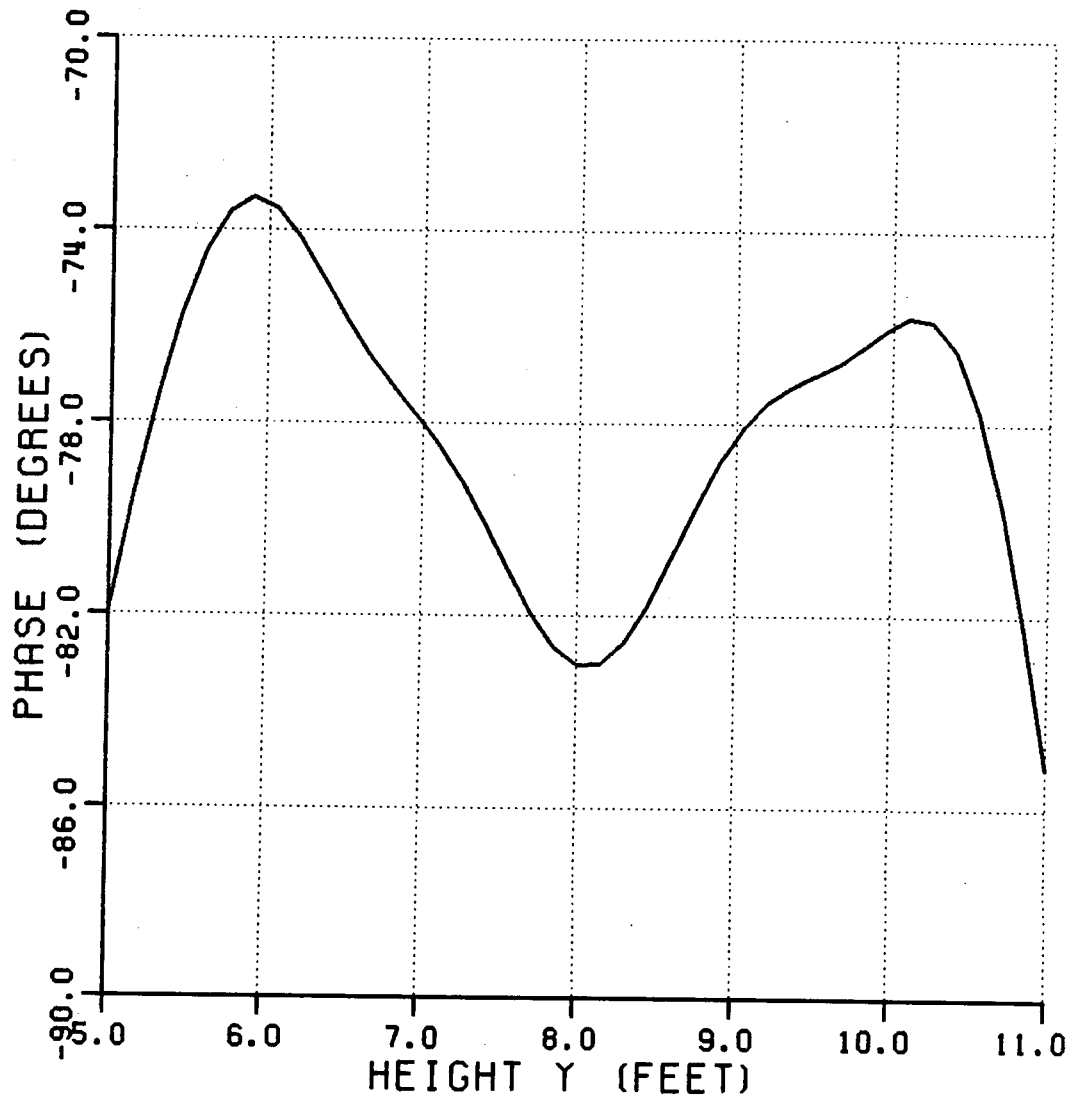
Figure 85: Phase of the total field from S3.1 (3 GHz). First order end point contributions subtracted.
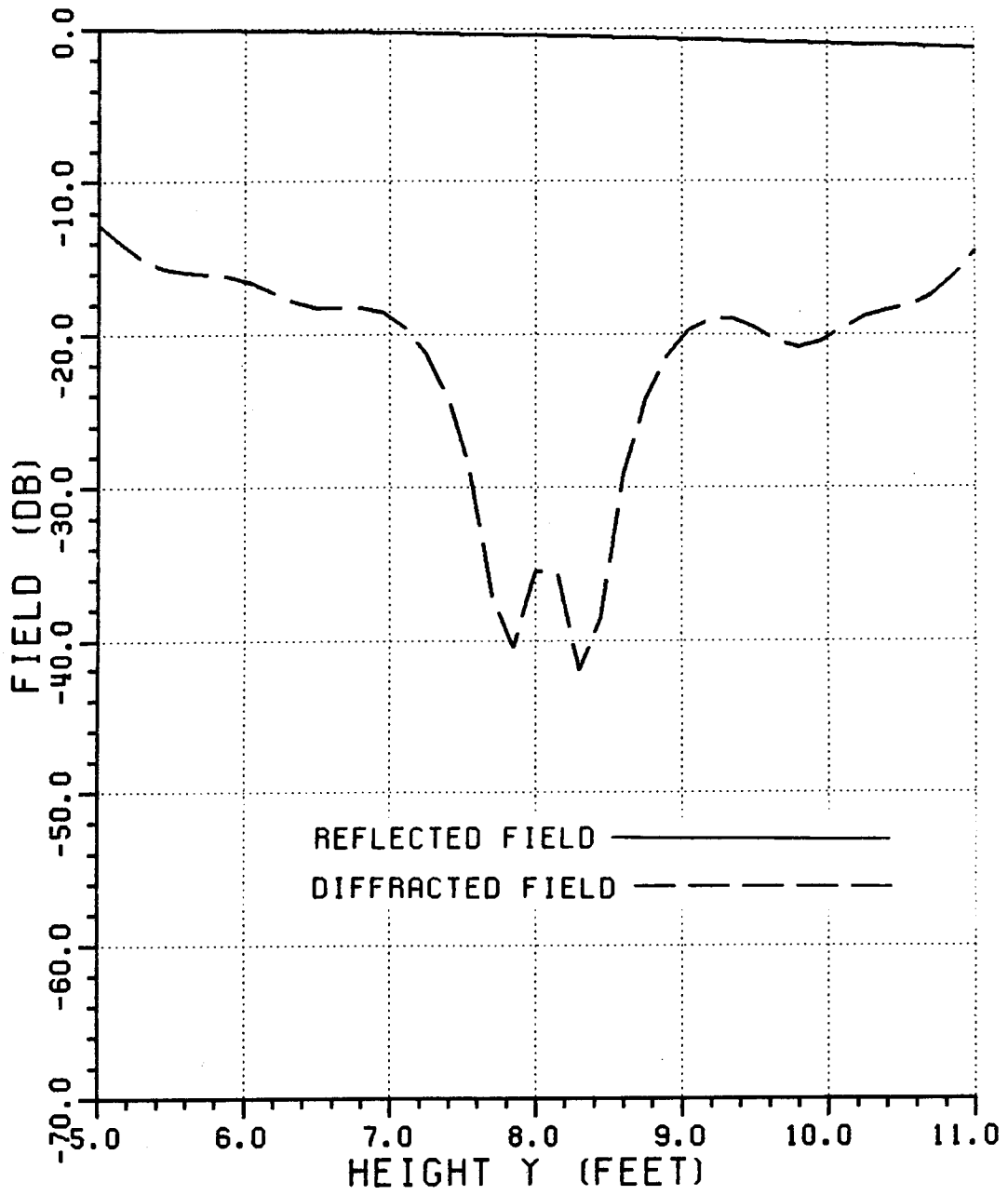
Figure 86: Normalized magnitude of the reflected and diffracted fields from S3.1 (3 GHz). First order end point contributions subtracted.

160
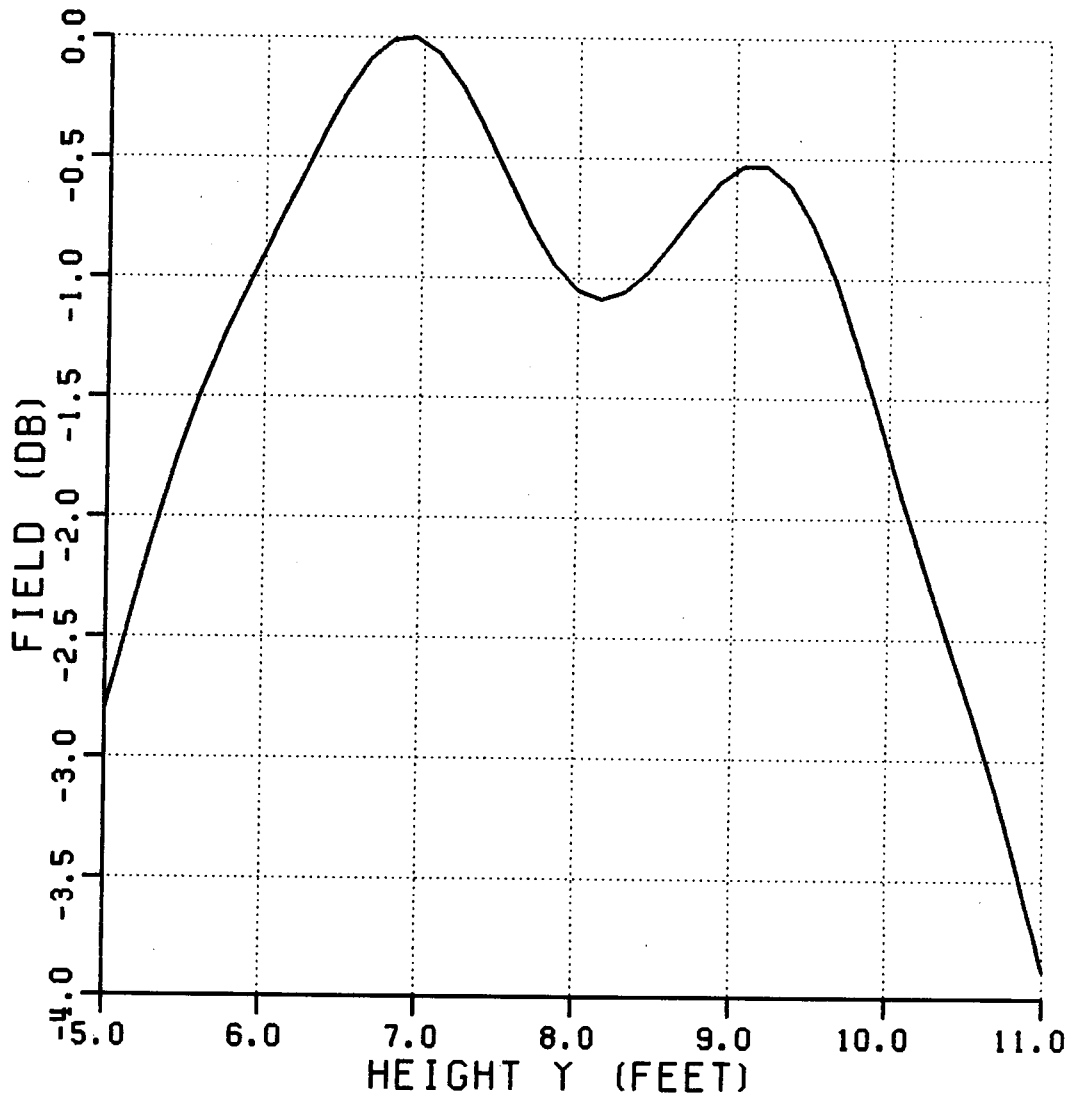
Figure 87: Normalized magnitude of the total field from S3.1 (3 GHz). First and second order end point contributions subtracted.

161
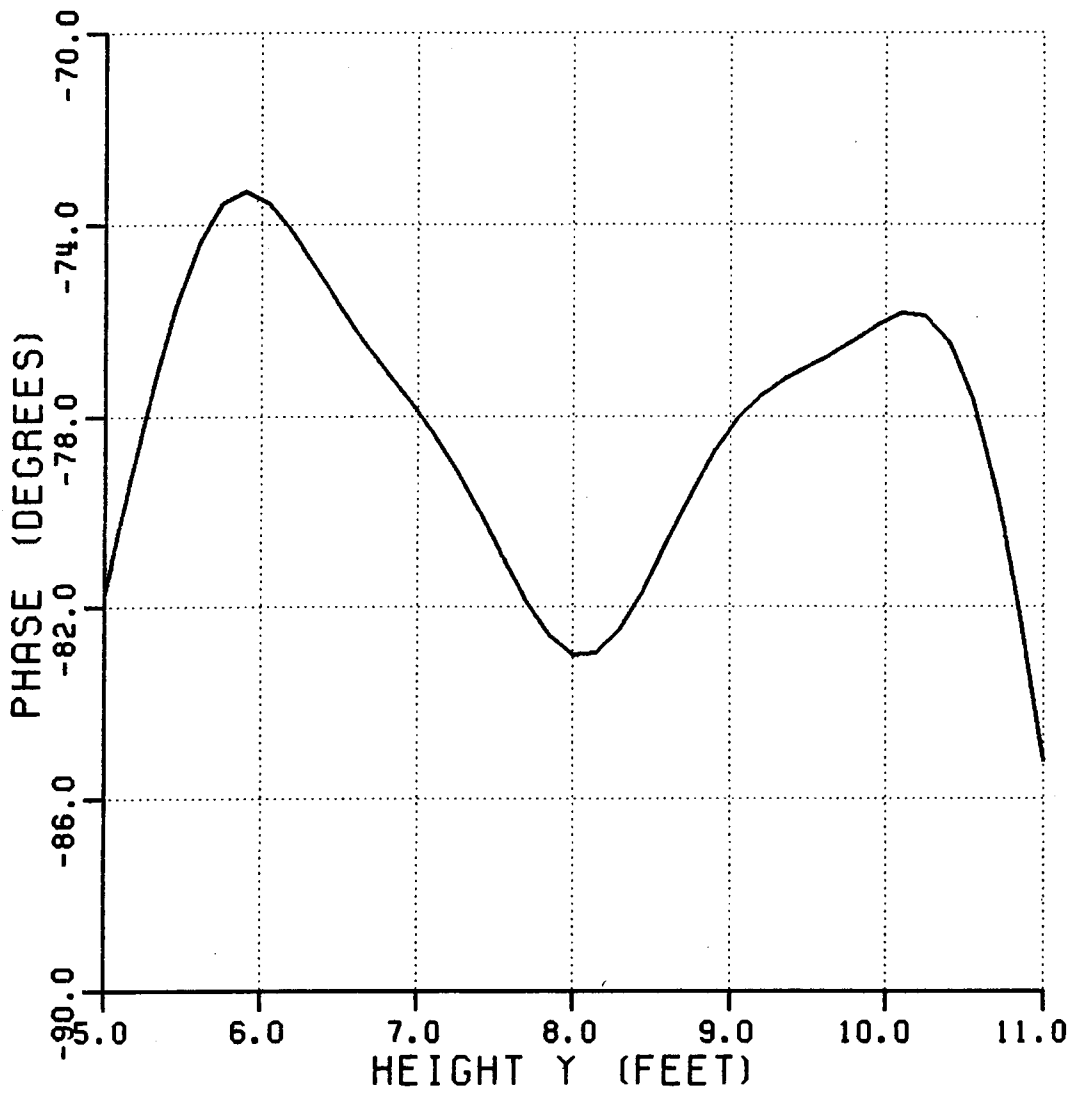
Figure 88: Phase of the total field from S3.1 (3 GHz). First and second order end point contributions subtracted.

162
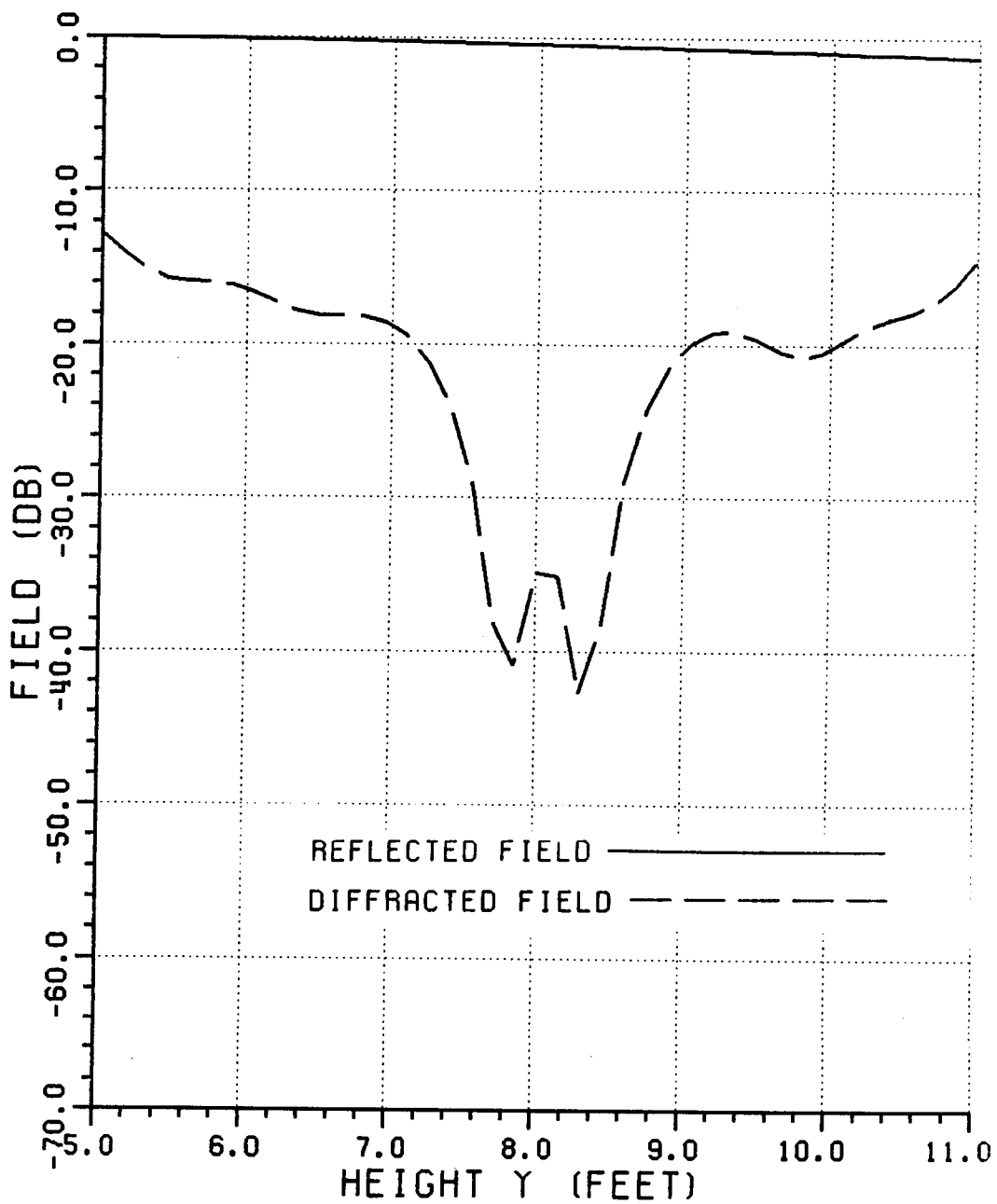
Figure 89: Normalized magnitude of the reflected and diffracted fields from S3.1 (3 GHz). First and second order end point contributions subtracted.

163
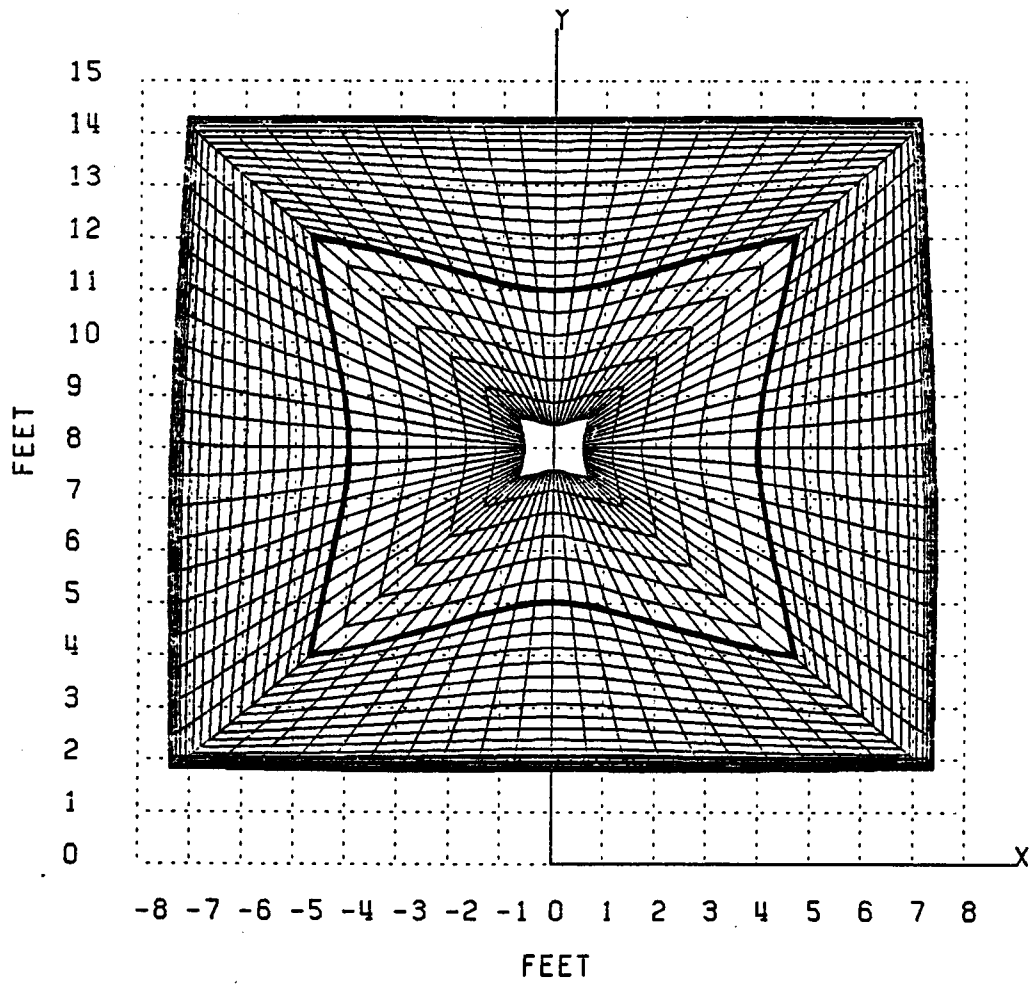
Figure 90: Three-dimensional parabolic reflector with cosine blended rolled edges (S3.2)(Front view).

164
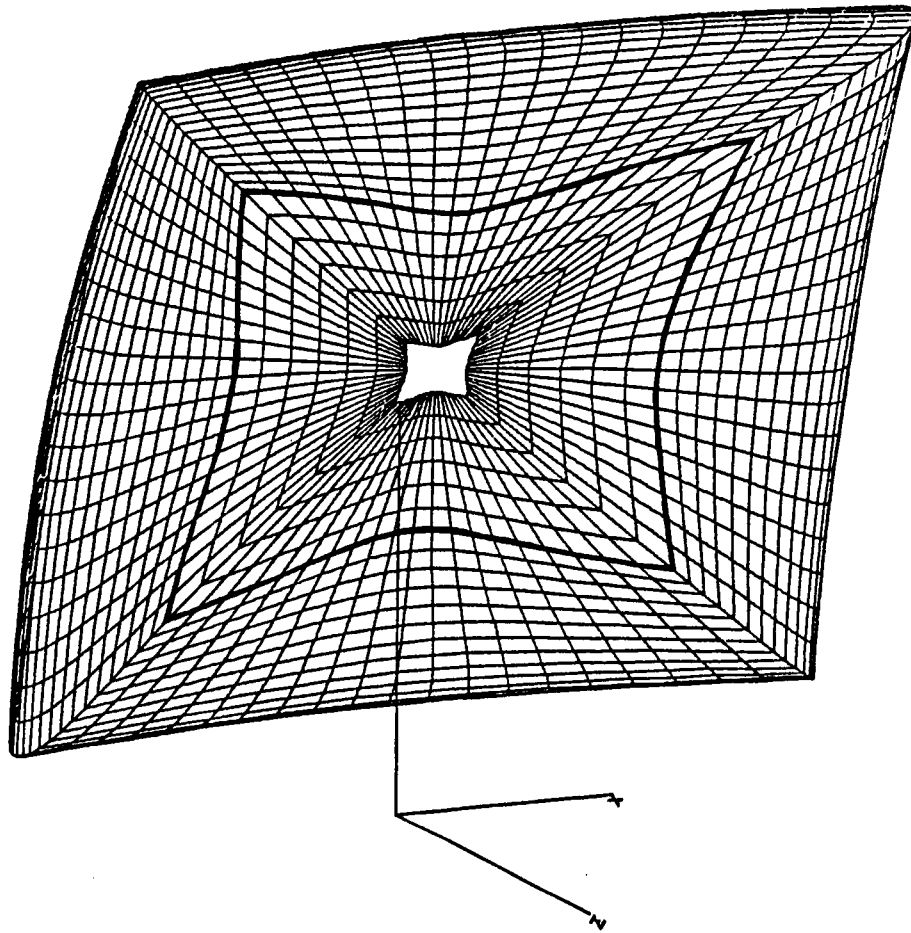
Figure 91: Three-dimensional parabolic reflector with cosine blended rolled edges (S3.2) (View angle: $\theta = 30^o, \phi = 150^o$).

165
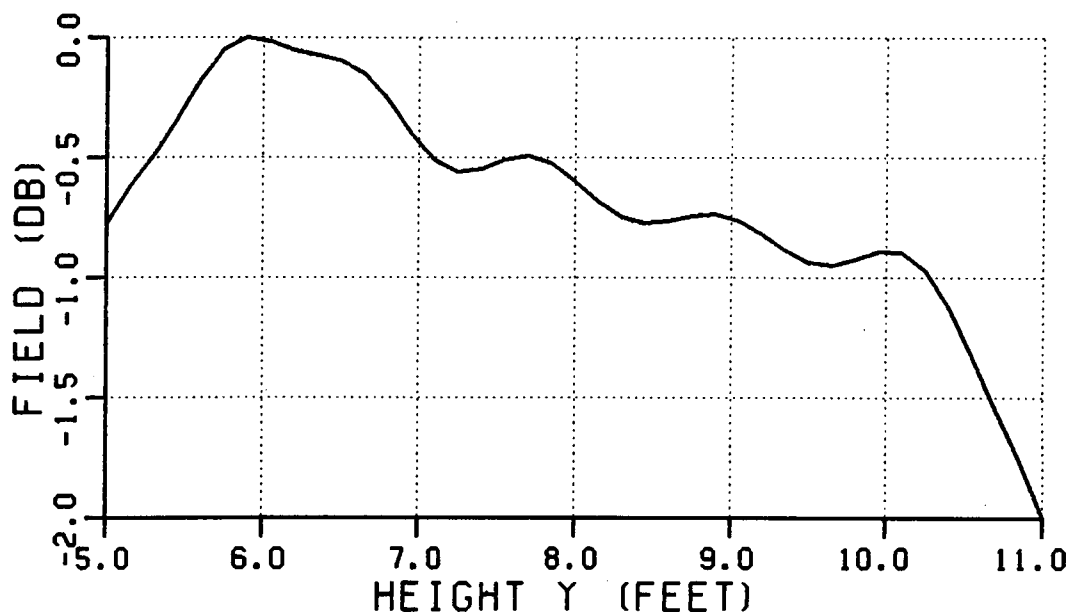
Figure 92: Normalized magnitude of the total field from S3.2 (3 GHz). No end point contributions subtracted.

patterns for the three-dimensional (S3.2) and two-dimensional (S2.2) reflectors. Comparison of Figures 94 and 100 indicate that the false contributions from the end point terms do have an effect on the pattern in this case. This is also evident from the high frequency ripple visible in Figures 92 and 93. Since the diffractions from the junction between the paraboloid and blended rolled edge are smaller than in the case with the pure elliptic rolled edge, the false scattering from the incident shadow boundaries are more significant. The subtraction of the contributions from the end point terms reduce the high frequency ripple errors as shown in Figures 98 and 99.

4.5 Main reflector design with Gregorian subreflector

Consider now S3.3, a parabolic reflector with $f_c = 7.25'$, cosine squared blended rolled surface terminations and a concave edge contour. S3.3 corresponds

166
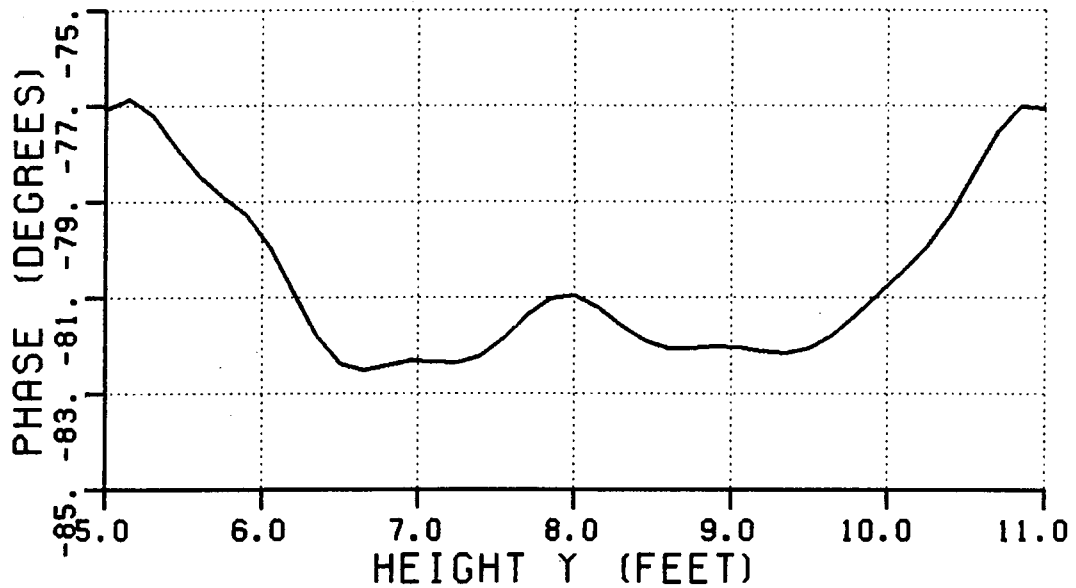
Figure 93: Phase of the total field from S3.2 (3 GHz). No end point contributions subtracted.

to S2.3 in that it is the yz-plane cut of S3.3. The surface characteristics of S3.3 are given in Table 16, and the surface is shown in Figures 101–103 for three viewing angles. The target zone is considered to be $8'$ wide and $6'$ high, with the center of the target zone $8.5'$ above the axis of symmetry of the paraboloid, and situated $20'$ away from the main origin along the z-axis. The main reflector is illuminated by a Gregorian subreflector system. For the purpose of this discussion it is assumed that the main reflector is illuminated by the GO field reflected from the subreflector only. Fields diffracted from the subreflector are thus deliberately ignored. The purpose of this deletion is to investigate the performance of the main reflector when illuminated by an ideal subreflector system. It is further assumed that there is no direct illumination from the feed or diffraction from the subreflector into the target zone. This is done in order to simulate the dual chamber configuration described in Chapter V.

167
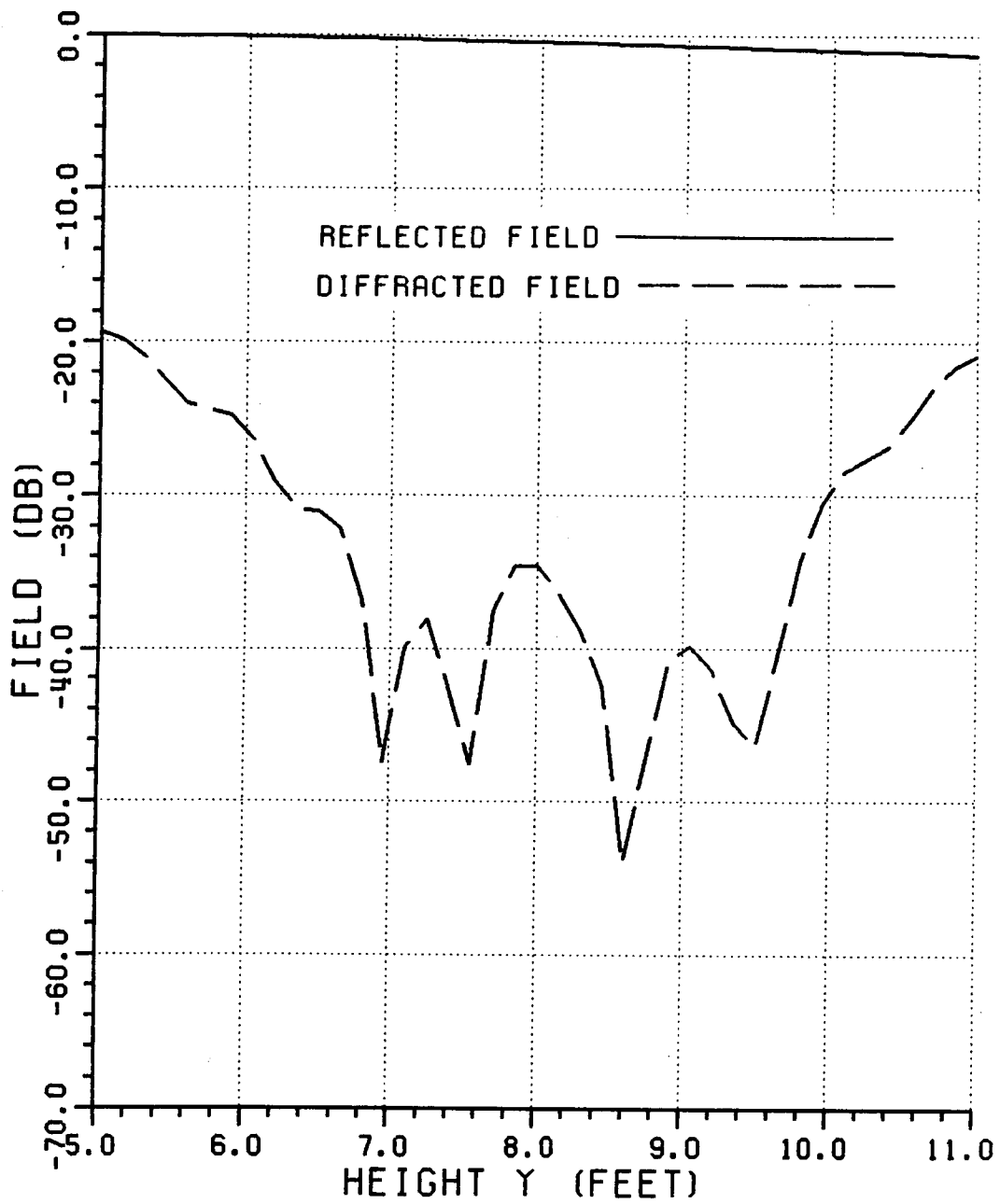
Figure 94: Normalized magnitude of the reflected and diffracted fields from S3.2 (3 GHz). No end point contributions subtracted.
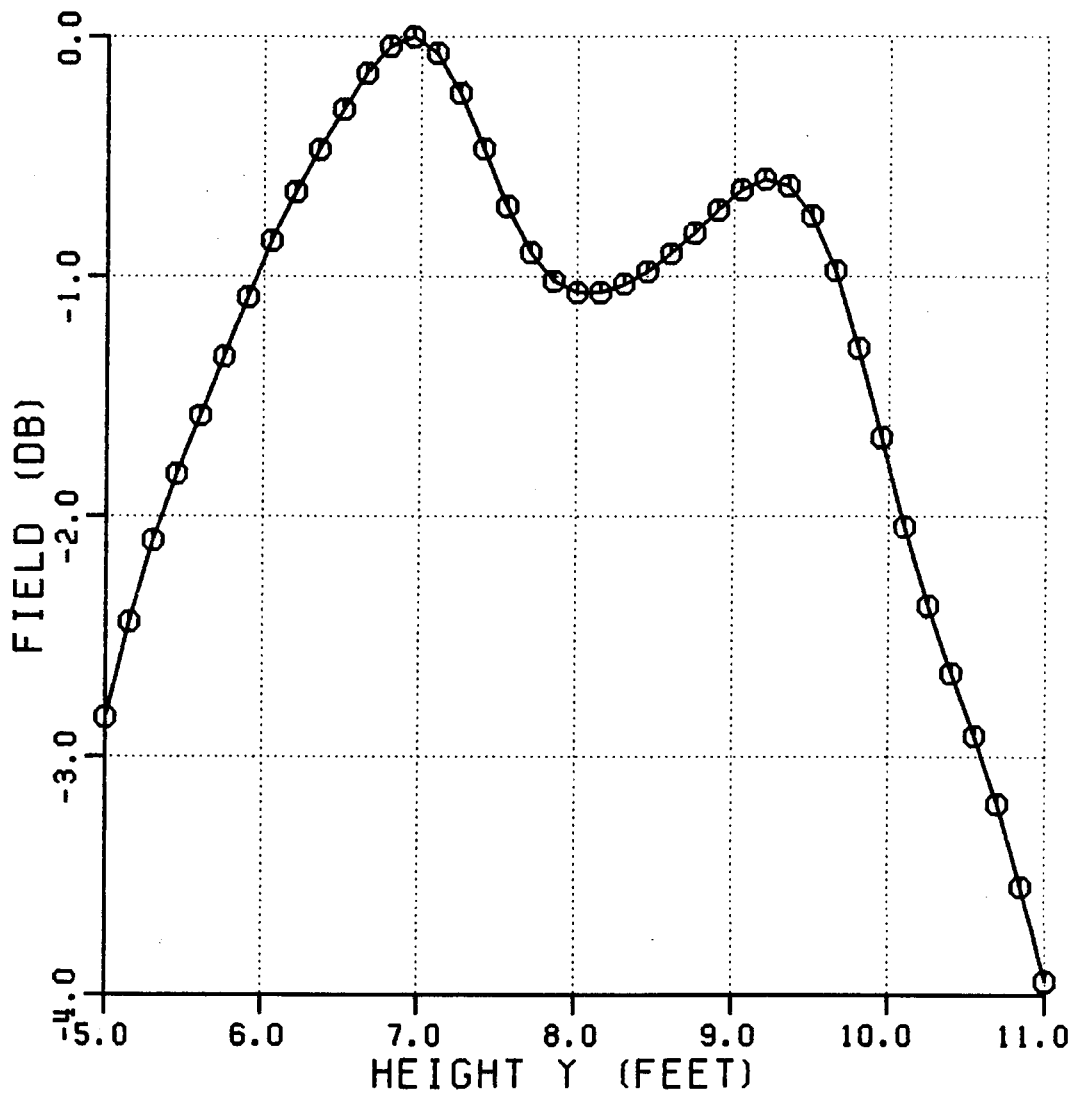
168
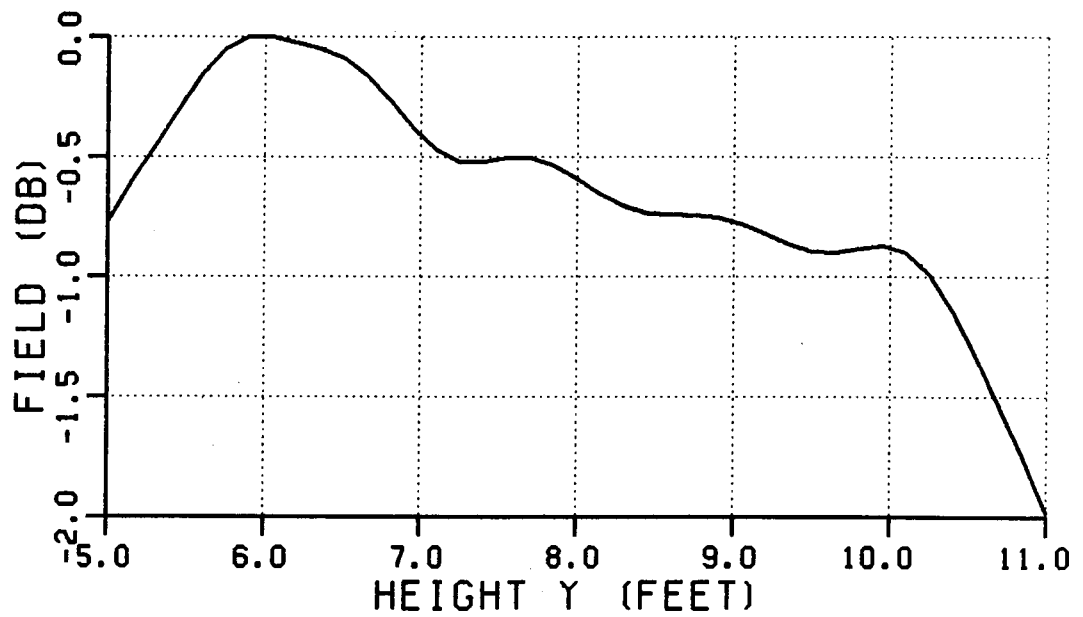
Figure 95: Normalized magnitude of the total field from S3.2 (3 GHz). First order end point contributions subtracted.
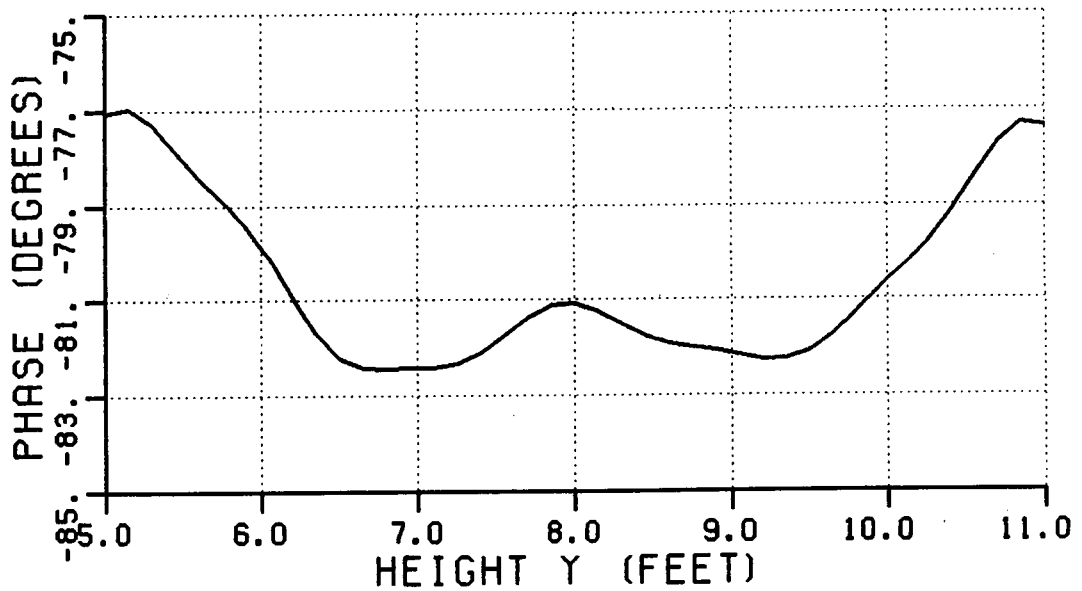
Figure 96: Phase the of total field from S3.2 (3 GHz). First order end point contributions subtracted.

169
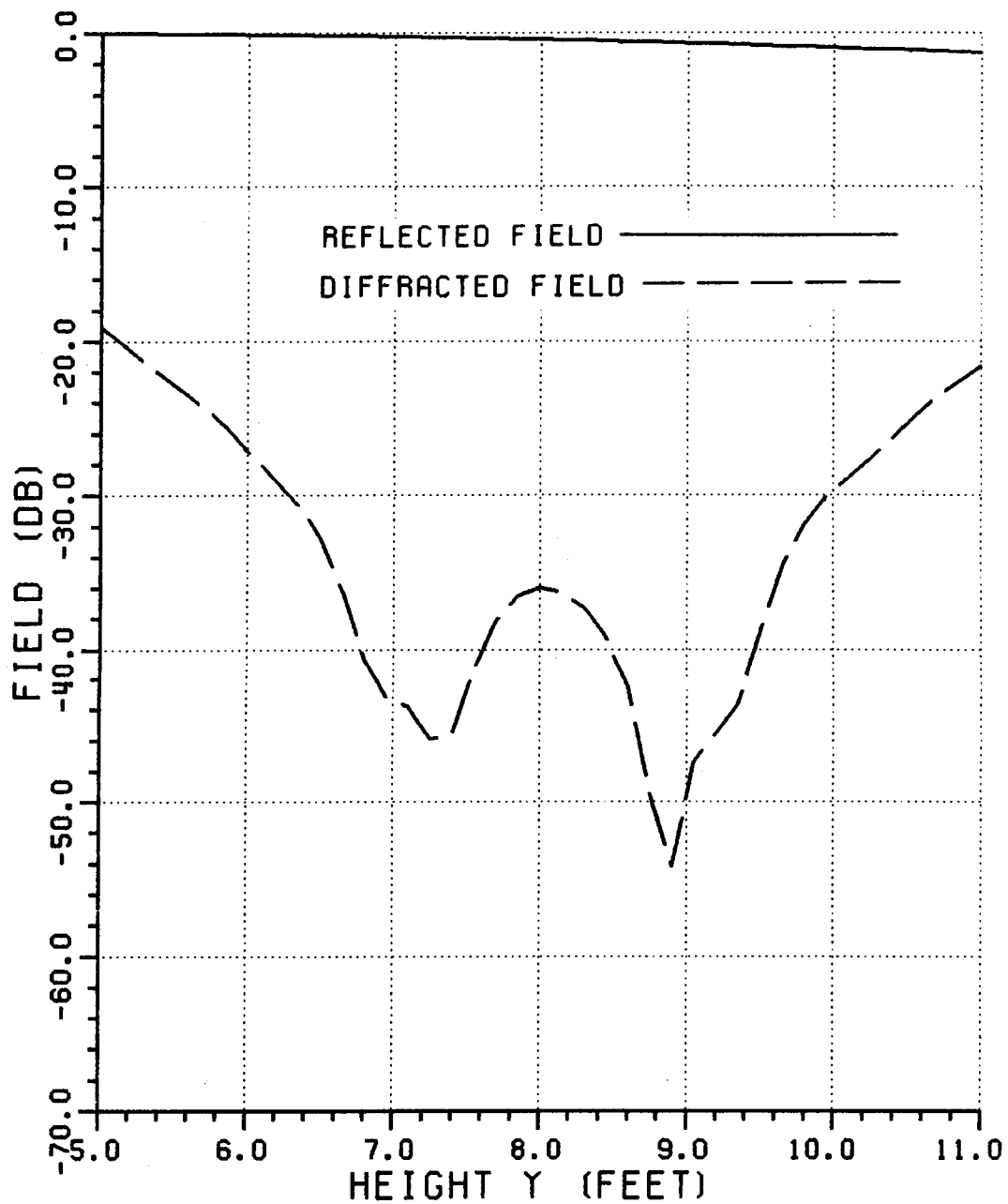
Figure 97: Normalized magnitude of the reflected and diffracted fields from S3.2 (3 GHz). First order end point contributions subtracted.

170
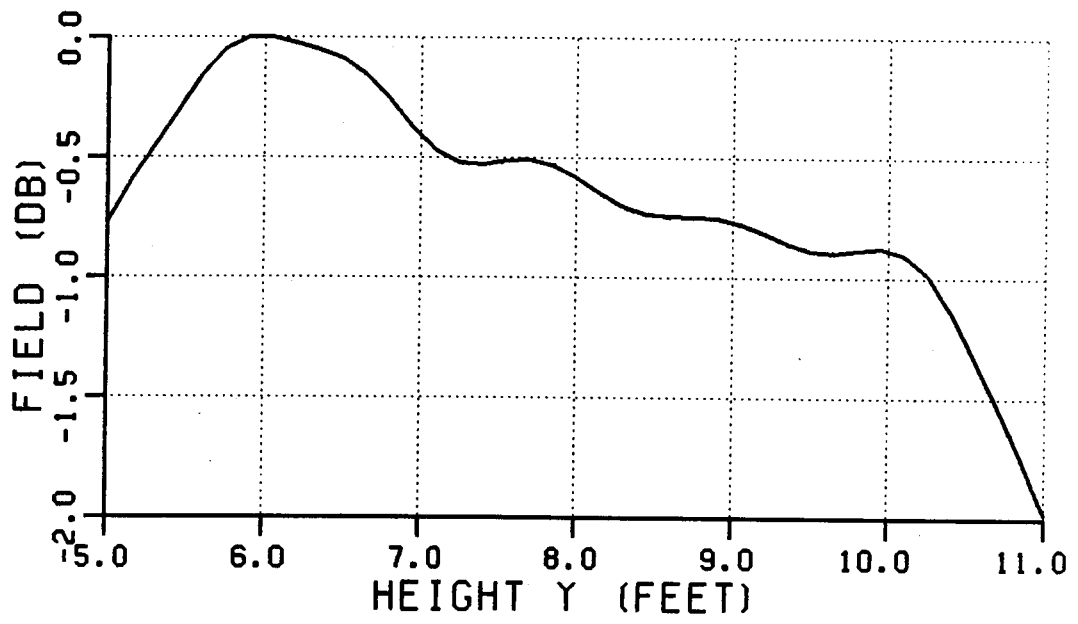
Figure 98: Normalized magnitude of the total field from S3.2 (3 GHz). First and second order end point contributions subtracted.
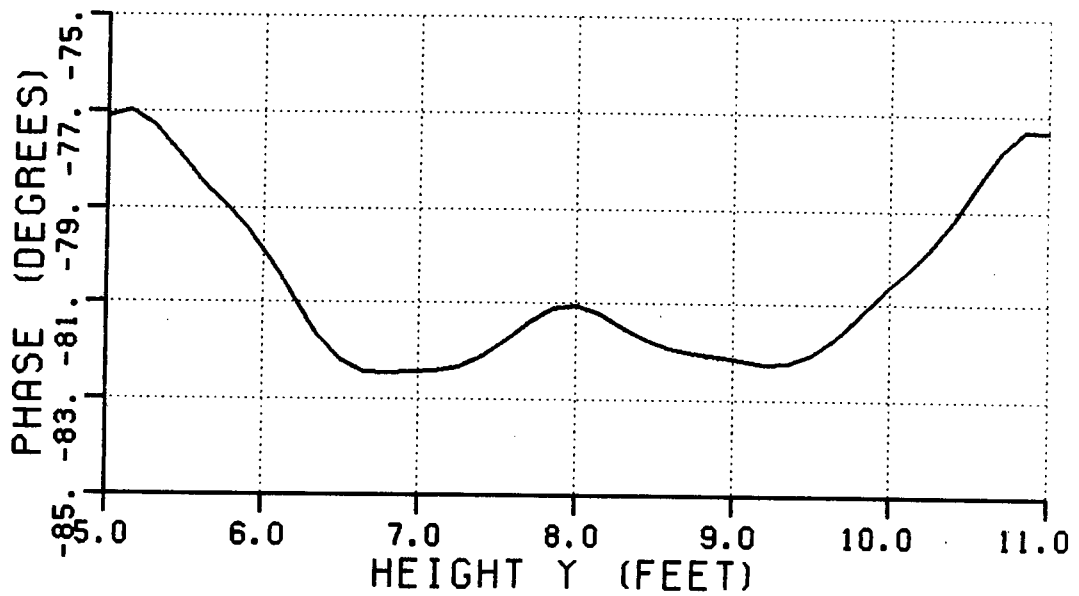
Figure 99: Phase of the total field from S3.2 (3 GHz). First and second order end point contributions subtracted.
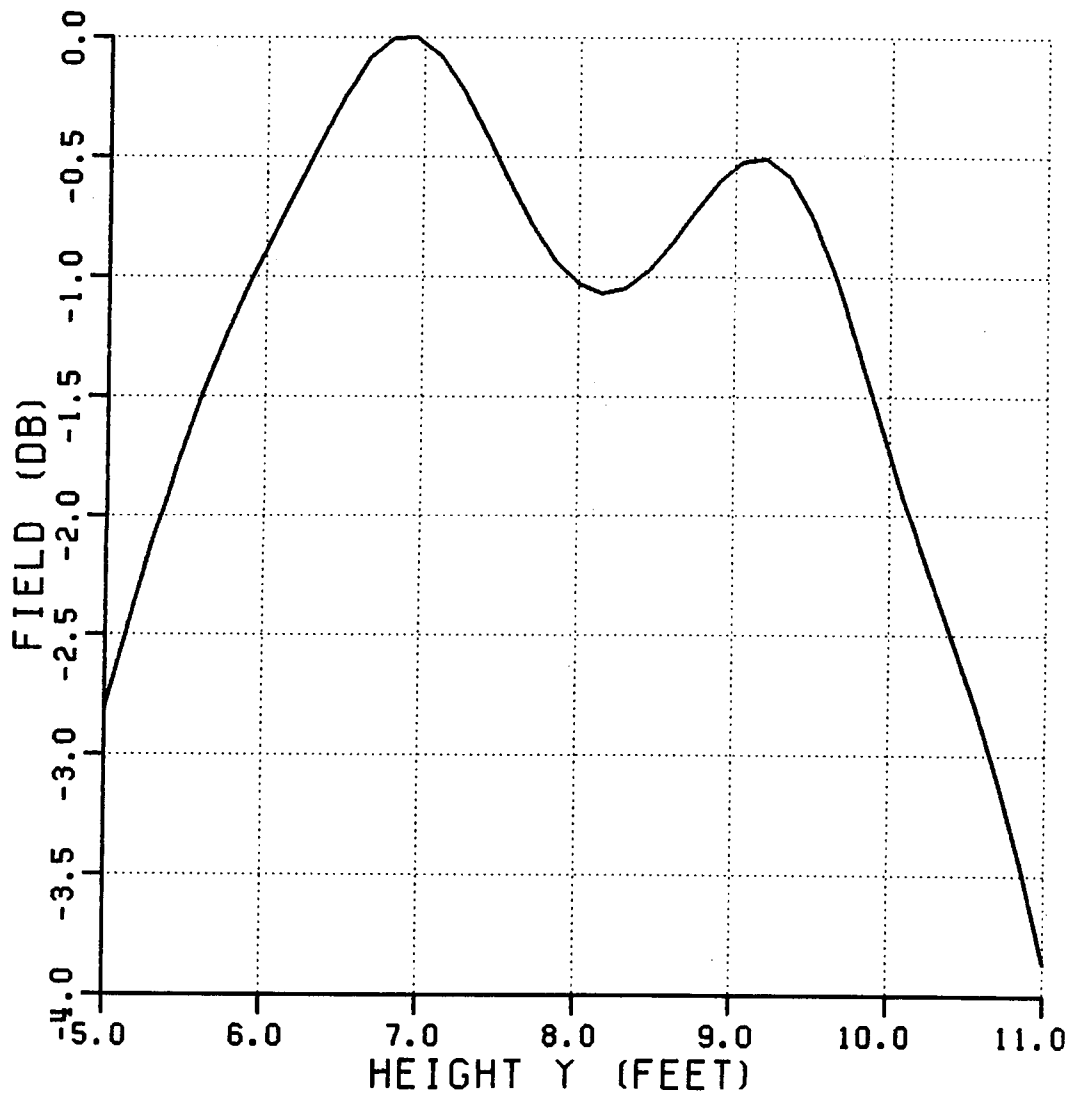
171
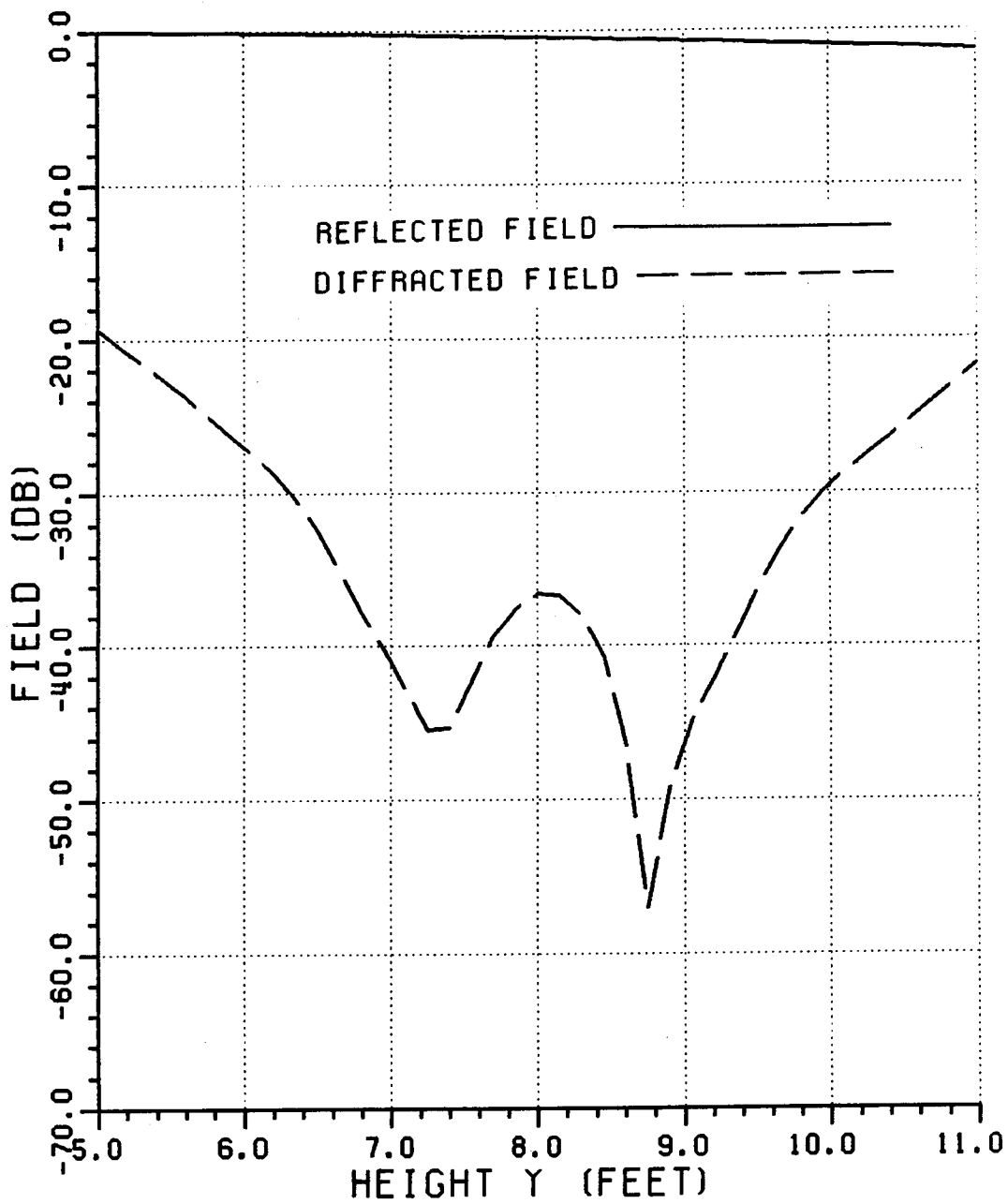
Figure 100: Normalized magnitude of the reflected and diffracted fields from S3.2 (3 GHz). First and second order end point contributions subtracted.

172

Table 16: Surface characteristics for S3.3.

Cosine Squared Blending	
f_c	$7.25'$
a_e	$3.4'$
b_e	$0.75'$
x_m	$6.8'$
γ_m	120°
y_{bot}	$5.5'$
y_{avg}	$8.5'$
y_{top}	$11.5'$
x_{left}	$-4'$
x_{right}	$4'$
a_{sr}	$5.25'$
b_{sr}	$4.308'$
f_{sr}	$3'$
β	5.5^o
α	20°
z_{pat}	$20'$
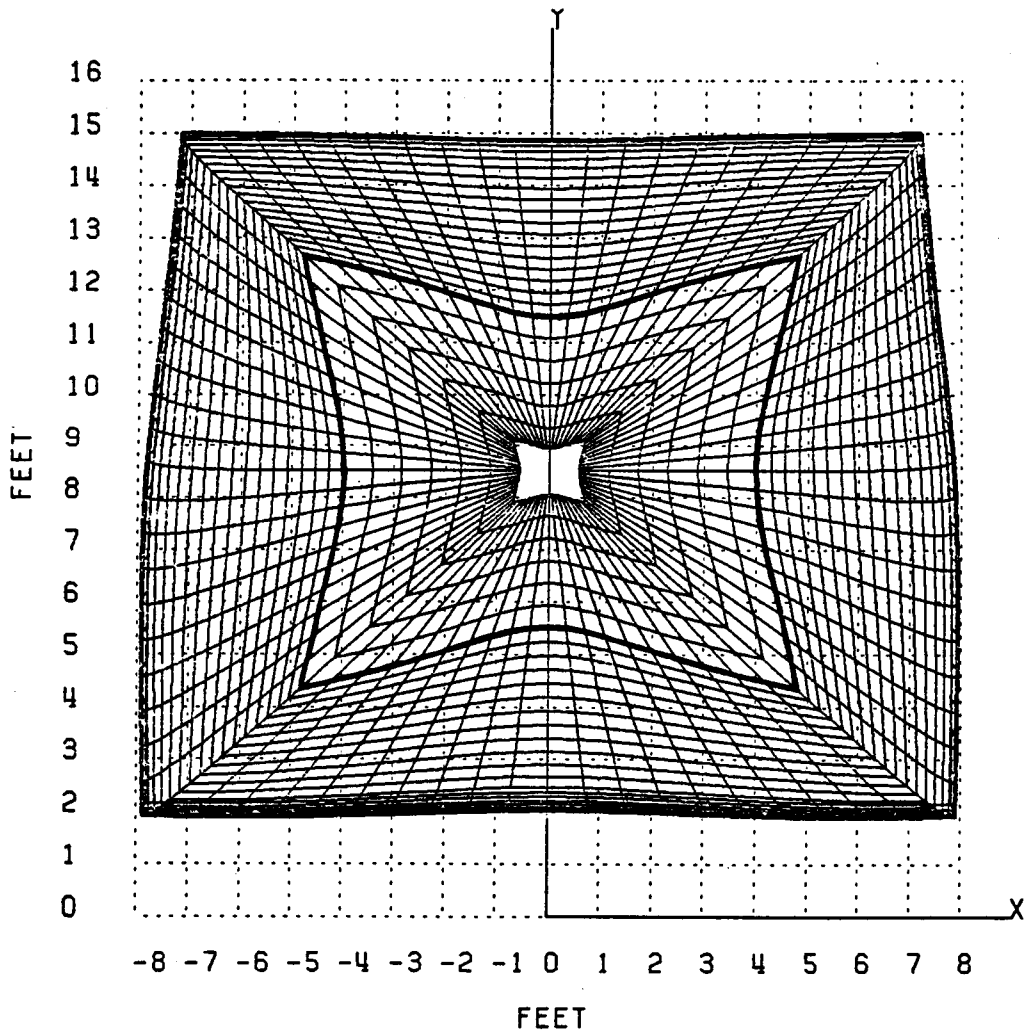
Figure 101: Three-dimensional parabolic reflector with cosine squared blended rolled edges (S3.3)(Front view).

174
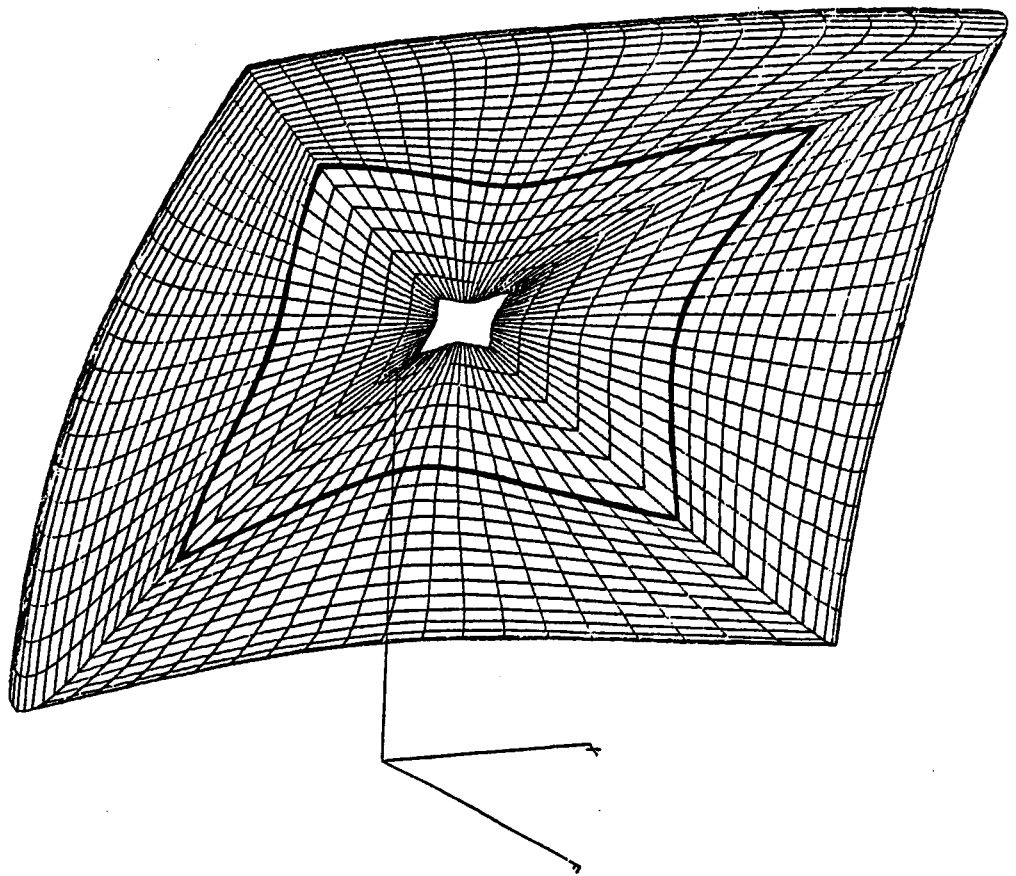
Figure 102: Three-dimensional parabolic reflector with cosine squared blended rolled edges (S3.3)(View angle: $\theta = 30^o, \phi = 150^o$).

175
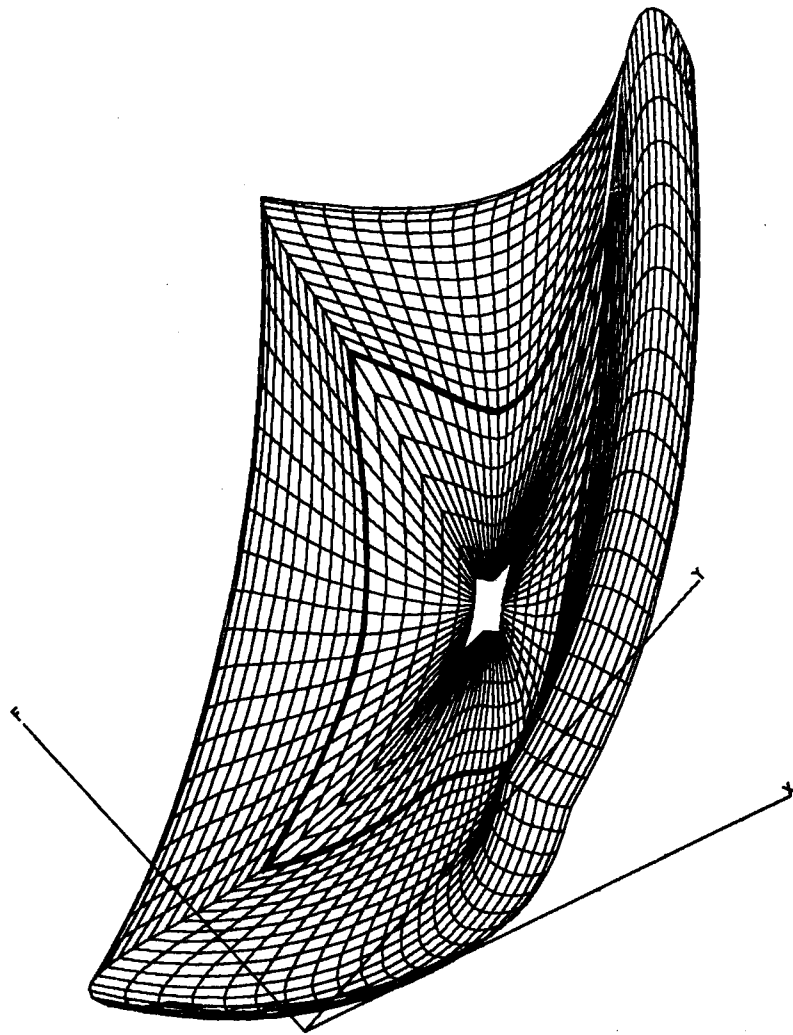
Figure 103: Three-dimensional parabolic reflector with cosine squared blended rolled edges (S3.3)(View angle: $\theta = 80^o, \phi = -30^o$).

176

C-3

The Gregorian subreflector is a spheroid which is defined in terms of its own $x_s y_s z_s$-coordinate system. The origin of this coordinate system is located at the center of the spheroid. The subreflector has a semi-major axis of length (a_{sr}) in the direction of its axis of symmetry $(z_s$-axis$)$, and semi-minor axes of length (b_{sr}) in the directions of the x_s-axis and y_s-axis, such that $a_{sr} > b_{sr}$. The focal points of the subreflector are located at a distance (f_{sr}) from the origin along the positive z_s-axis $(\mathbf{f}_{sr}^+)$ and negative z_s-axis $(\mathbf{f}_{sr}^-)$ respectively, as shown in Figure 104. The focal length is given by

$$f_{sr} = \sqrt{a_{sr}^2 - b_{sr}^2} \; . \tag{4.50}$$

The main axis of the subreflector is tilted at an angle (β) with respect to the axis of symmetry of the paraboloid, and the subreflector is placed such that $\mathbf{f}_{sr}^+$ coincides with the focal point of the parabolic main reflector (f_c). The primary feed is placed at the other focal point $(\mathbf{f}_{sr}^-)$. All rays originating from the point source at $\mathbf{f}_{sr}^-$ and reflected from the subreflector will pass through $\mathbf{f}_{sr}^+$, so that $\mathbf{f}_{sr}^+$ is thus a caustic for all rays reflected from the subreflector.

The primary feed antenna is assumed to be a Huygens source and is orientated such that its axis of symmetry $(z_f$-axis$)$ is tilted at an angle (α) relative to the main axis of the subreflector as shown in Figure 104. Chapter V is devoted towards the design of a dual chamber compact range configuration, where the assumptions that the diffracted fields from the subreflector and spillover from the feed can be ignored are justified, and the purpose of the tilt angles is explained. The transformation from main coordinates to subreflector coordinates is given by

$$\begin{pmatrix} x_s \\ y_s \\ z_s \end{pmatrix} = \begin{pmatrix} 1 & 0 & 0 \\ 0 & \cos\beta & -\sin\beta \\ 0 & \sin\beta & \cos\beta \end{pmatrix} \begin{pmatrix} x \\ y \\ z \end{pmatrix} + \begin{pmatrix} 0 \\ y_{e1} \\ z_{e1} \end{pmatrix} \tag{4.51}$$
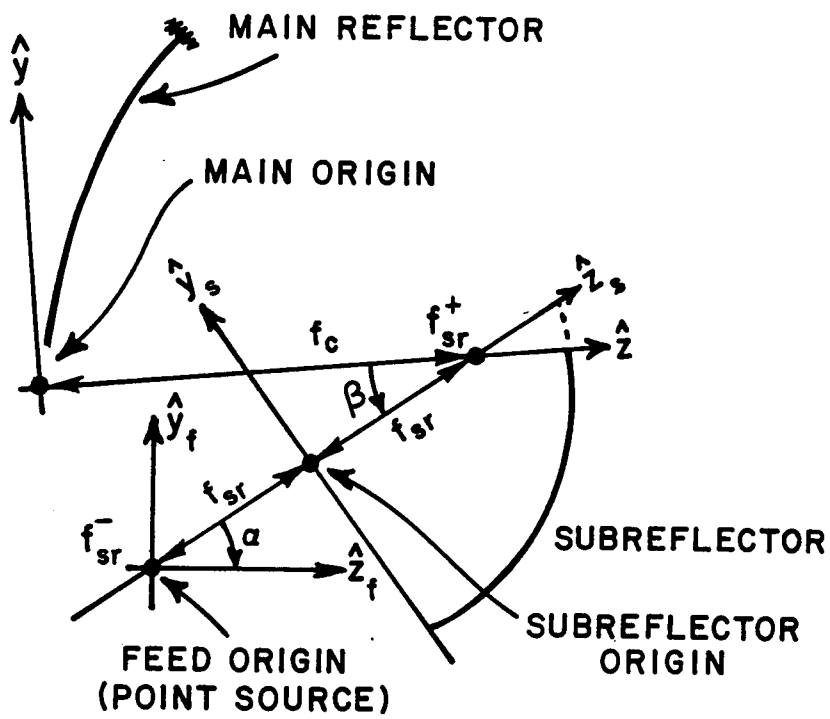
Figure 104: Subreflector coordinate system.

178

where

$$y_{e1} = r_o \sin \beta_e \qquad (4.52)$$

$$z_{e1} = -r_o \cos \beta_e \qquad (4.53)$$

$$\beta_e = \beta_{ec} + \beta \qquad (4.54)$$

$$\beta_{ec} = \begin{cases} \arctan(-y_1/z_1) & \text{if } z_1 \neq 0 \\ 90^o & \text{if } z_1 = 0 \end{cases} \qquad (4.55)$$

$$r_0 = \sqrt{y_1^2 + z_1^2} \qquad (4.56)$$

$$y_1 = -f_{sr} \sin \beta \text{ , and} \qquad (4.57)$$

$$z_1 = f_c - f_{sr} \cos \beta \text{ .} \qquad (4.58)$$

The geometry associated with this transformation is illustrated in Figure 105.

In order to calculate the scattered fields from the main reflector, it is necessary to determine the incident field at any point $\mathbf{P}_p(x_p, y_p, z_p)$ on the main reflector. The first step is to convert $\mathbf{P}_p$ to subreflector coordinates $[\mathbf{P}_p(x_{ps}, y_{ps}, z_{ps})]$ using the transformation given in Equation (4.51). The next step is to find the point $(\mathbf{P}_r)$ on the subreflector that is the reflection point for the ray intercepting $\mathbf{P}_p$.

Let the subreflector be described in its own coordinate system by the following parametric equation (see Appendix A):

$$\mathbf{r}_{spheroid}(u, v) = (b_{sr} \sin u \cos v)\hat{\mathbf{x}}_s + (b_{sr} \sin u \sin v)\hat{\mathbf{y}}_s + (a_{sr} \cos u)\hat{\mathbf{z}}_s \qquad (4.59)$$

so that $\mathbf{P}_r$ can be expressed as $\mathbf{P}_r(u_r, v_r)$. Since the spheroid is a body of revolution around the z_s-axis, the parameter (v) is the spherical angle (ϕ), while (u) corresponds to the spherical angle (θ).

Let $\mathbf{r}$ be the vector from $\mathbf{P}_p$ to $\mathbf{f}_{sr}^+$, such that

$$\mathbf{r} = \mathbf{f}_{sr}^+ - \mathbf{P}_p = r_{ms}\hat{\mathbf{r}} \qquad (4.60)$$

179
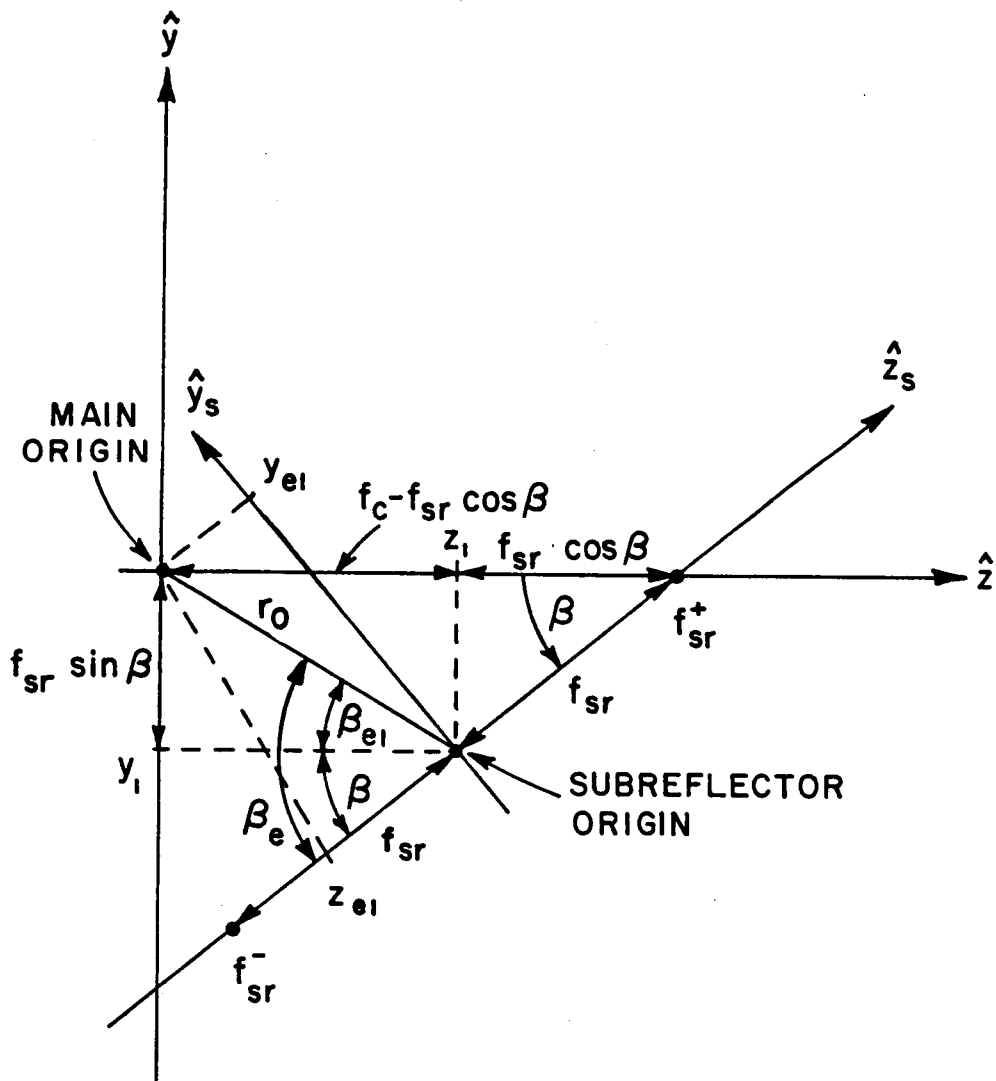
Figure 105: Main reflector to subreflector coordinate transformation.

180

and

$$\hat{\mathbf{r}} = r_1\hat{\mathbf{x}}_s + r_2\hat{\mathbf{y}}_s + r_3\hat{\mathbf{z}}_s \qquad (4.61)$$

where

$$r_1 \;=\; \frac{-x_{ps}}{r_{ms}} \qquad (4.62)$$

$$r_2 \;=\; \frac{-y_{ps}}{r_{ms}} \qquad (4.63)$$

$$r_3 \;=\; \frac{f_{sr} - z_{ps}}{r_{ms}} \;,\; \text{and} \qquad (4.64)$$

$$r_{ms} \;=\; \sqrt{x_{ps}^2 + y_{ps}^2 + (f_{sr} - z_{ps})^2} \;. \qquad (4.65)$$

It then follows that

$$\mathbf{P}_r \;=\; \mathbf{f}_{sr}^+ + l\hat{\mathbf{r}} \;,\; \text{and} \qquad (4.66)$$

$$l \;=\; |\mathbf{P}_r - \mathbf{f}_{sr}^+| \qquad (4.67)$$

where

$$b_{sr}\cos v_r \sin u_r \;=\; lr_1 \qquad (4.68)$$

$$b_{sr}\sin v_r \sin u_r \;=\; lr_2 \;,\; \text{and} \qquad (4.69)$$

$$a_{sr}\cos u_r \;=\; f_{sr} + lr_3 \qquad (4.70)$$

so that

$$v_r \;=\; \begin{cases} \arctan(r_2/r_1) & \text{if } r_1 \neq 0 \\ 90^o & \text{if } r_1 = 0, r_2 > 0 \\ -90^o & \text{if } r_1 = 0, r_2 < 0 \;,\; \text{and} \end{cases} \qquad (4.71)$$

$$l \;=\; \begin{cases} (b_{sr}/r_2)\sin v_r \sin u_r & \text{if } r_2 \neq 0 \\ (b_{sr}/r_1)\cos v_r \sin u_r & \text{if } r_2 = 0 \;. \end{cases} \qquad (4.72)$$

The unit vector ($\hat{\mathbf{r}}$) and distance (l) are shown in Figure 106. The reflection caustic distance (ρ_c) has the same magnitude as l, but has a negative sign. Note

181
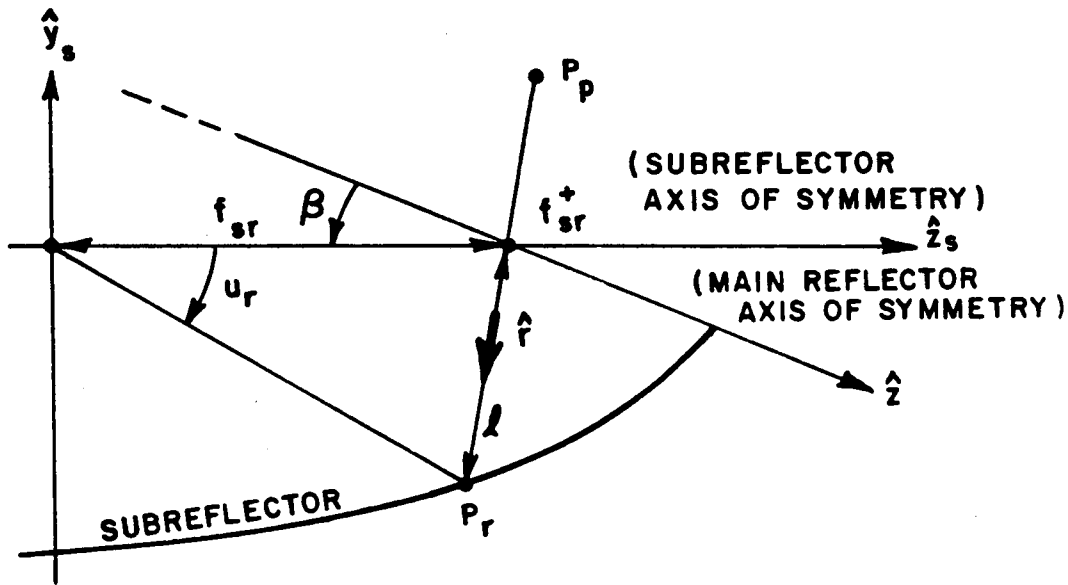
Figure 106: Reflection point on the subreflector.

that $u_r = 180^o$ in the case where $r_1 = r_2 = 0$ since $u_r = 0$ is not permitted by the dual chamber configuration described in Chapter V. From the above it is thus seen that

$$a_{sr} \cos u_r = f_{sr} + d_{sr} \sin u_r \qquad (4.73)$$

where

$$d_{sr} = \begin{cases} b_{sr}(r_3/r_2) \sin v_r & \text{if } r_2 \neq 0 \\ b_{sr}(r_3/r_1) \cos v_r & \text{if } r_2 = 0 \end{cases} \qquad (4.74)$$

and

$$\sin u_r = \frac{a_{sr}\sqrt{d_{sr}^2 + b_{sr}^2} - f_{sr}d_{sr}}{a_{sr}^2 + d_{sr}^2} . \qquad (4.75)$$

The positive sign of the square root is chosen since $\sin u_r > 0$. The reflection point on the subreflector is thus given by

$$\mathbf{P}_r = (b_{sr} \sin u_r \cos v_r)\hat{\mathbf{x}}_s + (b_{sr} \sin u_r \sin v_r)\hat{\mathbf{y}}_s + (a_{sr} \cos u_r)\hat{\mathbf{z}}_s \qquad (4.76)$$

182

or

$$\mathbf{P}_r = x_{rs}\hat{\mathbf{x}}_s + y_{rs}\hat{\mathbf{y}}_s + z_{rs}\hat{\mathbf{z}}_s \qquad (4.77)$$

where v_r is given in Equation (4.71) and u_r in Equation (4.75).

Once $\mathbf{P}_r$ is known, the field incident on $\mathbf{P}_r$ from the Huygens source at $\mathbf{f}_{sr}^-$ can be calculated. To do this, it is necessary to convert $\mathbf{P}_r$ to feed coordinates by using the following transformation:

$$\begin{pmatrix} x_f \\ y_f \\ z_f \end{pmatrix} = \begin{pmatrix} 1 & 0 & 0 \\ 0 & \cos\alpha & \sin\alpha \\ 0 & -\sin\alpha & \cos\alpha \end{pmatrix} \begin{pmatrix} x_s \\ y_s \\ z_s \end{pmatrix} + \begin{pmatrix} 0 \\ f_{sr}\sin\alpha \\ f_{sr}\cos\alpha \end{pmatrix} . \qquad (4.78)$$

Let the distance (R_f) from the Huygens source to $\mathbf{P}_r$ be given by

$$R_f = \sqrt{x_f^2 + y_f^2 + z_f^2} \qquad (4.79)$$

so that

$$\theta_f = \arccos(z_f/R_f) \text{ , and} \qquad (4.80)$$

$$\phi_f = \begin{cases} \arctan(y_f/x_f) & x_f \neq 0 \\ 90^o & x_f = 0 \text{ and } y_f > 0 \text{ , or } \theta_f = 0^o \\ -90^o & x_f = 0 \text{ and } y_f < 0 \text{ .} \end{cases} \qquad (4.81)$$

Note that the choice of $\phi_f = 90^o$ when $\theta_f = 0^o$ indicates that the Huygens source is y_f-polarized. The field incident on $\mathbf{P}_r$ can now be expressed in feed coordinates as

$$\mathbf{E}_R^i(R_f, \theta_f, \phi_f) = \mathbf{e}^i(\theta_f, \phi_f) \frac{e^{-jkR_f}}{R_f} \qquad (4.82)$$

where $\mathbf{e}^i$ is given in Equation (4.40). Using the transformation given in Equation (4.78), $\mathbf{e}^i$ can be expressed in subreflector coordinates as

$$\mathbf{e}^i(\theta_f, \phi_f) = [F_\theta(\theta_f, \phi_f) \cos\theta_f \cos\phi_f - F_\phi(\theta_f, \phi_f) \sin\phi_f]\hat{\mathbf{x}}_s$$

$$+[F_\theta(\theta_f, \phi_f)(\cos\theta_f \sin\phi_f \cos\alpha + \sin\theta_f \sin\alpha) +$$

$$F_\phi(\theta_f, \phi_f) \cos\phi_f \cos\alpha]\hat{\mathbf{y}}_s$$

$$+[F_\theta(\theta_f, \phi_f)(\cos\theta_f \sin\phi_f \sin\alpha - \sin\theta_f \cos\alpha) +$$

$$F_\phi(\theta_f, \phi_f) \cos\phi_f \sin\alpha]\hat{\mathbf{z}}_s \ . \tag{4.83}$$

The incident field at $\mathbf{P}_p$ on the main reflector is then given by

$$\mathbf{E}^r(\mathbf{P}_p) = [-\mathbf{E}_R^i + 2(\hat{\mathbf{n}} \cdot \mathbf{E}_R^i)\hat{\mathbf{n}}] \ A \ e^{-jks} \tag{4.84}$$

where $\hat{\mathbf{n}}$ is the unit vector normal to the subreflector surface at $\mathbf{P}_r$ (see Appendix A), and

$$s = |\ \mathbf{P}_p - \mathbf{P}_r\ | \tag{4.85}$$

or

$$s = \sqrt{(x_{ps} - x_{rs})^2 + (y_{ps} - y_{rs})^2 + (z_{ps} - z_{rs})^2} \ . \tag{4.86}$$

Since $s > l$, one finds that the spread factor (A) is given by

$$A = \begin{cases} l/(l-s) & \text{in three dimensions , and} \\ e^{j\pi/2}\sqrt{l/(s-l)} & \text{in two dimensions .} \end{cases} \tag{4.87}$$

As the electric field incident at $\mathbf{P}_p$ is now known in subreflector coordinates; ie.,

$$\mathbf{E}^i(\mathbf{P}_p) = E_x\hat{\mathbf{x}}_s + E_y\hat{\mathbf{y}}_s + E_z\hat{\mathbf{z}}_s \tag{4.88}$$

it can be converted to main coordinates by using the following transformation:

$$\begin{pmatrix} \hat{\mathbf{x}}_s \\ \hat{\mathbf{y}}_s \\ \hat{\mathbf{z}}_s \end{pmatrix} = \begin{pmatrix} 1 & 0 & 0 \\ 0 & \cos\beta & -\sin\beta \\ 0 & \sin\beta & \cos\beta \end{pmatrix} \begin{pmatrix} \hat{\mathbf{x}} \\ \hat{\mathbf{y}} \\ \hat{\mathbf{z}} \end{pmatrix} \ . \tag{4.89}$$

This transformation will give the incident electric field on the surface of the main reflector in main coordinates, so that it is in a suitable form for use in the PO

184

integration. Note that the total path length of a ray from the phase center of the Huygens source to the target plane, which is located at a distance (z_{pat}) from the main origin along the z-axis, is constant and equal to $2a_{sr} + f_c + z_{pat}$. The reflected field from the main reflector into the target zone is thus still a plane wave. The scattered fields from S3.3 were calculated along a cut in the yz-plane, located at a distance (z_{pat}) of $20'$ away from the main origin along the z-axis, at 3 GHz using the corrected PO method. The normalized magnitude and phase of the total field together with plots comparing the reflected fields with fields diffracted from the concave junctions are shown in Figures 107–115 for the cases where no end point contributions are subtracted, only first order end point contributions are subtracted and, finally, first and second order end point contributions are subtracted. Comparison of Figures 107–115 with Figures 48–56 indicate the agreement between the patterns for the three-dimensional (S3.3) and two-dimensional (S2.3) reflectors. The high frequency ripple in Figures 107 and 108 and the discrepancy in diffracted fields between Figures 109 and 115 indicate that the contributions from the false scattering centers at the incident shadow boundaries on the blended rolled edges have a significant effect on the pattern. Since the diffraction from the junction between the paraboloid and the rolled edges is small, the contributions from the end points terms are much more pronounced. Comparison of Figure 115 with Figure 56 indicates that the two-dimensional prediction of the diffracted field is much smaller than that obtained by the three-dimensional results. This discrepancy most likely results from an inaccurate subtraction of the end point contributions in the three-dimensional case.

Based on the results obtained from the two-dimensional analysis it was claimed in Section 3.4 that a reflector with blended rolled edges will have a significantly better performance than one with elliptic rolled edges. In this section it has been

185
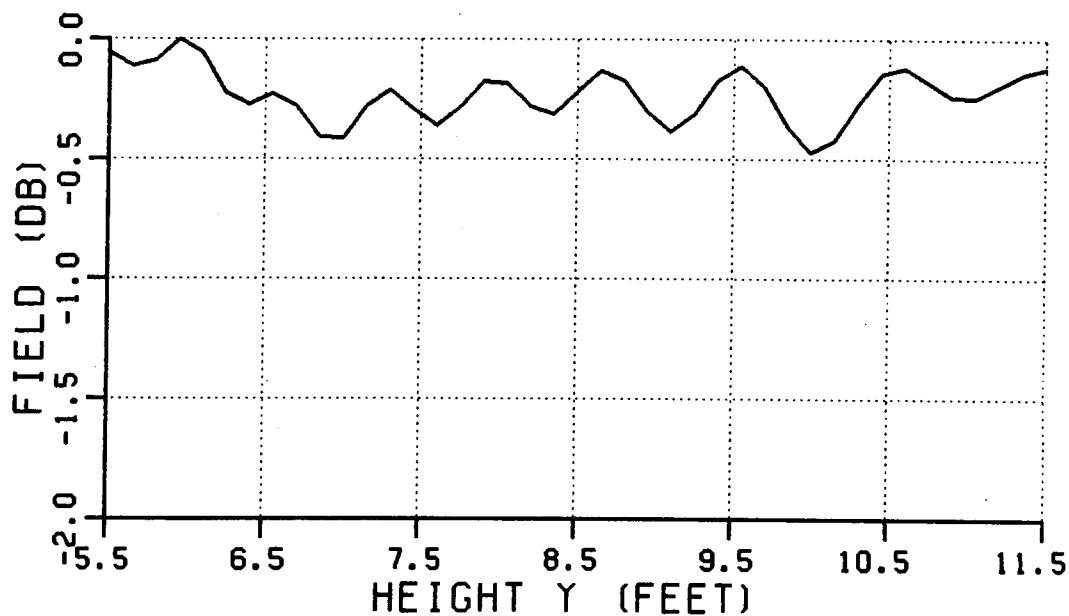
Figure 107: Normalized magnitude of the total field from S3.3 (3 GHz). No end point contributions subtracted.

shown that this claim holds true for three-dimensional reflectors as well. The performance improvement that can be obtained by choosing higher order blending functions as discussed in Sections 3.4.1 and 3.4.2 have now been verified for the three-dimensional case.

4.6 Comparative design example

A final design example, intended as a 1/3 scale model, will now be considered. A reflector with a concave edge contour is compared to one with a convex edge contour. Both reflectors have the same optimized cosine squared blended rolled edges. The reflectors are designated as S3.4 and S3.5 and shown in Figures 116–117, respectively. Note that the yz-profile shown in Figure 118 is the same for both reflectors, so that the dimensions of their target zones in the yz-plane are equal. The x-dimension of the target zone of S3.5 is smaller than that of S3.4 in order

186
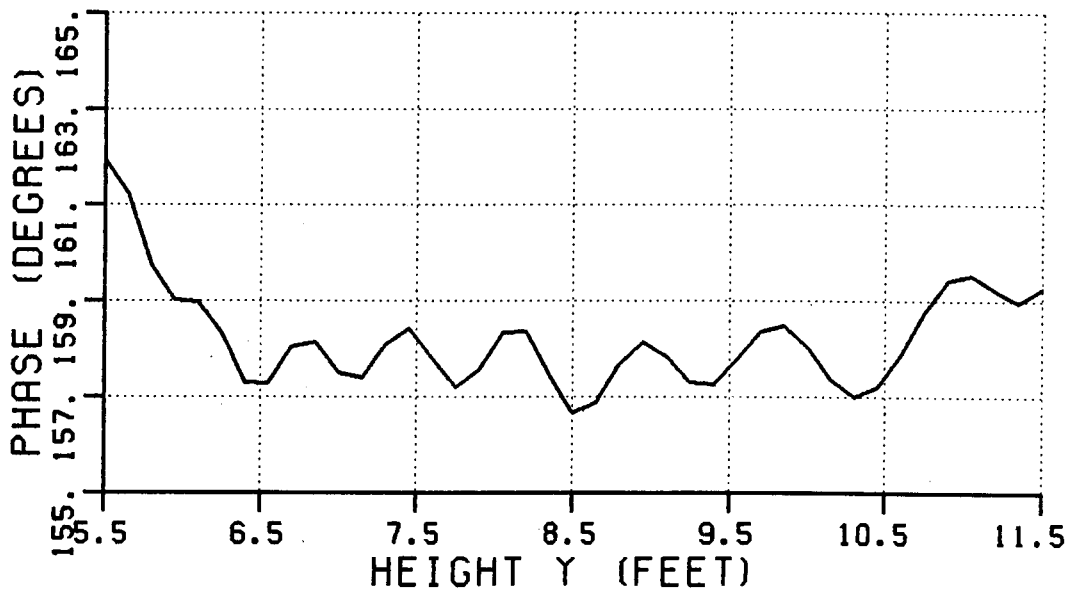
Figure 108: Phase of the total field from S3.3 (3 GHz). No end point contributions subtracted.

to accomodate the circular edge contour. The surface characteristics are given in Table 17.

The reflectors are illuminated by a Huygens source at the focus, tilted at an angle (α) as given in Equation (4.37). Field patterns were calculated at 3 GHz along a cut in the yz-plane, located at a distance (z_{pat}) of 8' away from the main origin along the z-axis. Fifty sample points were taken in the target zone. Figure 119 shows the normalized magnitude of the total field in the target zone; whereas, Figure 120 shows the magnitudes of the normalized reflected and diffracted fields. The phases of the total field in the target zone are shown in Figure 121.

These results clearly indicate that a concave edge contour has superior performance compared to a convex edge contour. The diffraction pattern of S3.5 shows a large lobe in the center of the target zone, which can be attributed to the caustic effect of the convex edge contour. The concave edge contour does not exhibit such

187
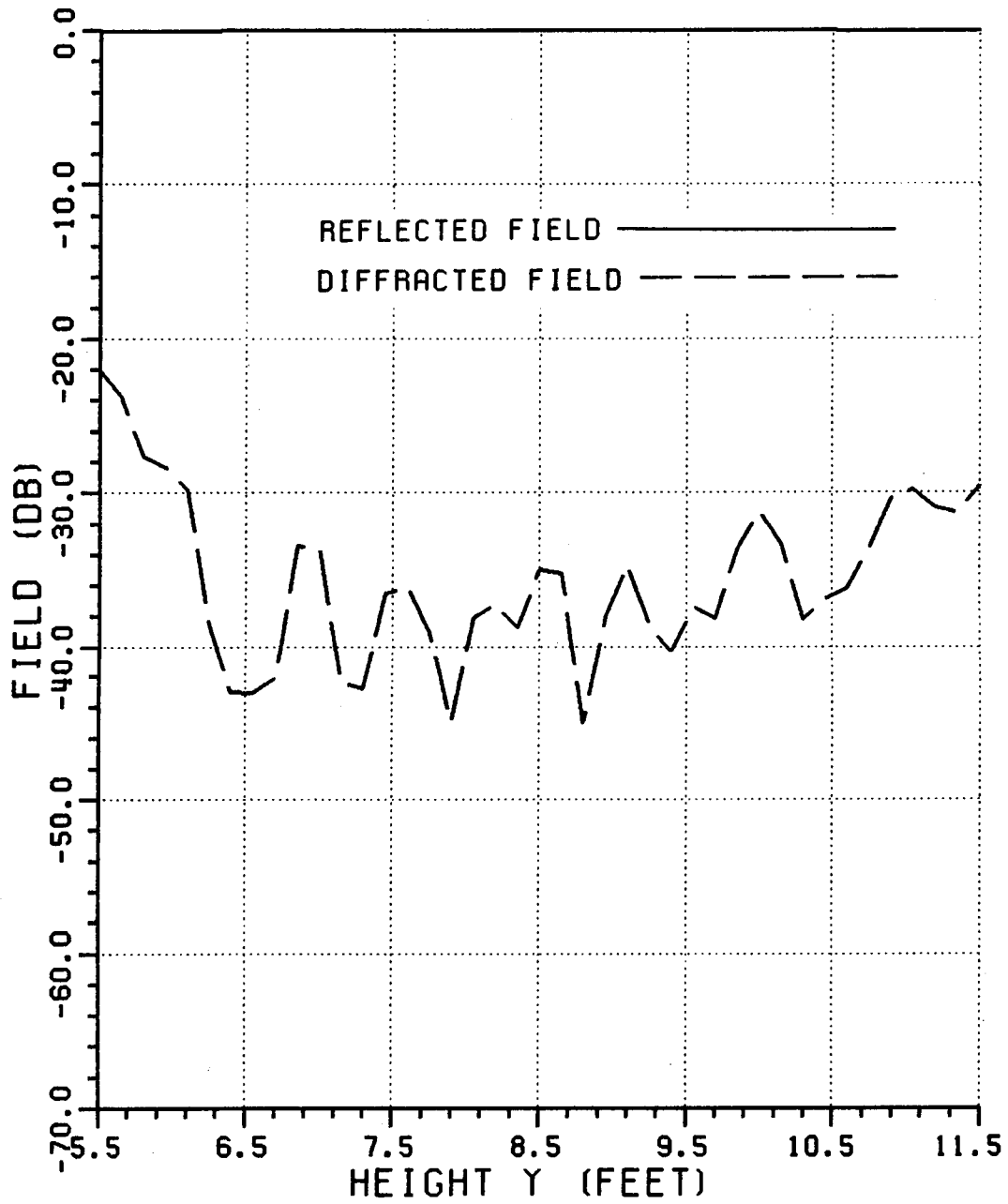
Figure 109: Normalized magnitude of the reflected and diffracted fields from S3.3 (3 GHz). No end point contributions subtracted.

188
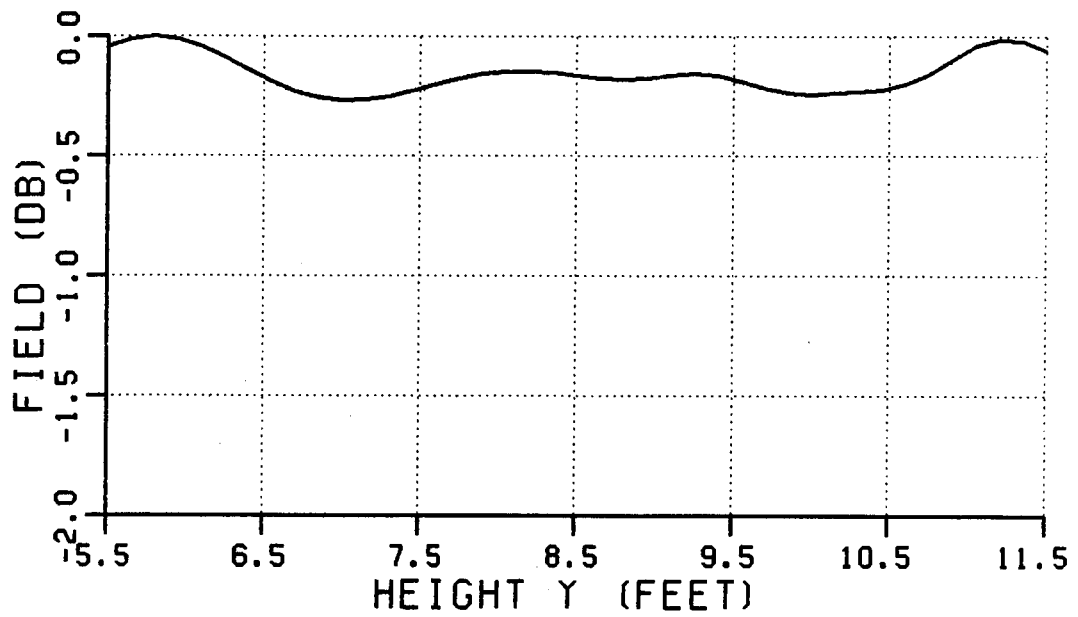
Figure 110: Normalized magnitude of the total field from S3.3 (3 GHz). First order end point contributions subtracted.
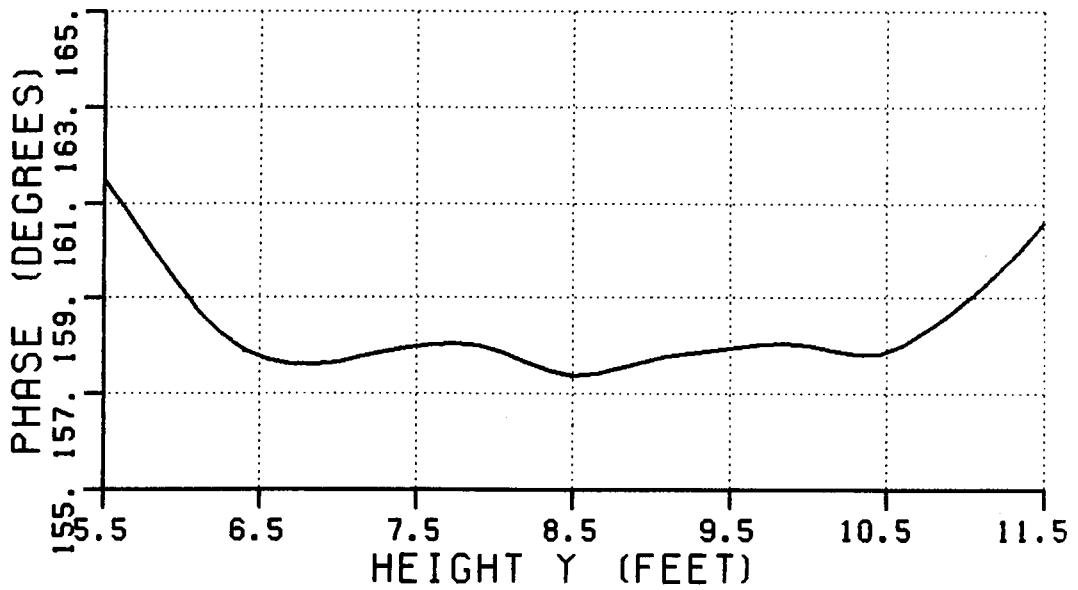
Figure 111: Phase of the total field from S3.3 (3 GHz). First order end point contributions subtracted.

189
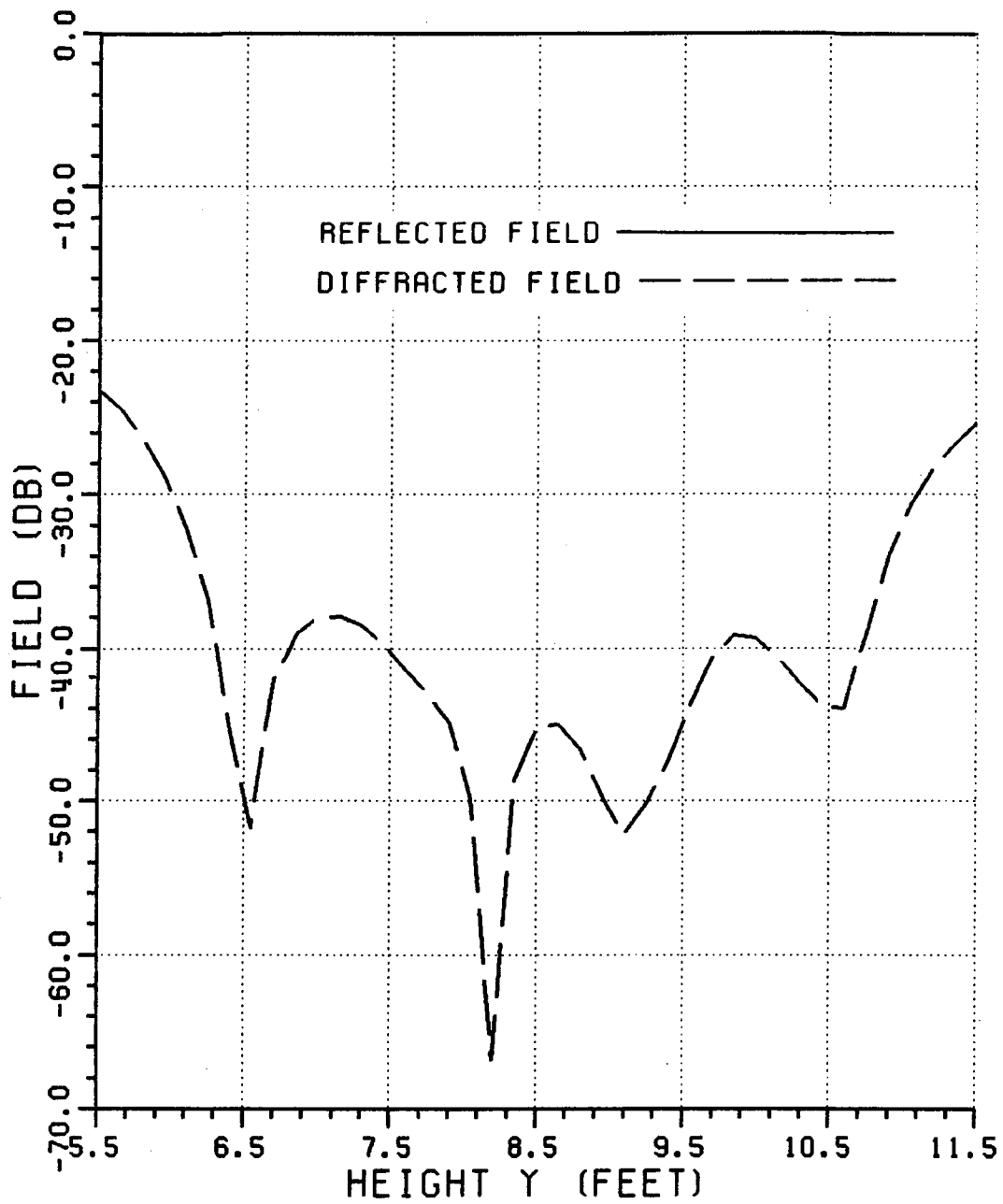
Figure 112: Normalized magnitude of the reflected and diffracted fields from S3.3 (3 GHz). First order end point contributions subtracted.

190
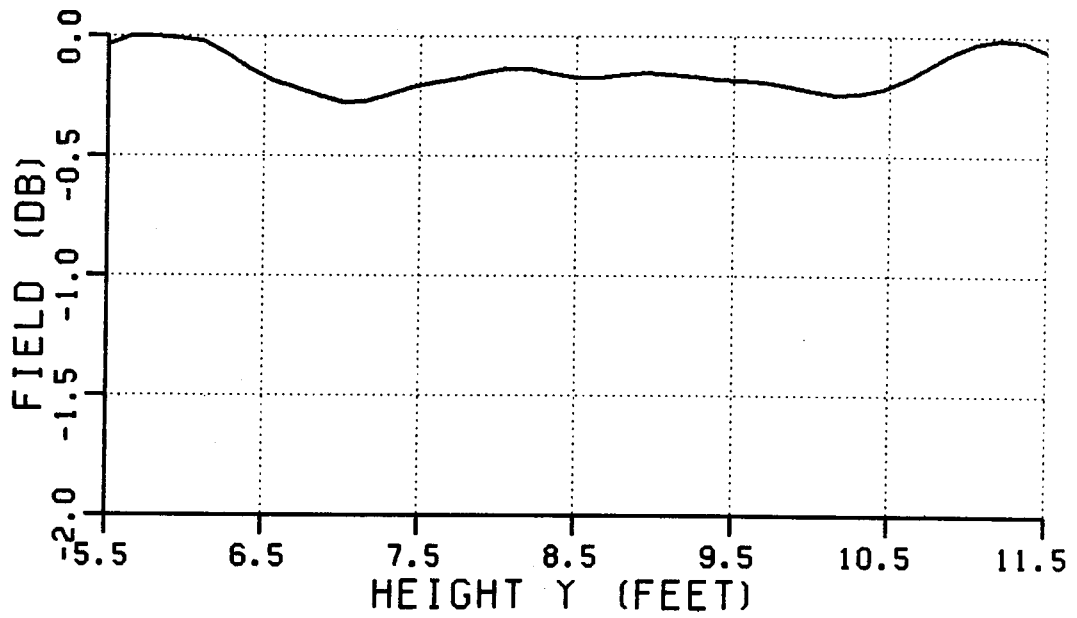
Figure 113: Normalized magnitude of the total field from S3.3 (3 GHz). First and second order end point contributions subtracted.
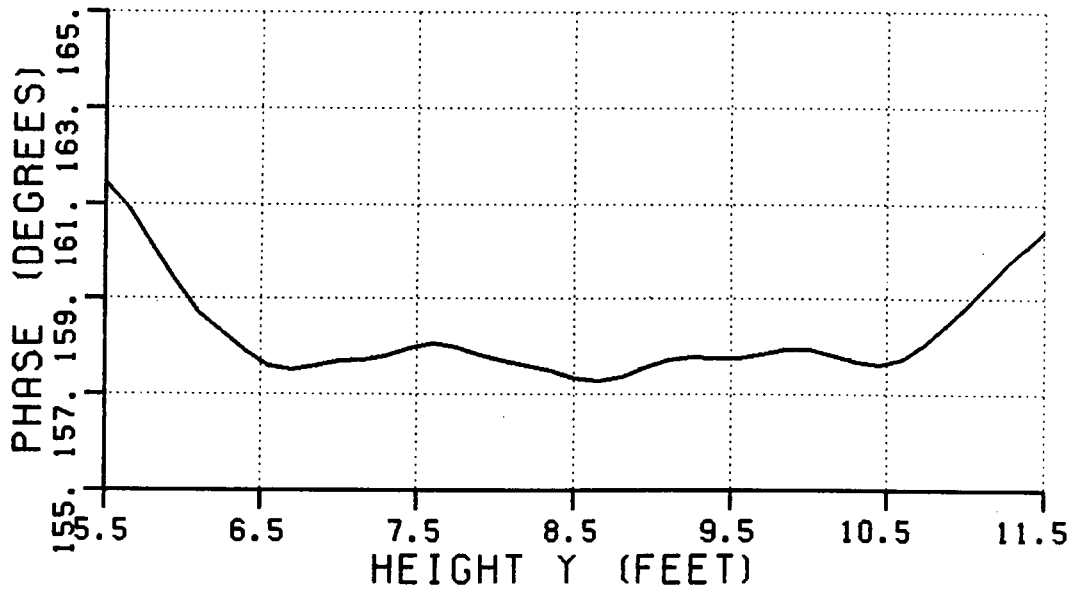
Figure 114: Phase of the total field from S3.3 (3 GHz). First and second order end point contributions subtracted.

191
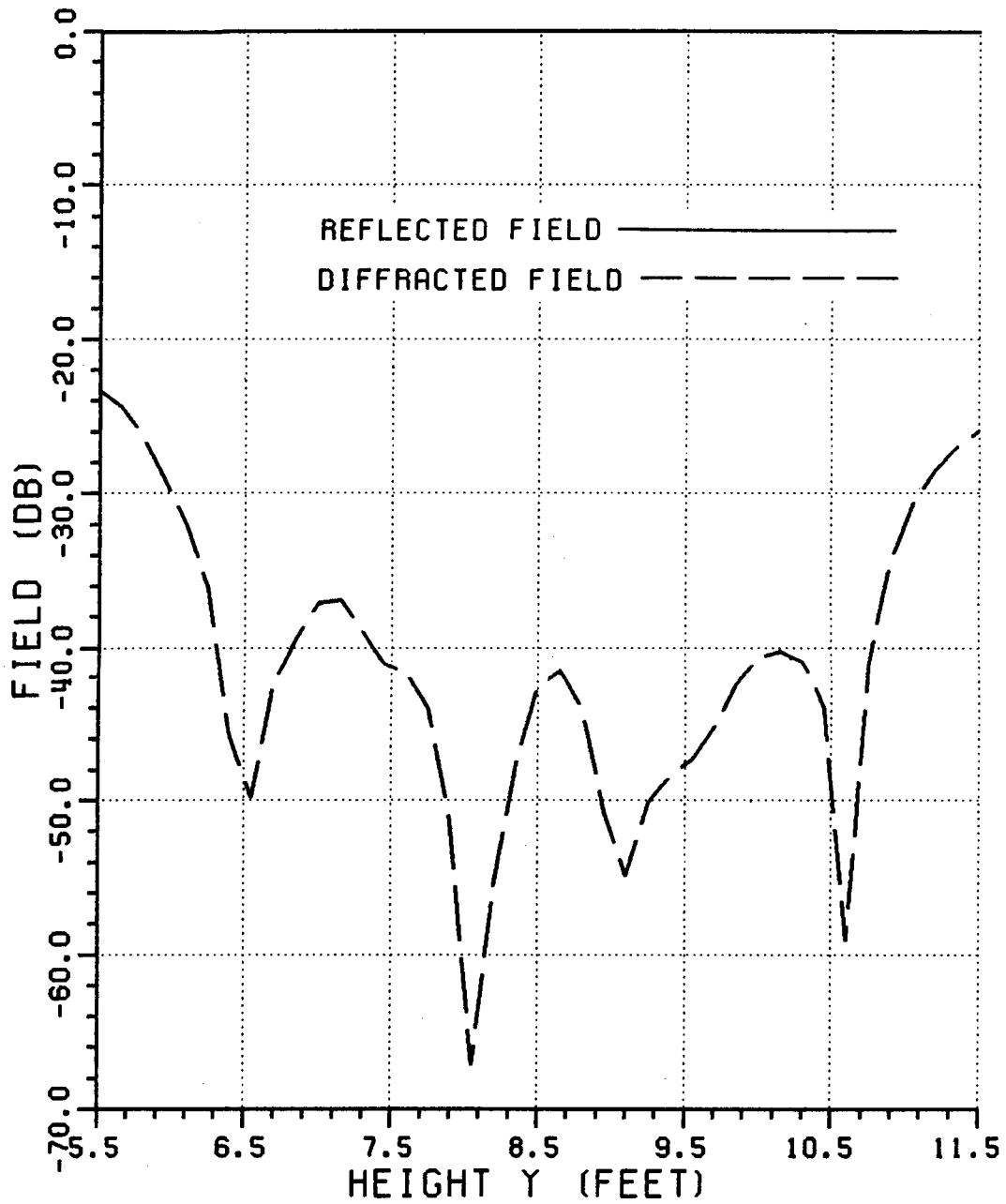
Figure 115: Normalized magnitude of the reflected and diffracted fields from S3.3
(3 GHz). First and second order end point contributions subtracted.

192

Table 17: Surface characteristics for S3.4 and S3.5.

	S3.4	S3.5
Blending	Cosine Squared	
Edge contour	Concave	Convex
f_c	$4'$	$4'$
a_e	$1.25'$	$1.25'$
b_e	$0.53'$	$0.53'$
x_m	$3.61'$	$3.61'$
γ_m	110°	110°
y_{bot}	$1.83'$	$1.83'$
y_{avg}	$2.83'$	$2.83'$
y_{top}	$3.83'$	$3.83'$
x_{left}	$-1.33'$	$-1'$
x_{right}	$1.33'$	$1'$
α	38.96^o	38.96^o
z_{pat}	$8'$	$8'$

a caustic effect, and an improvement of about 14 dB is obtained in the center of the target zone, exactly where it is most needed.
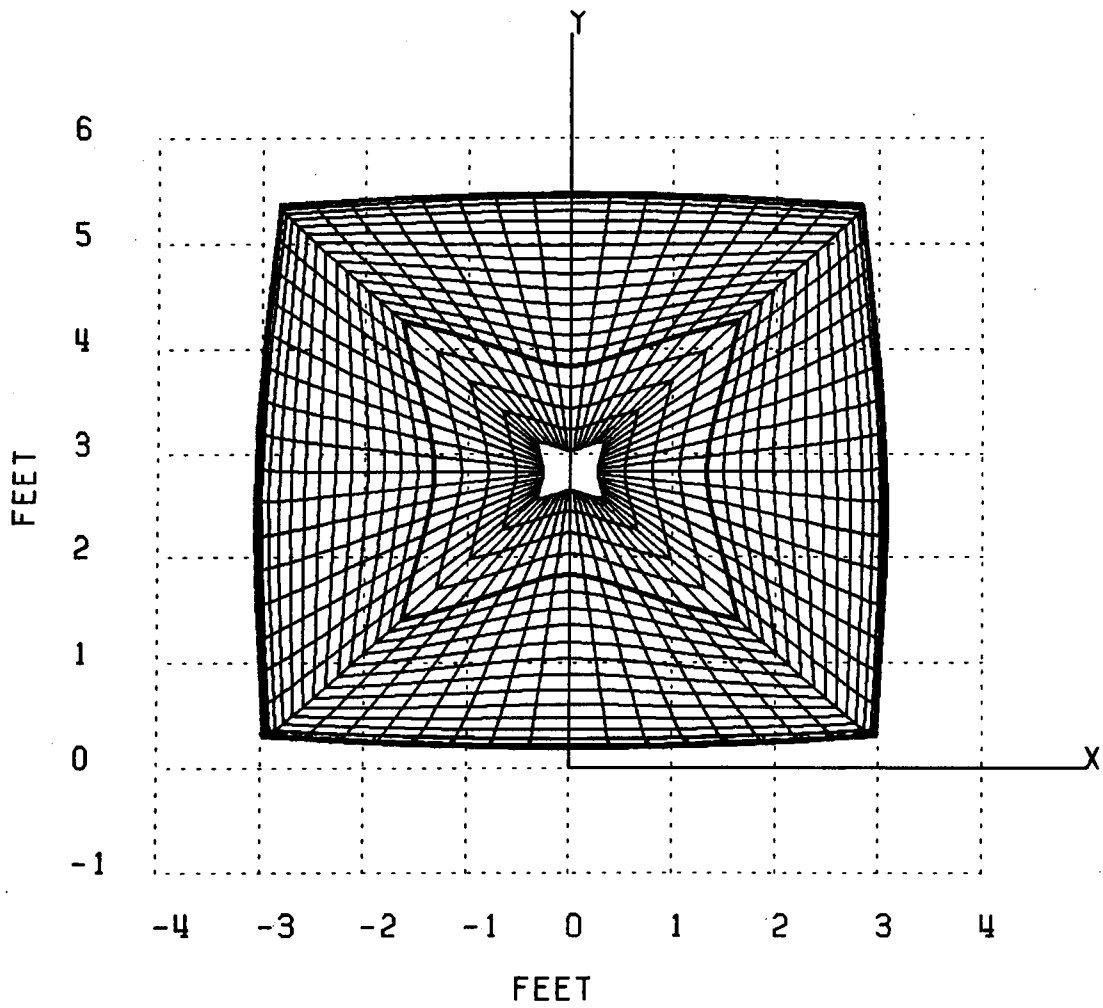
Figure 116: Three-dimensional parabolic reflector with a concave edge contour and cosine squared blended rolled edges (S3.4)(Front view).

194
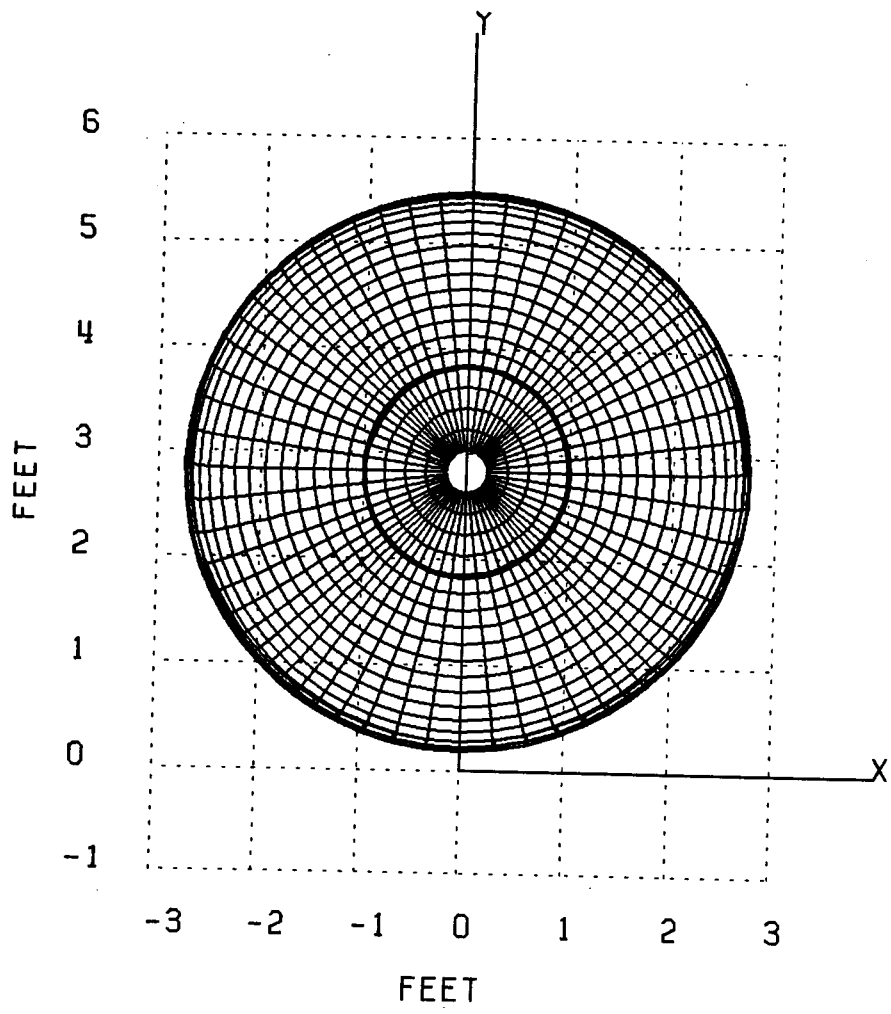
Figure 117: Three-dimensional parabolic reflector with a convex edge contour and cosine squared blended rolled edges (S3.5)(Front view).
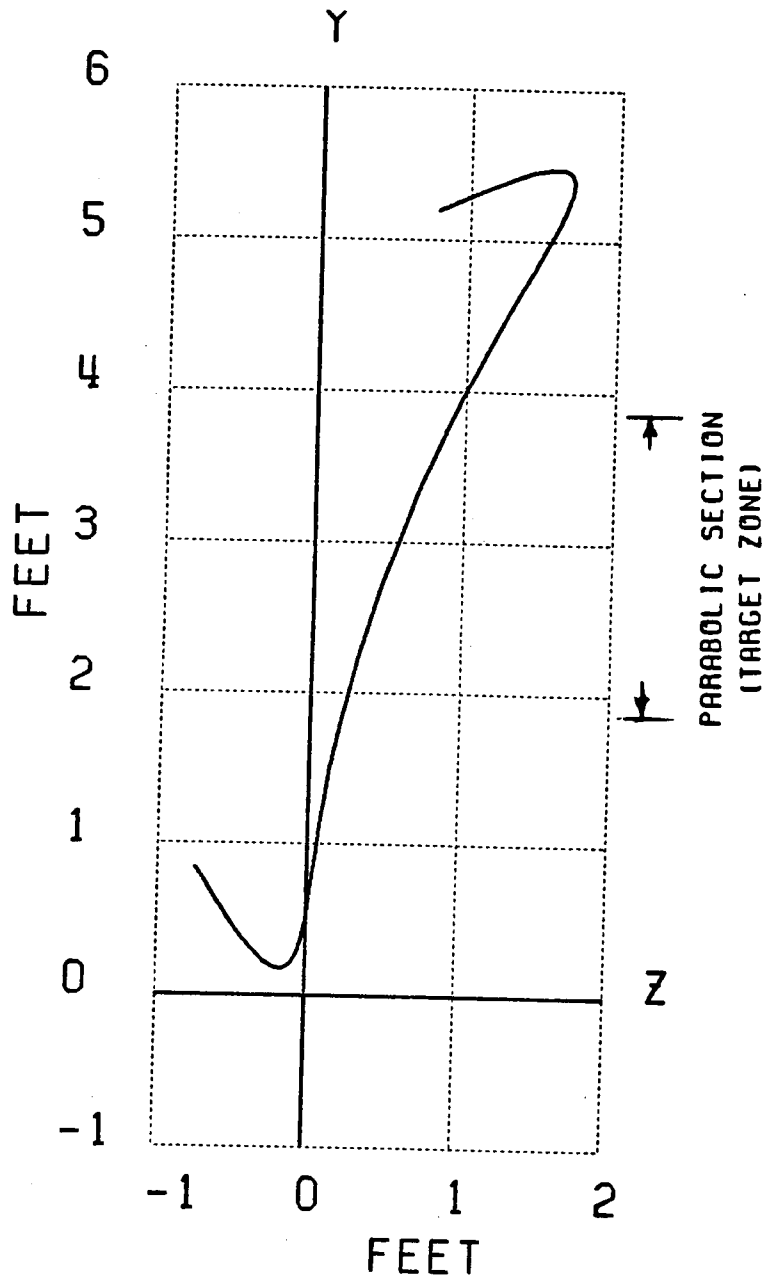
Figure 118: YZ-plane profile of S3.4 and S3.5.

196
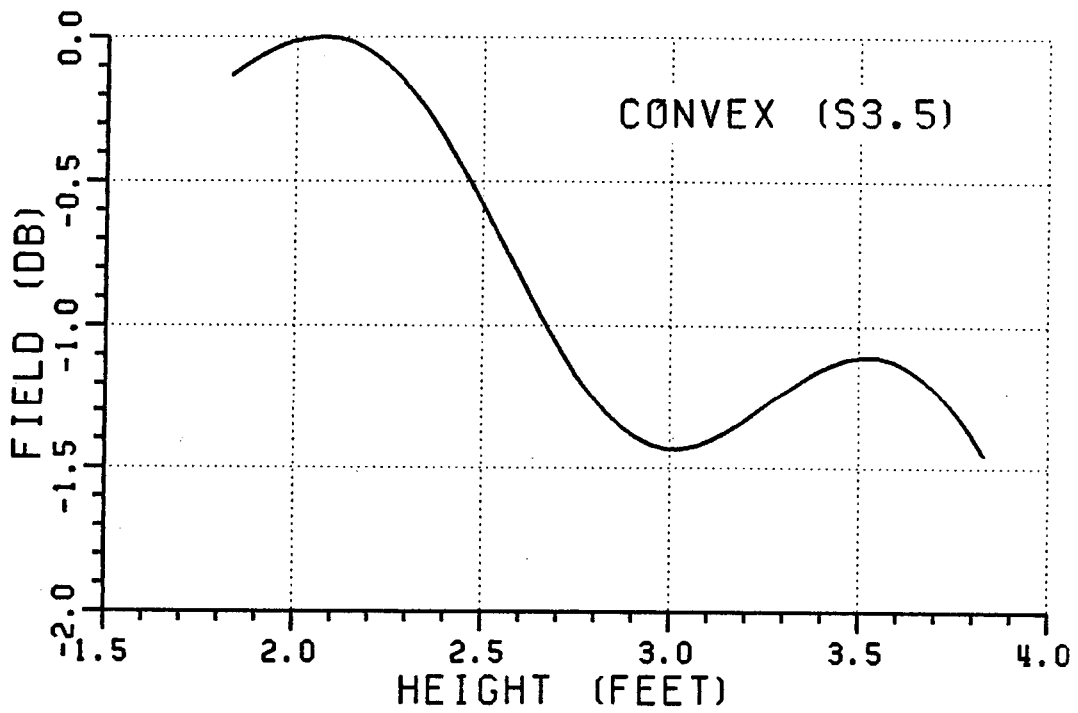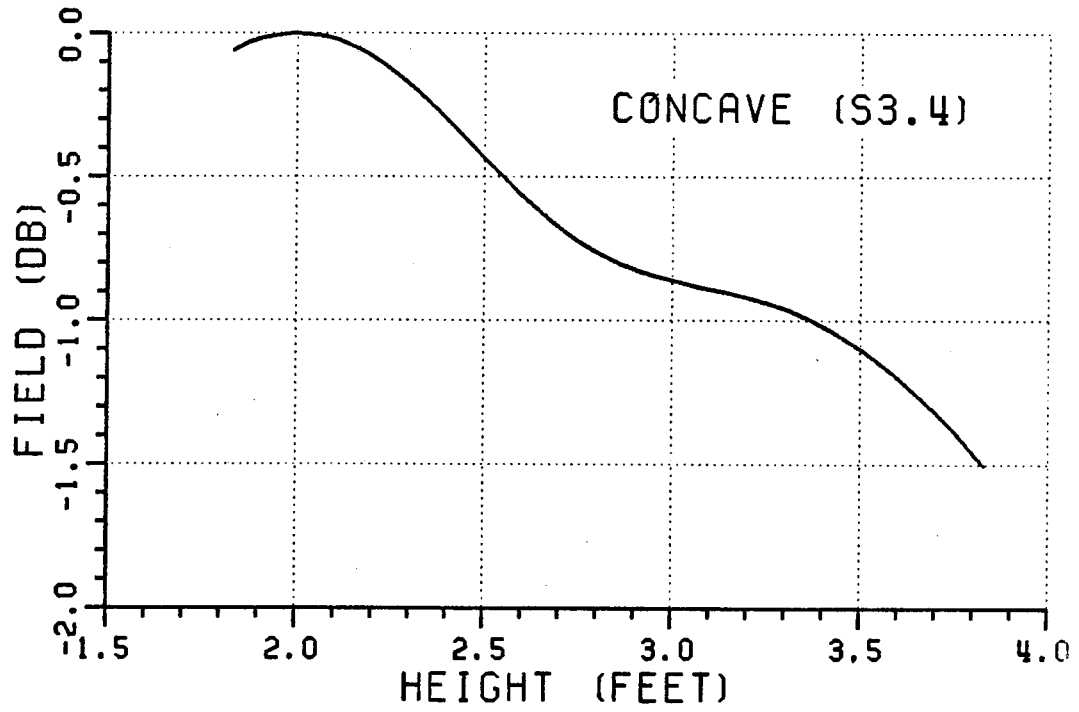
Figure 119: Normalized magnitude of the total field from S3.4 and S3.5 (3 GHz).
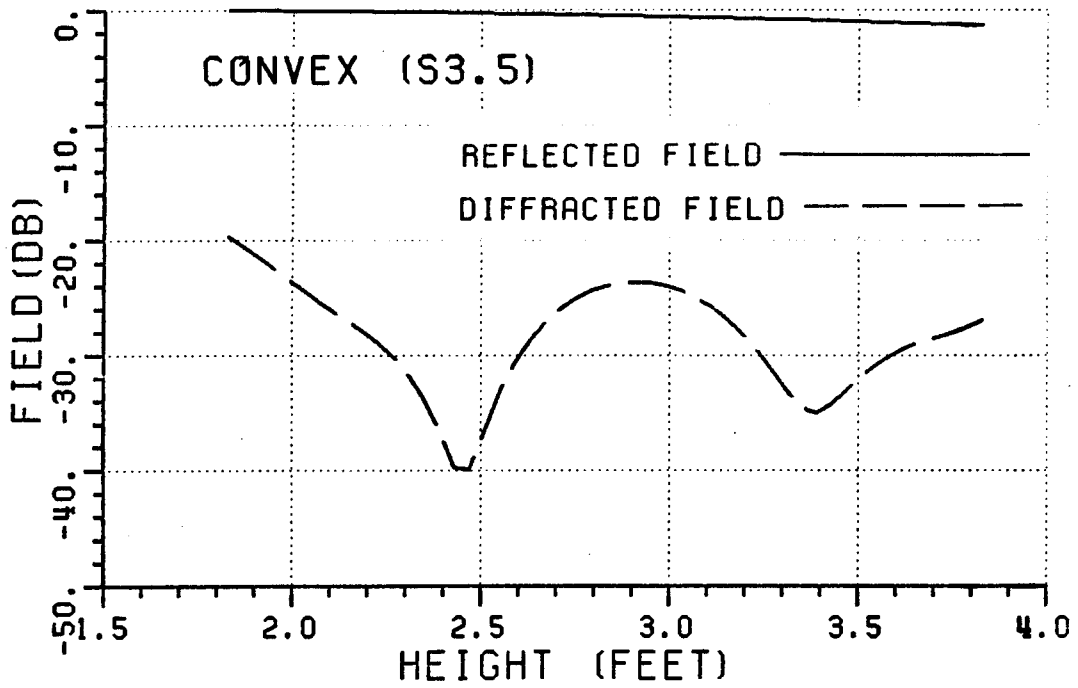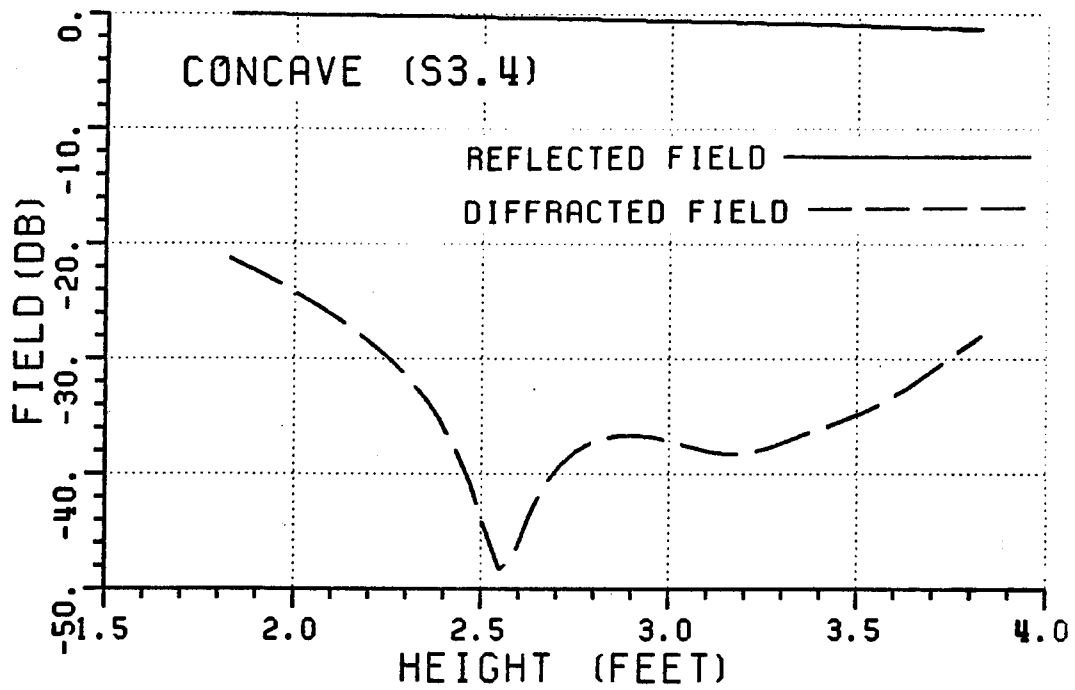
Figure 120: Normalized magnitude of the reflected and diffracted fields from S3.4 and S3.5 (3 GHz).
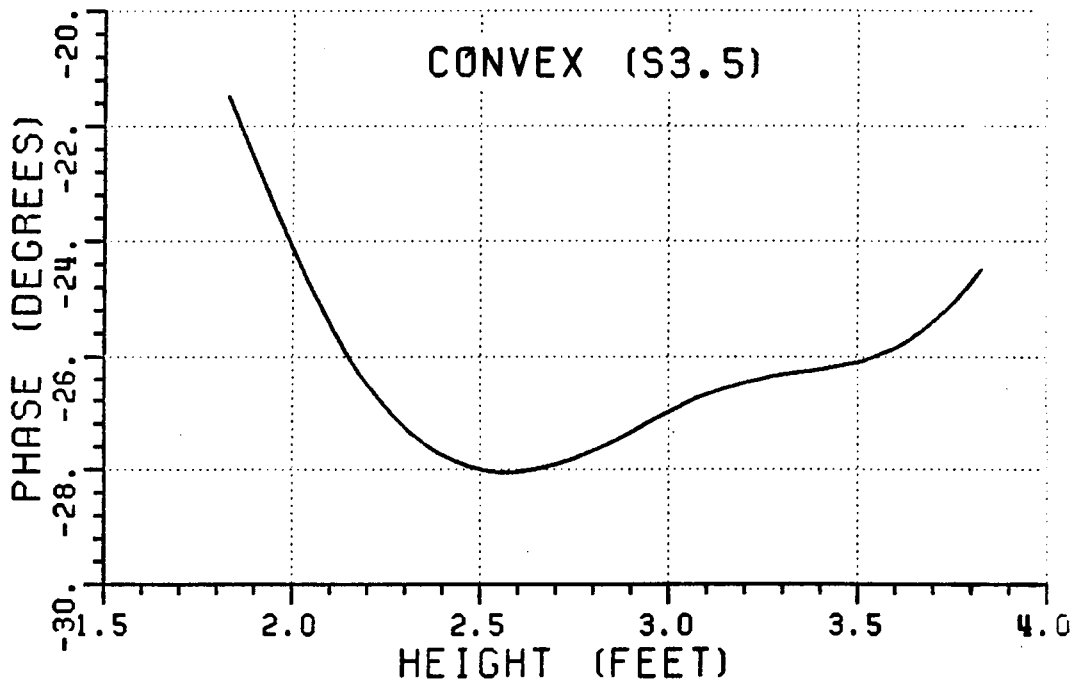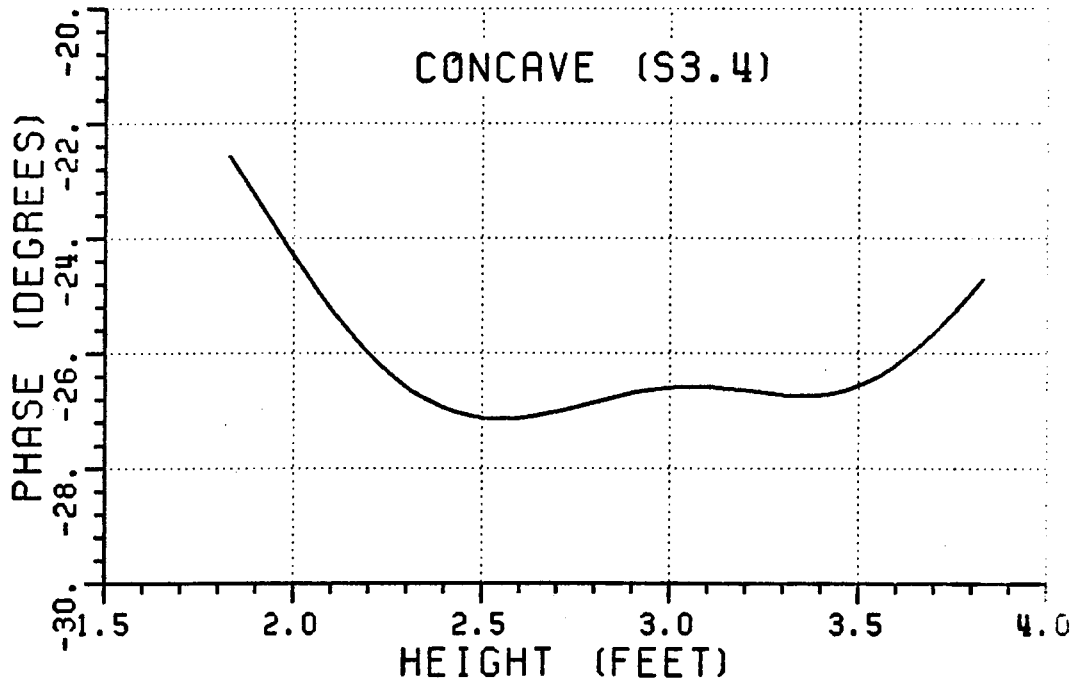
Figure 121: Phase of the total field from S3.4 and S3.5 (3 GHz).

CHAPTER V

A DUAL CHAMBER COMPACT RANGE CONFIGURATION

5.1 Introduction

This chapter describes a dual chamber compact range configuration, where the main reflector and target zone are located in the main chamber and a Gregorian subreflector together with the associated feed assemblies in the other. The two chambers are separated by an absorber fence, with a small coupling aperture to transmit signals from one chamber to the other. It will be shown that such a dual chamber system incorporating a Gregorian subreflector has several advantages over other configurations, especially in terms of the reduction of the amplitude taper and cross-polarization errors in the reflected plane wave. Stray scattered fields from the subreflector and spillover by the feed are virtually eliminated by the absorber fence. System performance is analyzed with and without the absorber fence to show that this is actually the case. It will also be shown how the coupling aperture should be shaped to minimize diffractions from the fence itself.

5.2 Compact range configurations

A compact range usually employs an offset parabolic reflector to convert the spherical wave radiated by a point source located at the focus of the reflector to a reflected plane wave for illumination of the target zone, as shown in Figure 122(a). An offset feed system is used to reduce aperture blockage, but requires that the
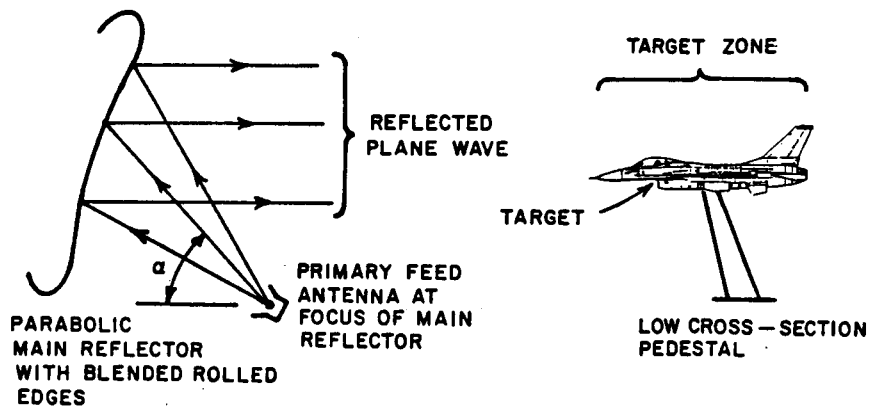
(a) FOCUS FED SYSTEM
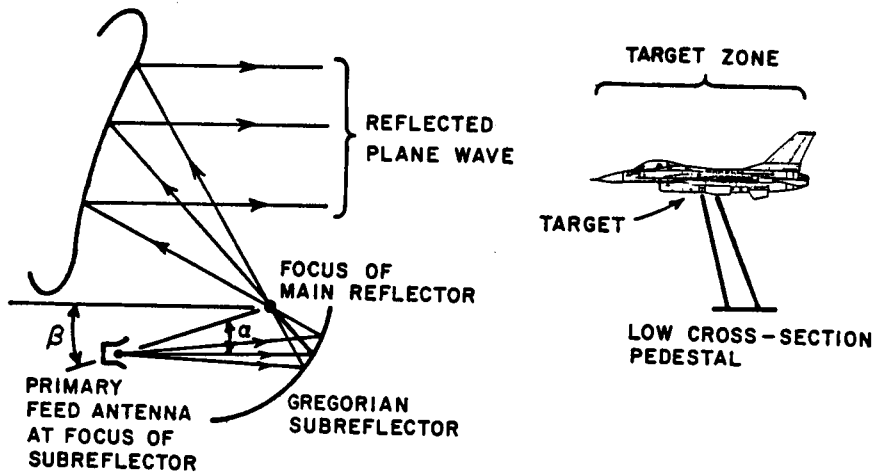
(b) GREGORIAN SUBREFLECTOR FED SYSTEM
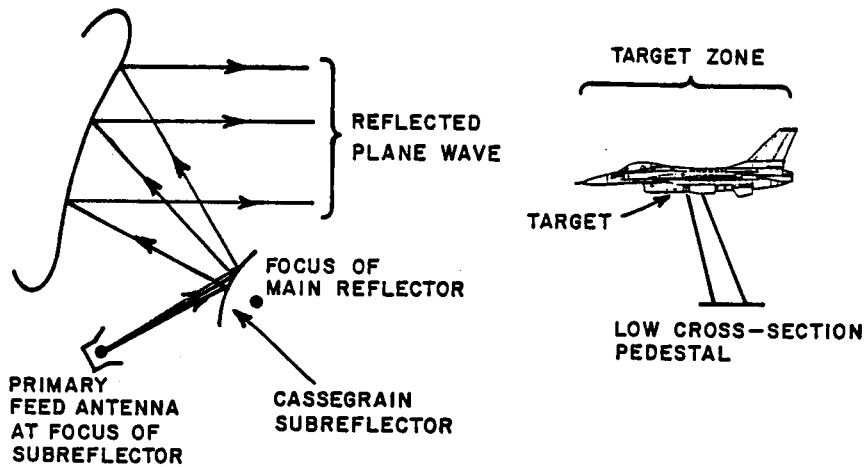
(c) CASSEGRAIN SUBREFLECTOR FED SYSTEM

Figure 122: Various compact range configurations.

201

axis of the feed be tilted at an angle (α) relative to the axis of the reflector[34] for proper illumination. Even though an offset system has many advantages, it also has several disadvantages. First, the spherical wave radiated by the point source has a $1/R$ spatial attenuation, and since all the points on the reflector surface are not an equal distance away from the focus this gives rise to an amplitude taper in the reflected plane wave. The cross-polarization errors inherent with offset focus-fed configurations is another shortcoming. Koffman has shown that when an *axially symmetric* parabolic reflector is illuminated by a Huygens source (ie., $\alpha = 0$), the cross-polarized fields in the aperture plane are eliminated[51]. A Huygens source results from crossed electric and magnetic dipoles of equal strength, so that the field radiated by a y-polarized Huygens source can be expressed as

$$\mathbf{E}(R, \theta, \phi) = (\hat{\theta} \sin \phi + \hat{\phi} \cos \phi) \cos^2(\theta/2) \frac{e^{-jkR}}{R} . \tag{5.1}$$

The cross-polarization associated with *offset* parabolic reflector systems has been studied by various researchers, among them Chu and Turrin[52], Dijk *et al*[53] and Gans and Semplak[54]. In the case of an offset reflector illuminated by a balanced feed like a Huygens source, it is found that the cross-polarization originates from the tilt angle (α) between the feed and the main reflector axes. The cross-polarization vanishes when $\alpha = 0$ and deteriorates as α increases.

Many of the problems encountered using a focus-fed system can be relieved by using an offset subreflector fed system instead, even though a subreflector feed system has its own disadvantages. Two types of subreflector configurations are potential candidates for compact range applications; viz., a Gregorian system using a concave elliptic subreflector as shown in Figure 122(b), and a Cassegrain system using a convex hyperbolic subreflector as shown in Figure 122(c). It will be shown that a Gregorian subreflector offers substantial advantages over a Cassegrain.

Hannan has shown that the equivalent focal length (f_e) of a subreflector/main reflector configuration is given by[55]

$$f_e = m \ f_c \tag{5.2}$$

where

$$m = \frac{e+1}{|e-1|} . \tag{5.3}$$

In these equations, e is the eccentricity of the subreflector, and f_c is the real focal length of the main reflector. Note that Equation (5.3) applies to the case where the axis of the subreflector is aligned with the axis of the main reflector. Since $m > 1$ for both Gregorian and Cassegrain subreflectors, $f_e > f_c$ for both systems. Consequently, one can use a main reflector with a shorter focal length, which ultimately reduces the chamber size. In addition, the edge diffracted fields from the main reflector into the target zone are also reduced because the target zone can be located closer to the main reflector as shown in Section 3.4.4. A larger equivalent focal length leads naturally to a reduced amplitude taper and smaller cross-polarization errors in the reflected field. The taper is improved because the distance from the virtual focus to the reflector surface is more nearly uniform[56]. The cross-polarization is related to the f/D ratio (where D is the diameter of the main reflector) and improves if this ratio increases. Since the subreflector/main reflector has a larger equivalent focal length than the focal length of the main reflector alone, the angle between the feed and main reflector axes is reduced[52], resulting in lower cross-polarization errors.

The reflected field amplitude taper and cross-polarization errors can both be reduced further by tilting the subreflector axis by an angle (β) relative to the main reflector axis and tilting the feed axis by an angle (α) relative to the subreflector axis, as shown in Figure 122(b). The tilt (β) rotates the subreflector pattern

relative to the main reflector, resulting in a reduced amplitude taper. Rudge and Adatia[57], Dragone[58], Mizugutch *et al*[59], Tanaka *et al*[60] and Shore[61] have shown that the cross-polarization errors in dual offset reflector systems can be eliminated if, in addition, the axis of the feed is tilted by an angle (α) relative to the subreflector axis such that

$$\tan \frac{\alpha}{2} = m \, \tan \frac{\beta}{2} \tag{5.4}$$

where m is given in Equation (5.3). The primary feed antenna is assumed to be a balanced linearly polarized feed. The effect of the two tilt angles is to have the depolarization arising from the two offset reflectors cancel each other. Note that these equations are valid for both Gregorian and Cassegrain systems. In the case where the subreflector axis is tilted by an angle (β), the equivalent focal length of the system is given by[62]

$$f_e = \frac{|1 - e^2|}{1 + e^2 - 2e \cos \beta} \, f_c \,. \tag{5.5}$$

Even though subreflector systems have many desirable qualities, they have some serious shortcomings. For example, the scattered fields from the subreflector that illuminate the main reflector and target zone as well as the spillover from the feed are highly undesirable. Adatia[63] has shown that the diffracted fields from the subreflector also have a very detrimental effect on the polarization purity. Rader[32] analyzed a Cassegrain subreflector for compact range applications and found that the diffractions from the subreflector edges result in an unacceptable field quality in the target zone. In order to reduce these diffractions he added blended rolled edges to the subreflector, but then found that higher order reflected fields from the rolled edges also cause too much ripple in the reflected plane wave. These problems make a Cassegrain subreflector unattractive for compact range applications.

204

A Gregorian subreflector, on the other hand, allows one to use a dual chamber approach as shown in Figure 123. Note that this antenna configuration is the same as the one described in Section 4.5 with main reflector S3.3. The yz-cut of the antennas is also shown in Figure 47. The main chamber contains only the main reflector and target zone. The Gregorian subreflector is oversized and placed in the second chamber along with the feed assemblies. The two chambers are separated by an absorber fence with a small coupling aperture to transmit the signals between the chambers. All the desired geometrical optics (GO) reflected rays from the subreflector pass through one of its focal points (see Figure 122(b)) which is coincident with the focal point of the main reflector. The coupling aperture between the two chambers is then positioned at this location so that the desired signal can propagate unperturbed from one chamber to the other. The diffracted fields from the subreflector and spillover from the feed are attenuated by the absorber fence before they can illuminate the main reflector and target zone. This approach virtually eliminates the subreflector scattered field and feed spillover problems, while retaining the benefits of a subreflector feed (ie., reduced amplitude taper and cross-polarization errors). Note that this solution cannot be applied to a Cassegrain subreflector, since the reflected rays from a Cassegrain diverge instead of passing through a caustic point as shown in Figure 122(c).

In order to compare the performance levels of the different feed configurations, consider the following three-dimensional reflector systems:

1. A Gregorian subreflector with both the subreflector and feed axes tilted ($\beta = 5.5^o, \alpha = 20^o$) and illuminated by a Huygens source of the type described in Equation (5.1). The subreflector has semi-major and semi-minor axes of lengths 5.25' and 4.308', respectively. The dimensions of the sub-
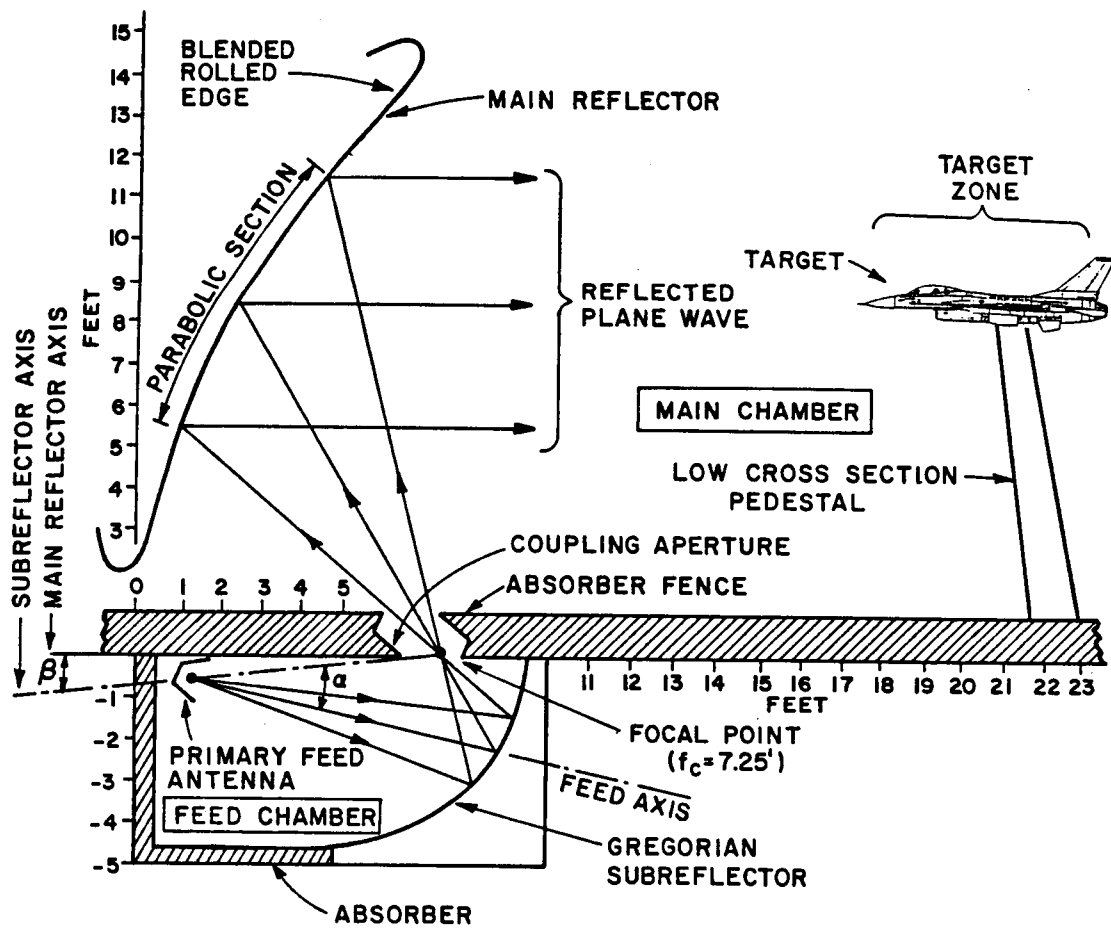
Figure 123: Dual chamber compact range configuration.

reflector and tilt angles (β and α) are chosen to optimize the taper of the reflected field[64], while maintaining the relationship between α and β given in Equation (5.4). The main reflector has a focal length of 7.25' and cosine squared blended rolled edges with a concave edge contour to reduce edge diffractions (S3.3 described in Section 4.5). The yz-cut of this configuration is shown in Figure 123.

2. The same configuration as in the previous case, except that the subreflector axis is aligned with that of the main reflector, and the feed axis is tilted so that the reflected ray along this direction illuminates the center of the projection of the target zone onto the parabolic reflector ($\beta = 0^o, \alpha = 17^o$).

3. A focus-fed system with a Huygens source at the focus of a parabolic reflector. The feed axis is tilted to point at the center of the projection of the target zone onto the parabolic section ($\alpha = 39^o$ as shown in Figure122(a)). The main reflector has a focal length of 12'.

Figure 124 shows the normalized GO reflected field along a vertical cut through the center of the target zone for the three cases. The amplitude tapers for cases 1, 2, and 3 are 0.05 dB, 0.3 dB and 1.3 dB, respectively. From this plot it is clear that even though the main reflectors in the first two cases have shorter focal lengths than that in the third case, the use of the subreflectors result in a substantial reduction in the taper of the reflected field. The taper is reduced even more when the subreflector axis is tilted relative to the main reflector axis. The cross-polarized GO fields relative to the copolarized GO fields are shown in Figure 125 along a horizontal cut through the center of the target zone. Note that the cross-polarization of the system where the subreflector axis is aligned with that of the main reflector (case 2) is much smaller than that of the focus-fed system (case 3),
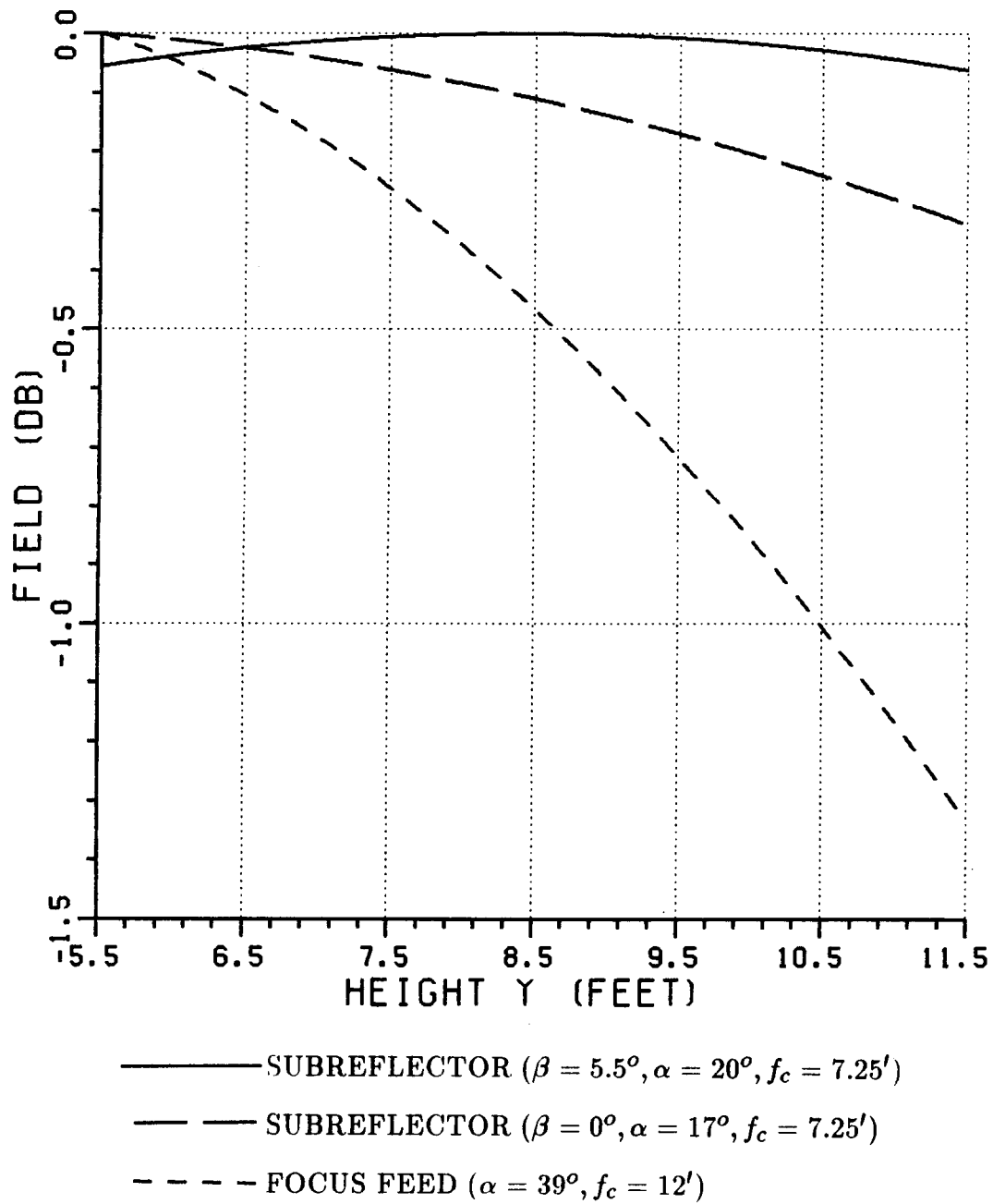
Figure 124: Normalized copolarized reflected fields in the target zone associated with various compact range configurations.
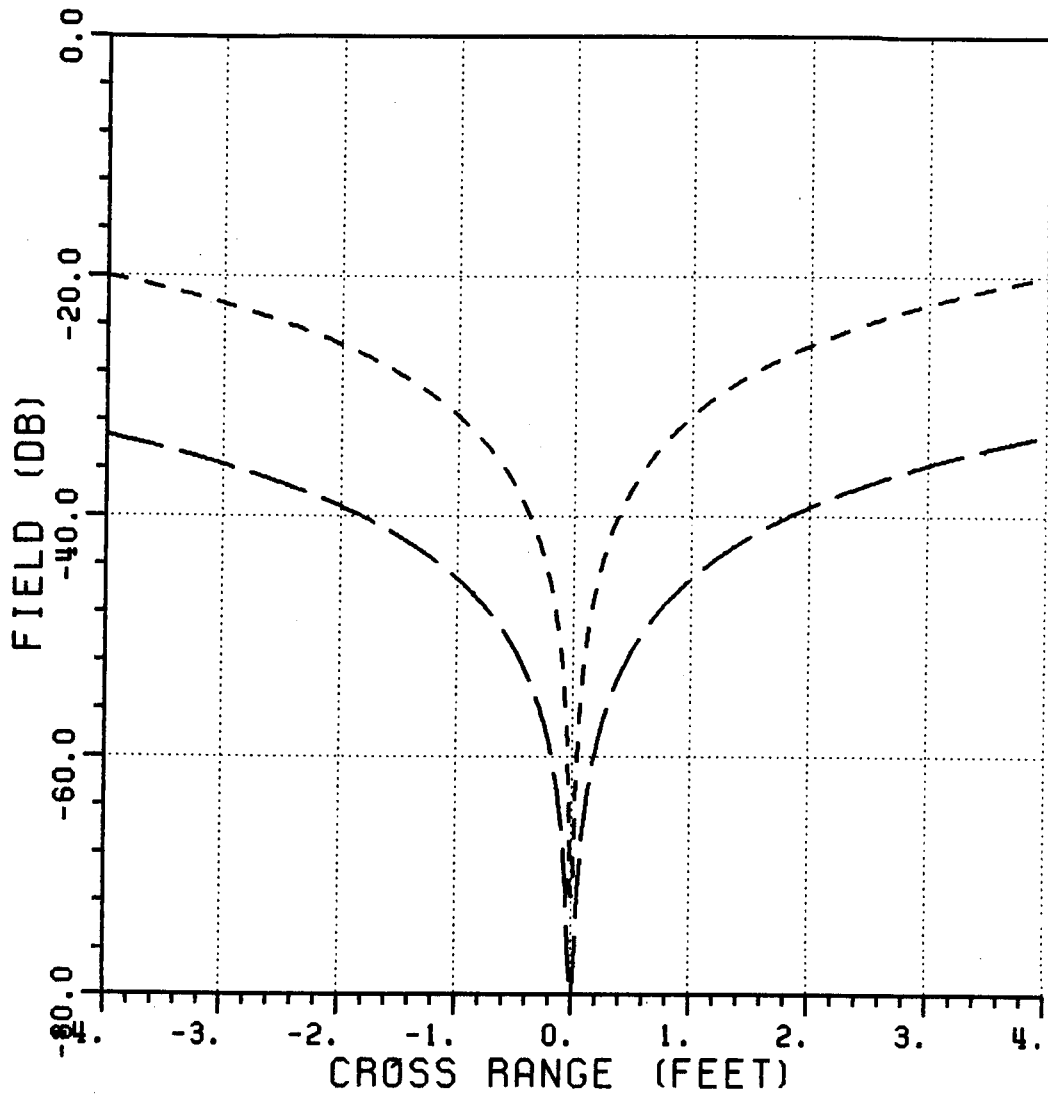
Figure 125: Cross-polarized fields in the target zone associated with various compact range configurations. Note that the cross-polarized fields are zero in the case where both subreflector and feed axes are tilted.

and that the cross-polarization has been eliminated for the case where both the subreflector and feed axes are tilted (case 1). The total field along a vertical cut through the center of the target zone for case 1 is shown in Figure 113, and includes the reflected field and the fields diffracted from the edges of the main reflector. Note that this result is uniform to within a few tenths of a decibel which makes for a very good approximation to a plane wave.

The advantages of using a Gregorian subreflector has been clearly demonstrated in this section. In the next section it will be shown how an extension of the subreflector surface reduces the edge diffracted fields from the subreflector that illuminate the main reflector . The rest of the chapter will be devoted to showing how the dual chamber configuration can significantly reduce the effects of the diffracted fields from the subreflector and spillover from the feed in the target zone. Particular attention is paid to the absorber fence which is used to separate the two chambers.

5.3   Geometry of a Gregorian subreflector

The Gregorian subreflector is a prolate spheroid defined in terms of its own $x_s y_s z_s$-coordinate system with the origin located at the center of the spheroid, as shown in Figure 104. It has a semi-major axis of length (a_{sr}) in the direction of the axis of symmetry (z_s-axis) and semi-minor axes of length (b_{sr}) in the directions of the x_s– and y_s–axes, such that $a_{sr} > b_{sr}$. The subreflector can thus be described by the following parametric equation:

$$\mathbf{r}(u,v) = b_{sr} \cos v \ \sin u \ \hat{\mathbf{x}}_s + b_{sr} \sin v \ \sin u \ \hat{\mathbf{y}}_s + a_{sr} \cos u \ \hat{\mathbf{z}}_s \qquad (5.6)$$

for $v_1 \le v \le v_2$ and $u_1 \le u \le u_2$. The focal points of the subreflector are located at a distance (f_{sr}) from the origin along the positive z_s-axis ($\mathbf{f}_{sr}^{+}$) and negative z_s-

axis (f_{sr}^-), respectively. The eccentricity and focal length are given, respectively, by

$$e = \sqrt{1 - (b_{sr}/a_{sr})^2} \text{ , and} \tag{5.7}$$

$$f_{sr} = \sqrt{a_{sr}^2 - b_{sr}^2} \text{ .} \tag{5.8}$$

The subreflector is placed such that f_{sr}^+ coincides with the focal point of the main reflector (f_c). The primary feed antenna is placed at the other focal point (f_{sr}^-). All rays originating from the point source at f_{sr}^- pass through f_{sr}^+ after reflection from the surface of the subreflector, so that f_{sr}^+ is a caustic point for all rays reflected from the subreflector. The fact that f_{sr}^+ is a caustic implies that the subreflector reflected field has a virtual point caustic at the focal point of the main reflector. Recall that the main reflector converts the spherical field radiated by a point source at its focus to a plane wave propagating in the direction of its axis of symmetry; ie., into the target zone. The ray reflected from the bottom edge of the subreflector will propagate along a reflection shadow boundary (RSB) at θ_r as shown in Figure 126. The ray illuminating the top edge will create a RSB in a similar way, so that the reflected field will exist only in the region, $\theta_r \le \theta \le 180^o$, and will be zero elsewhere.

Consider now the bottom edge of the subreflector. A diffracted field will emanate from this edge in order to make the total field (reflected plus diffracted fields) continuous. A Uniform Theory of Diffraction (UTD)[17] analysis shows that the diffracted field has a maximum amplitude along the shadow boundary. In order to minimize the effect of these diffracted rays on the illumination of the main reflector, the subreflector surface should be extended so that the RSB at θ_r is directed away from the main reflector. This can be done by increasing u_2 (see Equation (5.6)) which will result in a smaller value of θ_r. Note that θ_r should not

211
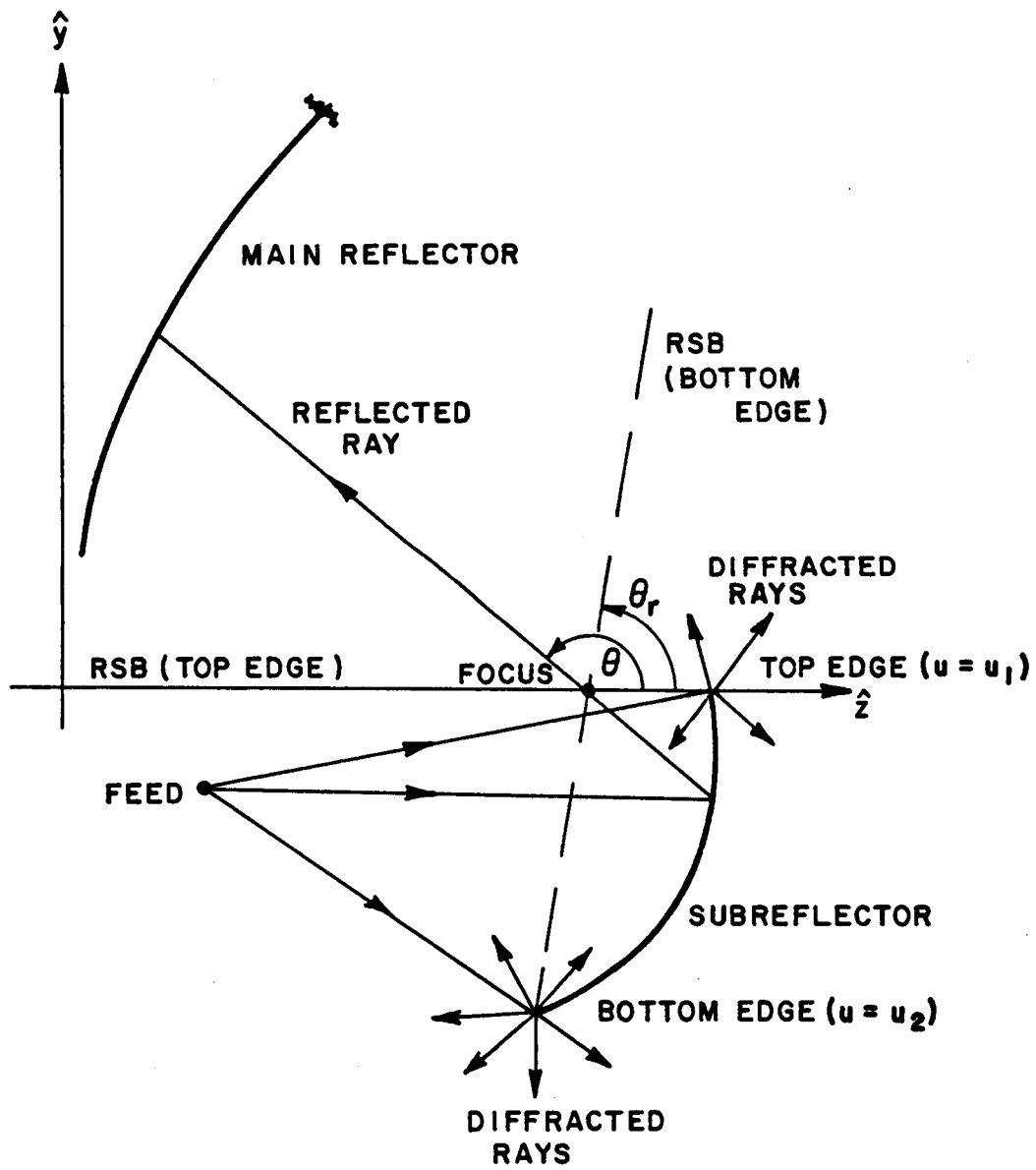
Figure 126: Scattering from the subreflector edges.

212

be too small, since the RSB will then point to the target zone, which is an equally undesirable situation. For the sake of future discussion, the fields diffracted from the subreflector edges will be referred to as "primary diffracted fields".

5.4 Analysis of the absorber fence

The purpose of the absorber fence is to isolate the two chambers and thus prevent diffraction from the subreflector from illuminating the main reflector as well as eliminating scattering from the subreflector and spillover from the feed from reaching the target zone. The absorber fence consists of a slab of electromagnetic absorbing material with a coupling aperture of width (w) around the focal point of the main reflector as shown in Figure 127. Since all GO rays reflected from the subreflector (ie., desired main reflector illumination) pass through the focal point and hence through the aperture, they will not be perturbed by the absorber fence. Note however that the concept of a ray implies a high frequency limit. In practice, the frequency is not infinitely high, so that the reflected field forms a caustic region which is confined to about a wavelength in diameter. The aperture width should therefore be large enough to accomodate the reflected beam at the lowest frequency of operation. Furthermore, the edges of the coupling aperture create incident shadow boundaries (ISB) for the primary diffracted rays, so that diffracted rays will emanate from these edges as shown in Figure 127. For the sake of future discussion, the fields diffracted from the periphery of the coupling aperture will be referred to as "secondary diffracted fields".

In order to develop an idea of the magnitude of this problem, the UTD is used to calculate a two-dimensional far field pattern at 10 GHz for the field scattered by the subreflector shown in Figure 123, in the direction of the main reflector. Two cases are considered; viz.,

213
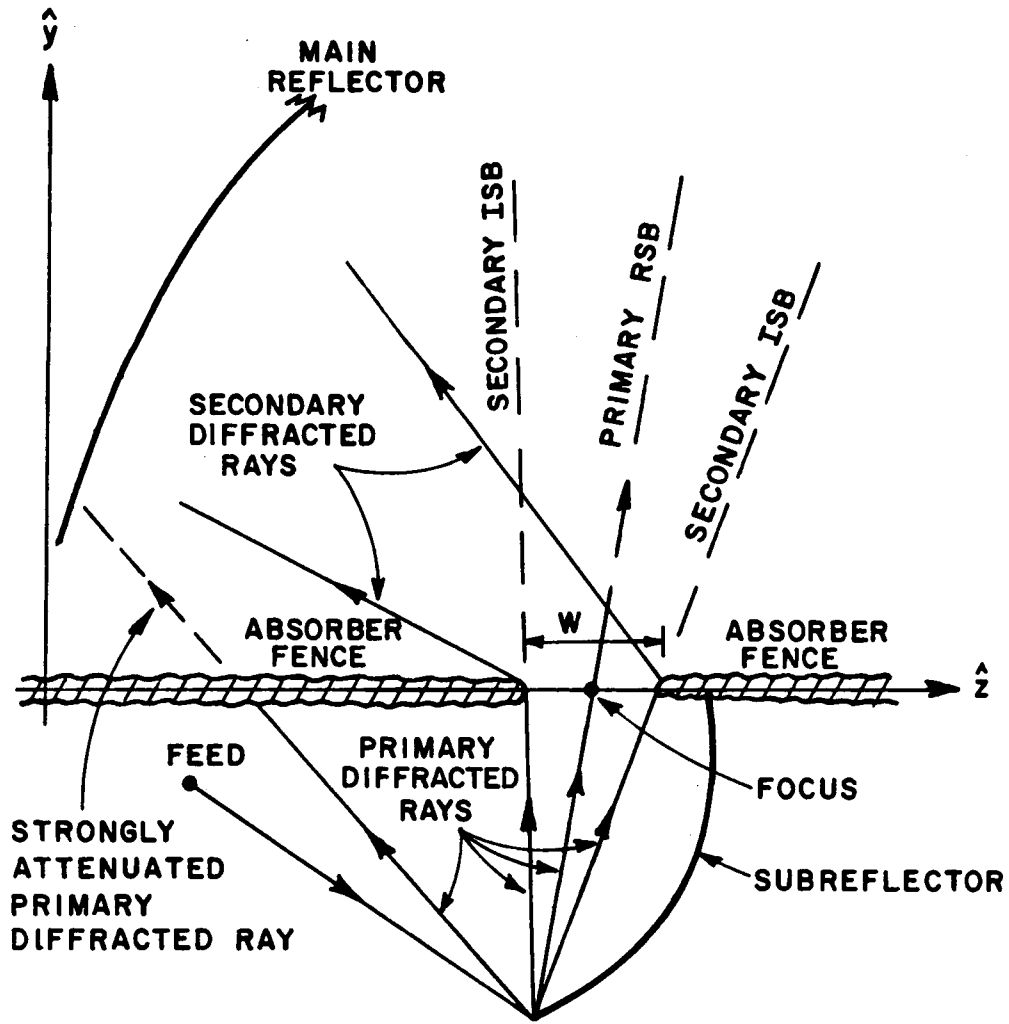
Figure 127: Scattering from the absorber fence.

214

1. No absorber fence present.

2. Absorber fence with a coupling aperture of width (w) present. For the purpose of this analysis it is assumed that the absorber material is infinitesimally thin and that there is no reflection from the material nor any transmission through it.

An electric line source with a uniform pattern is located at $\mathbf{f}_{sr}^-$. The subreflector surface characteristics are given in Table 16.

Consider first the case where no absorber fence is present. The yz-coordinates of the top and bottom edges of the subreflector are given by $(y_{top}, z_{top}) = (0', 2.253')$ and $(y_{bot}, z_{bot}) = (-4.576', -2.574')$, respectively, where the origin of the coordinate system has now been shifted to the focal point ($\mathbf{f}_{sr}^+$). Using the UTD solution, the scattered far field pattern from the subreflector in the direction of the main reflector is given by

$$E_x^t(\theta) = E^r + E_{top}^d + E_{bot}^d \tag{5.9}$$

where E^r is the reflected field, and E_{top}^d and E_{bot}^d are the diffracted fields from the top and bottom edges of the subreflector, respectively, as shown in Figure 128. Using Equation (2.3) one finds that the far field pattern of the reflected field is given by

$$E^r(\theta) = \frac{e^{-j(2ka_{sr} - 3\pi/4)}}{\sqrt{(2a_{sr})/l(\theta) - 1}} . \tag{5.10}$$

In this case the reflection caustic (ρ^r) is given by

$$\rho^r(\theta) = -l^r(\theta) \tag{5.11}$$

where l^r is the distance from the point of reflection on the subreflector to the focus ($\mathbf{f}_{sr}^+$). In the case of a half plane ($n = 2$), the diffraction coefficients in
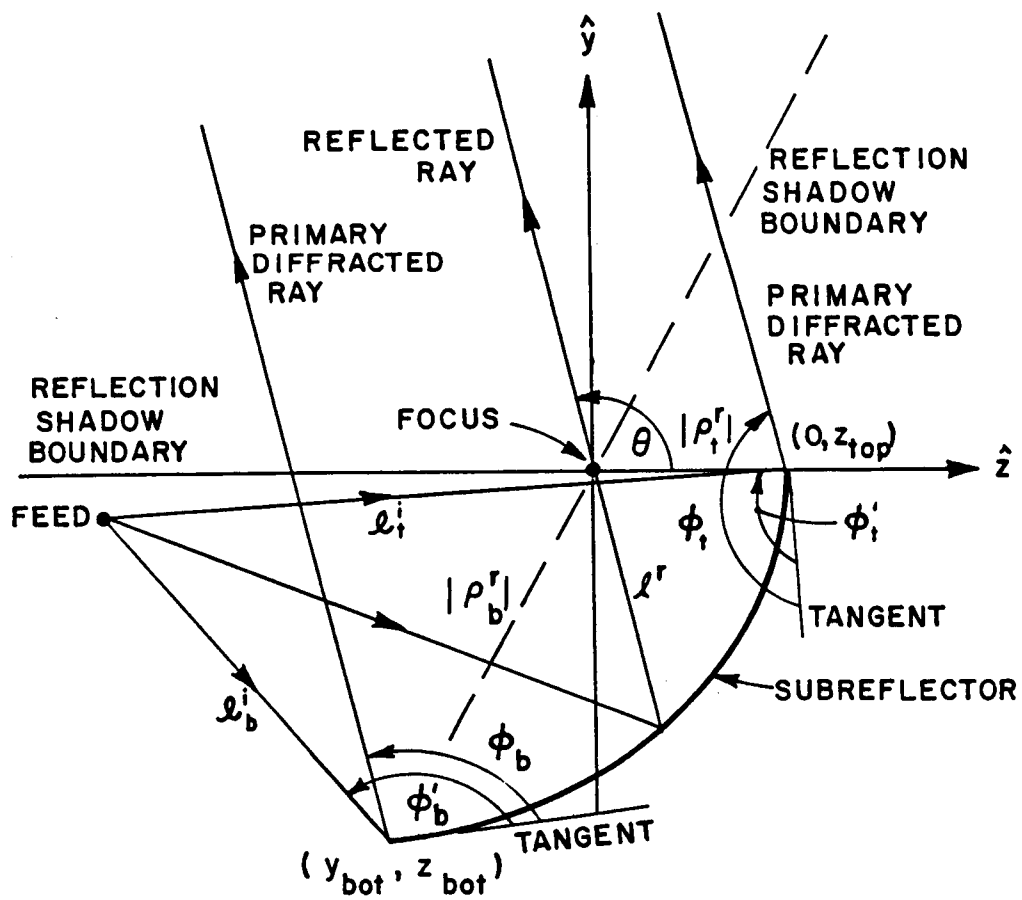
Figure 128: Scattering from subreflector with no absorber fence present.

Equation (2.11) can be expressed as

$$D_{s,h} = D^i(\phi - \phi', L^i) + R_{s,h}D^r(\phi + \phi', L^r) \tag{5.12}$$

where

$$D^i(\phi - \phi', L^i) = \frac{-e^{-j\pi/4}}{2\sqrt{2\pi k}} \left[\frac{F[kL^i a(\phi - \phi')]}{\cos\left(\frac{\phi - \phi'}{2}\right)} \right] \tag{5.13}$$

$$L^i = \frac{s\, s'}{s + s'} \tag{5.14}$$

$$D^r(\phi + \phi', L^r) = \frac{-e^{-j\pi/4}}{2\sqrt{2\pi k}} \left[\frac{F[kL^r a(\phi + \phi')]}{\cos\left(\frac{\phi + \phi'}{2}\right)} \right] \tag{5.15}$$

$$L^r = \frac{s\, \rho^r}{s + \rho^r} \text{ , and} \tag{5.16}$$

$$R_{s,h} = \text{acoustic soft/hard reflection coefficients of the}$$

$$\text{surface at the point of diffraction .}$$

The far field pattern of the diffracted field from the top edge is thus given by

$$E^d_{top}(\theta) = \frac{e^{-jkl^i_t}}{\sqrt{l^i_t}}[D^i(\phi_t - \phi'_t, l^i_t) - D^r(\phi_t + \phi'_t, \rho^r_t)]e^{jkz_{top}\cos\theta} \tag{5.17}$$

where

$$\rho^r_t = -z_{top} \text{ , and} \tag{5.18}$$

$$l^i_t = 2a_{sr} - |\rho^r_t| . \tag{5.19}$$

Similarly the far field pattern of the diffracted field from the bottom edge is given by

$$E^d_{bot}(\theta) = \frac{e^{-jkl^i_b}}{\sqrt{l^i_b}}[D^i(\phi_b - \phi'_b, l^i_b) - D^r(\phi_b + \phi'_b, \rho^r_b)]e^{jk(z_{bot}\cos\theta + y_{bot}\sin\theta)} \tag{5.20}$$

where

$$\rho_b^r = -\sqrt{y_{bot}^2 + z_{bot}^2} \text{ , and} \tag{5.21}$$

$$l_b^i = 2a_{sr} - |\rho_b^r| \text{ .} \tag{5.22}$$

This is obviously not the complete solution for the total scattered field, but serves to show the first order effects of the indicated field components on the pattern in the area of interest.

Consider now the case where an absorber fence is present. The coupling aperture in the fence is symmetrical around the focal point and is $2'$ wide as shown in Figure 129, with the rest of the configuration remaining the same. The scattered far field pattern in the direction of the main reflector is then given by

$$E_x^t(\theta) = E^r + E_{bot}^d + E_{right}^d + E_{left}^d \tag{5.23}$$

where E^r is the reflected field, E_{bot}^d is the diffracted field from the bottom edge of the subreflector, and E_{right}^d and E_{left}^d are diffracted fields from the right and left edges of the coupling aperture, respectively. The far field pattern of the field diffracted from the right edge of the aperture of the absorber fence due to illumination from the bottom edge of the subreflector is given by

$$E_{right}^d(\theta) = E_{right}^i \, D^i(\phi_r - \phi_r', l_r^i) e^{j\frac{kw}{2}\cos\theta} \tag{5.24}$$

where

$$E_{right}^i = \frac{e^{-jkl_b^i}}{\sqrt{l_b^i}} [D^i(\phi_b^r - \phi_b', l_b^i) - D^r(\phi_b^r + \phi_b', \rho_b^r)] \frac{e^{-jkl_r^i}}{\sqrt{l_r^i}} \text{ , and} \tag{5.25}$$

$$l_r^i = \sqrt{y_{bot}^2 + (\frac{w}{2} - z_{bot})^2} \text{ .} \tag{5.26}$$

Similarly the far field pattern of the field diffracted from the left edge of the aperture of the absorber fence due to illumination from the bottom edge of the
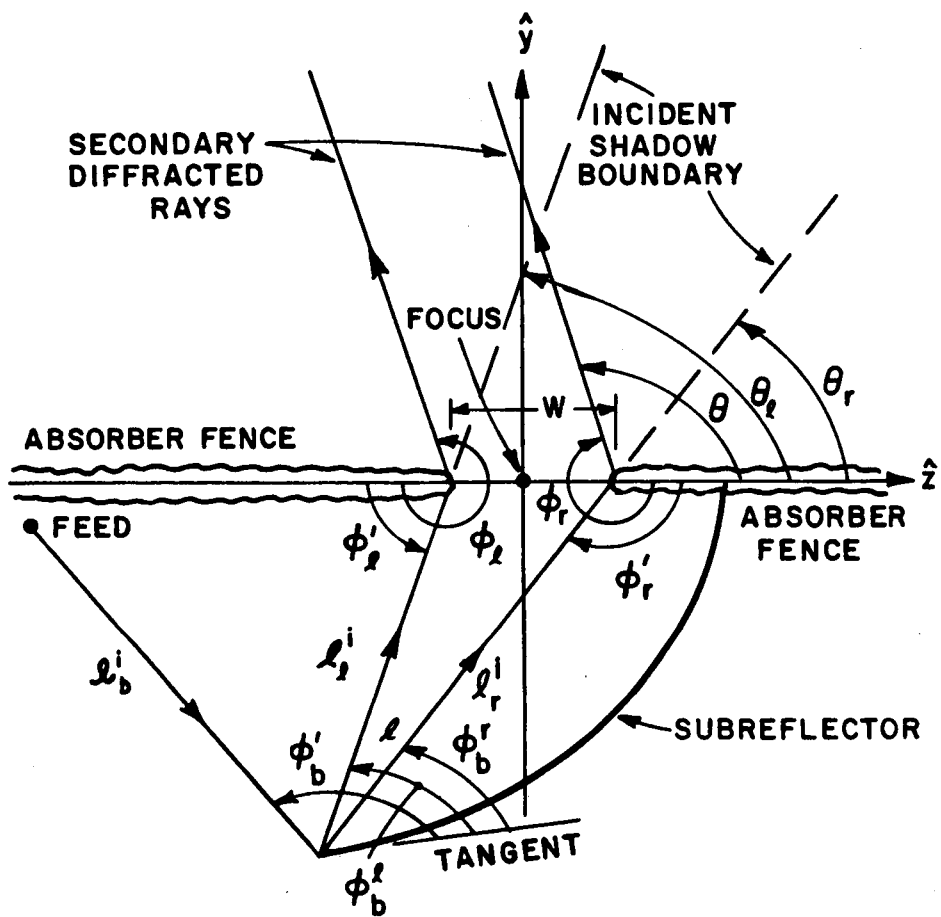
Figure 129: Scattering from subreflector with the absorber fence present.

subreflector is given by

$$E_{left}^d(\theta) = E_{left}^i \ D^i(\phi_l - \phi_l', l_l^i)e^{-j\frac{kw}{2}\cos\theta} \tag{5.27}$$

where

$$E_{left}^i = \frac{e^{-jkl_b^i}}{\sqrt{l_b^i}}[D^i(\phi_b^l - \phi_b', l_b^i) - D^r(\phi_b^l + \phi_b', \rho_b^r)]\frac{e^{-jkl_l^i}}{\sqrt{l_l^i}} \ , \text{ and} \tag{5.28}$$

$$l_l^i = \sqrt{y_{bot}^2 + (\frac{w}{2} + z_{bot})^2} \ . \tag{5.29}$$

The diffraction coefficient (D^r) is not included in the expressions for the diffracted fields from the edges of the aperture, since it has been assumed that there will be no reflections from the absorber and consequently no discontinuity in the reflected field. Note that the diffracted field from the top edge of the subreflector is shadowed by the absorber wall so that it does not contribute in the main chamber. It will be shown in Section 5.6 that shaping the aperture will cause the diffraction from the aperture due to direct illumination from the feed to have a minimal effect on the system performance.

Figure 130 shows the normalized total fields given by Equations (5.9) and (5.23); whereas, the normalized reflected and total diffracted fields are shown in Figure 131. The normalized component fields are shown in Figure 132, with the phases of the total and reflected fields shown in Figure 133. It is clear from Figure 130 that the addition of the absorber fence has reduced the ripple in the reflected field substantiably. Examination of Figure 131 shows that in the case where no absorber fence is present, the diffracted fields are about 31 dB below the level of the reflected fields in the angular region where the main reflector is illuminated. In the case where the absorber fence is present, the diffracted fields are about 40 dB below the the level of the reflected field in the same angular region. Examination of Figure 132 clearly shows the primary reflection shadow boundaries at $\theta = 60.6^o$

and $\theta = 180^o$, as well as the fact that the maxima of the diffracted fields occur at the shadow boundary and then decay for directions away from the RSB. The incident shadow boundaries of the primary diffracted field from the bottom edge of the subreflector at $\theta = 54^o$ and $\theta = 74^o$ are also visible in Figure 132. These results thus show that the use of an absorber fence as described would, in principle, improve the quality of the field illuminating the main reflector.

5.5 Shaping of the coupling aperture in the absorber fence to minimize diffraction

Commercially available absorbing material is far from perfect[65], and rays incident upon an absorber slab will be able to penetrate through it. The transmitted rays will, however, be strongly attenuated. The amount of attenuation will depend on the material characteristics (which are frequency dependent), but can be controlled by the thickness of the slab. Practical considerations dictated by the physical space available in the feed chamber will put a constraint on the maximum slab thickness that can be used. In addition to the attenuation by the absorber, the primary diffracted rays incident upon the absorber slab will also experience a decay due to the nature of the diffraction process as they move away from the shadow boundary as shown in the previous section.

In order to reduce the secondary diffraction, it is necessary to shape the absorber forming the periphery of the aperture. Keeping in mind that the amplitude of the secondary diffracted fields are proportional to the difference between the fields on either side of the ISB[66], a wedge-like shaping with wedge angle (ψ) is most appropriate. Let θ^e be a pattern angle measured from the subreflector as shown in Figure 134, with the ISB at θ^e_{sb}. The wedge ensures that the fields just outside the absorber (E_1 at $\theta^e = \theta^e_{sb} - \epsilon$) and those just inside the absorber

221
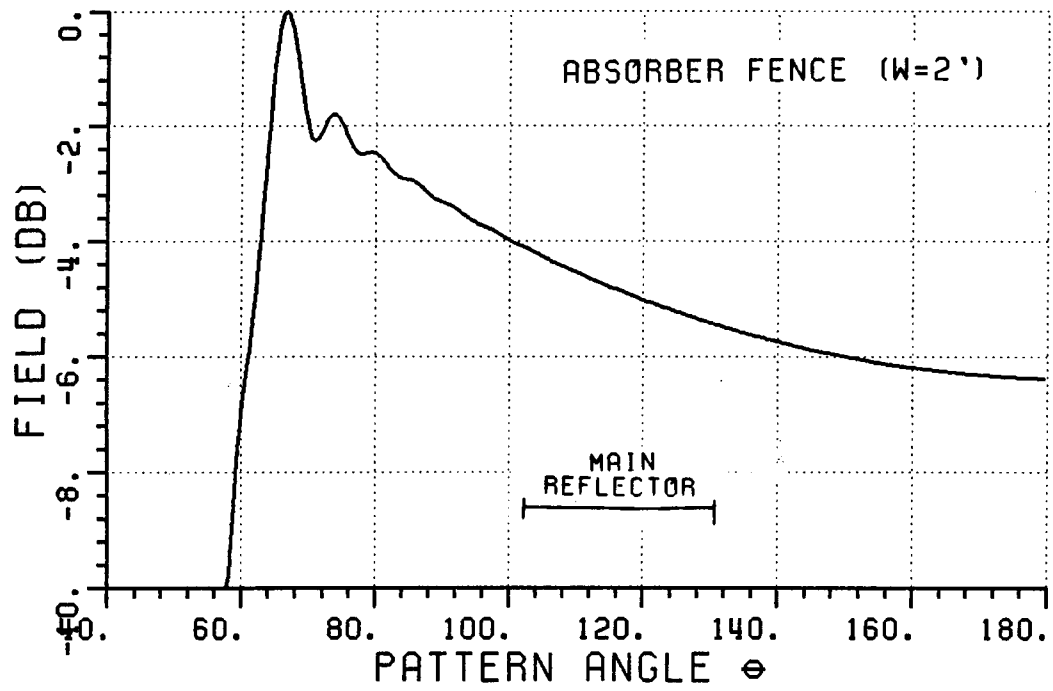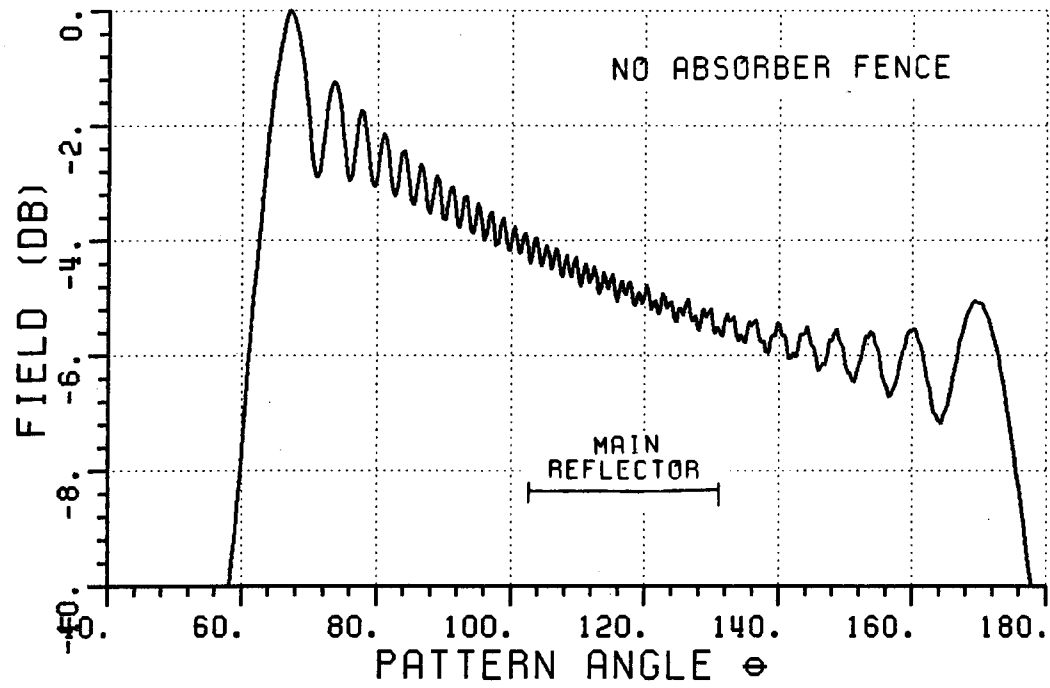
Figure 130: Normalized total field from the subreflector (10 GHz).

222
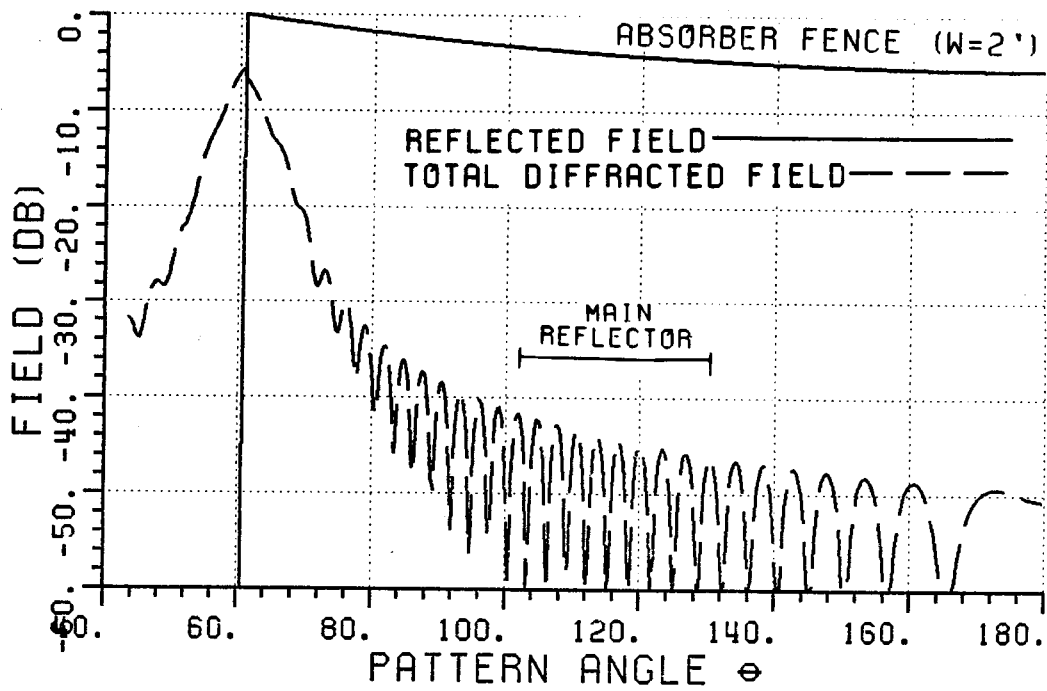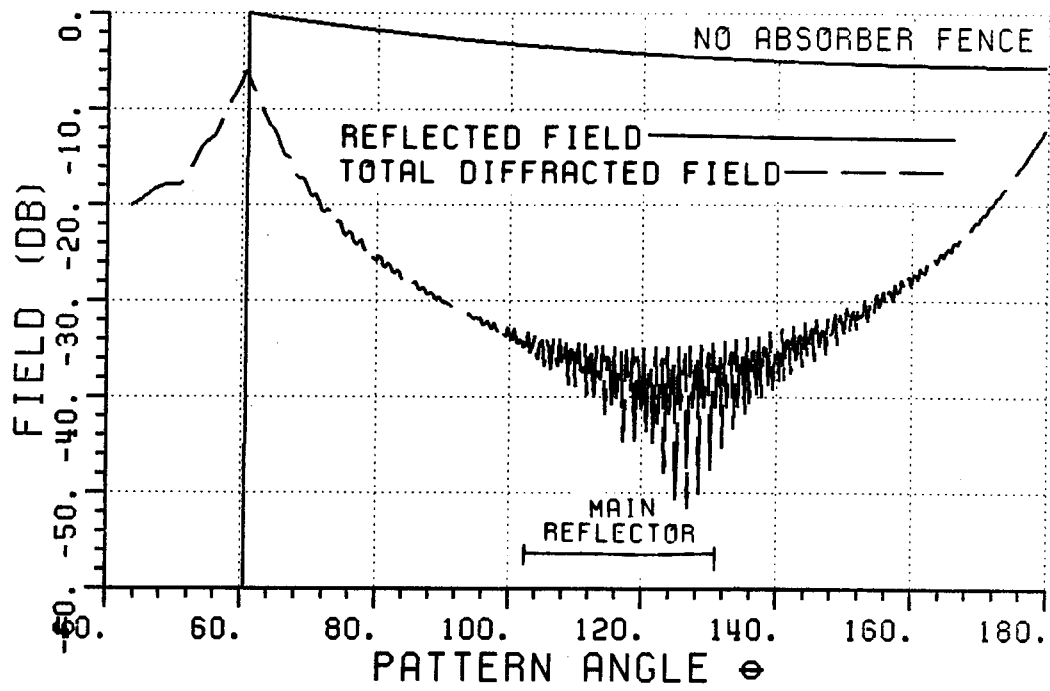
Figure 131: Normalized reflected and total diffracted field from the subreflector (10 GHz).
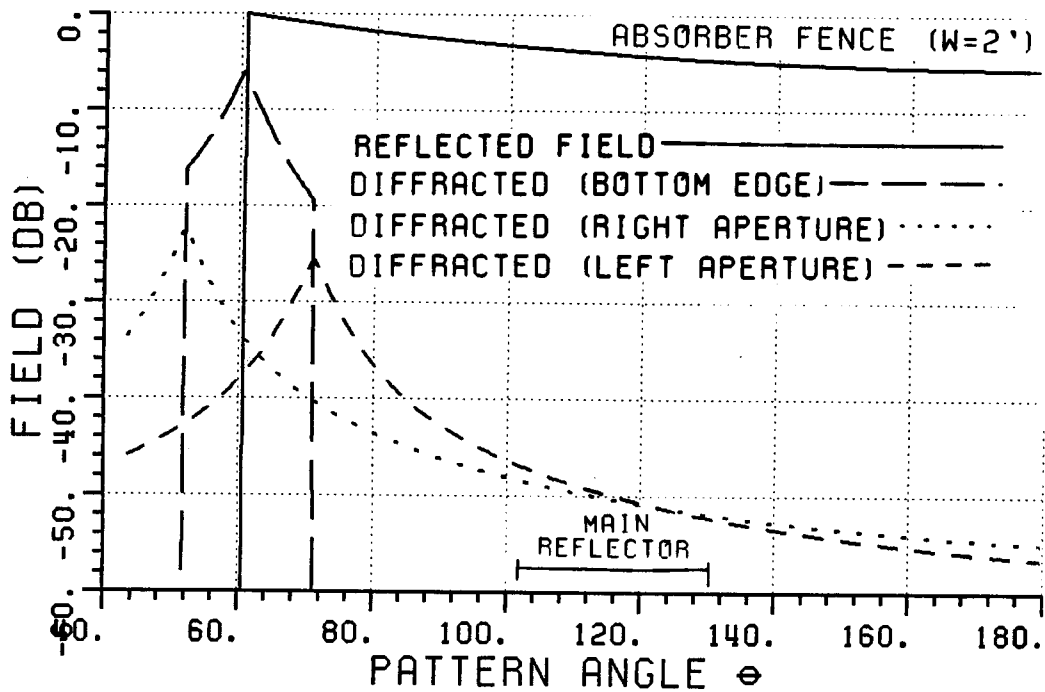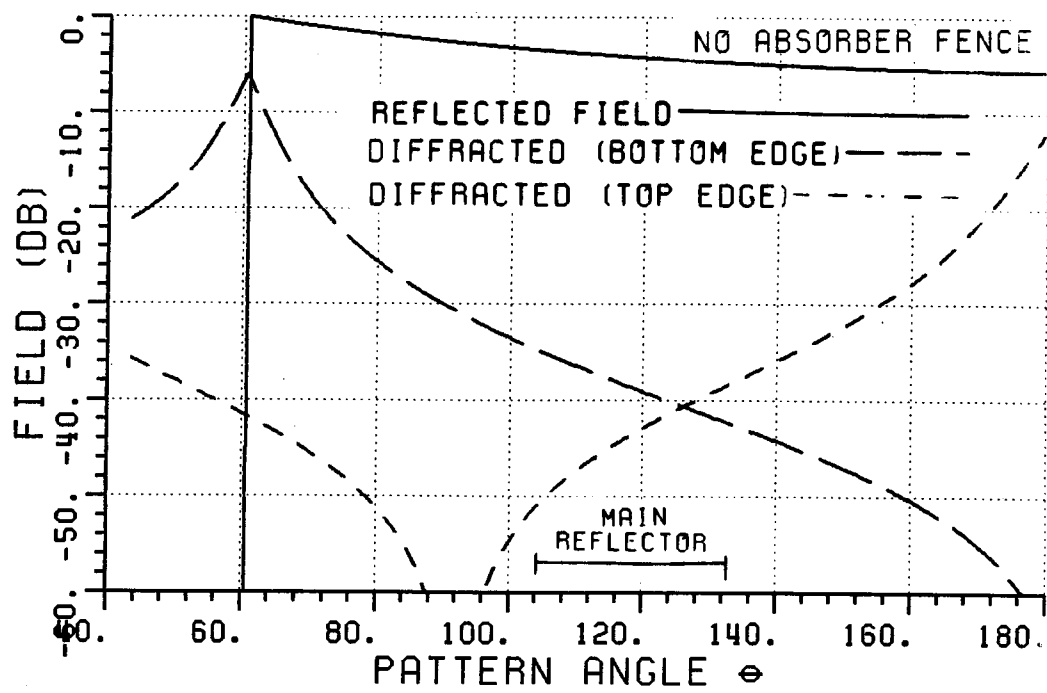
Figure 132: Normalized field components from the subreflector (10 GHz).
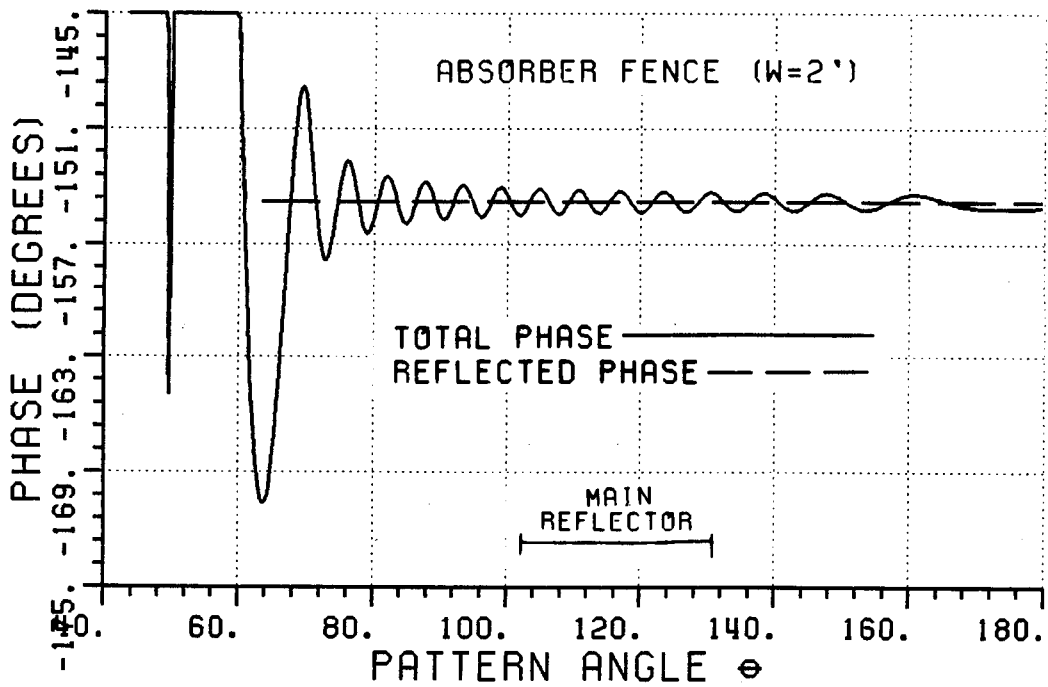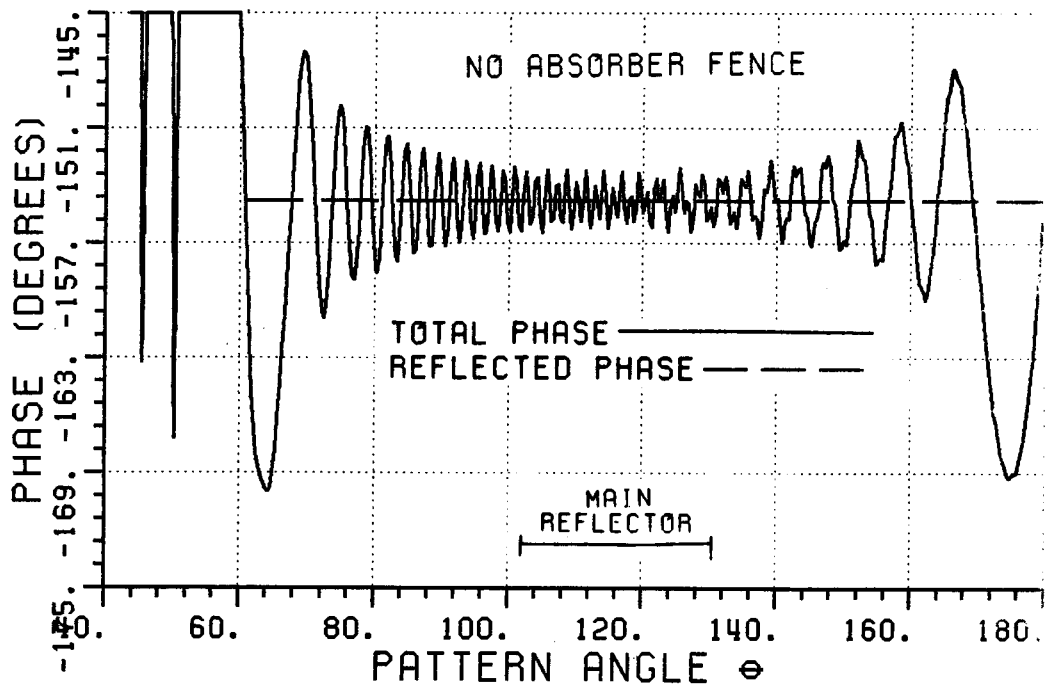
Figure 133: Phases of total and reflected fields from the subreflector (10 GHz).

225
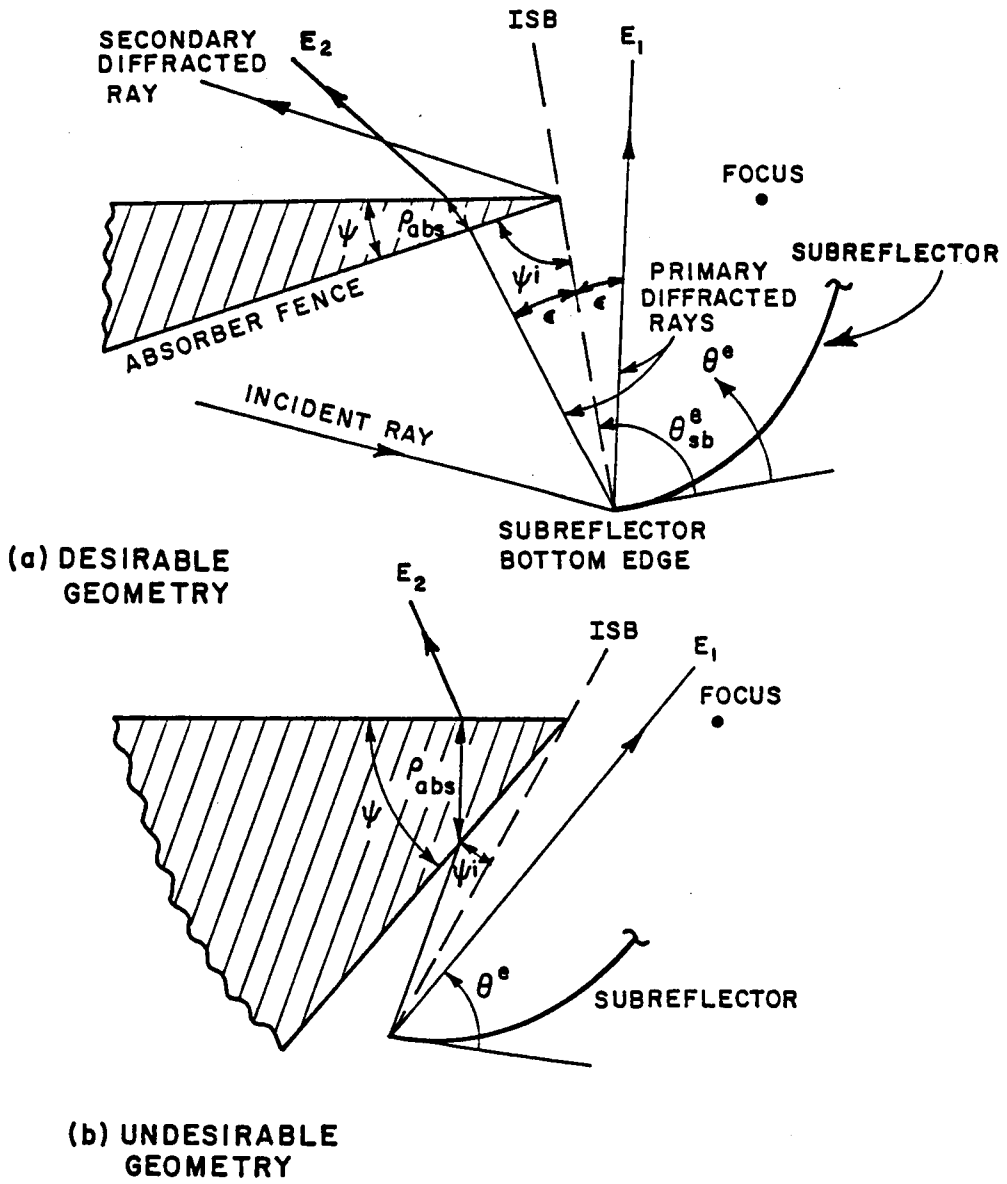
Figure 134: Conceptual wedge-like absorber aperture shape.

(E_2 at $\theta^e = \theta^e_{sb} + \epsilon$) are the same as ϵ goes to zero, and that the primary diffracted rays are attenuated gradually as they move away from the shadow boundary into the absorber; ie., as θ^e increases beyond θ^e_{sb}. Since there is then no difference between the fields on either side of the shadow boundary, the secondary diffracted rays are not first order diffracted fields, but rather slope diffracted fields. Slope diffracted fields correct discontinuities in the slope of a field on either side of a shadow boundary. If the difference in the slope is small, the slope diffracted fields can be much weaker than first order diffracted fields. Although the UTD slope diffraction coefficients for a lossy dielectric wedge do not exist at present, the principle still applies, as will be shown below.

In order for the slope diffracted secondary fields to be as small as possible, the difference in slope of the field on either side of the shadow boundary should also be as small as possible. Let ρ_{abs} be the distance that a ray travels through the absorber, as shown in Figure 134. To keep the slope diffracted fields small it is thus necessary to keep $d\rho_{abs}/d\theta^e$ small, since the attenuation is exponentially dependent on ρ_{abs}, and the phase shift is linearly related to ρ_{abs}. This concept can be translated into the geometrical consideration that the wedge angle (ψ) should be small, and that the angle with which the diffracted ray intercepts the face of the wedge at the ISB (ψ_i as shown in Figure 134) be close to 90°. On the other hand, ψ has to be large enough so that the slab reaches a sufficient thickness to attenuate the primary diffracted rays propagating in the direction of the main reflector. Desirable and undesirable geometries illustrating these concepts are illustrated in Figure 134.

A two-dimensional slab of absorbing material was analyzed using the method of moments[67] to investigate the effect of the size of the wedge angle on the magnitude of the fields diffracted from the apex of the wedge. (Note that the TE/TM

convention used in [67] is different from the convention used in this study). The method of moments is considered to be an exact solution within the constraints of numerical accuracy and in so far as the scattering body can be accurately modelled. However, because of the large number of variables involved its practical use is limited to bodies whose physical dimensions are small in terms of a wavelength. In the interest of computational efficiency, finite symmetrical slabs are considered as shown in Figure 135. In order to perform the moment method calculation the finite slab is divided into n_x divisions in the x-direction and n_y divisions in the y-direction, resulting in $n_x n_y$ cells. The incident field is a TE-polarized plane wave propagating in the x-direction. The patterns are calculated at a relatively low frequency in terms of normal compact range use (3 GHz) because of the limits imposed by the large number of variables that have to used with the moment method solution. In an attempt to isolate the diffraction effects from the apexes of the wedge, they are spaced a reasonable distance apart. It is assumed that the lossy dielectric material can be characterized by a complex permittivity; ie.,

$$\epsilon = \epsilon_0(\epsilon_r' - j\epsilon_r'') \tag{5.30}$$

where ϵ_0 is the permittivity of free space. The permeability is assumed to be that of free space (μ_0). As an example, the results for slabs with wedge angles of 90°, 14° and 26.6^o are shown in Figures 136–139. The emphasis of these results is on comparing the levels of the diffracted fields. The three slabs are designated as Q_0, Q_1 and Q_2 respectively, with the geometrical and material parameters given in Table 18. Figure 136 shows the normalized magnitudes of the total fields along a pattern cut parallel to the y-axis at a distance (x_{pat}) away from the main origin. For the cases considered, the scattered fields can be obtained by subtracting the incident fields from the total fields. The scattered fields relative to the incident
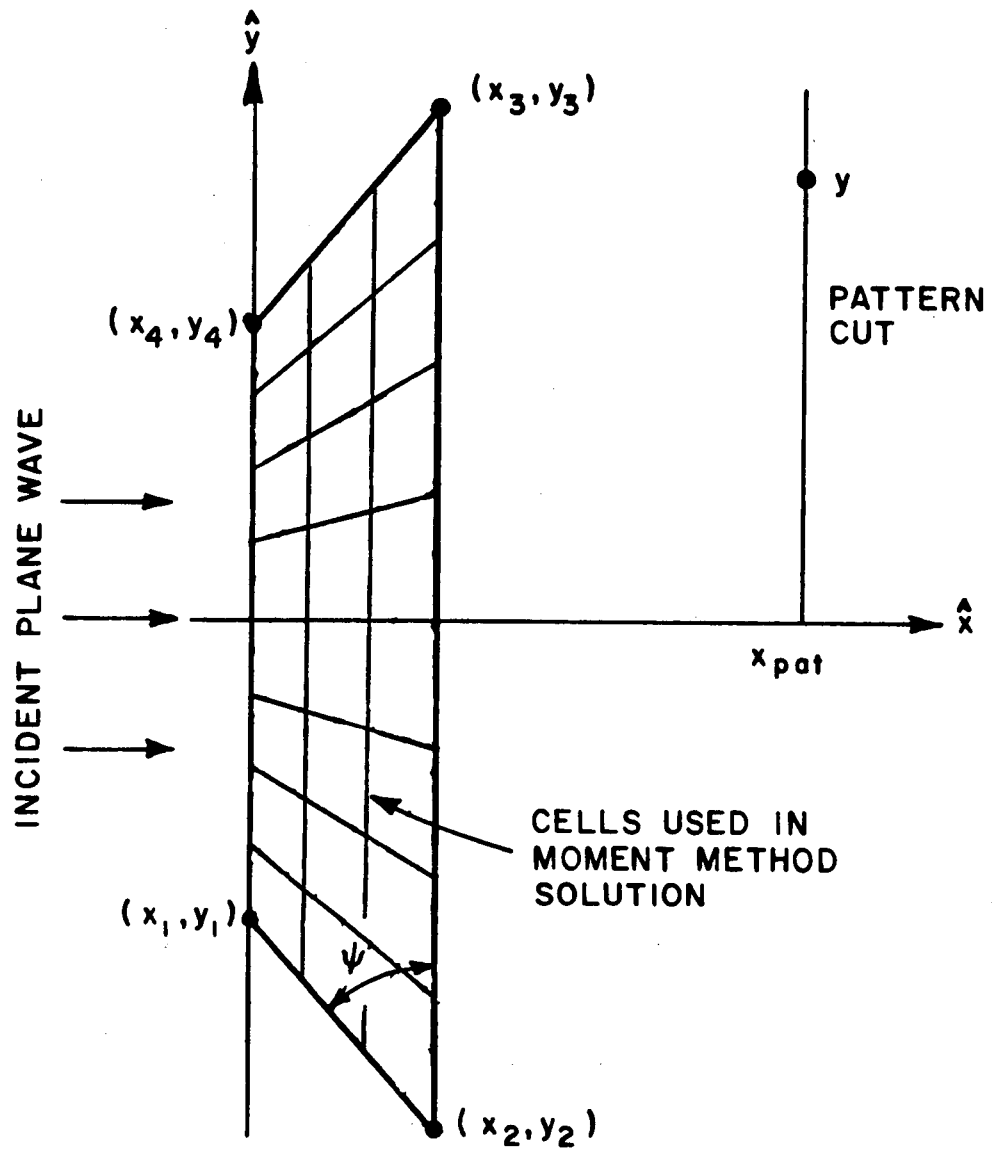
Figure 135: Finite symmetrical absorber slab.
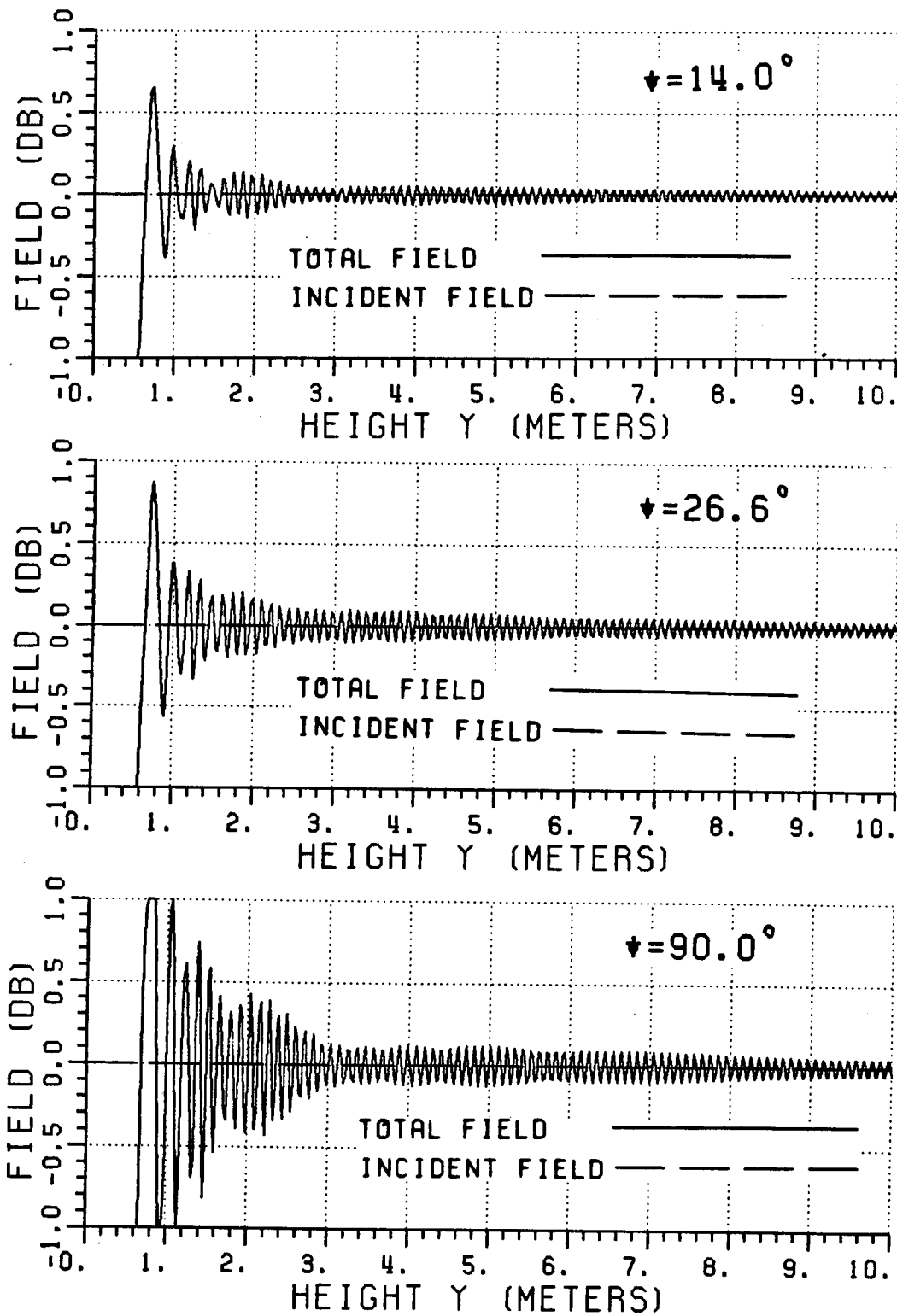
Figure 136: Normalized magnitude of total fields from finite symmetrical slabs with different wedge angles (3 GHz).

230
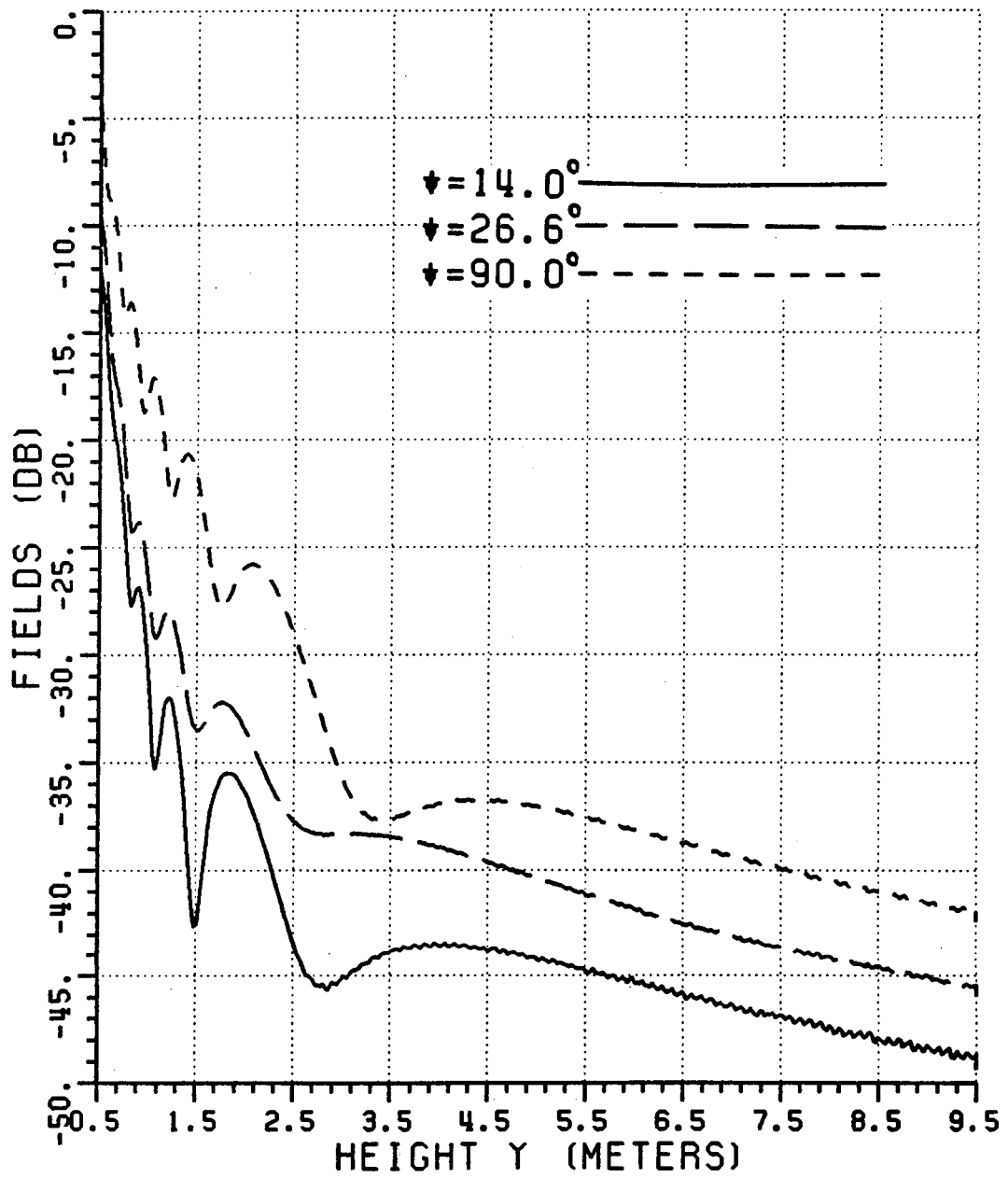
Figure 137: Diffracted fields (relative to incident fields) from finite symmetrical slabs with different wedge angles (3 GHz).

231
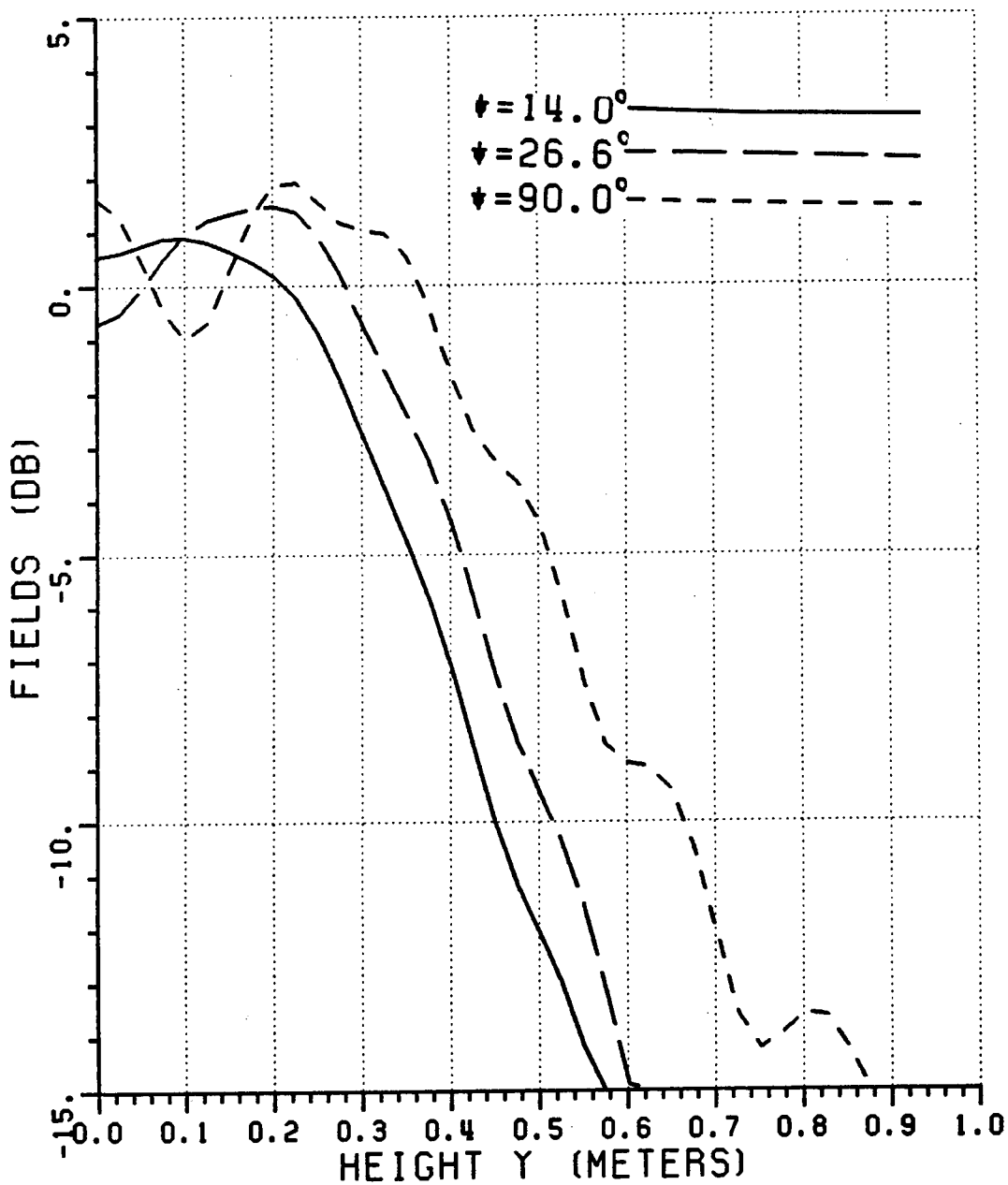
Figure 138: Detail of scattered fields (relative to the incident field) from finite symmetrical absorber slabs with different wedge angles (3 GHz).

232
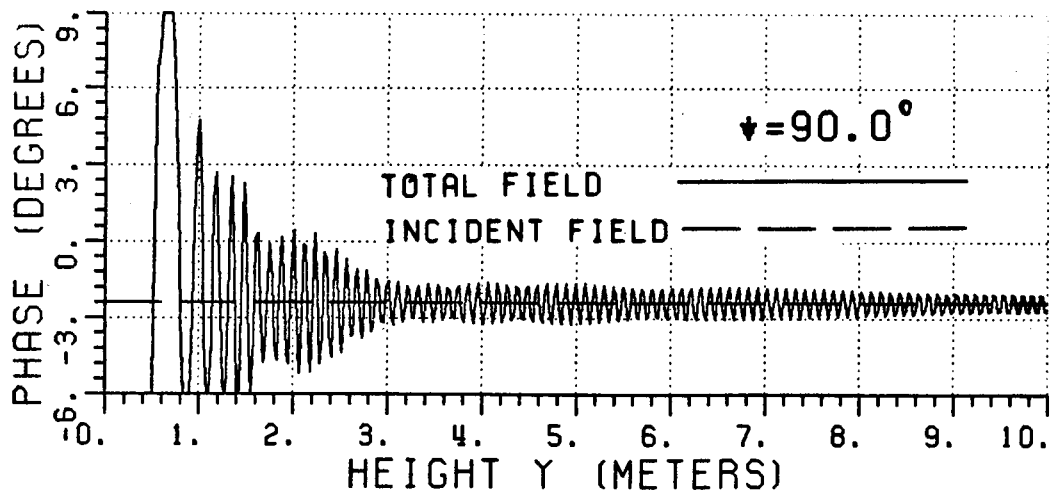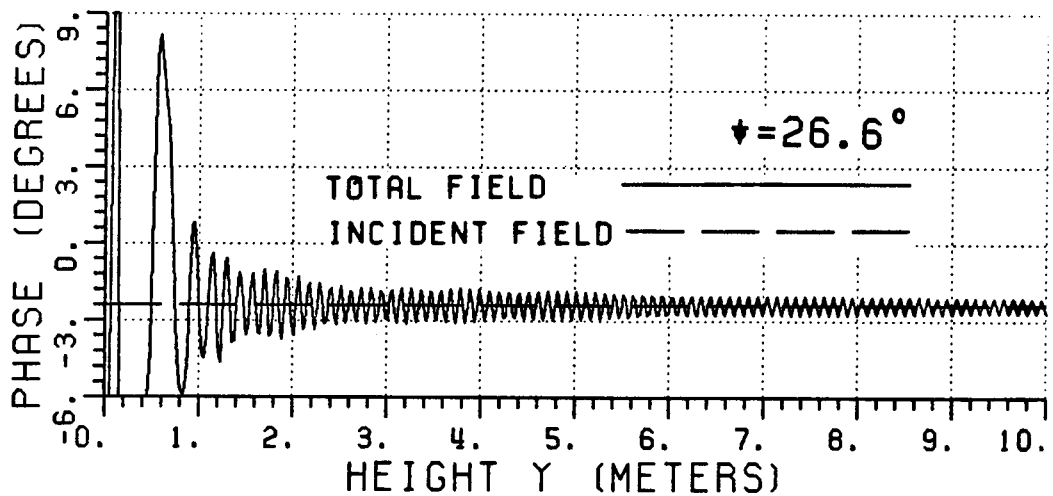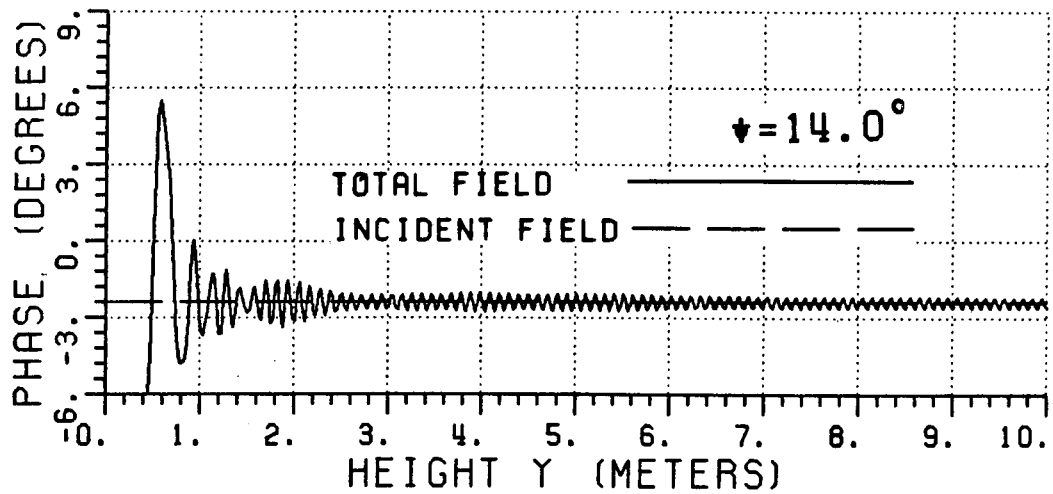
Figure 139: Phases of total fields from finite symmetrical slabs with different wedge angles (3 GHz).

233

Table 18: Parameters of the finite absorber slabs for comparison of the effect of the wedge angle (ψ).

	Q_0	Q_1	Q_2
ψ	90°	14°	26.6^o
x_1, y_1	0,-0.5	0,-0.1	0,-0.3
x_2, y_2	0.1,-0.5	0.1,-0.5	0.1,-0.5
x_3, y_3	0.1,0.5	0.1,0.5	0.1,0.5
x_4, y_4	0,0.5	0.1	0,0.3
ϵ_r'	1.5	1.5	1.5
ϵ_r''	1	1	1
n_x	6	8	8
n_y	51	60	60
x_{pat}	1	1	1
Dimensions in meters			

fields are shown in Figure 137. Note that the scattered fields are equal to the diffracted fields for $y > 0.5m$ in these examples. Figure 138 shows the scattered fields in detail in the region $0 < y < 1m$. Note that the peaks of the scattered fields do not occur at the geometrical ISB ($y_{isb} = 0.5m$), but are shifted towards the interior of the slabs. Figure 139 shows the phases of the total fields. Although these results are certainly not conclusive proof, they do indicate that, for the cases considered, a smaller wedge angle results in smaller diffracted fields. This is consistent with the previous contention that a smaller wedge angle results in smaller slope diffracted fields.

5.6 Design of an absorber fence

The analysis of a subreflector system with a realistic primary feed antenna and complex absorber fence is a very complicated problem, primarily due to the complexities involved in determining the scattering from a lossy dielectric wedge. However, building on the concepts developed above, one can discuss the general considerations that should be taken into account when designing an absorber fence, and in particular the coupling aperture.

The first step is to identify critical ray paths; ie., rays on the boundaries of desired and undesired illumination regions. The absorber fence should then be designed so as to leave the desired rays undisturbed and attenuate the undesired rays as much as possible and in such a way that the secondary diffracted rays created by the absorber fence have a minimal detrimental effect on the desired pattern. The coupling aperture of the absorber fence in Figure 123 is shown in detail in Figure 140. The critical ray paths in Figure 140 are indicated by the numbers 1–11; viz.,

(1),(2): Reflected from the subreflector to the bottom/top of the parabolic

235

section of the main reflector. These rays should be well clear of any part of the absorber fence, since they constitute the desired main reflector illumination.

(3),(4): Diffracted from the bottom edge of the subreflector to the bottom/top of the parabolic section of the main reflector. These rays should be strongly attenuated and therefore pass through a thick piece of absorber.

(5),(6): Diffracted from the top edge of the subreflector to the bottom/top of the parabolic section of the main reflector. These rays should be strongly attenuated and therefore pass through a thick piece of absorber.

(7): Reflected from the subreflector and passes through the top apex of the left side of the absorber fence aperture. As this ray moves deeper into the absorber, it approaches the primary RSB from the top edge of the subreflector. The ISB created by this ray should be directed away from the bottom edge junction.

(8),(9): Diffracted from the bottom edge of the subreflector and passes through the left/right side of the absorber fence aperture. Since it is assumed that the subreflector has an extended surface, these rays will propagate in a direction away from the main reflector.

(10): Reflected from the bottom edge of the subreflector along the RSB. This ray should not be directed towards either the main reflector or target zone.

(11): Direct from the primary feed antenna into the target zone; ie., spillover from the subreflector. This ray should be strongly attenuated and pass through a thick piece of absorber.

236

In order to satisfy the requirements of the critical rays, certain geometrical features can be incorporated nto the design of the absorber fence. The fence is terminated in wedges in the region of the aperture to facilitate a gradual attenuation of rays as they pass into the absorber and to ensure that the secondary diffractions from the fence are only small slope diffractions, as discussed in the previous section. The proposed absorber geometry is not intended to be an optimum design, but serves to illustrate the design approach. Figure 140 shows the yz-cut of a three-dimensional antenna configuration. The complete design would of course be three-dimensional, so that the left and right sides of the fence as shown in Figure 140 are representative of any cut through the coupling aperture. Consider now features (A)–(D):

(A): This wedge is needed to gradually attenuate rays (3), (4) and (11). Ray (8) propagates along the ISB created by the apex of the corresponding wedge, so that the resulting field diffracted from A will have a maximum amplitude in the direction of ray (8). Point A should thus be chosen such that ray (8) propagates in a direction away from the main reflector and target zone. Note that the ISB at A due to direct illumination from the feed, and hence direction of maximum diffraction amplitude, is not pointed at the main reflector. The thickness of the absorber should be sufficient to eliminate any effects due to these diffractions.

(B): This wedge is needed to gradually attenuate ray (7), which propagates along the ISB created by the apex of the corresponding wedge, so that the resulting field diffracted from B will have a maximum amplitude in the direction of ray (7). Point B should thus be chosen such that ray (7) does not point in the direction of the parabolic section of

the main reflector or the junction. Note that A and B together with the slopes of the corresponding wedges should also be chosen such that the path length of ray (4) through the absorber is long enough so that it is sufficiently attenuated by the time it reaches the parabolic section of the main reflector.

(C): This wedge is needed to start the gradual attenuation of ray (9). This wedge should also be thick enough to attenuate ray (11).

(D): The length of absorber from D to the top edge of the subreflector is needed to attenuate the primary diffracted rays from the top edge of the subreflector.
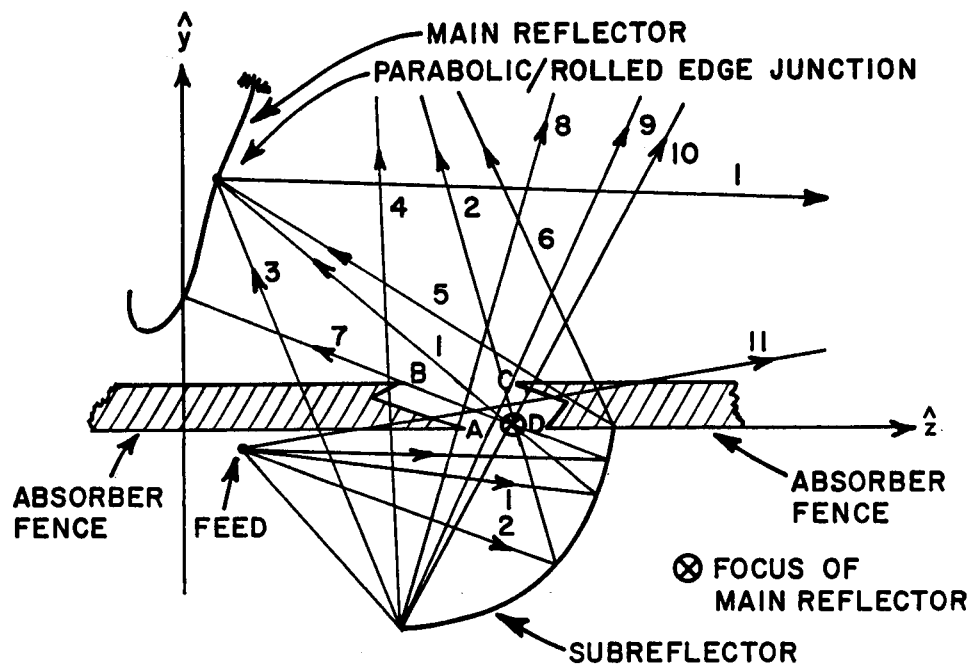
Figure 140: Design of the coupling aperture in the absorber fence.

CHAPTER VI

FORWARD SCATTERING FROM A HOMOGENEOUS LOSSY DIELECTRIC SLAB WITH WEDGE TERMINATIONS

6.1 Introduction

In this chapter the forward scattered field from a two-dimensional homogeneous slab of electromagnetic absorber with a wedge termination is analyzed. This structure is related to the absorber fence described in Chapter V. In order to analyze the absorber fence a technique is required whereby the forward scattering from electrically large structures can be obtained, since the moment method technique used in Section 5.5 is only practical for structures that are small in terms of a wavelength, and the UTD cannot be used since the diffraction coefficient for a lossy wedge is not known.

The problem of scattering from a dielectric wedge, and particularly a lossy dielectric wedge, is a complicated one to solve due in part to the difficult nature of the boundary conditions. DeWitt[65] has investigated pyramidal and wedge absorber structures that are used mainly to cover the walls, floor, ceiling and other static structures in an anechoic chamber. He concentrated on the backscatter characteristics of the absorber, but reported that many of the published solutions for scattering from dielectric wedges are either too limited or too complicated for practical use. In this chapter, a technique combining ray tracing and aperture integration is proposed; whereby, the forward scattering from a homogeneous lossy
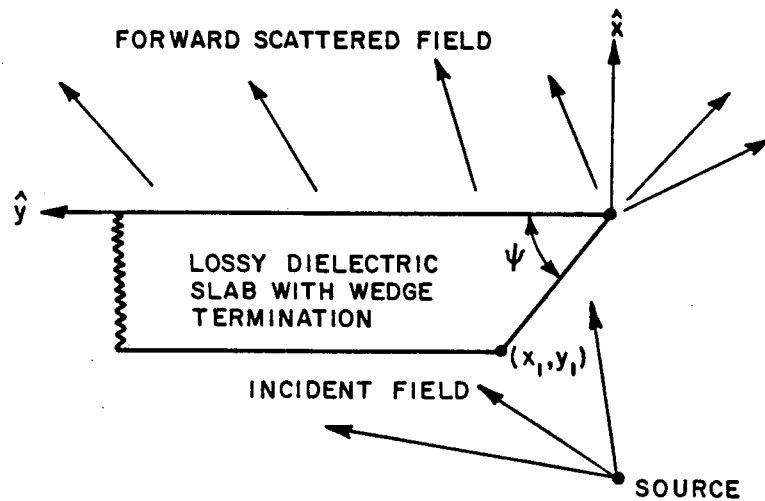
Figure 141: Forward scattering from a semi-infinite homogeneous lossy dielectric slab with a wedge termination.

dielectric slab with a wedge termination is determined. Consider the slab with a wedge termination and wedge angle (ψ) as shown in Figure 141. It is required to find the field in the region $x > 0$, with a source located in the region ($x < x_1, y < y_1$). Let a planar aperture be defined along the entire y-axis. The fields in the aperture are calculated through ray tracing, from which the equivalent currents in the aperture are found. An aperture integration is then performed over the aperture ($-\infty < y < \infty$) to find the total field at the field point.

Consider now that part of the aperture where the slab is present ($0 \leq y < \infty$). The aperture field in this region is found by tracing rays through the slab. The equivalent current in the aperture is then expressed in terms of the fields transmitted through the slab. Once the aperture current has been determined, the contribution to the total field at the field point from this part of the aperture is found by numerical integration. Since the integration would have to be performed numerically from $y = 0$ to $y = \infty$, this is not very feasible from a numerical

viewpoint. However, since the slab is assumed to be very lossy (it is after all an electromagnetic absorber), it is reasonable to assume that the field transmitted through it will only be significant in that area of the aperture where the wedge termination is present; ie., in the area around $(0 \leq y \leq y_1)$. The aperture field in that part of the aperture where the parallel section of the slab is present $(y_1 \leq y < \infty)$ will reduce as y increases, since rays propagating through the entire width of the slab will be strongly attenuated. As an approximation, the numerical integration need thus only be performed from $y = 0$ up to some point $(y = y_{small})$ where the transmitted field has been attenuated sufficiently to have an insignificant contribution. This point (y_{small}) corresponds the aperture location where the field becomes smaller than a predetermined level (E_z^{min}) and depends on the accuracy of the solution required, the geometry and material characteristics of the slab and the cost of running the integration on a computer. Note that the aperture field will be smaller than or equal to E_z^{min} for all $y > y_{small}$. In the case of a finite slab with wedge terminations on both ends, the integration can be performed over the entire length of the slab if the length of the slab is reasonable, as will be shown in Section 6.2.

Consider now that part of the aperture where the slab is not present $(-\infty < y \leq 0)$. It is shown in Appendix B that the integral in this region can be evaluated by the method of stationary phase. This leads to closed form expressions corresponding to a direct ray (stationary term) and a diffracted ray (end point term).

It is assumed that the homogeneous lossy dielectric material can be characterized by a complex permittivity; ie.,

$$\epsilon = \epsilon_0 (\epsilon_r' - j \epsilon_r'') \tag{6.1}$$

242

Table 19: Relative permittivities of typical absorber material.

Frequency (GHz)	ϵ_r'	ϵ_r''
1	3.00	0.59
3	1.50	0.69
10	1.45	0.58
100	1.30	0.03

where ϵ_0 is the permittivity of free space. The permittivity of absorber material is highly frequency dependent as shown in Table 19, where ϵ_r' and ϵ_r'' values for a typical absorber material[65] are listed for various frequencies. The permeability is assumed to be that of free space (μ_0). The two-dimensional TE case is considered throughout, but the technique can also be applied to the TM and/or three-dimensional cases.

6.2 Finite homogeneous lossy dielectric slab with wedge terminations and plane wave illumination

Consider now a finite homogeneous slab of lossy dielectric material with wedge terminations and plane wave illumination as shown in Figure 142. The plane wave is assumed to propagate in the x-direction. In order to obtain the transmitted field in the aperture, incident rays must be traced as they propagate through the slab. Consider first a wedge termination. The wedge is defined in a xy-coordinate system as shown in Figure 143, with the wedge corners designated as (x_1, y_1) and (x_2, y_2). For the purpose of this discussion (x_2, y_2) is located at the origin. The aperture is considered to be along the entire y-axis. Analysis of the ray path indicates that there is a transmission coefficient (T_1) at the free space/dielectric interface
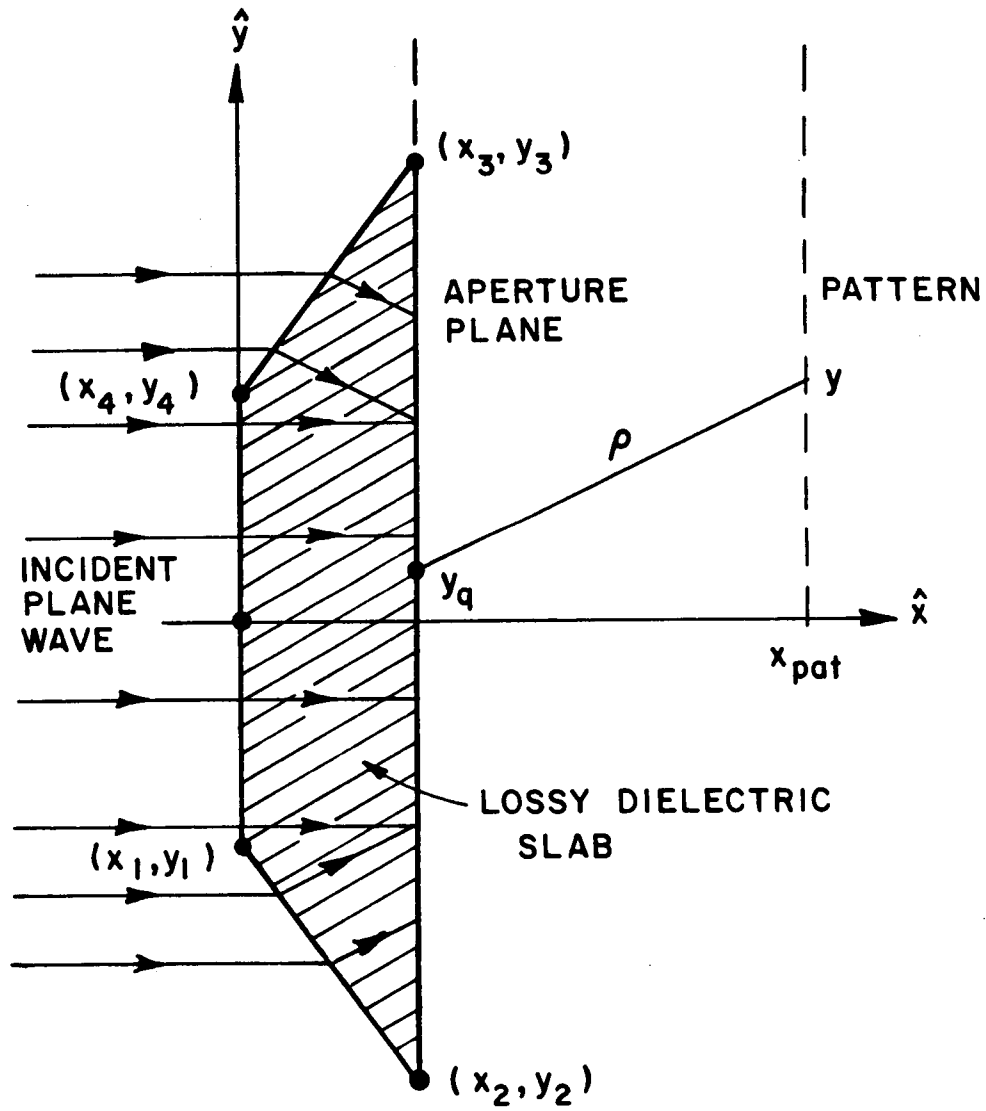
Figure 142: Finite homogeneous lossy dielectric slab with wedge terminations.
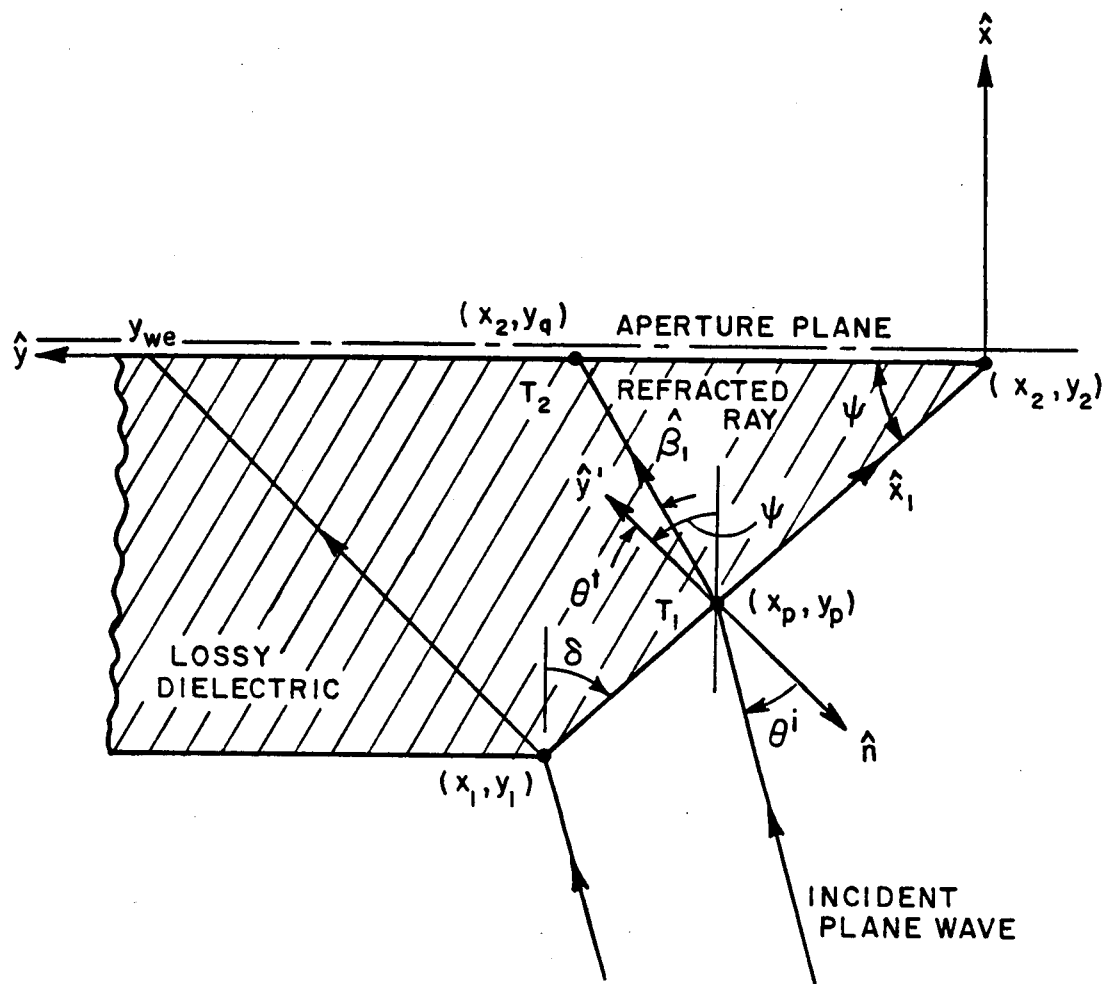
Figure 143: Refraction through a homogeneous lossy dielectric wedge.

as well as a propagation constant (β_1) and attenuation constant (α_1) as the ray propagates through the wedge. These parameters are determined in a $x'y'$-system that is compatible with the side of the wedge. Once the ray has passed through the first interface, it must be transformed into a coordinate system (xy-system) that is compatible with the aperture plane, since the two sides of the wedge are not parallel. A transmission coefficient (T_2) at the dielectric/free space interface is then found, after which the equivalent current in the aperture is determined, and the aperture integration performed. The GO spread factor (see Equation (2.2)) is equal to one in the case of a plane wave incident upon a planar interface.

6.2.1 Free space/dielectric interface

Consider now a ray propagating in free space that is obliquely incident at an angle (θ^i) on a lossy dielectric slab as shown in Figure 144. Let the incident field be a homogeneous plane wave which is given by

$$E_z^i = C e^{-jk(x' \sin \theta^i + y' \cos \theta^i)} \tag{6.2}$$

where k is the free space propagation constant and C is an arbitrary complex constant. The incident magnetic field is given by Maxwell's equations[22] as

$$\mathbf{H}^i = \frac{j}{\omega \mu_0} \nabla \times \mathbf{E}^i \tag{6.3}$$

or

$$\mathbf{H}^i = \frac{j}{\omega \mu_0} \left(\hat{\mathbf{x}}' \frac{\partial E_z^i}{\partial y'} - \hat{\mathbf{y}}' \frac{\partial E_z^i}{\partial x'} \right) \tag{6.4}$$

so that the tangential magnetic field at the interface ($y' = 0$) is given by

$$H_{x'}^i = \frac{k \cos \theta^i}{\omega \mu_0} C e^{-jk(x' \sin \theta^i + y' \cos \theta^i)} \tag{6.5}$$
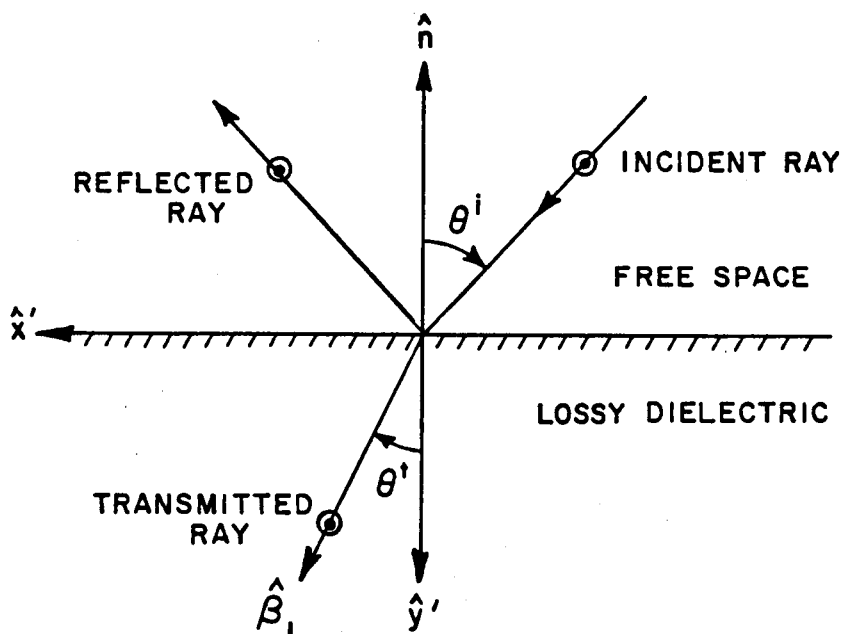
Figure 144: Refraction through a free space/dielectric interface.

where ω is the angular frequency of the field. Since the reflection angle is known to be equal to the incident angle[22], the reflected fields are given by

$$E_z^r = \Gamma_1 C e^{-jk(x'\sin\theta^i - y'\cos\theta^i)} \text{ , and} \tag{6.6}$$

$$H_{x'}^r = \frac{-k\cos\theta^i}{\omega\mu_0}\Gamma_1 C e^{-jk(x'\sin\theta^i - y'\cos\theta^i)} \tag{6.7}$$

where Γ_1 is a complex reflection constant. Stratton[68] has shown that the field transmitted into the dielectric can be expressed as

$$E_z^t = T_1 C e^{-j\beta_1(x'\sin\theta^t + y'\cos\theta^t)} e^{-\alpha_1 y'} \text{ .} \tag{6.8}$$

Applying Equation (6.4) to Equation (6.8), it follows that

$$H_{x'}^t = \frac{\beta_1\cos\theta^t - j\alpha_1}{\omega\mu_0}T_1 C e^{-j\beta_1(x'\sin\theta^t + y'\cos\theta^t)} e^{-\alpha_1 y'} \tag{6.9}$$

where

$$T_1 \quad = \quad \text{complex transmission coefficient}$$

247

$$\beta_1 = \text{propagation constant in the dielectric}$$

$$\alpha_1 = \text{attenuation constant in the dielectric , and}$$

$$\theta^t = \text{real transmission angle .}$$

Examination of Equation (6.8) shows that the transmitted field in the lossy dielectric is an inhomogeneous plane wave. The phase planes propagate in the direction

$$\hat{\beta}_1 = \hat{x}' \sin \theta^t + \hat{y}' \cos \theta^t \tag{6.10}$$

while the amplitude attenuates in the y'-direction. The transmitted field has to satisfy the wave equation[22]; ie.,

$$\nabla^2 E_z^t + k_1^2 E_z^t = 0 \tag{6.11}$$

where k_1 is the complex propagation constant in the dielectric, which is given by

$$k_1 = \omega \sqrt{\mu_0 \epsilon} = k \sqrt{\epsilon_r' - j \epsilon_r''} \ . \tag{6.12}$$

Applying Equation (6.11) to Equation (6.8), one finds that

$$\alpha_1^2 - \beta_1^2 = -k^2 \epsilon_r' \ , \text{ and} \tag{6.13}$$

$$2 \, \alpha_1 \beta_1 \, \cos \theta^t = k^2 \epsilon_r'' \ . \tag{6.14}$$

The variables Γ_1, T_1, θ^t, β_1 and α_1 can be determined by using Equations (6.13) and (6.14) and the boundary conditions that the tangential electric and magnetic fields should be continuous across the interface at $y' = 0$; ie.,

$$E_z^i + E_z^r = E_z^t \ , \text{ and} \tag{6.15}$$

$$H_{x'}^i + H_{x'}^r = H_{x'}^t \ . \tag{6.16}$$

Enforcement of the boundary conditions yield the relations

$$1 + \Gamma_1 = T_1 \tag{6.17}$$

248

$$k \cos \theta^i (1 - \Gamma_1) = (\beta_1 \cos \theta^t - j\alpha_1)T_1 \text{ , and} \tag{6.18}$$

$$k \sin \theta^i = \beta_1 \sin \theta^t \text{ .} \tag{6.19}$$

Solving for Equations (6.13), (6.14) and (6.17)–(6.19), one finds that

$$\beta_1 = k\sqrt{\frac{\epsilon_r' + \sin^2 \theta^i + \sqrt{(\epsilon_r' - \sin^2 \theta^i)^2 + (\epsilon_r'')^2}}{2}} \tag{6.20}$$

$$\alpha_1 = \sqrt{\beta_1^2 - k^2 \epsilon_r'} \tag{6.21}$$

$$\theta^t = \arcsin\left(\frac{k \sin \theta^i}{\beta_1}\right) \tag{6.22}$$

$$T_1 = \frac{2k \cos \theta^i}{k \cos \theta_i + \beta_1 \cos \theta^t - j\alpha_1} \text{ , and} \tag{6.23}$$

$$\Gamma_1 = T_1 - 1 \text{ .} \tag{6.24}$$

6.2.2 Transformation of coordinates

In order to transform the ray parameters to a coordinate system compatible with the aperture (xy-system), consider the transformation shown in Figure 145 which is given by

$$\hat{\mathbf{x}}' = \hat{\mathbf{x}} \cos \delta - \hat{\mathbf{y}} \sin \delta \text{ , and} \tag{6.25}$$

$$\hat{\mathbf{y}}' = \hat{\mathbf{x}} \sin \delta + \hat{\mathbf{y}} \cos \delta \tag{6.26}$$

where δ is the angle with which the $x'y'$-system is rotated with respect to the xy-system. Note that δ is related to the wedge angle (ψ) by the following equation:

$$\delta + \psi = 90^o \text{ .} \tag{6.27}$$

Let the electric field that is transmitted into the dielectric (as given in Equation (6.8)) be expressed as

$$E_z^t = T_1 C e^{(\hat{\mathbf{x}}' \gamma_x' + \hat{\mathbf{y}}' \gamma_y') \cdot (x' \hat{\mathbf{x}}' + y' \hat{\mathbf{y}}')} \tag{6.28}$$

249
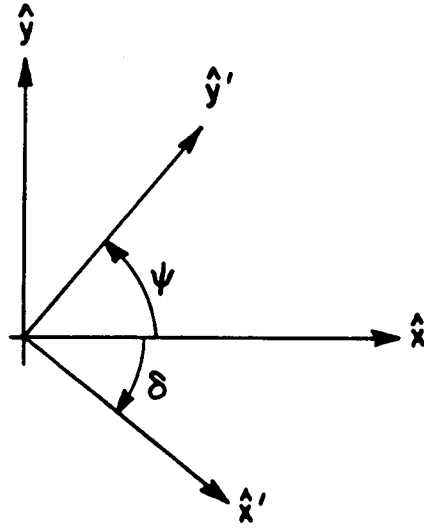
Figure 145: Wedge coordinate transformation.

where

$$\gamma'_x = -j\beta_1 \sin \theta^t \text{ , and} \tag{6.29}$$

$$\gamma'_y = -(\alpha_1 + j\beta_1 \cos \theta^t) \text{ .} \tag{6.30}$$

The transmitted electric field can, however, also be written as

$$E_z^t = T_1 C e^{(\hat{x}'\gamma'_x + \hat{y}'\gamma'_y)\cdot(x\hat{x}+y\hat{y})} \text{ .} \tag{6.31}$$

Equation (6.31) represents the field that is transmitted into the dielectric in the xy-system. Substituting Equations (6.25) and (6.26) into Equation (6.31), one finds that

$$E_z^t = T_1 C e^{-x(\alpha_x + j\beta_x)} e^{-y(\alpha_y + j\beta_y)} \tag{6.32}$$

where

$$\alpha_x = \alpha_1 \sin \delta \tag{6.33}$$

$$\alpha_y = \alpha_1 \cos \delta \tag{6.34}$$

250
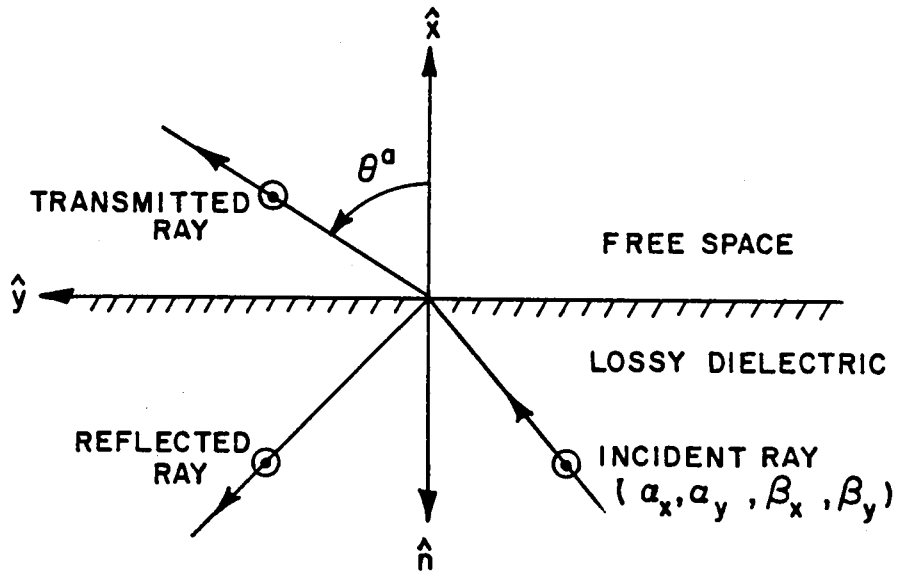
Figure 146: Refraction through a dielectric/free space interface.

$$\beta_x = \beta_1 \sin(\theta^t + \delta) \text{ , and} \qquad (6.35)$$

$$\beta_y = \beta_1 \cos(\theta^t + \delta) \text{ .} \qquad (6.36)$$

6.2.3 Dielectric/free space interface

Consider now a ray propagating through a lossy dielectric such that it is obliquely incident on a dielectric/free space interface as shown in Figure 146. Let the incident field have the following form:

$$E_z^i = C e^{-x(\alpha_x + j\beta_x)} e^{-y(\alpha_y + j\beta_y)} \qquad (6.37)$$

where C is an arbitrary complex constant, and α_x, β_x, α_y and β_y are given in Equations (6.33)–(6.36). Applying Equation (6.4) to Equation (6.37), one finds that the incident magnetic field is given by

$$H_y^i = \frac{jC}{\omega\mu_0}(\alpha_x + j\beta_x) e^{-x(\alpha_x + j\beta_x)} e^{-y(\alpha_y + j\beta_y)} \text{ .} \qquad (6.38)$$

The reflected fields are then given by:

$$E_z^r = \Gamma_2 C e^{x(\alpha_x + j\beta_x)} e^{-y(\alpha_y + j\beta_y)} \text{ , and} \qquad (6.39)$$

251

$$H_y^r = -\Gamma_2 \frac{jC}{\omega\mu_0}(\alpha_x + j\beta_x)e^{x(\alpha_x+j\beta_x)}e^{-y(\alpha_y+j\beta_y)} \qquad (6.40)$$

where Γ_2 is a complex reflection coefficient. The field transmitted from the dielectric into free space is given by

$$E_z^t = T_2 C e^{-j\beta_0(x\cos\theta^a+y\sin\theta^a)}e^{-\alpha_0(-x\sin\theta^a+y\cos\theta^a)} \text{ , and} \qquad (6.41)$$

$$\begin{aligned}H_y^t = \frac{-T_2 C}{\omega\mu_0}(\beta_0\cos\theta^a + j\alpha_0\sin\theta^a) \\ e^{-j\beta_0(x\cos\theta^a+y\sin\theta^a)}e^{-\alpha_0(-x\sin\theta^a+y\cos\theta^a)}\end{aligned} \qquad (6.42)$$

where T_2 is a complex transmission coefficient and θ^a is a real angle. Note that the field in free space is attenuated in a direction perpendicular to the direction of propagation. This is allowed by Maxwell's equations, as shown below. It is necessary to introduce a complex propagation constant of the form $\alpha + j\beta$ for the field transmitted into free space in order to match the complex propagation constant of the tangential field in the dielectric slab at the interface. The transmitted field has to satisfy the wave equation; ie.,

$$\nabla^2 E_z^t + k^2 E_z^t = 0 . \qquad (6.43)$$

Applying Equation (6.43) to Equation (6.41) one finds that

$$\alpha_0^2 - \beta_0^2 = -k^2 . \qquad (6.44)$$

The variables Γ_2, T_2, θ^a, β_0 and α_0 can be determined by using Equation (6.44) and the boundary condition that the tangential fields should be continuous across the interface at $x = 0$. Enforcement of the boundary condition yield the following relations:

$$1 + \Gamma_2 = T_2 \qquad (6.45)$$

$$\alpha_y = \alpha_0 \cos\theta^a \qquad (6.46)$$

252

$$\beta_y = \beta_0 \sin \theta^a \text{ , and} \tag{6.47}$$

$$(\alpha_x + j\beta_x)(1 - \Gamma_2) = T_2(-\alpha_0 \sin \theta^a + j\beta_0 \cos \theta^a) \text{ .} \tag{6.48}$$

Solving for Equations (6.44)–(6.48) one finds that

$$\beta_0 = \sqrt{\frac{\beta_{0+} + k^2 + \sqrt{\beta_{0+}^2 + 2k^2\beta_{0-} + k^4}}{2}} \tag{6.49}$$

$$\alpha_0 = \sqrt{\beta_0^2 - k^2} \tag{6.50}$$

$$\theta^a = \arcsin\left(\frac{\beta_y}{\beta_0}\right) \tag{6.51}$$

$$T_2 = \frac{2(\alpha_x + j\beta x)}{(\alpha_x - \alpha_0 \sin \theta^a) + j(\beta_x + \beta_0 \cos \theta^a)} \text{ , and} \tag{6.52}$$

$$\Gamma_2 = T_2 - 1 \tag{6.53}$$

where

$$\beta_{0+} = \alpha_y^2 + \beta_y^2 \text{ , and} \tag{6.54}$$

$$\beta_{0-} = \alpha_y^2 - \beta_y^2 \text{ .} \tag{6.55}$$

6.2.4 Total aperture field in the region $y_2 \leq y \leq y_3$

Let the incident ray intercept the wedge at (x_p, y_p) as shown in Figure 143. The refracted ray will be transmitted to a point (x_2, y_q) in the aperture, where

$$y_q(x_p) = (x_2 - x_p)\tan(\psi - \theta^t) + y_p \text{ .} \tag{6.56}$$

The transmitted magnetic field in that part of the aperture which is illuminated by rays propagating through the wedge is given by

$$H_y^{ap}(y_q) = \frac{-T_1 T_2}{Z_0}\left(\frac{\beta_0 \cos \theta^a + j\alpha_0 \sin \theta^a}{k}\right) e^{-j\beta_1 \rho_{abs}} e^{-\alpha_1 y'_{abs}} \tag{6.57}$$

for $y_2 \leq y_q \leq y_{we}$, where

$$y_{we} = y_q(x_1) \tag{6.58}$$

$$\rho_{abs} = \sqrt{(x_2 - x_p)^2 + (y_q - y_p)^2} \text{ , and} \tag{6.59}$$

$$y'_{abs} = \rho_{abs} \cos \theta^t \tag{6.60}$$

253

if the plane $y' = 0$ is chosen as the phase reference. Note that H_y^{ap} as given in Equation (6.57) is applicable to rays entering the wedge part of the slab between y_1 and y_2 as shown by Figure 142. A similar analysis yields the aperture field due to rays entering the wedge part of the slab between y_3 and y_4. The aperture field due to rays entering the middle part of the slab ($y_1 \leq y \leq y_4$) is obtained by setting $\theta^i = 0$ when evaluating Equation (6.57). This is thus a special case where the plane wave is perpendicularly incident on the slab. One finds that the aperture field in the middle of the slab due to rays entering the slab between y_1 and y_4 is given by

$$H_y^{ap} = \frac{-T_3 T_4}{Z_0} e^{-jk_1(x_2 - x_1)} \quad \text{for } y_1 \leq y_q \leq y_4 \qquad (6.61)$$

where k_1 is given in Equation (6.12),

$$T_3 = \frac{2k}{k + k_1} , \text{ and} \qquad (6.62)$$

$$T_4 = \frac{2k_1}{k_1 + k} . \qquad (6.63)$$

6.2.5   Total forward scattered field

Consider now a homogeneous finite symmetric dielectric slab with wedge terminations as shown in Figure 142. Since a moment method solution will be used to compare the results obtained from the aperture integration technique, the symmetry is utilized in the interest of computational efficiency. Symmetry is not, however, required for the technique to be applicable. A pattern cut is taken at a distance (x_{pat}) from the origin along a line parallel to the y-axis. The aperture is considered to be located along a line parallel to the y-axis, just outside the slab. Note that $x_1 = x_4 = 0$ in this case. The total field along the pattern cut is found by integrating the surface current in the aperture and is given by[11]

$$E_z^s(y) = \frac{-kZ_0}{4} \int_{-\infty}^{\infty} J_z(y_q) H_0^{(2)}(k\rho) \, dy_q \qquad (6.64)$$

254
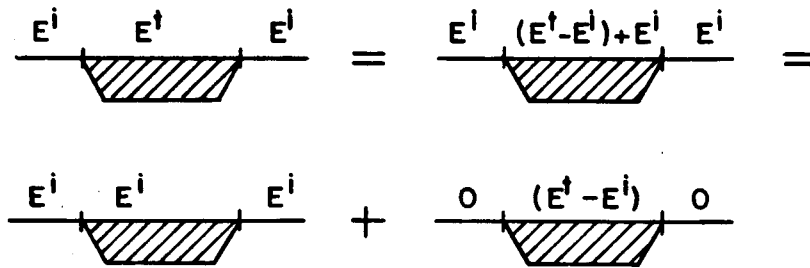
Figure 147: Composition of the aperture fields for a finite dielectric slab.

where

$$J_z = \text{electric surface current in the aperture}$$

$$H_0^{(2)} = \text{Hankel function of the second kind and order zero}$$

$$y = \text{field point position along the pattern cut , and}$$

$$\rho = \sqrt{(x_2 - x_{pat})^2 + (y_q - y)^2} \,. \tag{6.65}$$

To perform the numerical integration from $-\infty$ to $+\infty$ would not be feasible. This dilemma is solved, however, by subtracting and adding the incident field from the transmitted field in that part of the aperture where the slab is present. The total field in the aperture is then the superposition of the incident field, which is present from $-\infty$ to $+\infty$, and the scattered field $(E_z^t - E_z^i)$, which is present only in that part of the aperture where the slab is present $(y_2 \leq y \leq y_3)$. This situation is graphically illustrated in Figure 147. The aperture integration need thus only be performed over the length of the slab, since integration of E_z^i (which now extends over the entire aperture) will just give E_z^i (with the phase adjusted

accordingly) back at the field point. The total field at the field point will thus be the superposition of the incident field and the integration of the equivalent current produced by $E_z^t - E_z^i$ over that part of the aperture where the slab is present. Since the aperture is planar, the equivalent surface current is given by[22]

$$J_z(y_q) = 2[H_y^{ap}(y_q) - H_y^i(x_2)] \quad \text{for } y_2 \le y_q \le y_3 \tag{6.66}$$

where

$$H_y^i(x) = \frac{-e^{-jkx}}{Z_0} \tag{6.67}$$

and $H_y^{ap}(y_q)$ is given in Equations (6.57) and (6.61). Depending on the geometry and material characteristics, areas in the middle part of the slab may exist where a particular point in the aperture is illuminated by rays that are transmitted through the middle of the slab as well as through one or both of the wedge sides. This situation is shown in Figure 142.

The total field at a field point along the pattern cut is thus given by

$$E_z^s(y) = E_z^i(x_{pat}) - \frac{kZ_0}{2} \int_{y_2}^{y_3} [H_y^{ap}(y_q) - H_y^i(x_2)] H_0^{(2)}(k\rho) \, dy_q \tag{6.68}$$

where

$$E_z^i(x) = e^{-jkx} . \tag{6.69}$$

Note that if $k\rho$ is large, then the large argument form of the Hankel function can be used; ie.,

$$H_0^{(2)}(x) \ \rightarrow \ \sqrt{\frac{2}{\pi x}} e^{-j(x-\pi/4)} \quad \text{as} \ x \rightarrow \infty \tag{6.70}$$

so that

$$E_z^s(y) = E_z^i(x_{pat}) - e^{j\pi/4} Z_0 \sqrt{\frac{k}{2\pi}} \int_{y_2}^{y_3} [H_y^{ap}(y_q) - H_y^i(x_2)] \frac{e^{-jk\rho}}{\sqrt{\rho}} \, dy_q \tag{6.71}$$

when $k\rho$ is large. This equation is valid for all pattern points in this example.

256

Table 20: Parameters of finite absorber slabs.

	Q_1	Q_2	Q_3	Q_4
ψ	14°	26.6^o	14°	26.6^o
x_1, y_1	0,-0.1	0,-0.3	0,-0.1	0,-0.3
x_2, y_2	0.1,-0.5	0.1,-0.5	0.1,-0.5	0.1,-0.5
x_3, y_3	0.1,0.5	0.1,0.5	0.1,0.5	0.1,0.5
x_4, y_4	0,0.1	0,0.3	0,0.1	0,0.3
ϵ_r'	1.5	1.5	3.0	3.0
ϵ_r''	1	1	0.59	0.59
n_x	8	8	6	6
n_y	60	60	55	55
n_a	600	600	300	300
x_{pat}	1	1	1	1
Dimensions in meters				

6.2.6 Results

In order to verify the validity of the aperture integration technique, the scattered field obtained from Equation (6.71) is compared to that obtained by a moment method solution as described in Section 5.5. Four cases are considered; viz., geometries Q_1 and Q_2 (as discussed in Section 5.5) as well as geometries Q_3 and Q_4. The geometrical and material parameters are given in Table 20. Note that Q_3 and Q_4 are the same size as Q_1 and Q_2, respectively, but their material characteristics are different. Q_3 and Q_4 are not as lossy as Q_1 and Q_2, but they are much denser. Simpson's method is used to implement the integration in Equation (6.71)

257

with n_a sample points in the aperture. Patterns are calculated at 3 GHz for Q_1 and Q_2, and at 1 GHz for Q_3 and Q_4. Figures 148–152 compare the results obtained by applying the moment method and aperture integration techniques to Q_1, Figures 153–157 for Q_2, Figures 158–160 for Q_3, and Figures 161–163 for Q_4. Due to the symmetry, the results are shown in the region $y > 0$ only. Figures 148, 153, 158 and 161 show the magnitude of the total field along the pattern cut as well as the aperture field and incident field. Figures 149 and 154 show the detail amplitude of the ripple in the total field for Q_1 and Q_2 at large distances. The scattered field can be obtained by subtracting the incident field from the total field in the case of the moment method, and is given by the integration term in Equation (6.71) in the case of the aperture technique. For the geometries, material characteristics and pattern cut considered, the scattered field will be equal to the diffracted field in the region $y \geq y_3$. The scattered fields are shown in Figures 150, 155, 159 and 162. Figures 151, 156, 160 and 163 show the phase of the total field along the pattern cut as well as the phase of the incident field; whereas, Figures 152 and 157 show the ripple in the phase of the total field in detail for Q_1 and Q_2. The discrepancies between the results obtained from the moment method and aperture integration techniques indicate that the latter is indeed only an approximation. Nevertheless, it does predict the scattered field, and thus also the fields diffracted by the wedges, to an acceptable accuracy. The main advantage of this technique is that electrically large structures can be analyzed in a computationally efficient manner. The inaccuracies in the results obtained by the aperture integration technique are probably due to the fact that not all mechanisms have been accounted for. The most obvious is the effect of reflected rays in the interior of the slab. These rays are multiply reflected in the interior of the wedge before being transmitted into free space. This effect would be most noticeable near the apex of a wedge, since
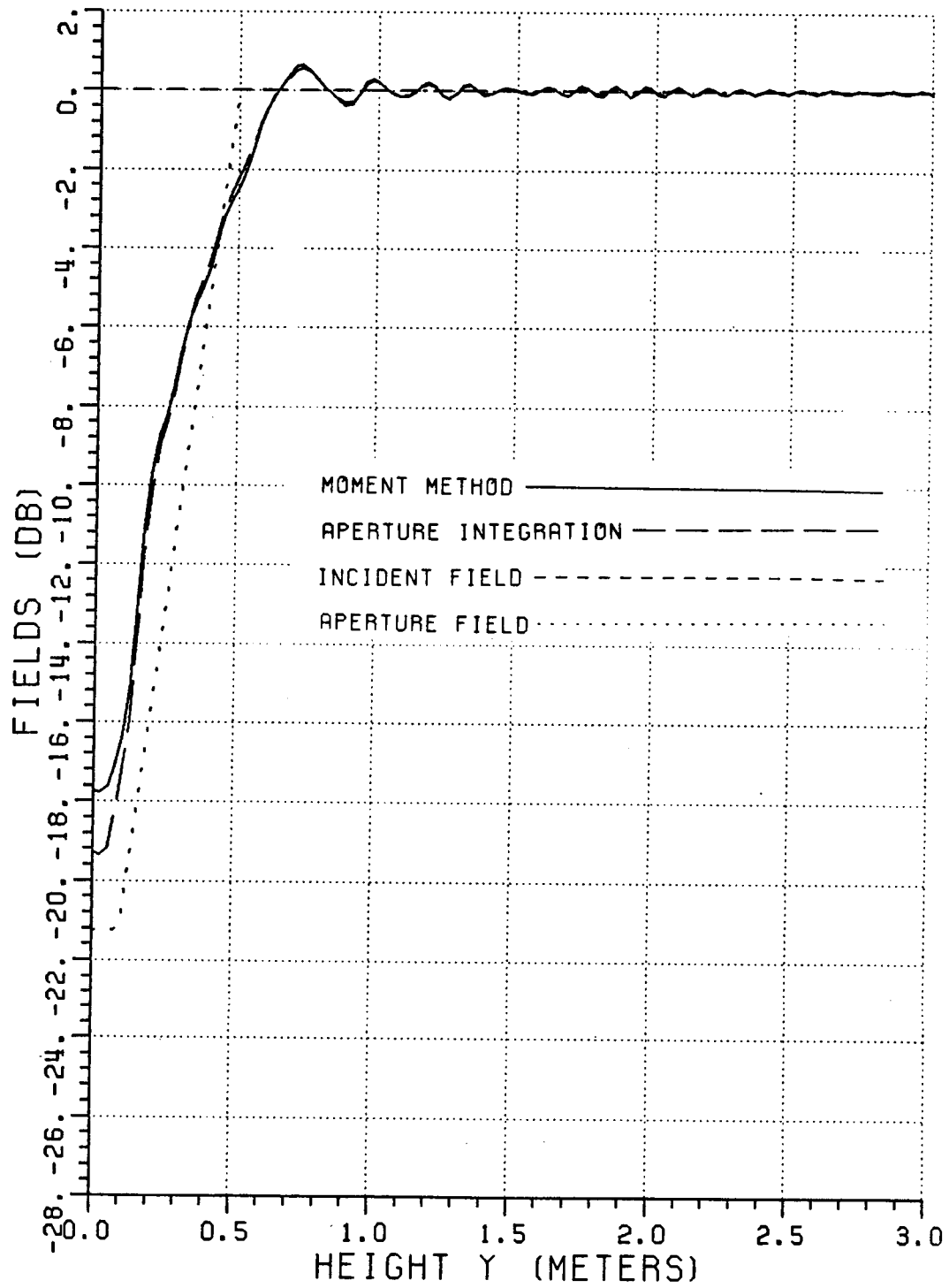
Figure 148: Normalized magnitude of the total fields for Q_1 (3 GHz).

259
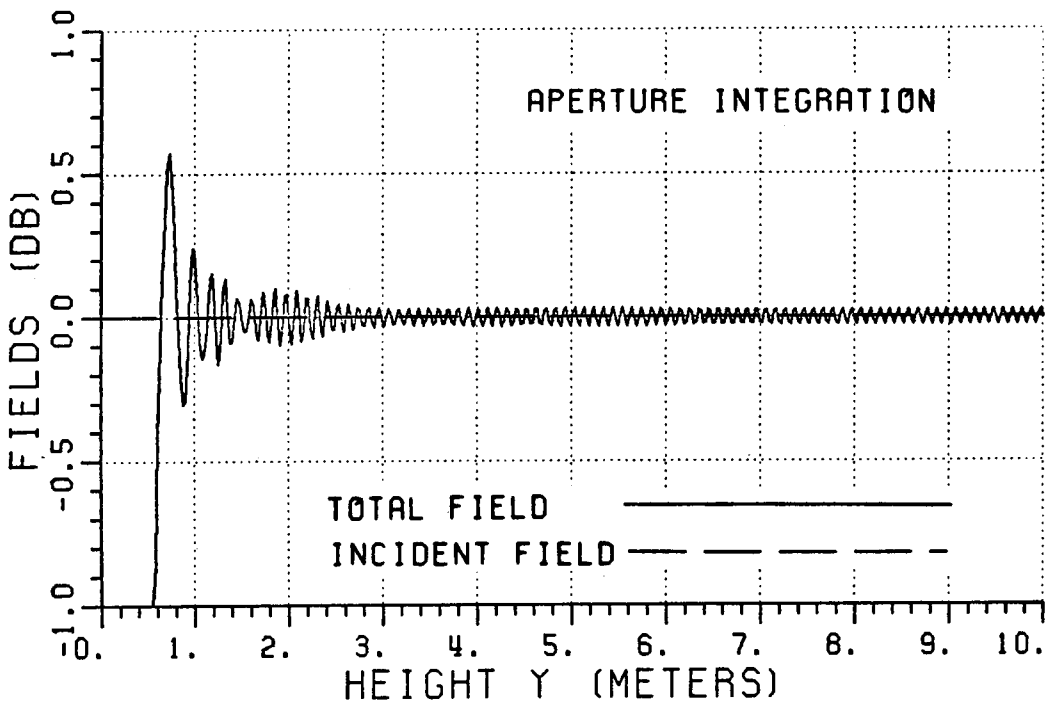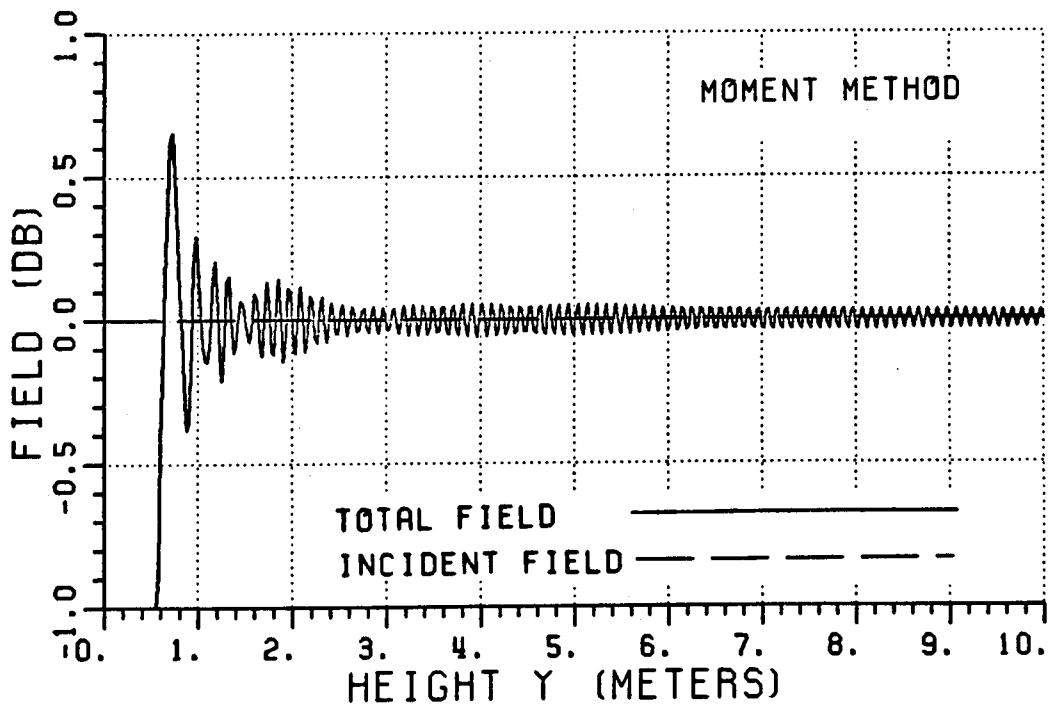
Figure 149: Detail of the ripple in the magnitude of the total fields for Q_1
(3 GHz).
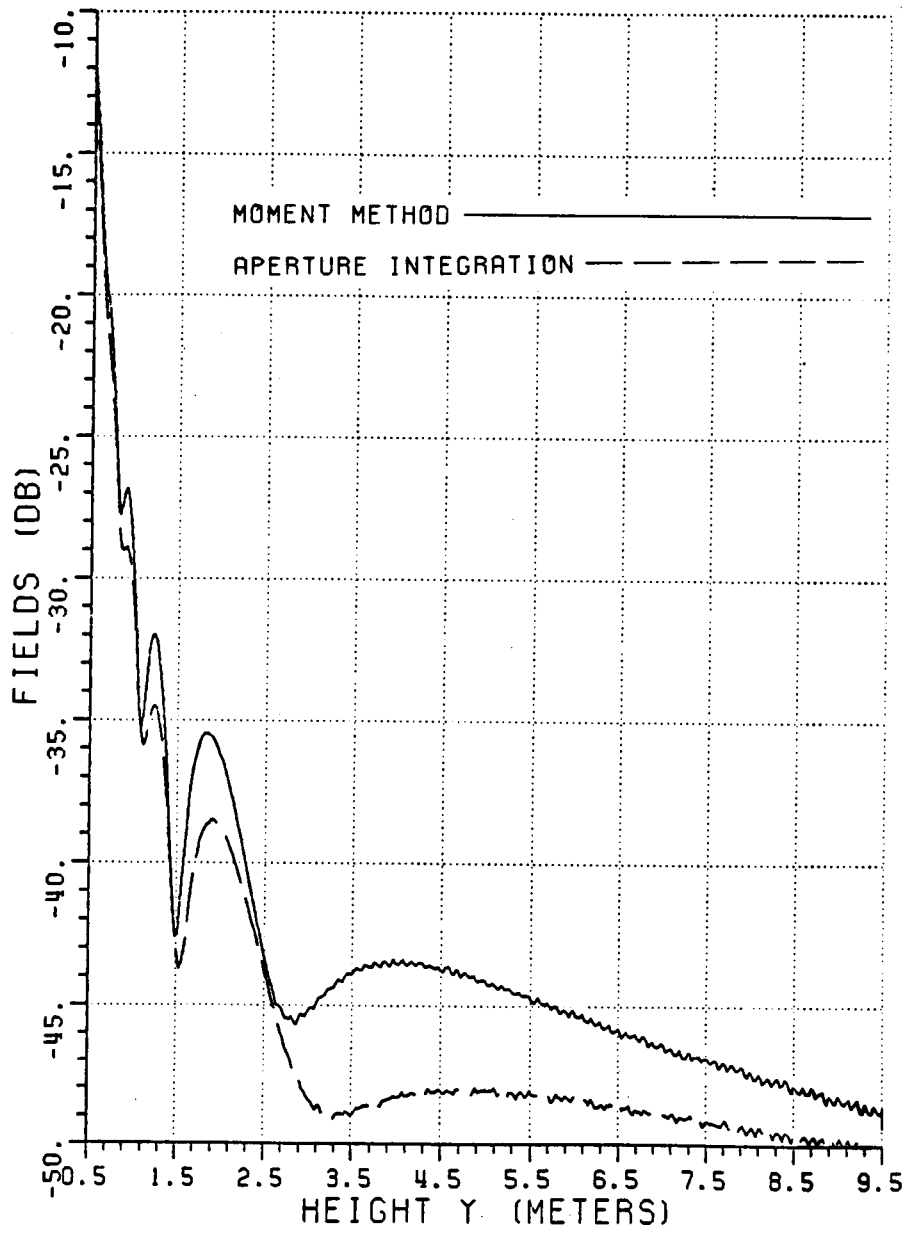
Figure 150: Scattered fields (relative to incident field) for Q_1 (3 GHz).

261
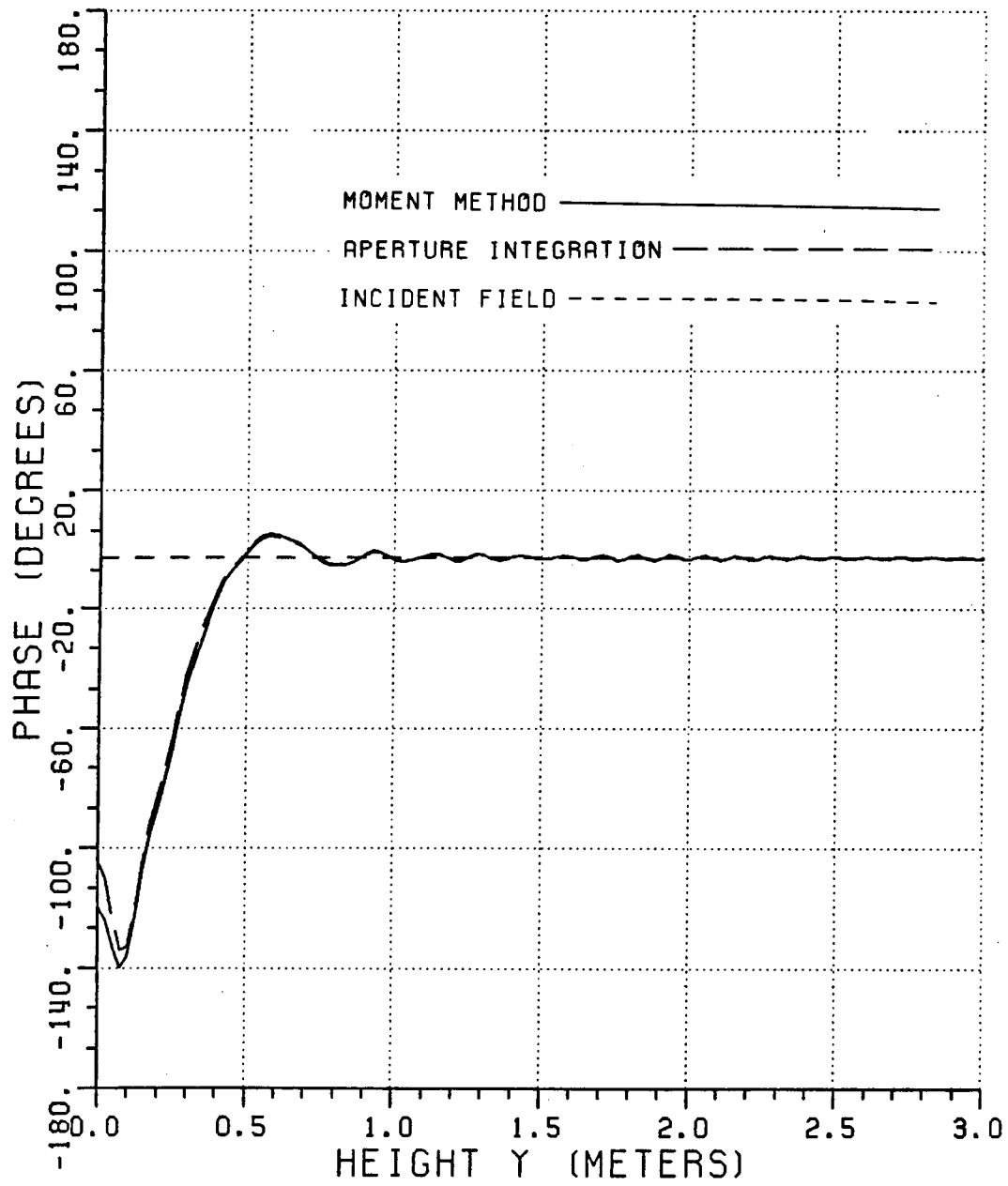
Figure 151: Phases of the total fields for Q_1 (3 GHz).
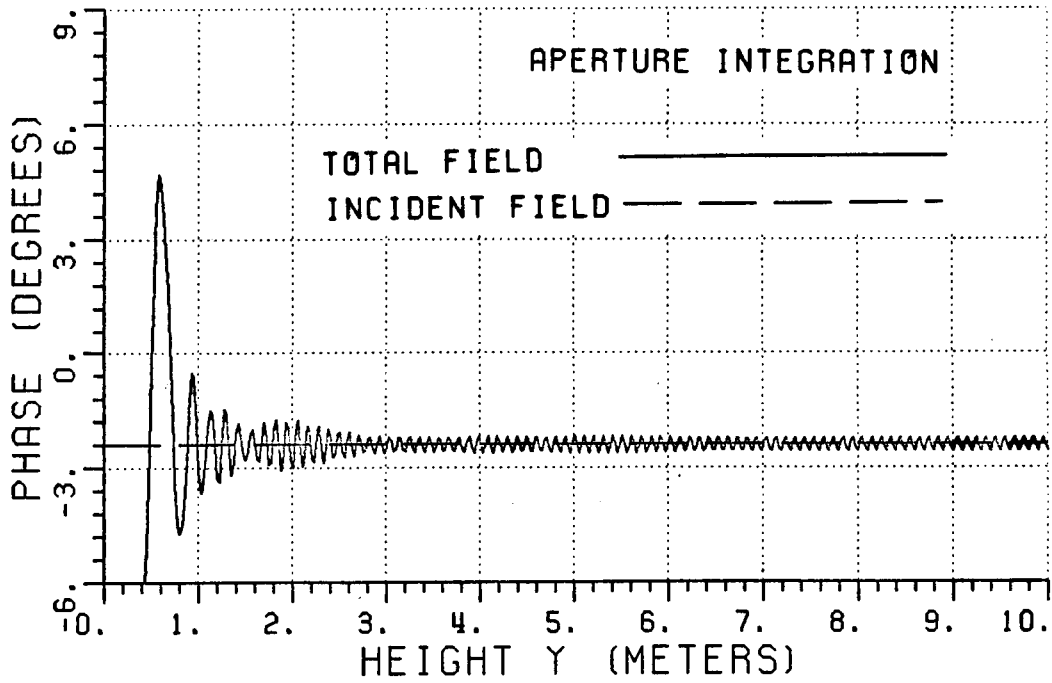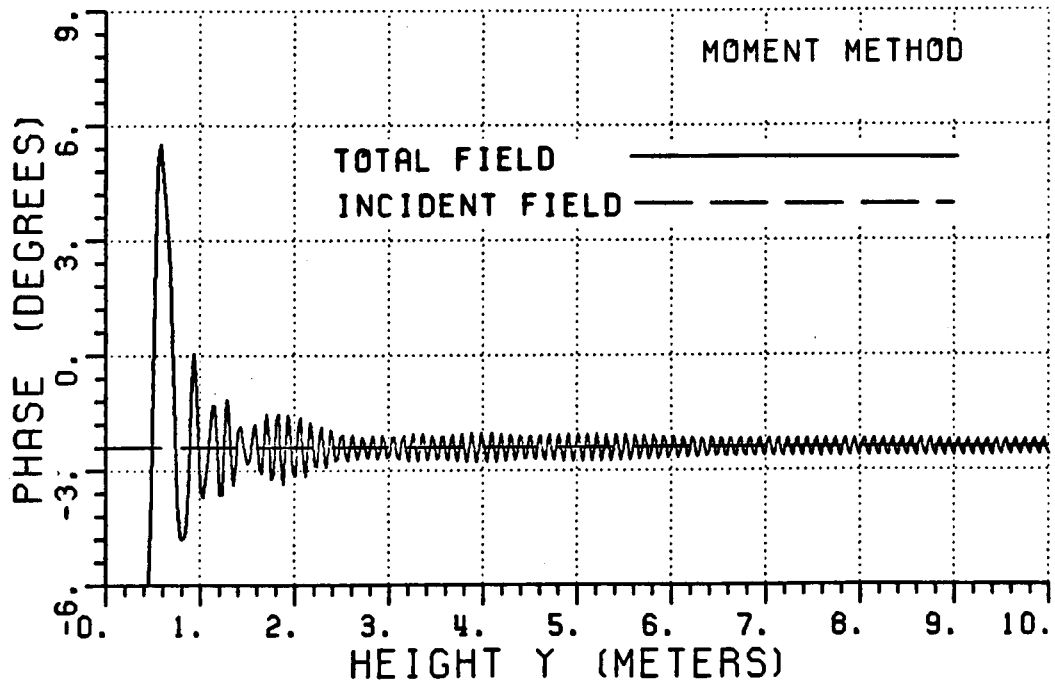
Figure 152: Detail of the ripple in the phases of the total fields for Q_1 (3 GHz).
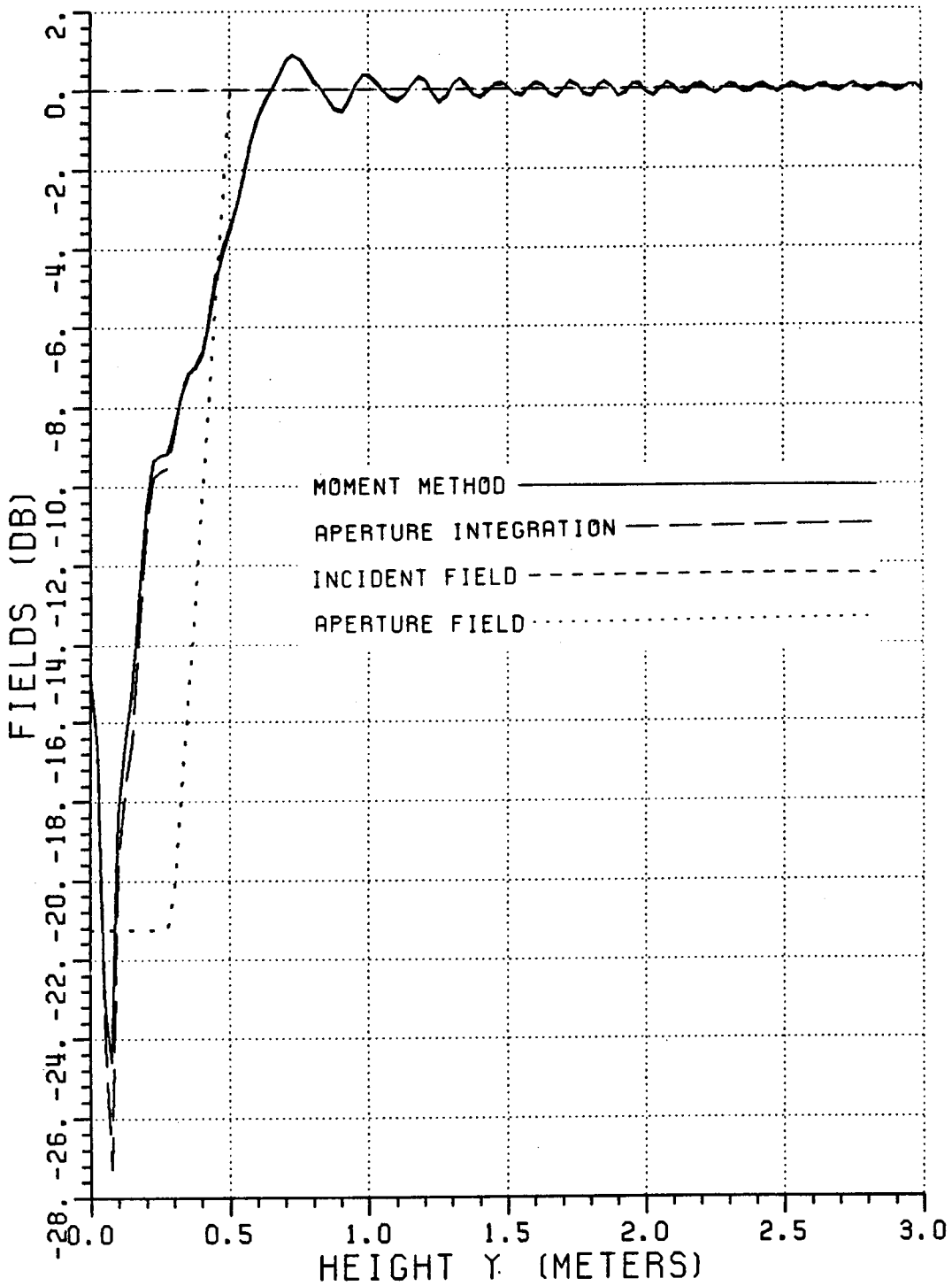
Figure 153: Normalized magnitude of the total fields for Q_2 (3 GHz).
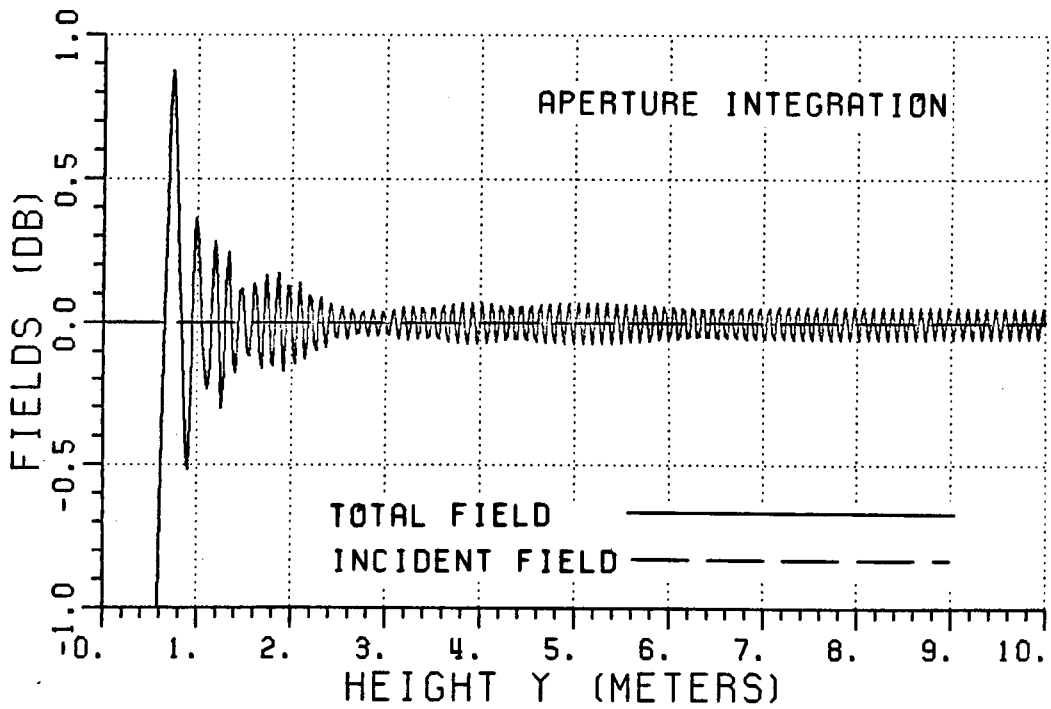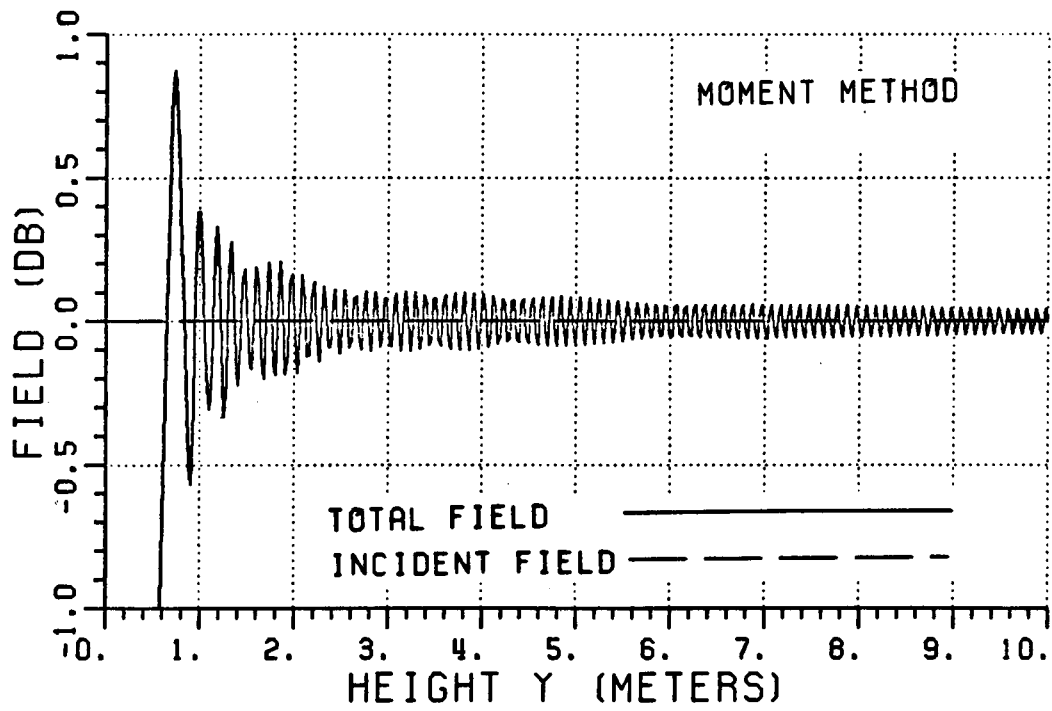
Figure 154: Detail of the ripple in the magnitude of total fields for Q_2 (3 GHz).
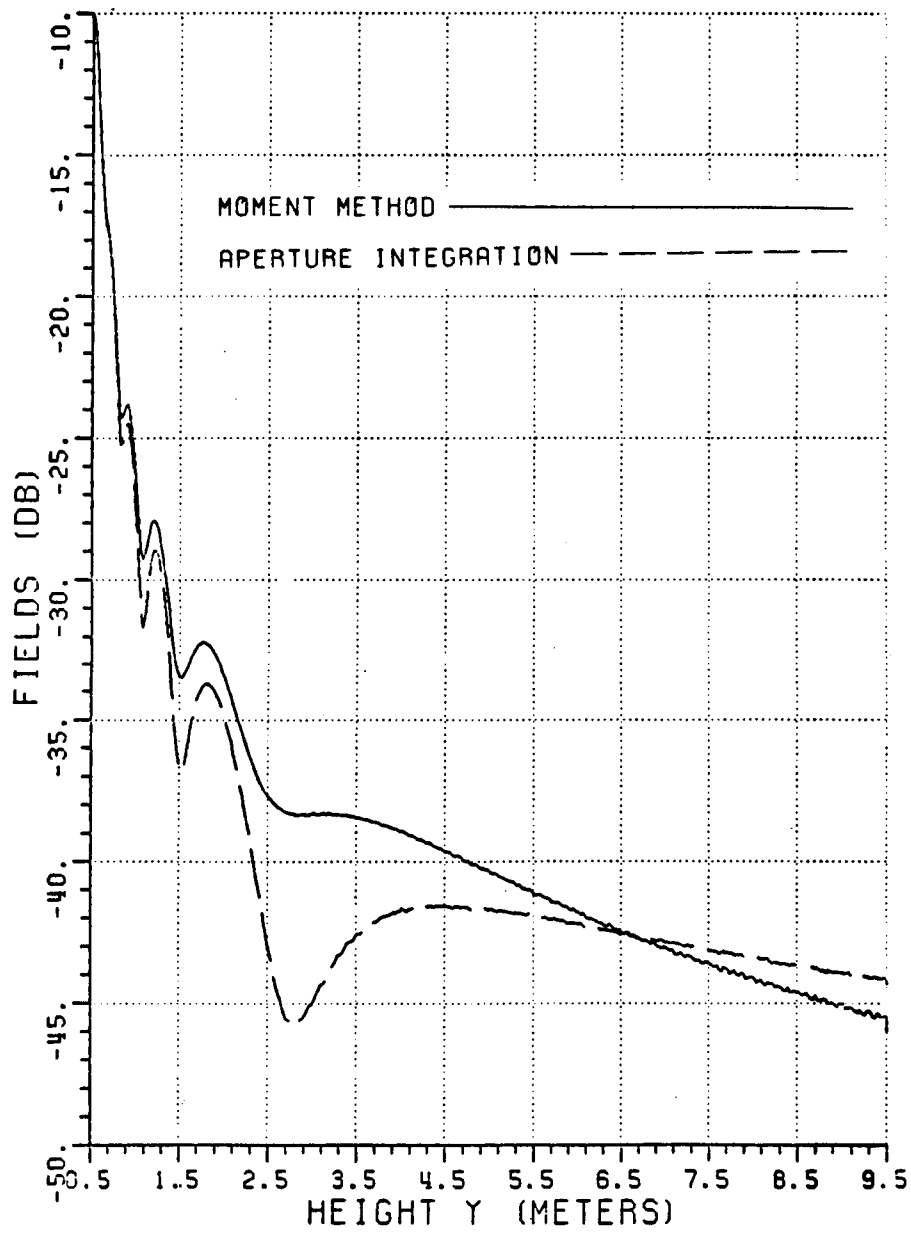
Figure 155: Scattered fields (relative to incident field) for Q_2 (3 GHz).

266
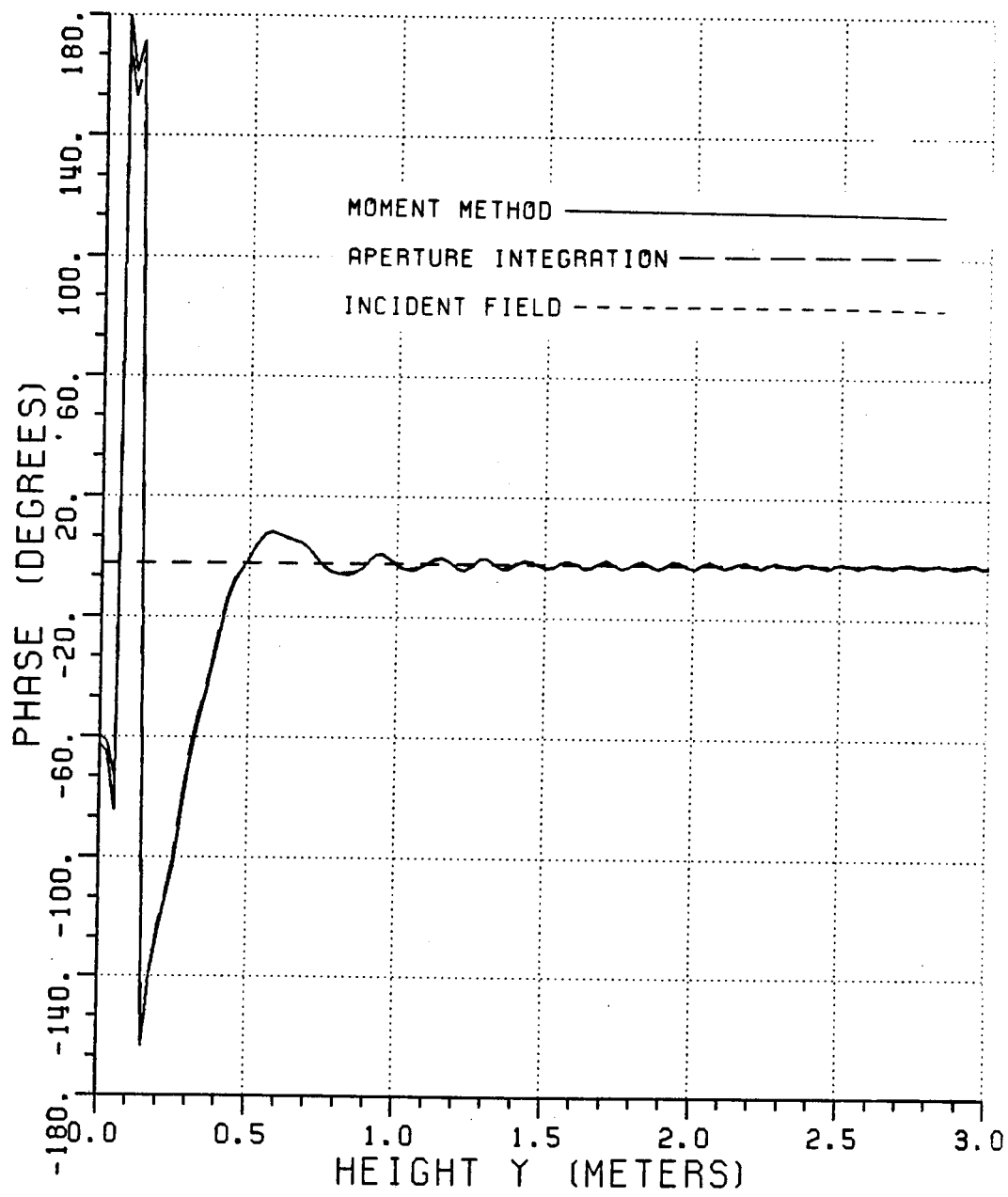
Figure 156: Phases of the total fields for Q_2 (3 GHz).

267
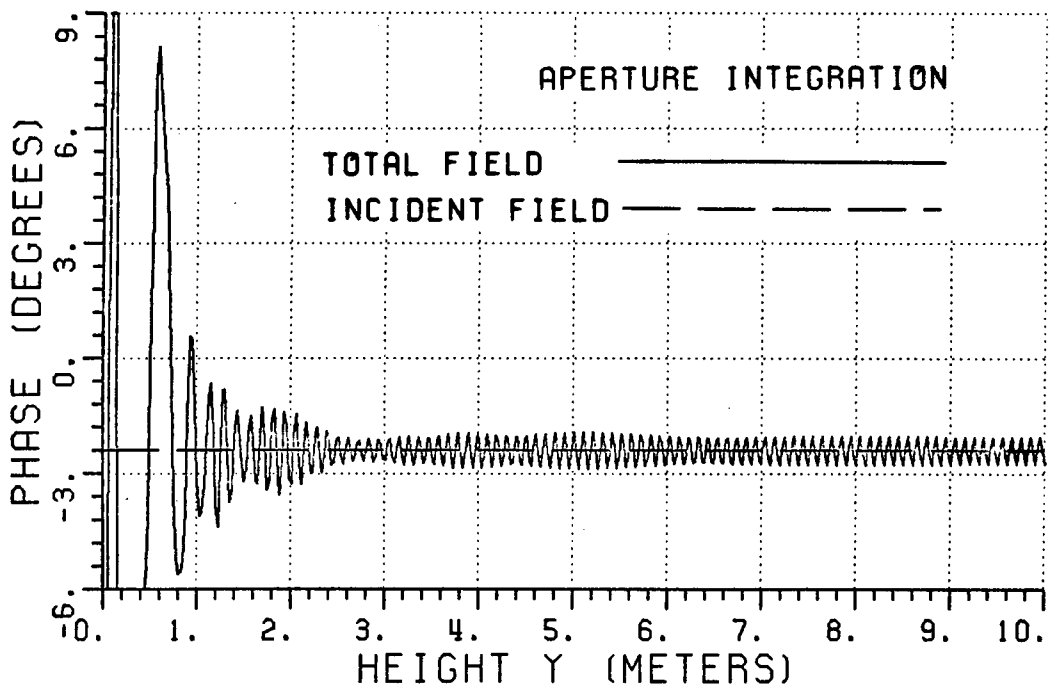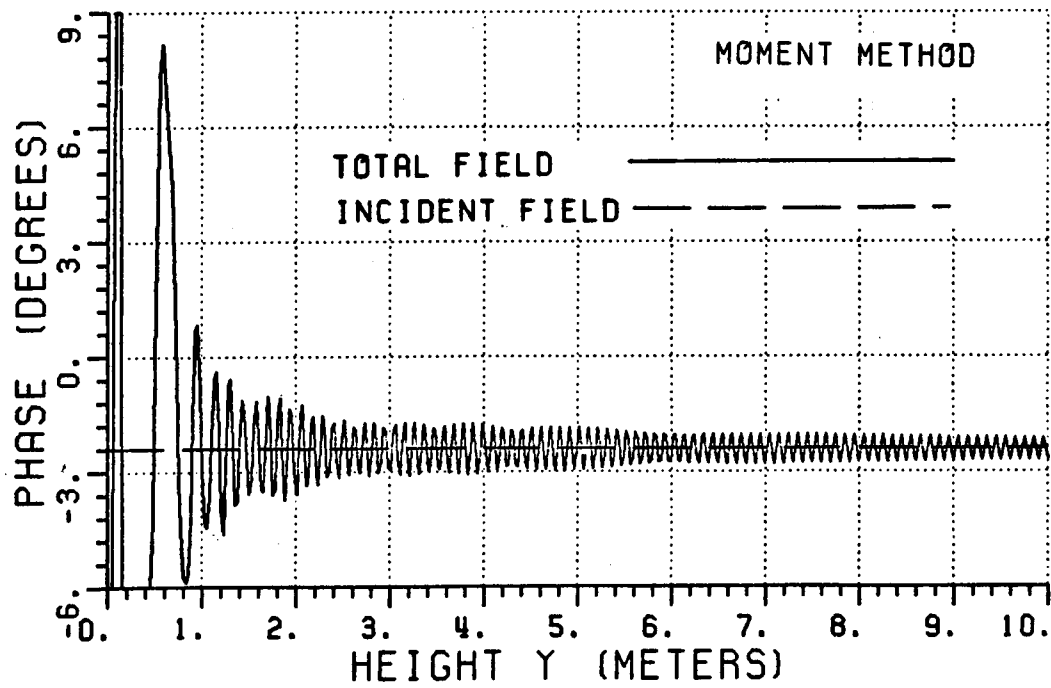
Figure 157: Detail of the ripple in the phases of the total fields for Q_2 (3 GHz).
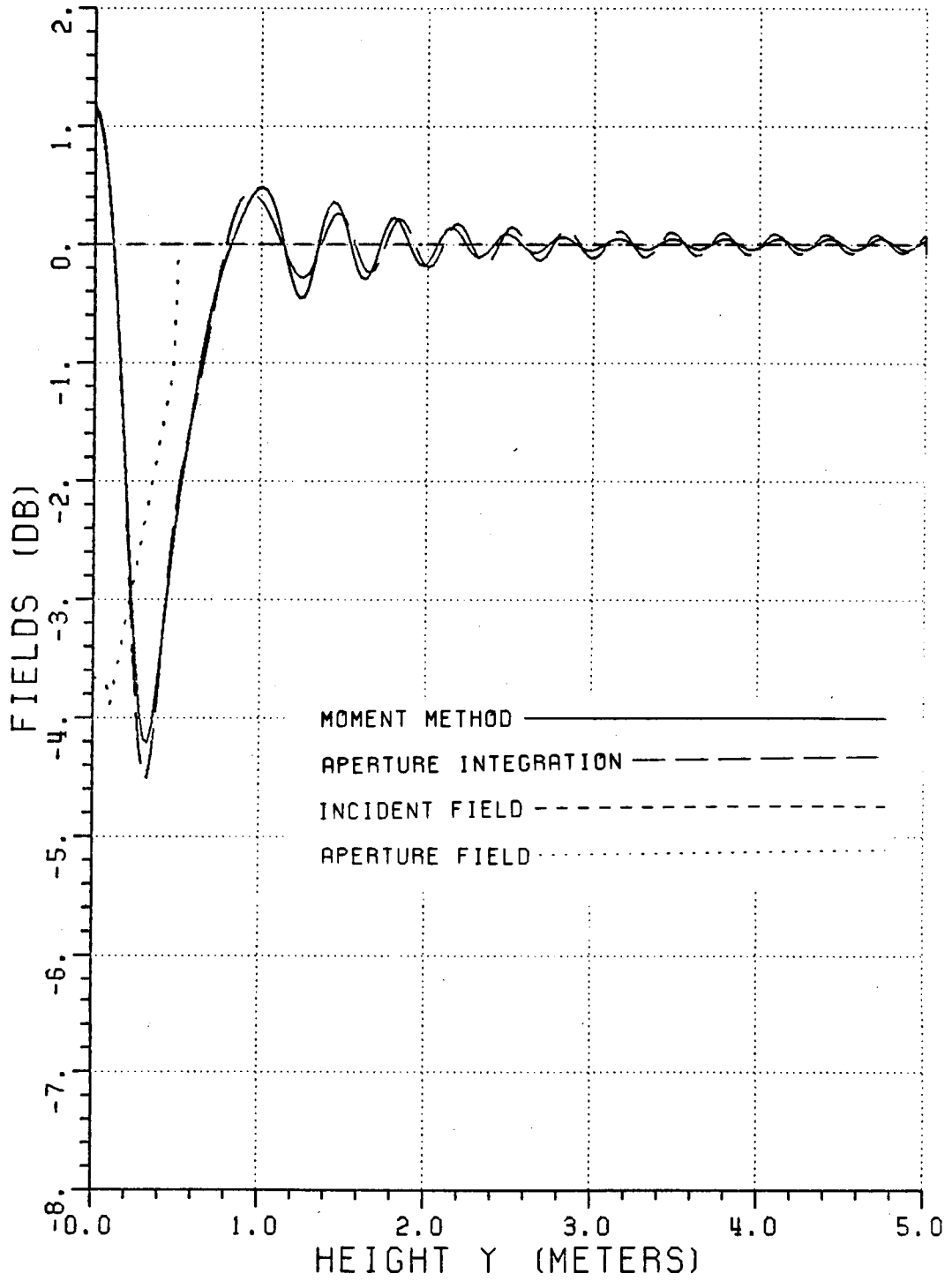
Figure 158: Normalized magnitude of the total fields for Q_3 (1 GHz).
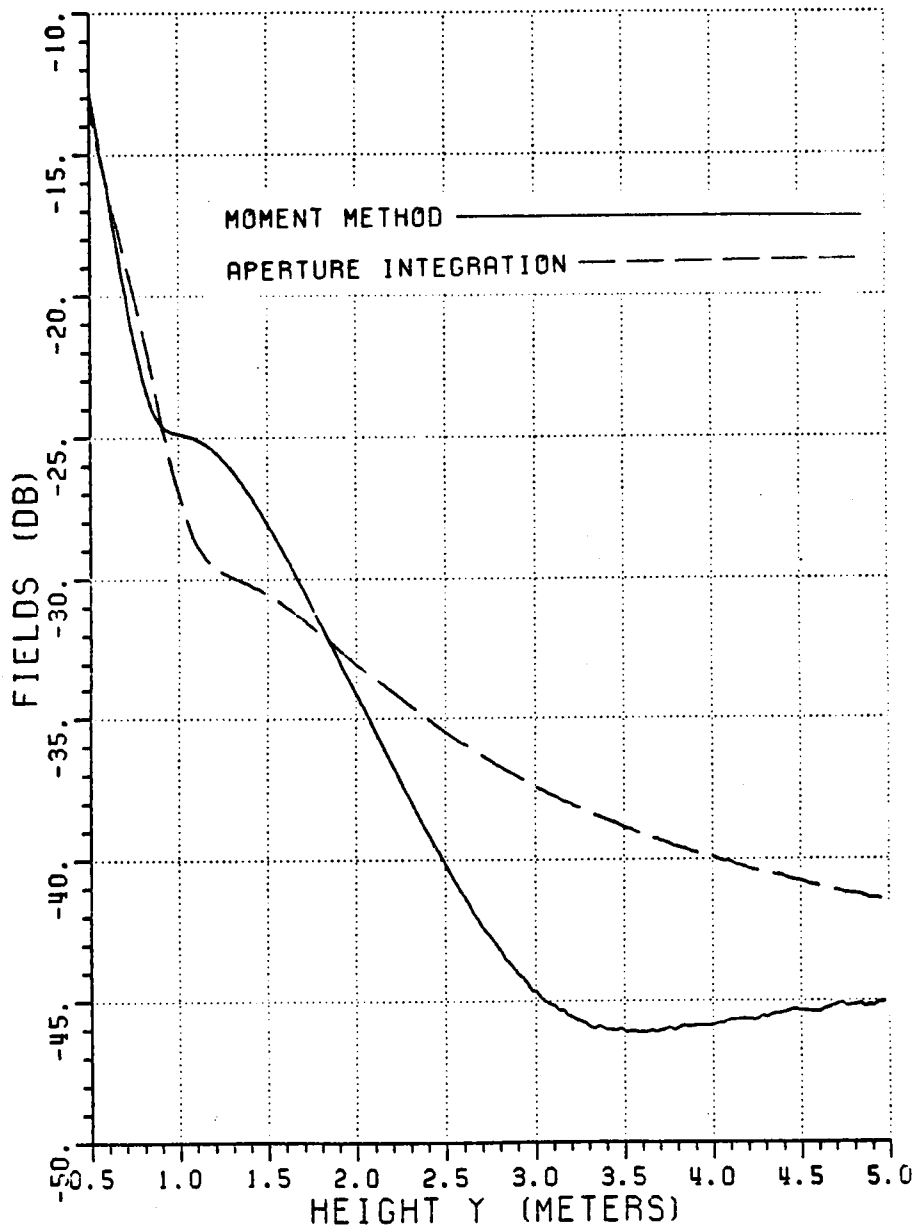
Figure 159: Scattered fields (relative to incident field) for Q_3 (1 GHz).
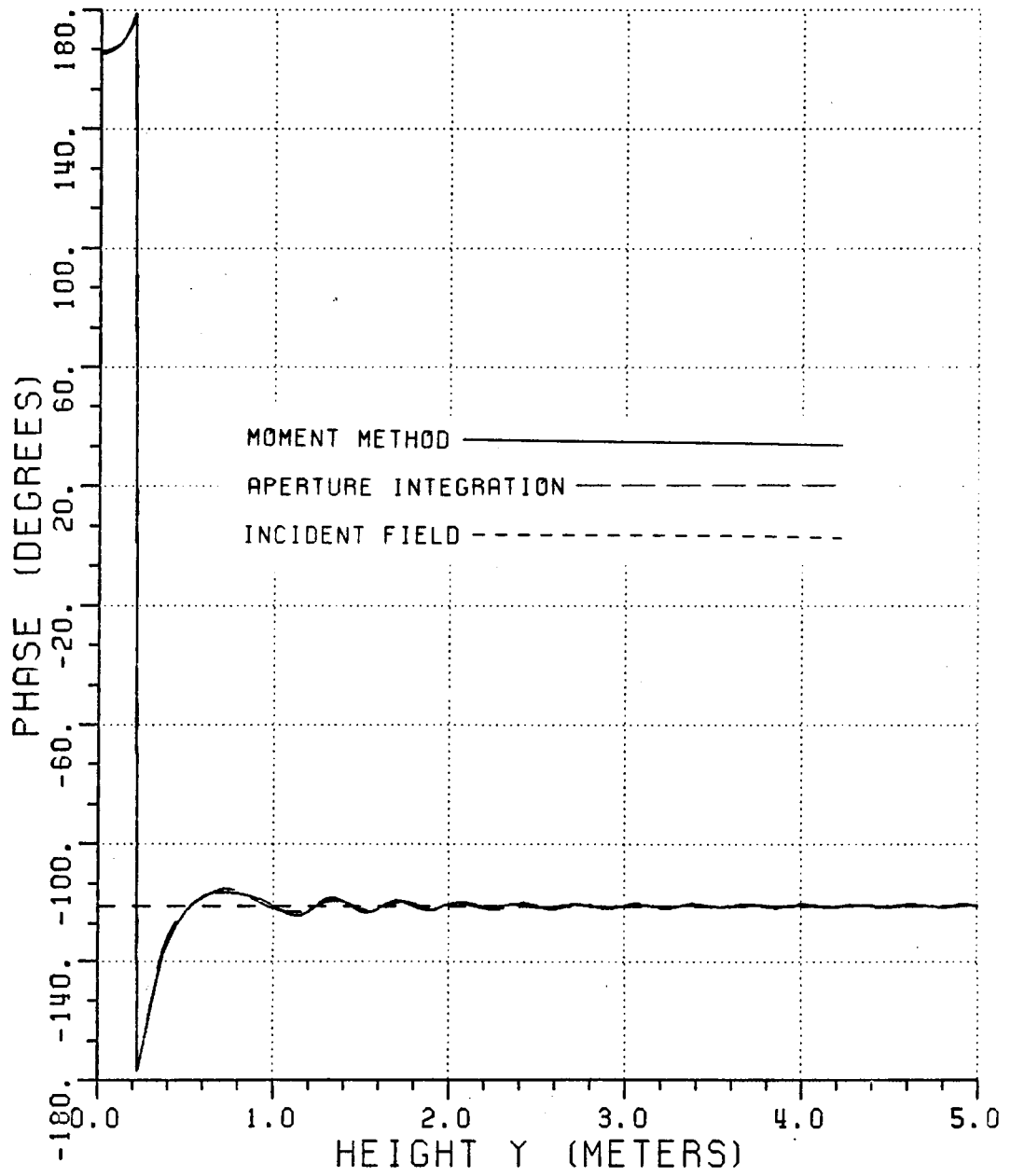
Figure 160: Phases of the total fields for Q_3 (1 GHz).

271
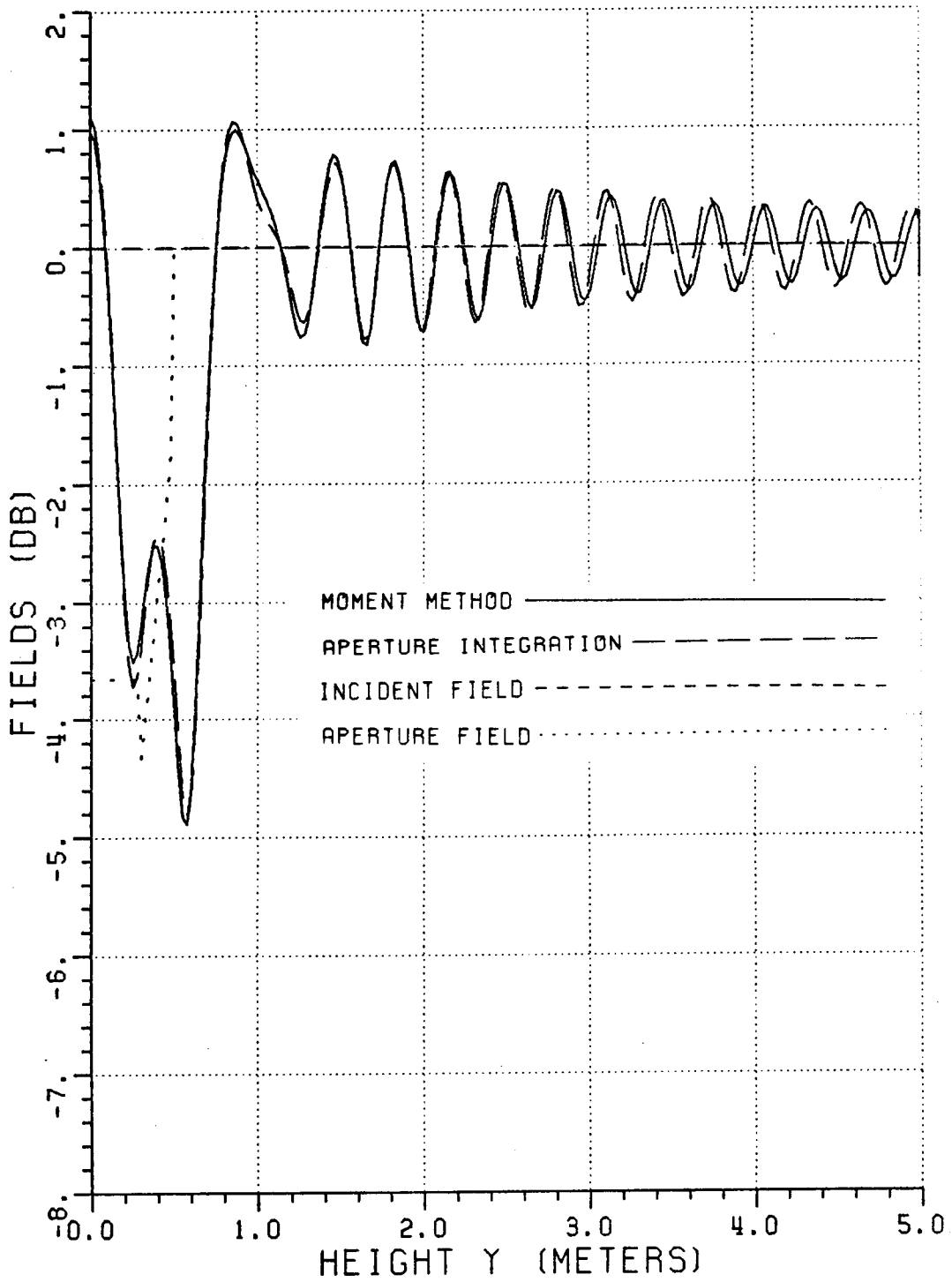
Figure 161: Normalized magnitude of the total fields for Q_4 (1 GHz).
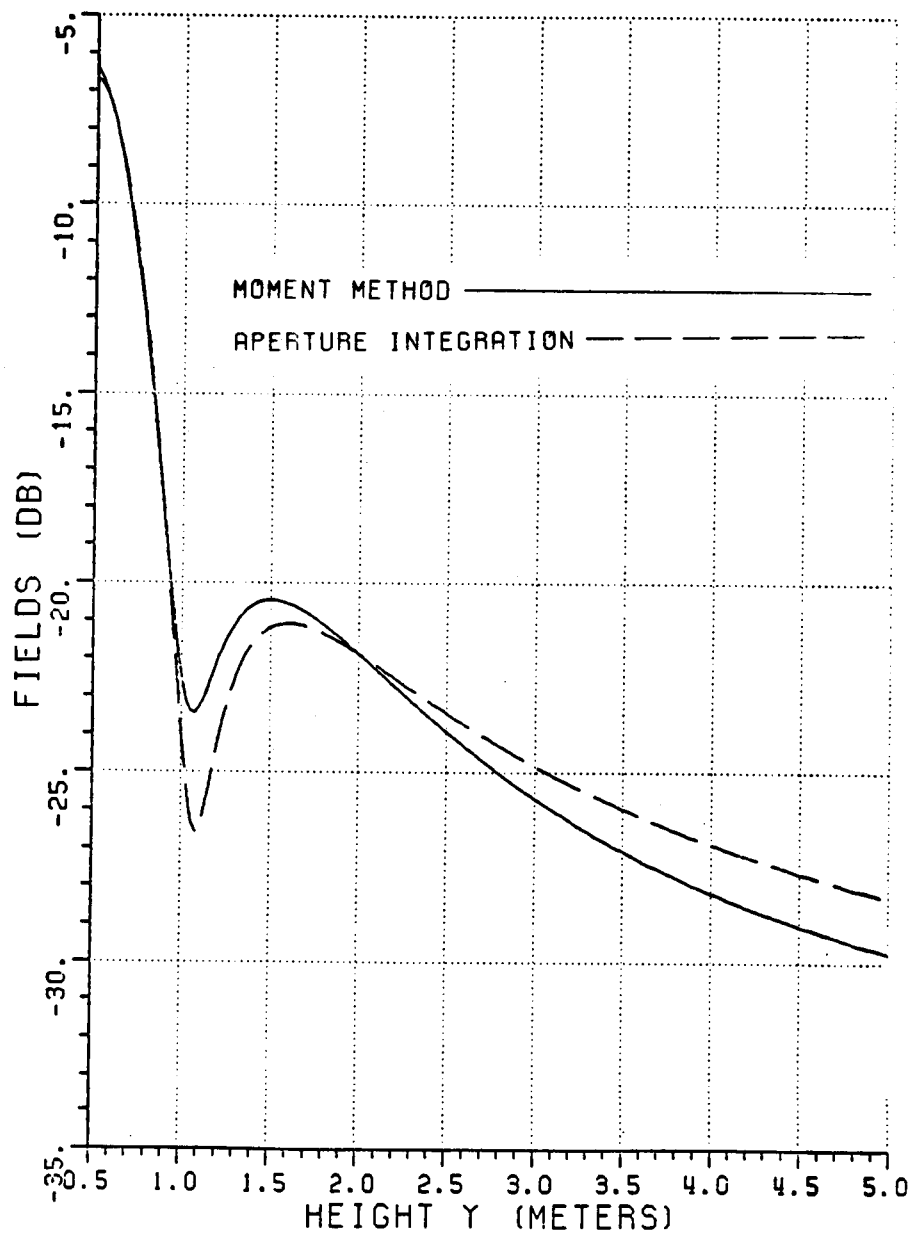
Figure 162: Scattered fields (relative to incident field) for Q_4 (1 GHz).

C - 4
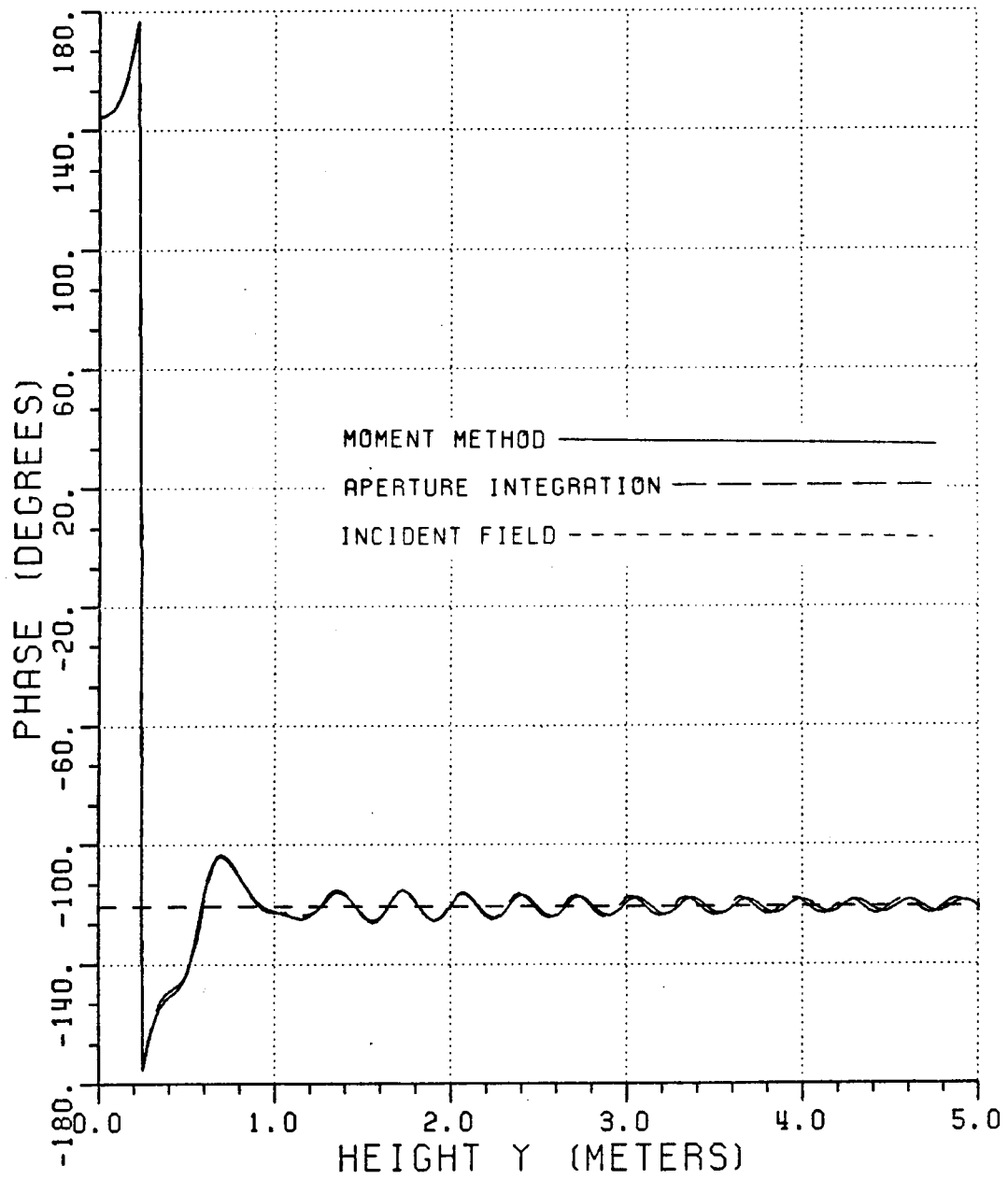
Figure 163: Phases of the total fields for Q_4 (1 GHz).

the path length of a ray in this region through the lossy absorber will be short. Since the attenuation is exponentially dependent on this path length, the attenuation will also be small. As the ray moves away from apex into the interior of the slab, the path length in the absorber and hence also the attenuation will increase so that multiply reflected rays will be too weak to have much effect. The effect due to this mechanism will be smaller in the case of lossier material. Since the refracted fields are discontinuous across the edges (x_1, y_1) and (x_2, y_2), diffracted fields will emanate from these points to make the total field continuous. These diffracted fields will also contribute to the aperture field. Unfortunately, the form of this field is not known which leads to the motivation for the use of the aperture integration technique. The case of rays that are reflected from the side of the wedge back into free space have not been taken into account as they will not influence the pattern in the region of interest.

6.3 Semi-infinite homogeneous lossy dielectric slab with a wedge termination and line source illumination

6.3.1 Aperture regions

The results of the previous section indicate that the proposed aperture integration technique can be used to analyze the forward scattering from a finite homogeneous lossy dielectric slab with wedge terminations that is illuminated by a plane wave. The technique will now be extended to the case of a semi-infinite slab with a wedge termination that is illuminated by a line source. Since the source is now assumed to be a line source, the incident fields on the slab have cylindrical wavefronts rather than the planar wavefronts as in Section 6.2. The plane wave transmission coefficients can still be used, since the ray is assumed to exhibit local plane wave characteristics. Other than in the plane wave case,

however, the refracted rays in this case need to be multiplied by a spread factor (see Equation (2.2)) that will account for the conservation of energy in a ray tube refracted through the free space/dielectric interface.

Let the wedge be defined in a xy-coordinate system as shown in Figure 164, with the source located at (x_s, y_s), and let (x_2, y_2) be located at the origin for the purpose of this discussion. For the purpose of this analysis it is further assumed that the source is located such that $y_s < y_1$ and $x_s < x_1$. As in the previous section, the aperture is taken to be along the entire y-axis. Note that in the case of a semi-infinite slab, the aperture can be divided into two regions; viz., that part in which the slab is present ($y \geq y_2$), and that part where it is not ($y \leq y_2$). The total forward scattered field in the region $x > 0$ can thus be expressed as

$$E_z^s(\rho, \phi) = -e^{j\pi/4} Z_0 \sqrt{\frac{k}{2\pi}} \int_{-\infty}^{\infty} H_y^{ap}(y_q) \frac{e^{-jk\rho'}}{\sqrt{\rho'}} \, dy_q \qquad (6.72)$$

or

$$E_z^s(\rho, \phi) = E_z^{sd} + E_z^{sa} \qquad (6.73)$$

where

$$\rho = \text{radial pattern distance}$$

$$\phi = \text{pattern angle}$$

$$H_y^{ap}(y_q) = \text{tangential magnetic field in the aperture}$$

$$E_z^{sa} = \text{contribution to } E_z^s \text{ from the aperture where}$$
$$\text{the slab is not present } (y \leq y_2)$$

$$E_z^{sd} = \text{contribution to } E_z^s \text{ from the aperture where}$$
$$\text{the slab is present } (y \geq y_2)$$
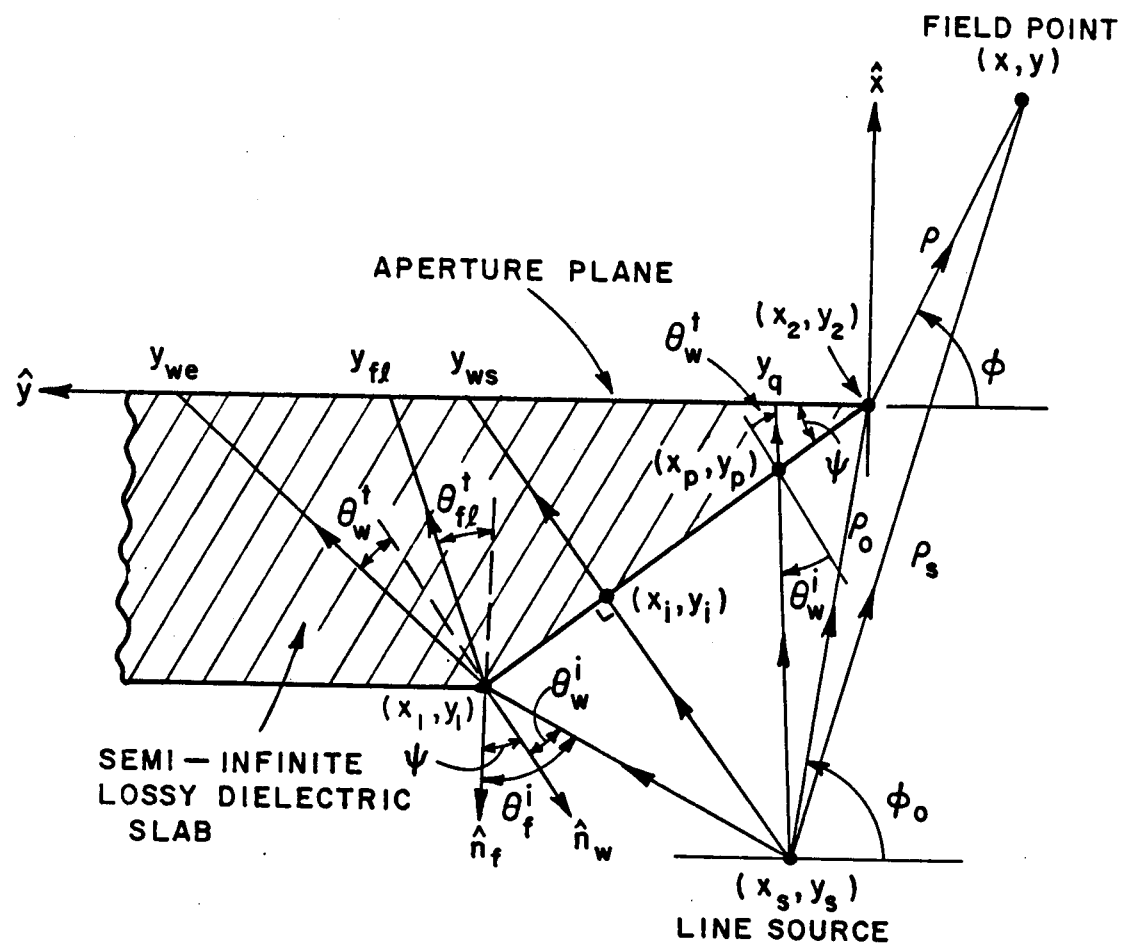
Figure 164: Refraction through a lossy dielectric wedge with line source illumination.

277

and

$$\rho' = \sqrt{(x_2 - x)^2 + (y_q - y)^2} \; . \tag{6.74}$$

Note that (x_2, y_q) is the point in the aperture and (x, y) is the field point; ie.,

$$x = \rho \, \sin\phi \; , \text{ and} \tag{6.75}$$

$$y = -\rho \, \cos\phi \; . \tag{6.76}$$

The fields can thus be expressed as

$$E_z^{sa} = -e^{j\pi/4} Z_0 \sqrt{\frac{k}{2\pi}} \int_{-\infty}^{y_2} H_y^{ap}(y_q) \frac{e^{-jk\rho'}}{\sqrt{\rho'}} \, dy_q \; , \text{ and} \tag{6.77}$$

$$E_z^{sd} = -e^{j\pi/4} Z_0 \sqrt{\frac{k}{2\pi}} \int_{y_2}^{\infty} H_y^{ap}(y_q) \frac{e^{-jk\rho'}}{\sqrt{\rho'}} \, dy_q \; . \tag{6.78}$$

In the high frequency case (where k is large), the integral in Equation (6.77) can be evaluated by the method of stationary phase to yield

$$E_z^{sa} \approx E_z^{sai} + E_z^{sad} \tag{6.79}$$

where E_z^{sai} is the direct incident ray resulting from the stationary point term; ie.,

$$E_z^{sai} = \begin{cases} \dfrac{e^{-jk\rho_s}}{\sqrt{\rho_s}} & 0 \le \phi \le \phi_0 \\ 0 & \text{otherwise} \end{cases} \tag{6.80}$$

and E_z^{sad} is the ray diffracted from (x_2, y_2) resulting from the end point contribution, such that

$$E_z^{sad} = \frac{e^{-jk\rho_0}}{\sqrt{\rho_0}} D^{ep}(\phi_0, \phi, L) \frac{e^{-jk\rho}}{\sqrt{\rho}} \tag{6.81}$$

where

$$\rho_s = \sqrt{(x - x_s)^2 + (y - y_s)^2} \tag{6.82}$$

$$\rho_0 = \sqrt{(x_2 - x_s)^2 + (y_2 - y_s)^2} \tag{6.83}$$

$$\rho = \sqrt{(x - x_2)^2 + (y - y_2)^2} \tag{6.84}$$

$$\phi_0 = \arccos\left(\frac{y_s - y_2}{\rho_0}\right) \tag{6.85}$$

$$D^{ep}(\phi_0, \phi, L) = \frac{e^{-j\pi/4}\sin\phi_0}{\sqrt{2\pi k}(\cos\phi_0 - \cos\phi)} F\left[\frac{kL}{2}\left(\frac{\cos\phi_0 - \cos\phi}{\sin\phi_0}\right)^2\right] \tag{6.86}$$

$$L = \frac{\rho_0\,\rho}{\rho_0 + \rho}\ ,\ \text{and} \tag{6.87}$$

$$F = \text{transition function (see Equation (2.21))} .$$

Equations (6.80)–(6.87) are derived in Appendix B. The closed form expressions obtained from the stationary phase approximation method thus eliminates the need to evaluate the integral in Equation (6.77) numerically from $-\infty$ to y_2.

In order to evaluate E_z^{sd}, the integral in Equation (6.78) must, however, be performed numerically. Note that the integration need not be performed from y_2 to ∞, but as an approximation it need only be performed from $y = y_2$ to that point (y_{small}) in the aperture where the aperture field falls below a specified level (E_z^{min}) as discussed in Section 6.1. The tangential magnetic field (H_y^{ap}) must be found at every point in the aperture by tracing rays through the dielectric slab as in the previous section. Let the point where a ray enters the slab be designated as (x_p, y_p), and the corresponding point where the same ray intercepts the aperture be designated as (x_2, y_q). Two cases need to be considered; ie., rays entering the wedge ($y_2 \le y_p \le y_1$) and rays entering the parallel section ($y_1 \le y_p$).

6.3.2 Oblique incidence on a flat slab illuminated by a line source

Consider now the case where the rays enter the parallel section of the slab at an oblique angle (θ_f^i) as shown in Figure 165. The subscript (f) refers the *flat* part of the slab. In contrast to the case of plane wave incidence where θ_f^i is the same for all rays, the case of line source illumination discussed here results in a different θ_f^i for each ray. These rays will illuminate the aperture in the region ($y_{fl} \le y_q < \infty$),
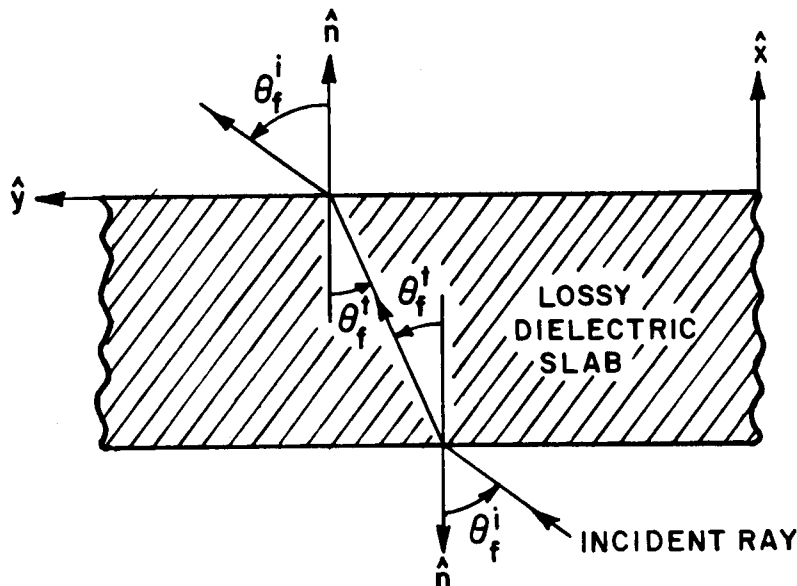
Figure 165: Refraction through a lossy dielectric slab with plane wave illumination.

where the ray intercepting the aperture at (x_2, y_{fl}) enters the parallel section at (x_1, y_1) as shown in Figure 164, such that

$$y_{fl} = (x_2 - x_1)\tan\theta_{fl}^t + y_1 \qquad (6.88)$$

where θ_{fl}^t is the transmitted angle relative to the normal ($\hat{x}$) at (x_1, y_1) (see Equation (6.22)). The equations governing the free space/dielectric interface where the ray enters the slab have been derived in the previous section, and are given in Equations (6.20)–(6.24). Since the two faces of the slab are parallel, the coordinate transformation of Equations (6.25) and (6.26) does not apply here, and the transmitted field in the lossy dielectric slab thus attenuates in the x-direction only. In order to derive the parameters applicable at the dielectric/free space interface where the ray intercepts the aperture, consider a field incident on the dielectric/free space interface from the dielectric side, such that

$$E_z^i = Ce^{-x(\alpha_1 + j\beta_1 \cos\theta_f^t)}e^{-y(j\beta_1 \sin\theta_f^t)} \qquad (6.89)$$

where C is an arbitrary complex constant and θ_f^t is a real angle. Applying Equation (6.4) to Equation (6.89), one finds that the tangential incident magnetic field is given by

$$H_y^i = C\frac{-(\beta_1 \cos \theta_f^t - j\alpha_1)}{\omega\mu_0}e^{-x(\alpha_1+j\beta_1 \cos \theta_f^t)}e^{-y(j\beta_1 \sin \theta_f^t)} \ . \tag{6.90}$$

The reflected fields are given by

$$E_z^r = \Gamma_5 C \, e^{x(\alpha_1+j\beta_1 \cos \theta_f^t)}e^{-y(j\beta_1 \sin \theta_f^t)} \ , \text{ and} \tag{6.91}$$

$$H_y^r = \Gamma_5 C\frac{(\beta_1 \cos \theta_f^t - j\alpha_1)}{\omega\mu_0}e^{x(\alpha_1+j\beta_1 \cos \theta_f^t)}e^{-y(j\beta_1 \sin \theta_f^t)} \tag{6.92}$$

where Γ_5 is a complex reflection coefficient. The fields transmitted into free space can be expressed as

$$E_z^t = T_5 C e^{-jk(x \cos \theta^a + y \sin \theta^a)} \ , \text{ and} \tag{6.93}$$

$$H_y^t = -T_5 C\frac{\cos \theta^a}{Z_0}e^{-jk(x \cos \theta^a + y \sin \theta^a)} \tag{6.94}$$

where T_5 is a complex transmission coefficient and θ^a is a real angle. Note that in the case of the parallel slab, the field that is transmitted into free space does not attenuate, in contrast to the field that is transmitted into free space through a wedge. (Recall that such a ray attenuates in a direction perpendicular to the direction of propagation). The variables Γ_5, T_5 and θ^a can be found by enforcing the boundary conditions that the tangential fields be continuous across the interface at $x = 0$; ie.,

$$1 + \Gamma_5 = T_5 \tag{6.95}$$

$$\beta_1 \sin \theta_f^t = k \sin \theta^a \ , \text{ and} \tag{6.96}$$

$$(\beta_1 \cos \theta_f^t - j\alpha_1)(1 - \Gamma_5) = T_5 k \cos \theta^a \ . \tag{6.97}$$

Comparing Equation (6.96) with Equation (6.19), one finds that

$$\theta^a = \theta_f^i \tag{6.98}$$

281

so that the ray transmitted through the slab into free space propagates in the same direction as the incident ray. Solving for Equations (6.95) and (6.97), one finds that

$$T_5 = \frac{2(\beta_1 \cos \theta_f^t - j\alpha_1)}{k \cos \theta_f^i + \beta_1 \cos \theta_f^t - j\alpha_1} \text{ , and} \tag{6.99}$$

$$\Gamma_5 = T_5 - 1 . \tag{6.100}$$

The total tangential magnetic field in the aperture due to rays entering the parallel slab is thus given by

$$H_y^{aps}(y_q) = \begin{cases} -Y_0 \, T_1 T_5 \cos \theta_f^i \, A \, e^{-\alpha_1 y_{abs}} \dfrac{e^{-j(k\rho_{air} + \beta_1 \rho_{abs})}}{\sqrt{\rho_{air}}} & \text{for } y_{fl} \leq y_q \\ 0 & \text{elsewhere} \end{cases} \tag{6.101}$$

where

$$\rho_{air} = \sqrt{(x_1 - x_s)^2 + (y_p - y_s)^2} \tag{6.102}$$

$$\rho_{abs} = \sqrt{(x_1 - x_2)^2 + (y_p - y_q)^2} \text{ , and} \tag{6.103}$$

$$y_{abs} = x_2 - x_1 . \tag{6.104}$$

In the case of a cylindrical wave incident upon a planar interface the spread factor is given by[27, p. 170]

$$A = \sqrt{\frac{\rho_{air} \cos \theta_f^t}{m \rho_{abs} \cos \theta_f^i + \rho_{air} \cos \theta_f^t}} \tag{6.105}$$

where

$$m = \frac{k \cos \theta_f^i}{\beta_1 \cos \theta_f^t} . \tag{6.106}$$

Note that the factor $(1/\sqrt{\rho_{air}})$ has been incorporated into Equation (6.101) to account for the spatial attenuation from the line source.

The problem remains to solve for the entry point (x_1, y_p), given any point $(y_q \geq y_{fl})$ in the aperture and a fixed source location (x_s, y_s). The equation of the incident ray can be expressed as

$$y_p = (x_1 - x_s) \tan \theta_f^i + y_s \qquad (6.107)$$

and the equation of the refracted ray as

$$y_q = (x_2 - x_1) \tan \theta_f^t + y_p \ . \qquad (6.108)$$

Equating y_q in Equations (6.107) and (6.108), one finds that solving the following non-linear equation

$$(x_1 - x_s) \tan \theta_f^i + (x_2 - x_1) \tan \theta_f^t + (y_s - y_q) = 0 \qquad (6.109)$$

with the relation between θ_f^i and θ_f^t given in Equations (6.20) and (6.22), will yield θ_f^i and θ_f^t. This equation can be solved iteratively by using an appropriate computer routine, and the entry point (x_1, y_p) can then be found by substituting θ_f^i into Equation (6.107).

6.3.3 Oblique incidence on a wedge illuminated by a line source

Consider now the case where a ray enters the wedge part of the slab at an oblique angle (θ_w^i) at (x_p, y_p) as shown in Figure 164. The subscript (w) refers to the *wedge* part of the slab. Note that θ_w^i is different for each ray. Such a ray will illuminate the aperture in the region $(y_2 \leq y_q \leq y_{we})$, where the ray intercepting the aperture at (x_2, y_{we}) enters the wedge at (x_1, y_1) as shown in Figure 164. The aperture field resulting from a plane wave illuminating the wedge is given in Equation (6.57). In this case, however, the wedge is illuminated by a line source. The total magnetic field in the aperture due to rays entering the wedge is thus

given by

$$H_y^{apw}(y_q) = -Y_0\, T_1 T_2 \left(\frac{\beta_0 \cos\theta^a + j\alpha_0 \sin\theta^a}{k} \right) A\, e^{-\alpha_1 y_{abs}} \frac{e^{-j(k\rho_{air} + \beta_1 \rho_{abs})}}{\sqrt{\rho_{air}}}$$

(6.110)

for $y_2 \le y_q \le y_{we}$ where ρ_{abs} and y_{abs} are given in Equations (6.59) and (6.60), and

$$A = \sqrt{\frac{\rho_{air} \cos\theta_w^t}{m\rho_{abs} \cos\theta_w^i + \rho_{air} \cos\theta_w^t}}$$

(6.111)

$$m = \frac{k\cos\theta_w^i}{\beta_1 \cos\theta_w^t}\ , \text{ and}$$

(6.112)

$$\rho_{air} = \sqrt{(x_p - x_s)^2 + (y_p - y_s)^2}\ .$$

(6.113)

Note that the factor $(1/\sqrt{\rho_{air}})$ has been incorporated nto Equation (6.110) to account for the spatial attenuation from the line source.

The problem still remains to find the entry point (x_p, y_p), on the wedge given a point (x_2, y_q) in the aperture and a fixed source location (x_s, y_s). Consider the ray that intercepts the wedge perpendicularly. Let the entry point for this ray be (x_i, y_i), and the point where the ray intercepts the aperture be (x_2, y_{ws}) as shown in Figure 164. The entry and intercepting points are given by

$$x_i = \left(\frac{x_1}{a} + x_s a + y_s - y_1 \right) \left(\frac{a}{a^2 + 1} \right)$$

(6.114)

$$y_i = a(x_s - x_i) + y_s$$

(6.115)

$$y_{ws} = \frac{(x_2 - x_s)(x_2 - x_1)}{y_1 - y_2} + y_s\ , \text{ and}$$

(6.116)

$$a = \frac{x_2 - x_1}{y_2 - y_1}\ .$$

(6.117)

Having determined the point (x_i, y_i), one finds that

$$y_{we} = (x_2 - x_1)\tan(\psi \mp \theta_w^t) \quad \text{if } x_i \overset{<}{\underset{>}{}} x_1$$

(6.118)

$$\hat{n}_f = \text{ unit vector normal to parallel slab } (= -\hat{x}).$$

(6.119)

284

$$\psi \quad = \quad \text{angle between } \hat{n}_w \text{ and } \hat{n}_f \text{ (= wedge angle)}$$

$$\theta_w^t \quad = \quad \text{angle of ray transmitted into the dielectric}$$

$$\text{relative to } -\hat{n}_w \text{ (see Equation (6.22))}$$

$$\hat{n}_w \quad = \quad \text{unit vector normal to wedge, and}$$

To solve for (x_p, y_p), one uses the fact that (x_p, y_p) lies on the wedge, so that

$$x_p = \frac{(x_2 - x_1)(y_p - y_1)}{y_2 - y_1} + x_1 \tag{6.120}$$

or

$$x_p = a y_p + b \tag{6.121}$$

where a is given in Equation (6.117) and

$$b = x_1 - a y_1 . \tag{6.122}$$

The equation of the incident ray is given by

$$y_p = (x_p - x_s) \tan \gamma_{ni} + y_s \tag{6.123}$$

where

$$\gamma_{ni} = \psi \mp \theta_w^i \quad \text{if } y_q \gtrless y_{ws} . \tag{6.124}$$

The equation of the refracted ray is given by

$$y_p = y_q - (x_2 - x_p) \tan \gamma_{nt} \tag{6.125}$$

where

$$\gamma_{nt} = \psi \mp \theta_w^t \quad \text{if } y_q \gtrless y_{ws} . \tag{6.126}$$

Solving for Equations (6.121)–(6.126), one finds that

$$y_p = \frac{y_q - x_2 \tan \gamma_{nt} + b \tan \gamma_{nt}}{1 - a \tan \gamma_{nt}} = \frac{y_s + b \tan \gamma_{ni} - x_s \tan \gamma_{ni}}{1 - a \tan \gamma_{ni}} . \tag{6.127}$$

285

Equation (6.127) can be solved iteratively by using an appropriate computer routine, if one keeps in mind that θ_w^i and θ_w^t are related by Equation (6.22). Once θ_w^i and θ_w^t have been found, (x_p, y_p) can be determined from Equations (6.127) and (6.120).

The total magnetic field in that part of the aperture where the slab is present $(y \geq y_2)$ is thus given by

$$H_y^{ap}(y_q) = H_y^{aps}(y_q)U(y_q - y_{fl}) + H_y^{apw}(y_q)[U(y_q - y_2) - U(y_q - y_{we})] \quad (6.128)$$

where

$$U(x) = \begin{cases} 1 & \text{if } x \geq 0 \\ 0 & \text{if } x < 0 \ . \end{cases} \quad (6.129)$$

Note that H_y^{aps} is given in Equation (6.101) and H_y^{apw} is given in Equation (6.110). Equation (6.128) can be substituted into Equation (6.78) to give the field scattered from the slab (E_z^{sd}). The total field is then given by Equation (6.73).

6.3.4 Results

In this section the forward scattered fields from a semi-infinite absorber slab with a wedge termination is calculated for three cases. Consider the geometry of Figure 164. It is assumed that an electric line source with a uniform pattern is located at $(x_s, y_s) = (-4.576', 1.574')$ and that the absorber slab is $0.5'$ thick; ie., $x_2 - x_1 = 0.5'$. Note that the position of the source corresponds to the location of the bottom edge of the subreflector in Figure 123, where it is assumed that the coupling aperture is $2'$ wide. The origin in this case is located at the apex of the wedge, rather than at the focal point of the subreflector.

The total field given in Equation (6.73) is calculated for three slabs, designated as Q_5, Q_6 and Q_7, with wedge angles (ψ) equal to 7.1^o, 14.0^o and 17.4^o, respectively. The absorber parameters are given in Table 21. Patterns are cal-

Table 21: Parameters of semi-infinite absorber slabs.

	Q_5	Q_6	Q_7
ψ	7.1^o	14.0^o	17.4^o
x_1, y_1	$-0.5', 4'$	$-0.5', 2'$	$-0.5', 1.6'$
x_2, y_2	$0', 0'$	$0', 0'$	$0', 0'$
ϵ_r'	1.5	1.5	1.5
ϵ_r''	1	1	1

culated at 3 GHz along a line parallel to the y-axis at a constant x-displacement of $5'$. The aperture integration is performed by Simpson's method, with aperture spacings of 0.1λ. The aperture field is integrated from $y = y_2$ to $y = 11.87'$, at which point the aperture field (E_z^{min}) is 45 dB below the level that the field would have been if there was no absorber present.

The field patterns for the total field (see Equation (6.73)), field due to the end point contribution from (x_2, y_2) (see Equation (6.81)) and the scattered field obtained from the aperture integration over the slab (see Equation (6.78)) are shown in Figures 166–168 for Q_5, Q_6 and Q_7, respectively. Note that the scattered field obtained from the aperture integration over the slab does not have a peak along the geometrical ISB ($y_{isb} = -1.72'$ at $x = 5'$), but that the peak is shifted towards the interior of the slab. This effect was also observed in Section 5.5 where finite slabs were illuminated by a plane wave. It is due to the ray bending associated with propagation through the dielectric medium.

The total fields for the three cases are compared in Figure 169. It is clear from this figure that the magnitude of the ripple in the total field decreases as the wedge angle (ψ) decreases, as expected. Note, however, that although the ripple decreases

287

as ψ decreases, the total field in the region around the apex ($y_{isb} \leq y \leq 8'$) increases as ψ decreases. This is due to the fact that a smaller wedge angle results in a thinner slab in the region of the apex, so that the transmitted field in this region is stronger. In the region away from the apex ($y > 8'$), one finds that the field values are the same for the three cases (except for the ripple). This is to be expected since the rays are travelling primarily through the parallel section of the slab, and all the slabs have an equal thickness. In the region $y < y_{isb}$, one finds that the field values are also the same for the three cases (except for the ripple). This is to be expected, since the total field in this region is given by the direct and end point contributions of the integration over the free space half plane, with the diffracted field from the slab superimposed. Since the wedge with the largest wedge angle ($Q_7; \psi = 17.4^o$) has the strongest diffracted field, one would thus expect the total field from this slab to have the largest ripple in the region $y > y_{isb}$. Similarly, one would expect the wedge with the smallest wedge angle ($Q_5; \psi = 7.1^o$) to have the smallest ripple in this region. This is indeed the case, as shown in Figure 169.

As indicated in Section 5.6, the wedge terminations of the coupling aperture of the absorber fence has to be designed such that diffractions from the absorber fence is minimized. It has been shown that a smaller wedge angle results in smaller diffracted fields. In addition, the transmitted fields through the absorber fence have to be attenuated sufficiently. A smaller wedge angle leads to a thinner slab near the apex, which result in stronger transmitted fields. The design of the absorber fence, and in particular the wedge angles of the coupling aperture terminations, will thus be based on a compromise between small diffractions and weak transmitted fields.
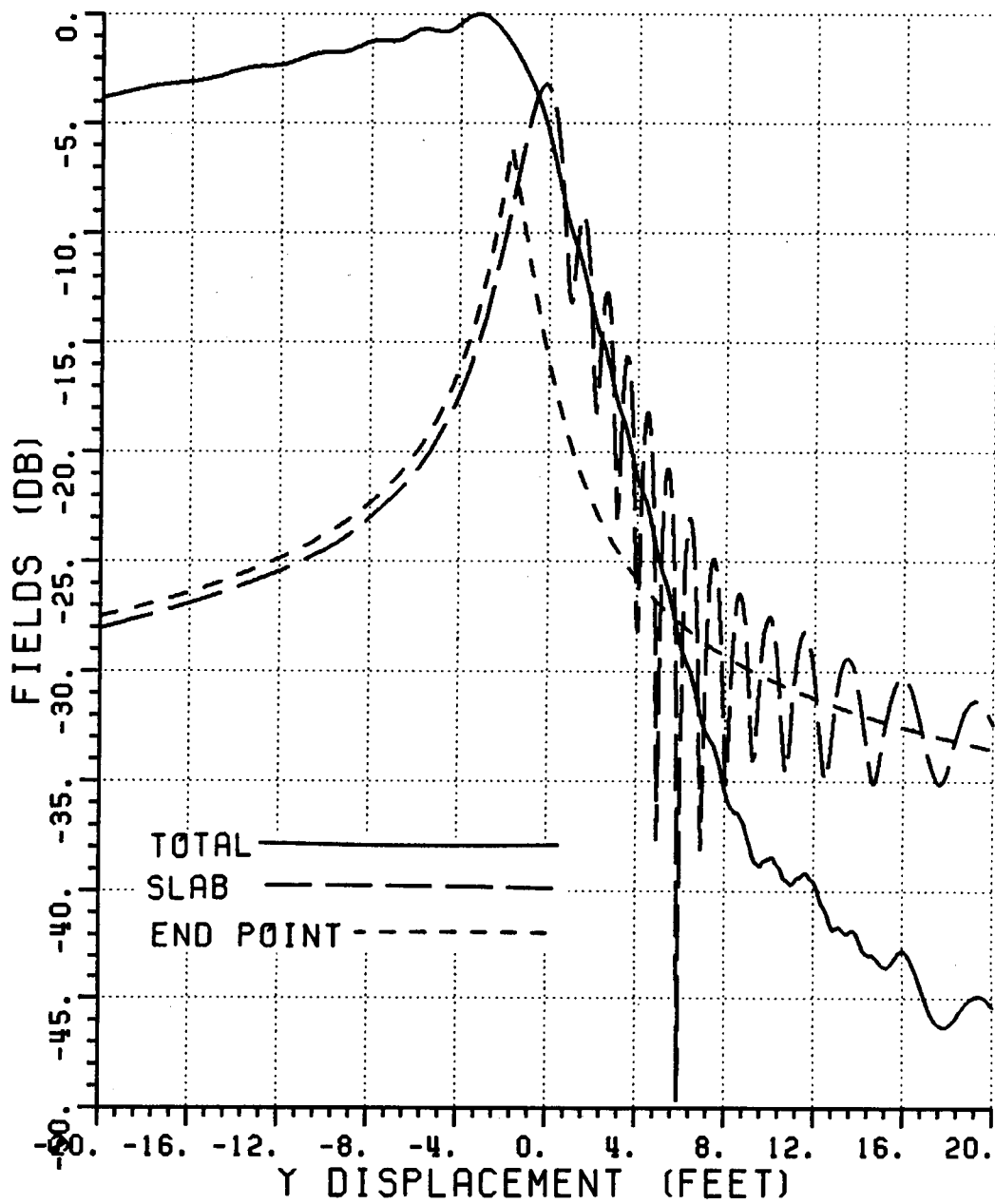
Figure 166: Scattered fields from Q_5 (3 GHz).

289
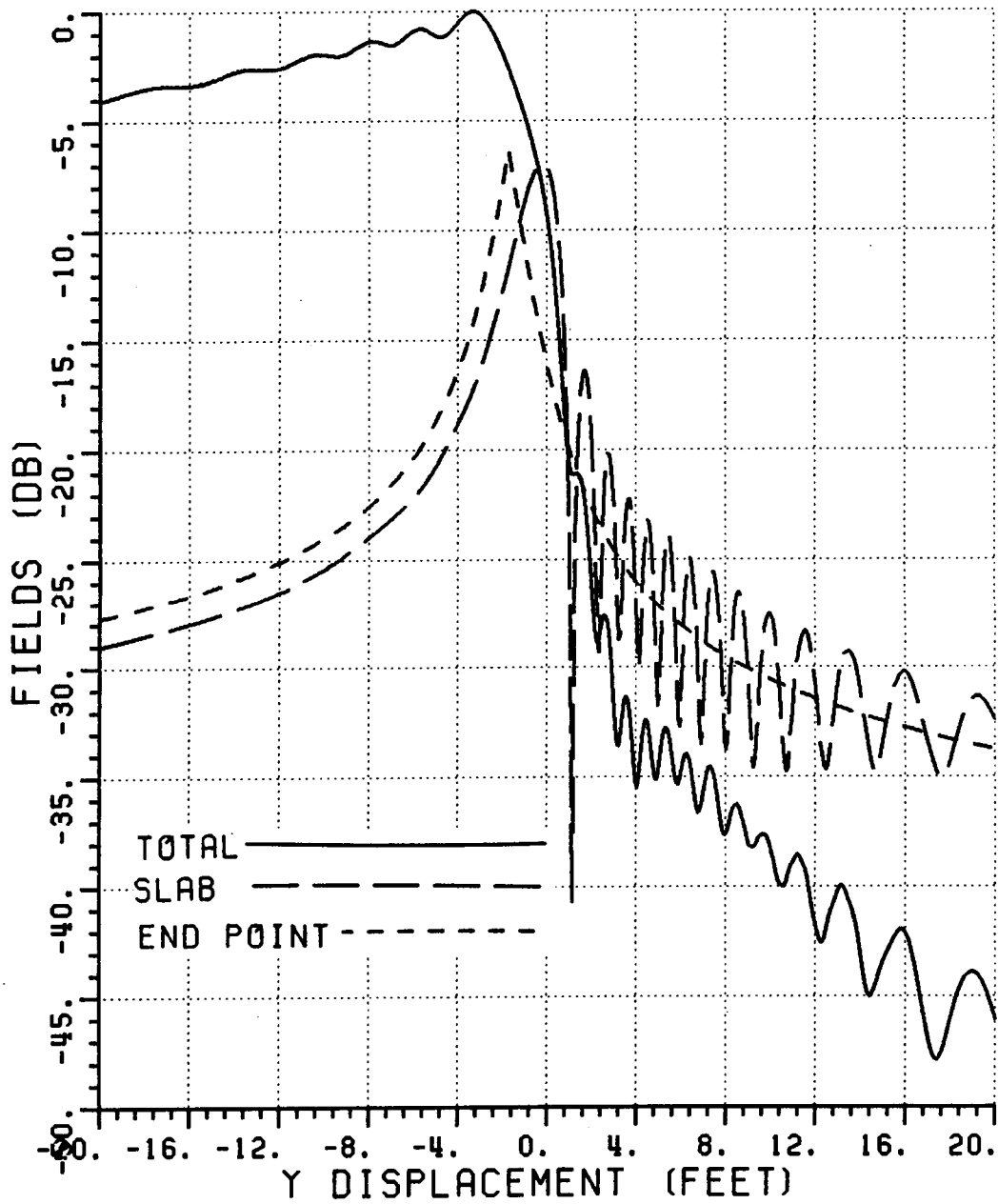
Figure 167: Scattered fields from Q_6 (3 GHz).
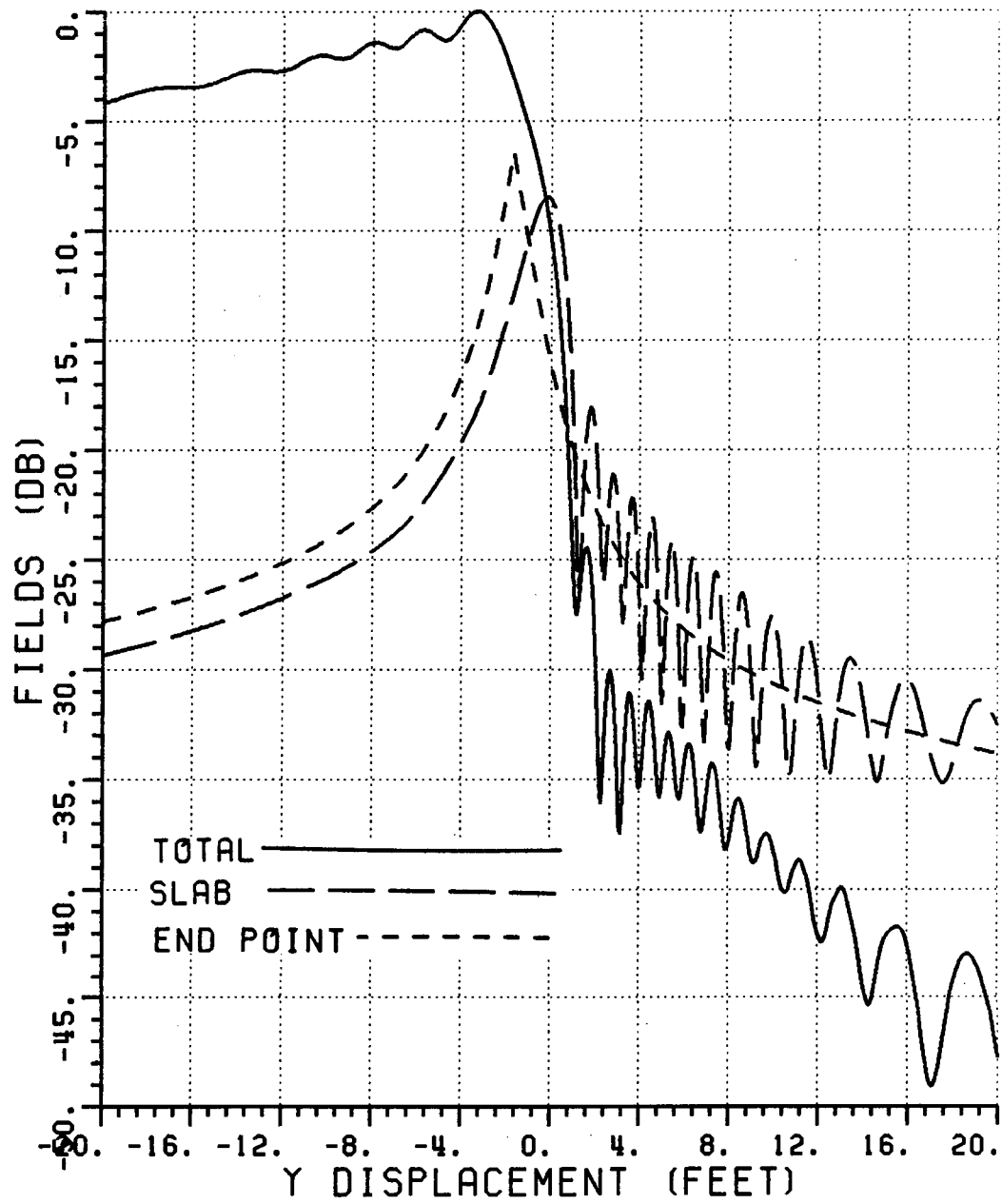
Figure 168: Scattered fields from Q_7 (3 GHz).

291
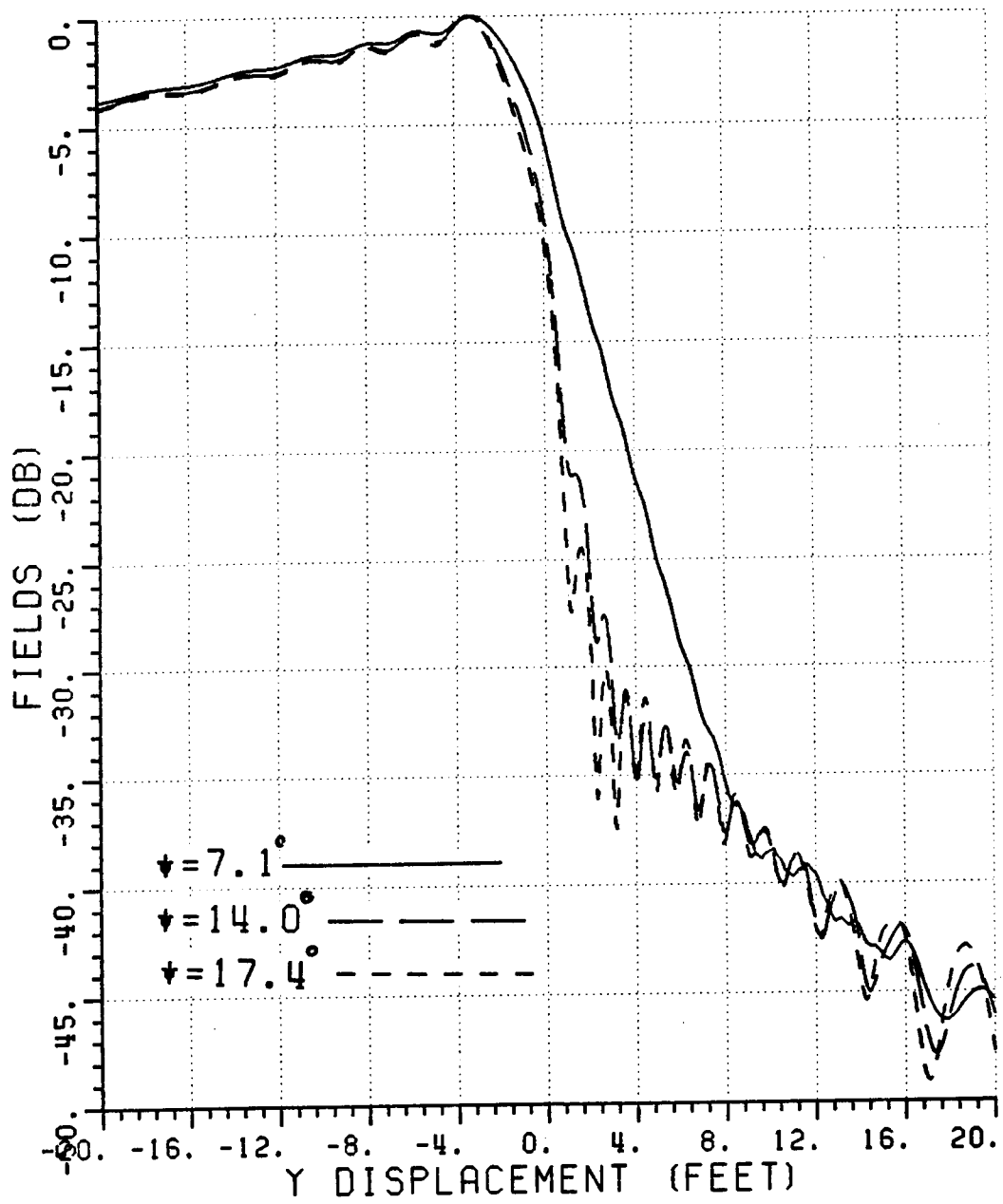
Figure 169: Scattered fields from semi-infinite absorber slabs.

CHAPTER VII

SUMMARY AND CONCLUSIONS

This study has shown that the performance of a compact range can be enhanced by improving the design of the main reflector and incorporating a dual chamber configuration with a Gregorian subreflector feed system. The quality of the plane wave illuminating the target zone is improved with respect to a reduction in the amplitude taper, ripple and cross-polarization errors.

It has been shown that the diffractions from the edges of the parabolic main reflector are reduced if rolled surface terminations are added to the parabola. First generation rolled edges were elliptic in shape, resulting in a continuous surface slope across the parabola/rolled edge junction, but it has a discontinuity in the surface radius of curvature across the junction. The edge diffracted fields can be reduced even more by smoothly blending the rolled surface terminations from a parabola into an ellipse. Blended rolled edges ensure that the radius of curvature as well as the slope of the surface are continuous across the junction. By choosing an appropriate blending function, one can design the rolled edges such that the first and higher order derivatives of the radius of curvature are continuous across the junction as well. The impetus for obtaining a smoother junction is that a smoother junction results in a more continuous reflected field which leads to a weaker edge diffracted field and ultimately less ripple in the total field. A relation between the n-th order blending function and the corresponding error term that results in

a discontinuity of the n-th order derivative of the radius of curvature across the junction was derived, and it was shown how the blending parameters should be chosen to minimize the error term. An algorithm for designing optimized blended rolled edges was consequently developed, based on an analysis of the error term. Several two-dimensional design examples were discussed, and the reduction in edge diffracted fields resulting from blended rolled edges were clearly illustrated.

The edge diffracted fields from three-dimensional reflectors can further be reduced by shaping the contour of the junction between the parabolic section and rolled edge contours. It was shown that a concave edge contour has superior performance over conventional convex and rectangular edge contours. Design equations for a complete three-dimensional main reflector incorporating blended rolled edges and a concave edge contour were developed. Several three-dimensional main reflectors were analyzed using a new corrected physical optics method; whereby, the end point contributions from false scattering centers on the incident shadow boundary of the main reflector are removed. The results confirmed that the edge diffractions from a three-dimensional main reflector can be significantly reduced if the reflector has a concave edge contour and blended rolled edges.

A dual chamber compact range configuration was proposed; whereby, the main reflector and target zone are contained in one chamber and an oversized Gregorian subreflector with feed assemblies in the second, smaller, chamber. The chambers are isolated from one another by an absorber fence, with a small coupling aperture to transmit signals between them. It was shown that the use of a subreflector system results in a significant reduction in the amplitude taper and cross-polarization errors in the illumination of the target zone. In addition, the absorber fence virtually eliminates the effects of diffraction from the subreflector and spillover from the feed on the desired illumination.

In order to minimize the secondary diffractions from the absorber fence, the coupling aperture should be shaped. It was shown that a wedge termination is most appropriate, and that the selection of a wedge angle depends on a compromise between weak diffracted and transmitted fields. In order to analyze the scattering from the coupling aperture, a new technique to calculate the forward scattering from a homogeneous, lossy absorber slab with a wedge termination was developed. The technique combines the tracing of rays through the absorber with aperture integration. Several finite slabs with wedge terminations and plane wave illumination were analyzed, and the results compared with those obtained from the moment method. It was found that the new aperture integration technique can predict the scattering from the absorber slabs within an acceptable accuracy. The technique was then expanded to enable one to determine the forward scattering from a semi-infinite absorber slab with a wedge termination and line source illumination. The results confirmed that a smaller wedge angle results in less ripple in the scattered field but also in a stronger transmitted field.

Several topics for further research have become apparent during the course of this study; viz.,

1. Investigation of ways whereby the physical optics integration of three-dimensional main reflectors can be performed faster and cheaper.

2. The extension of the equations for the derivatives of the blended rolled edges to three dimensions, and the optimization algorithm to three-dimensional reflectors. The present algorithm analyzes one plane, which enables one to design optimized circularly symmetric reflectors. A three-dimensional extension would enable one to optimize in three-dimensions, which would be particularly useful for designing optimized reflectors with concave edge

295

contours. One would probably find that the blending parameters would have to change continuously around the perimeter of the edge contour in order to obtain an optimized three-dimensionsal design; ie., a "blending of the blending parameters".

3. The optimization algorithm can be automated, so that a computer can determine the optimized blending parameters with minimal human intervention.

4. The development of an optimized shaping of the concave edge contour of the main reflector.

5. Improvement of the aperture integration technique for determining the scattering from a lossy dielectric slab with a wedge termination. Higher order internal reflections can be taken into account, especially near the apex of the wedge. The technique can be extended to include multilayer cases and more complicated geometries.

6. Development of an analysis of the dual chamber design which includes the effects of the coupling aperture diffractions in order to predict the field quality in the target zone.

APPENDIX A

APPLICATIONS OF DIFFERENTIAL GEOMETRY

In this appendix, differential geometry[69] is used to derive expressions for the unit vector normal to a 3-dimensional surface, the radius of curvature and tangential vector of a 2-dimensional curve as well as the radius of curvature and its derivatives for a blended rolled edge.

A.1 Unit vector normal to a surface

Let a surface in three dimensions be given by the following parameterized equation:

$$\mathbf{r}(u,v) = [\, x(u,v),\ y(u,v),\ z(u,v) \,] \,. \qquad (A.1)$$

The partial derivatives of $\mathbf{r}$ are given by

$$\mathbf{r}_u \;=\; \left[\, \frac{\partial x}{\partial u},\, \frac{\partial y}{\partial u},\, \frac{\partial z}{\partial u} \,\right] \,,\ \text{and} \qquad (A.2)$$

$$\mathbf{r}_v \;=\; \left[\, \frac{\partial x}{\partial v},\, \frac{\partial y}{\partial v},\, \frac{\partial z}{\partial v} \,\right] \,. \qquad (A.3)$$

The unit vector normal to the surface can then be expressed as

$$\hat{\mathbf{n}}(u,v) = \frac{\mathbf{r}_u \times \mathbf{r}_v}{|\, \mathbf{r}_u \times \mathbf{r}_v \,|} \,. \qquad (A.4)$$

Depending on the application, one may be concerned with the inward or outward normal to the surface. They are related by

$$\hat{\mathbf{n}}_{in} = -\hat{\mathbf{n}}_{out} \,. \qquad (A.5)$$
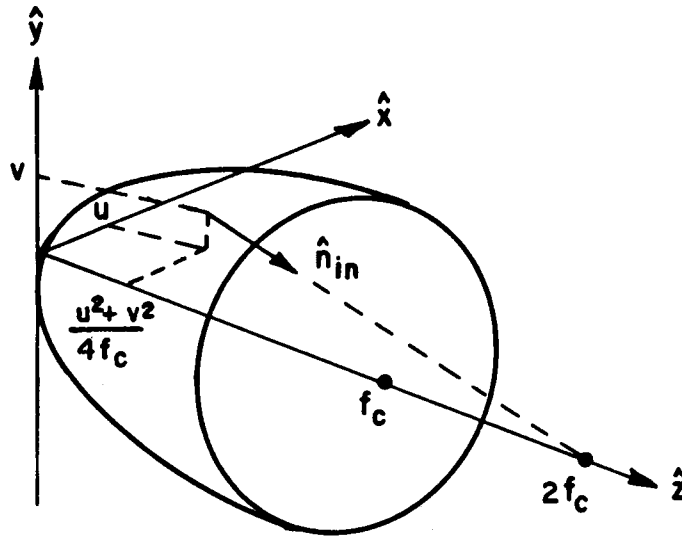
Figure 170: Paraboloid.

In the case of bodies of revolution, the inward normal points towards the axis
of symmetry, and the outward normal away from it. Two special cases are now
considered; viz., a paraboloid and a spheroid.

A.1.1 Paraboloid

Consider a paraboloid with the z-axis as its axis of symmetry as shown in
Figure 170. This surface can be expressed as

$$\mathbf{r}(u,v) = \left[u, \; v, \; \frac{u^2 + v^2}{4f_c} \right] \qquad (A.6)$$

where

$$u = x \text{ displacement}$$

$$v = y \text{ displacement , and}$$

$$f_c = \text{focal length .}$$

In this case one then finds that

$$\mathbf{r}_u = \left[1, \, 0, \, \frac{u}{2f_c} \right] , \text{ and} \qquad (A.7)$$

$$\mathbf{r}_v = \left[0, \, 1, \, \frac{v}{2f_c} \right] \qquad (A.8)$$

so that

$$\hat{\mathbf{n}}_{in}(u,v) = \left[\frac{-u}{\sqrt{u^2 + v^2 + 4f_c^2}}, \, \frac{-v}{\sqrt{u^2 + v^2 + 4f_c^2}}, \, \frac{2f_c}{\sqrt{u^2 + v^2 + 4f_c^2}} \right] . \qquad (A.9)$$

Notice that $\hat{\mathbf{n}}_{in}$ points towards the point $(0, 0, 2f_c)$.

A.1.2 Spheroid

A spheroid is an ellipsoid with two axes lengths the same, such that it is a body of revolution. Consider now a spheroid with the z-axis as its axis of symmetry. Let the axis length along the direction of the z-axis be a_e, and along the direction of the x- and y-axes be b_e. This configuration is shown in Figure 171. The spheroid can be described by the following parametric equation:

$$\mathbf{r}(u,v) = [\, b_e \cos v \sin u, \, b_e \sin v \sin u, \, a_e \cos u \,] \qquad (A.10)$$

where $0^o \leq v \leq 360^o$ and $0^o \leq u \leq 180^o$. Since the spheroid is a body of revolution around the z-axis, the parameter v is the spherical angle (ϕ). The parameter u corresponds to the spherical angle (θ), and they are related by

$$\tan \theta = \frac{b_e}{a_e} \tan u . \qquad (A.11)$$

In this case then,

$$\mathbf{r}_u = [\, b_e \cos v \cos u, \, b_e \sin v \cos u, \, -a_e \sin u \,] , \text{ and} \qquad (A.12)$$

$$\mathbf{r}_v = [\, -b_e \sin v \sin u, \, b_e \cos v \sin u, \, 0 \,] \qquad (A.13)$$

299
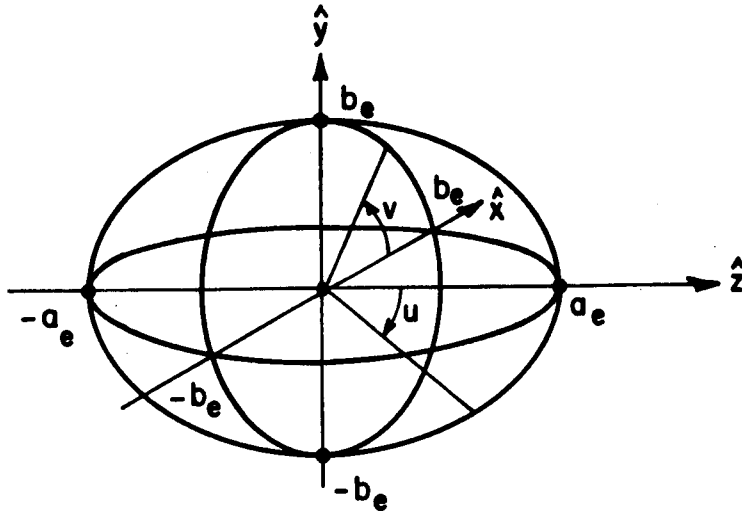
Figure 171: Spheroid.

so that

$$\mathbf{n}_{in}(u, v) = \left[\frac{-\cos v \sin u}{b_e}, \ \frac{-\sin v \sin u}{b_e}, \ \frac{-\cos u}{a_e} \right] . \qquad (A.14)$$

The unit vector normal to the surface is then given by

$$\hat{\mathbf{n}}_{in} = \frac{\mathbf{n}_{in}}{\mid \mathbf{n}_{in} \mid} . \qquad (A.15)$$

Notice that in the case where $a_e = b_e$, the spheroid becomes a sphere. In this case $\hat{n}_{out}$ is equal to the spherical radial unit vector, and $u = \theta$.

A.2 Radius of curvature and tangential vector of a 2-dimensional curve

Consider a curve in the yz-plane, given by the parameterized equation

$$\mathbf{r}(\gamma) = [\ 0, \ y(\gamma), \ z(\gamma)\ ] . \qquad (A.16)$$

The curvature (κ) at γ is given by

$$\kappa(\gamma) = \frac{\mid \mathbf{r}'(\gamma) \times \mathbf{r}''(\gamma) \mid}{\mid \mathbf{r}'(\gamma) \mid^3} \qquad (A.17)$$

300

where

$$\mathbf{r}'(\gamma) = \frac{d\mathbf{r}(\gamma)}{d\gamma} = [\, 0,\ y'(\gamma),\ z'(\gamma)\,]\ ,\ \text{and} \qquad (A.18)$$

$$\mathbf{r}''(\gamma) = \frac{d^2\mathbf{r}(\gamma)}{d\gamma^2} = [\, 0,\ y''(\gamma),\ z''(\gamma)\,]\ . \qquad (A.19)$$

The radius of curvature (R_c) at γ is then given by

$$R_c(\gamma) = \frac{1}{\kappa(\gamma)} \qquad (A.20)$$

so that

$$R_c(\gamma) = \frac{|\,\mathbf{r}'\,|^3}{|\,\mathbf{r}' \times \mathbf{r}''\,|}\ . \qquad (A.21)$$

However,

$$|\,\mathbf{r}' \times \mathbf{r}''\,| = |\,y'z'' - y''z'\,| \qquad (A.22)$$

so that

$$R_c(\gamma) = \frac{[(y')^2 + (z')^2]^{\frac{3}{2}}}{|\,y'z'' - y''z'\,|}\ . \qquad (A.23)$$

The vector tangential to the curve is given by

$$\mathbf{t}(\gamma) = \mathbf{r}'(\gamma) \qquad (A.24)$$

so that

$$\hat{\mathbf{t}} = \frac{\mathbf{t}}{|\mathbf{t}|} = (t_1, t_2) \qquad (A.25)$$

and since $\hat{\mathbf{n}} \cdot \hat{\mathbf{t}} = 0$, one finds that

$$\hat{\mathbf{n}} = (t_2, -t_1)\ . \qquad (A.26)$$

Two special cases will be considered; viz., an ellipse and a parabola.
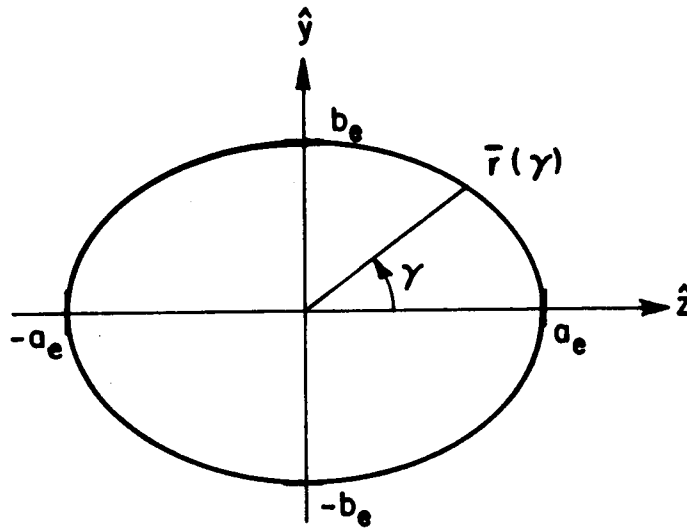
Figure 172: Ellipse.

A.2.1 Ellipse

Consider the ellipse described by

$$\mathbf{r}(\gamma) = [\, 0, \; b_e \sin\gamma, \; a_e \cos\gamma \,]. \qquad (A.27)$$

The semi-major and semi-minor axes lengths are a_e and b_e, respectively. Notice that the angle γ is not a real angle, but a parametric one. In this case one, finds that

$$y' \;=\; b_e \cos\gamma \qquad\qquad (A.28)$$

$$y'' \;=\; -b_e \sin\gamma \qquad\qquad (A.29)$$

$$z' \;=\; -a_e \sin\gamma \;,\text{ and} \qquad\qquad (A.30)$$

$$z'' \;=\; -a_e \cos\gamma \qquad\qquad (A.31)$$

so that

$$\mathbf{t}(\gamma) = [\, 0, \; b_e \cos\gamma, \; -a_e \sin\gamma \,] \;,\text{ and} \qquad (A.32)$$

302

$$R_c(\gamma) = \frac{(a_e^2 \sin^2 \gamma + b_e^2 \cos^2 \gamma)^{\frac{3}{2}}}{a_e b_e}. \tag{A.33}$$

At $\gamma = 0$ and $\gamma = 90^o$, one finds that

$$R_c(0) = \frac{b_e^2}{a_e} \tag{A.34}$$

$$R_c(90^o) = \frac{a_e^2}{b_e}, \text{ and} \tag{A.35}$$

$$\frac{dR_c}{d\gamma}(0^o, 90^o) = 0. \tag{A.36}$$

Note that it is assumed that $a_e > b_e$ so that $R_c(0) < R_c(90^o)$. This is also evident from Figure 172.

A.2.2   Parabola

Consider the parabola described by

$$\mathbf{r}(\gamma) = \left[0, \gamma, \frac{\gamma^2}{4f_c} \right]. \tag{A.37}$$

In this case γ is the height (y) shown in Figure 173, and f_c is the focal length. Thus, one finds that

$$y'(\gamma) = 1 \tag{A.38}$$

$$y''(\gamma) = 0 \tag{A.39}$$

$$z'(\gamma) = \frac{\gamma}{2f_c}, \text{ and} \tag{A.40}$$

$$z''(\gamma) = \frac{1}{2f_c} \tag{A.41}$$

so that

$$\mathbf{t}(\gamma) = \left[0, 1, \frac{\gamma}{2f_c} \right], \text{ and} \tag{A.42}$$

$$R_c(y) = 2f_c \left[1 + \left(\frac{y}{2f_c} \right)^2 \right]^{\frac{3}{2}}. \tag{A.43}$$
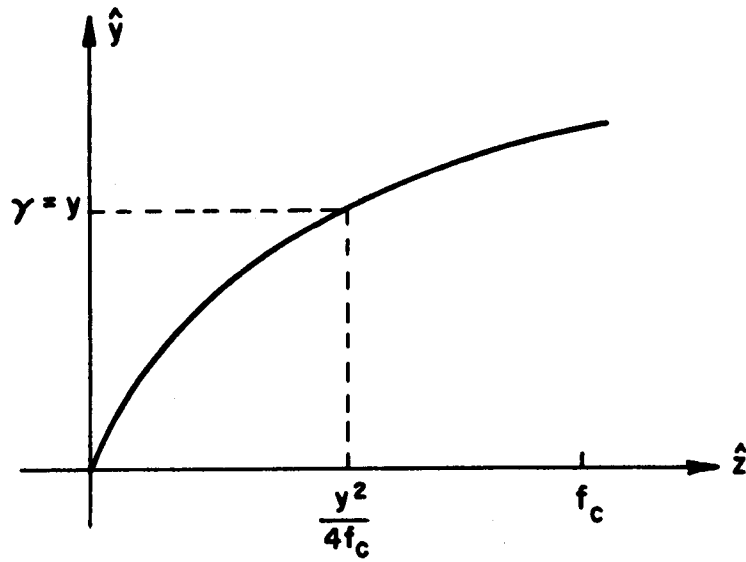
Figure 173: Parabola.

The derivatives of R_c with respect to y are given by

$$R_c'(y) \;=\; \frac{3y}{2f_c}\sqrt{1+(y/2f_c)^2} \tag{A.44}$$

$$R_c''(y) \;=\; \frac{3y^2}{8f_c^3\sqrt{1+(y/2f_c)^2}} + \frac{3}{2f_c}\sqrt{1+(y/2f_c)^2} \tag{A.45}$$

$$R_c'''(y) \;=\; \frac{9y}{8f_c^3\sqrt{1+(y/2f_c)^2}} - \frac{3y^3}{32f_c^5\sqrt[3]{1+(y/2f_c)^2}}, \text{ and} \tag{A.46}$$

$$R_c^{iv}(y) \;=\; \frac{9}{8f_c\sqrt{1+(y/2f_c)^2}} - \frac{9y^2}{16f_c^5\sqrt[3]{1+(y/2f_c)^2}} $$
$$+ \frac{9y^4}{128f_c^7\sqrt[5]{1+(y/2f_c)^2}} \,. \tag{A.47}$$

A.2.3 Blended rolled edge

The blended rolled edge is described in Section 3.4. In this section expressions will be derived for the radius of curvature (R_c) and the first four derivatives of R_c in the yz-plane.

304

It is useful to evaluate the derivatives of R_c of the blended surface with respect to y rather than γ. This serves as a standardization for comparison of different types of blending, and makes it convenient to compare the derivatives of R_c of the blended surface at the junction with that of the parabola (see Equations (A.44)–(A.47)). In addition to deriving the general expressions for the radius of curvature of the rolled edge (R_c) and its derivatives for all γ, the derivatives of R_c at the top junction ($\gamma = 0$) will also be evaluated as a special case. This is necessary in order to examine the continuity of the derivatives of R_c across the junction. A similar analysis can be performed at the bottom junction. In the rest of this section a prime will denote differentiation with respect to γ, and (y_j, z_j) will indicate the coordinates of the junctions.

The general two-dimensional blended rolled surface is expressed in the yz-plane by Equations (3.73)–(3.75) such that

$$\mathbf{r}_{blend}(\gamma) = y(\gamma)\hat{\mathbf{y}} + z(\gamma)\hat{\mathbf{z}} \tag{A.48}$$

where

$$y(\gamma) = (B\gamma + y_j)[1 - b(\gamma)] + [C\sin\gamma + D(1 - \cos\gamma) + y_j]b(\gamma) \tag{A.49}$$

$$z(\gamma) = \frac{(B\gamma + y_j)^2}{4f_c}[1 - b(\gamma)] + [E\sin\gamma + F(1 - \cos\gamma) + z_j]b(\gamma) \tag{A.50}$$

where

$$B = \frac{\pm(x_m/\gamma_m)}{\sqrt{1 + (y_j/2f_c)^2}} \tag{A.51}$$

$$C = \frac{\pm a_e}{\sqrt{1 + (y_j/2f_c)^2}} \tag{A.52}$$

$$D = \frac{b_e y_j}{2f_c\sqrt{1 + (y_j/2f_c)^2}} \tag{A.53}$$

$$E = \frac{\pm a_e y_j}{2f_c\sqrt{1 + (y_j/2f_c)^2}} \text{ , and} \tag{A.54}$$

305

$$F = \frac{-b_e}{\sqrt{1 + (y_j/2f_c)^2}} \; . \tag{A.55}$$

The ($\pm$) sign refers to the top and bottom junctions respectively. The following expressions are useful in evaluation of the derivatives of R_c at the junctions:

$$E - \frac{Cy_j}{2f_c} = 0 \tag{A.56}$$

$$F - \frac{Dy_j}{2f_c} = -b_e\sqrt{1 + (y_j/2f_c)^2} \; , \text{ and} \tag{A.57}$$

$$C + \frac{Ey_j}{2f_c} = \pm a_e\sqrt{1 + (y_j/2f_c)^2} \tag{A.58}$$

where the ($\pm$) sign refers to the top and bottom junctions respectively.

1) Radius of curvature

The radius of curvature is given by Equation (A.23) such that

$$R_c(\gamma) = \frac{R_u(\gamma)}{R_l(\gamma)} \tag{A.59}$$

where

$$R_u(\gamma) = \sqrt[3]{(y')^2 + (z')^2} \; , \text{ and} \tag{A.60}$$

$$R_l(\gamma) = |\, y'z'' - y''z' \,| \; . \tag{A.61}$$

In this case, one finds that

$$y'(\gamma) = b(C\cos\gamma + D\sin\gamma - B) \tag{A.62}$$
$$+ b'(C\sin\gamma + D(1 - \cos\gamma) - B\gamma) + B$$

$$y''(\gamma) = b(D\cos\gamma - C\sin\gamma) + 2b'(C\cos\gamma + D\sin\gamma - B) \tag{A.63}$$
$$+ b''(C\sin\gamma + D(1 - \cos\gamma) - B\gamma)$$

$$z'(\gamma) = b\left(E\cos\gamma + F\sin\gamma - \frac{B(B\gamma + y_j)}{2f_c}\right) \tag{A.64}$$

$$+ b' \left(E \sin \gamma + F(1 - \cos \gamma) + z_j - \frac{(B\gamma + y_j)^2}{4f_c} \right) + \frac{B(B\gamma + y_j)}{2f_c} \text{ , and}$$

$$z''(\gamma) = b \left(F \cos \gamma - E \sin \gamma - \frac{B^2}{2f_c} \right) \tag{A.65}$$

$$+ 2b' \left(E \cos \gamma + F \sin \gamma - \frac{B(B\gamma + y_j)}{2f_c} \right)$$

$$+ b'' \left(E \sin \gamma + F(1 - \cos \gamma) + z_j - \frac{(B\gamma + y_j)^2}{4f_c} \right) + \frac{B^2}{2f_c} \; .$$

At the junctions ($\gamma = 0$) one finds that

$$y'(0) = B \tag{A.66}$$

$$y''(0) = 2b'(C - B) \tag{A.67}$$

$$z'(0) = \frac{By_j}{2f_c} \text{ , and} \tag{A.68}$$

$$z''(0) = 2b' \left(E - \frac{By_j}{2f_c} \right) + \frac{B^2}{2f_c} \tag{A.69}$$

so that

$$R_u(0) = \mid B \mid^3 \sqrt[3]{1 + (y_j/2f_c)^2} \text{ , and} \tag{A.70}$$

$$R_l(0) = \mid \frac{B^3}{2f_c} + 2b'B \left(E - \frac{Cy_j}{2f_c} \right) \mid \; . \tag{A.71}$$

Substituting Equation (A.56) into the equations above, one finds that

$$R_c^{blend} = 2f_c \sqrt[3]{1 + (y_j/2f_c)^2} = R_c^{parabola} \; . \tag{A.72}$$

The use of a blending function will thus ensure that the radius of curvature is always continuous across the junction. Note that is this true for the top and bottom junctions.

2) First derivative

The first derivative of R_c with respect to y is given by

$$\frac{dR_c}{dy} = \frac{dR_c}{d\gamma} \frac{d\gamma}{dy} = \frac{1}{y'} \frac{dR_c}{d\gamma} \tag{A.73}$$

where

$$\frac{dR_c}{d\gamma} = \frac{R_l R_u' - R_l' R_u}{(R_l)^2} .$$

(A.74)

In this case, one finds that

$$R_u'(\gamma) = 3\sqrt{(y')^2 + (z')^2}(y'y'' + z'z'')$$

(A.75)

$$R_l'(\gamma) = \pm(y'z''' - z'y''') \text{ if } y'z'' \gtrless z'y''$$

(A.76)

$$y'''(\gamma) = -b(C\cos\gamma + D\sin\gamma) + 3b'(D\cos\gamma - C\sin\gamma)$$

$$+3b''(C\cos\gamma + D\sin\gamma - B)$$

$$+b'''(C\sin\gamma + D(1 - \cos\gamma) - B\gamma) , \text{ and}$$

(A.77)

$$z'''(\gamma) = -b(F\sin\gamma + E\cos\gamma) + 3b'\left(F\cos\gamma - E\sin\gamma - \frac{B^2}{2f_c}\right)$$

$$+3b''\left(E\cos\gamma + F\sin\gamma - \frac{B(B\gamma + y_j)}{2f_c}\right)$$

$$+b'''\left(E\sin\gamma + F(1 - \cos\gamma) + z_j - \frac{(B\gamma + y_j)^2}{4f_c}\right) .$$

(A.78)

In order to examine the continuity of the first derivative at the top junction, it is neccesary to evaluate dR_c/dy at $\gamma = 0$. Assume that $b(\gamma)$ is a first order blending function, so that $b(0) = 0$ and $b'(0) \neq 0$. One then finds that the following holds at the top junction:

$$y'(0) = B$$

(A.79)

$$y''(0) = 2b'(C - B)$$

(A.80)

$$y'''(0) = 3b'D + 3b''(C - B)$$

(A.81)

$$z'(0) = \frac{By_j}{2f_c}$$

(A.82)

$$z''(0) = 2b'\left(E - \frac{By_j}{2f_c}\right) + \frac{B^2}{2f_c} , \text{ and}$$

(A.83)

$$z'''(0) = 3b'\left(F - \frac{B^2}{2f_c}\right) + 3b''\left(E - \frac{By_j}{2f_c}\right) .$$

(A.84)

Since $B > 0$ at the top junction, it follows that:

$$R_l(y_{top}) = y'z'' - y''z' .$$ (A.85)

One thus finds that

$$R_l(0) = \frac{B^3}{2f_c}$$ (A.86)

$$R_l'(0) = -3b'B\left(b_e\sqrt{1+(y_j/2f_c)^2} + \frac{B^2}{2f_c}\right)$$ (A.87)

$$R_u(0) = B^3\sqrt[3]{1+(y_j/2f_c)^2} , \text{ and}$$ (A.88)

$$R_u'(0) = 6b'B^2\left(a_e[1+(y_j/2f_c)^2] - B\sqrt[3]{1+(y_j/2f_c)^2}\right)$$ (A.89)
$$+\frac{3B^4\sqrt{1+(y_j/2f_c)^2}}{4f_c^2}$$

so that

$$\left(\frac{dR_c}{dy}\right)^{blend}(\gamma=0) = \frac{3y_j\sqrt{1+(y_j/2f_c)^2}}{2f_c}$$ (A.90)
$$+\frac{b'\,12f_c}{B^2}\left(a_e[1+(y_j/2f_c)^2]\right.$$
$$+\frac{f_cb_e}{B}[1+(y_j/2f_c)^2]^2 - \frac{B}{2}\sqrt[3]{1+(y_j/2f_c)^2}\right) .$$

Using Equation (A.44), it follows that the following is true at the top junction:

$$\left(\frac{dR_c}{dy}\right)^{blend} = \left(\frac{dR_c}{dy}\right)^{parabola} + b'(0)\epsilon_1$$ (A.91)

where

$$\epsilon_1 = \frac{12f_c[1+(y_j/2f_c0^2]^2}{(x_m/\gamma_m)}\left(\frac{a_e}{(x_m/\gamma_m)} + \frac{f_cb_e\sqrt[3]{1+(y_j/2f_c)^2}}{(x_m/\gamma_m)^2} - \frac{1}{2}\right) .$$ (A.92)

3) Second derivative

The second derivative of R_c with respect to y is given by

$$\frac{d^2R_c}{dy^2} = \frac{1}{y'}\frac{d}{d\gamma}\left(\frac{dR_c}{dy}\right)$$ (A.93)

where

$$\frac{d}{d\gamma}\left(\frac{dR_c}{dy}\right) = \frac{d}{d\gamma}\left(\frac{dR_c}{d\gamma}\frac{1}{y'}\right) = \frac{y'(d^2R_c/d\gamma^2) - y''(dR_c/d\gamma)}{(y')^2} \qquad (A.94)$$

so that

$$\frac{d^2R_c}{dy^2} = \frac{y'(d^2R_c/d\gamma^2) - y''(dR_c/d\gamma)}{(y')^3} \; . \qquad (A.95)$$

It is found that

$$\frac{d^2R_c}{d\gamma^2} = \frac{R_l(R_l R_u'' - R_l'' R_u) - 2R_l'(R_l R_u' - R_l' R_u)}{(R_l)^3} \qquad (A.96)$$

where

$$R_u''(\gamma) = 3\sqrt{(y')^2 + (z')^2}[y'y''' + (y'')^2 + (z'')^2 + z'z'''] \qquad (A.97)$$
$$+ \frac{3(y'y'' + z'z'')^2}{\sqrt{(y')^2 + (z')^2}}$$

$$R_l''(\gamma) = \pm(y'z^{iv} + y''z''' - y'''z'' - y^{iv}z') \text{ if } y'z'' \gtrless y''z' \qquad (A.98)$$

$$y^{iv}(\gamma) = (b - 6b'')(C\sin\gamma - D\cos\gamma) - 4b'(C\cos\gamma + D\sin\gamma) \qquad (A.99)$$
$$+ 4b'''(C\cos\gamma + D\sin\gamma - B)$$
$$+ b^{iv}(C\sin\gamma + D(1 - \cos\gamma) - B\gamma) \; , \text{ and}$$

$$z^{iv}(\gamma) = b(E\sin\gamma - F\cos\gamma) - 4b'(F\sin\gamma + E\cos\gamma) \qquad (A.100)$$
$$+ 6b''\left(F\cos\gamma - E\sin\gamma - \frac{B^2}{2f_c}\right)$$
$$+ 4b'''\left(E\cos\gamma + F\sin\gamma - \frac{B(B\gamma + y_j)}{2f_c}\right)$$
$$+ b^{iv}\left(E\sin\gamma + F(1 - \cos\gamma) + z_j - \frac{(B\gamma + y_j)^2}{4f_c}\right) \; .$$

Consider now $b(\gamma)$ to be a second order blending function, so that $b(0) = 0$, $b'(0) = 0$ and $b''(0) \neq 0$. One then finds that the following holds at the top junction:

$$y'(0) = B \qquad (A.101)$$

$$y''(0) = 0 \tag{A.102}$$

$$y'''(0) = 3b''(C - B) \tag{A.103}$$

$$y^{iv}(0) = 6b''D + 4b'''(C - B) \tag{A.104}$$

$$z'(0) = \frac{By_j}{2f_c} \tag{A.105}$$

$$z''(0) = \frac{B^2}{2f_c} \tag{A.106}$$

$$z'''(0) = 3b''\left(E - \frac{By_j}{2f_c}\right) \text{ , and} \tag{A.107}$$

$$z^{iv}(0) = 6b''\left(F - \frac{B^2}{2f_c}\right) + 4b'''\left(E - \frac{By_j}{2f_c}\right) \tag{A.108}$$

so that

$$R_l(0) = \frac{B^3}{2f_c} \tag{A.109}$$

$$R_l'(0) = 0 \text{ , and} \tag{A.110}$$

$$R_l''(0) = -6b''B\left(b_e\sqrt{1 + (y_j/2f_c)^2} + \frac{B^2}{2f_c}\right) - 3b''\frac{B^2}{2f_c}(C - B) \text{ .} \tag{A.111}$$

Since $y''(0) = 0$ and $R_l'(0) = 0$, one finds that

$$\frac{d^2R_c}{dy^2}(\gamma = 0) = \frac{R_l R_u'' - R_l'' R_u}{(R_l y')^2} \tag{A.112}$$

where

$$R_u(0) = B^3\sqrt[3]{1 + (y_j/2f_c)^2} \text{ , and} \tag{A.113}$$

$$R_u''(0) = \frac{3B^5\sqrt{1 + (y_j/2f_c)^2}}{4f_c^2} + \frac{3B^5 y^2}{16f_c^4\sqrt{1 + (y_j/2f_c)^2}} \tag{A.114}$$
$$+ 9B^2 b''\left(a_e[1 + (y_j/2f_c)^2] - B\sqrt[3]{1 + (y_j/2f_c)^2}\right) \text{ .}$$

Combining the equations above with Equation (A.45), one finds that the following is true at the top junction:

$$\left(\frac{d^2R_c}{dy^2}\right)^{blend} = \left(\frac{d^2R_c}{dy^2}\right)^{parabola} + b''(0)\epsilon_2 \tag{A.115}$$

where

$$\epsilon_2 = \frac{24 f_c \sqrt[5]{1 + (y_j/2f_c)^2}}{(x_m/\gamma_m)^2} \left(\frac{a_e}{(x_m/\gamma_m)} + \frac{f_c b_e \sqrt[3]{1 + (y_j/2f_c)^2}}{(x_m/\gamma_m)^2} - \frac{1}{2} \right) . \quad (A.116)$$

4) Third derivative

The third derivative of R_c with respect to y is given by

$$\frac{d^3 R_c}{dy^3} = \frac{1}{y'} \frac{d}{d\gamma} \left(\frac{d^2 R_c}{dy^2} \right) \quad (A.117)$$

where

$$\frac{d}{d\gamma} \left(\frac{d^2 R_c}{dy^2} \right) = \frac{d}{d\gamma} \left(\frac{y'(d^2 R_c/d\gamma^2) - y''(dR_c/d\gamma)}{(y')^3} \right) \quad (A.118)$$

so that

$$\frac{d^3 R_c}{dy^3} = \frac{(y')^2(d^3 R_c/d\gamma^3) - 3y'y''(d^2 R_c/d\gamma^2) + [3(y'')^2 - y'y'''](dR_c/d\gamma)}{(y')^5} . \quad (A.119)$$

It is found that

$$\frac{d^3 R_c}{d\gamma^3} = \frac{R_{g3}}{(R_l)^4} \quad (A.120)$$

where

$$R_{g3} = (R_l)^2 (R_l R_u''' + R_l' R_u'' - R_l'' R_u' - R_l''' R_u) \quad (A.121)$$

$$-4 R_l R_l' (R_l R_u'' - R_l'' R_u)$$

$$+[6(R_l')^2 - 2R_l R_l''](R_l R_u' - R_l' R_u)$$

$$R_u'''(\gamma) = 3\sqrt{(y')^2 + (z')^2}[y'y^{iv} + 3(y''y''' + z''z''') + z'z^{iv}] \quad (A.122)$$

$$+ \frac{9(y'y'' + z'z'')[y'y''' + (y'')^2 + (z'')^2 + z'z''']}{\sqrt{(y')^2 + (z')^2}}$$

$$- \frac{3(y'y'' + z'z'')^3}{\sqrt[3]{(y')^2 + (z')^2}}$$

312

$$R_l'''(\gamma) = \pm[y'z^v + 2(y''z^{iv} - z''y^{iv}) - z'y^v] \text{ if } y'z'' \gtreqless y''z' \qquad (A.123)$$

$$y^v(\gamma) = (b - 10b'')(C\cos\gamma + D\sin\gamma) \qquad (A.124)$$

$$+(10b''' - 5b')(D\cos\gamma - C\sin\gamma)$$

$$+5b^{iv}(C\cos\gamma + D\sin\gamma - B)$$

$$+b^v(C\sin\gamma + D(1 - \cos\gamma) - B\gamma) \text{ , and}$$

$$z^v(\gamma) = (b - 10b'')(E\sin\gamma + F\cos\gamma) \qquad (A.125)$$

$$+5b'(E\sin\gamma - F\cos\gamma)$$

$$+10b'''\left(F\cos\gamma - E\sin\gamma - \frac{B^2}{2f_c}\right)$$

$$+5b^{iv}\left(E\cos\gamma + F\sin\gamma - \frac{B(B\gamma + y_j)}{2f_c}\right)$$

$$+b^v\left(E\sin\gamma + F(1 - \cos\gamma) + z_j - \frac{(B\gamma + y_j)^2}{4f_c}\right) .$$

5) Fourth derivative

The fourth derivative of R_c with respect to y is given by

$$\frac{d^4R_c}{dy^4} = \frac{d}{dy}\left(\frac{d^3R_c}{dy^3}\right) = \frac{1}{y'}\frac{d}{d\gamma}\left(\frac{d^3R_c}{dy^3}\right) \qquad (A.126)$$

where

$$\frac{d}{d\gamma}\left(\frac{d^3R_c}{dy^3}\right) = \frac{d}{d\gamma}\left(\frac{(y')^2(d^3R_c/d\gamma^3) - 3y'y''(d^2R_c/d\gamma^2) + [3(y'')^2 - y'y'''](dR_c/d\gamma)}{(y')^5}\right)$$

$$\qquad (A.127)$$

so that

$$\frac{d^4R_c}{dy^4} = \frac{R_{c4}}{(y')^7} \qquad (A.128)$$

where

$$R_{c4} = (y')^3(d^4R_c/d\gamma^4) - 6(y')^2(d^3R_c/d\gamma^3) \qquad (A.129)$$

313

$$+[15y'(y'')^2 - 4(y')^2 y'''](d^2 R_c/d\gamma^2)$$

$$+[10y'y''y''' - (y')^2 y^{iv} - 15(y'')^3](dR_c/d\gamma) \ .$$

Furthermore, one finds that

$$\frac{d^4 R_c}{d\gamma^4} = \frac{R_{g4}}{(R_l)^5} \tag{A.130}$$

where

$$R_{g4} = (R_l)^3[R_l R_u^{iv} + 2(R_l' R_u''' - R_l''' R_u') - R_l^{iv} R_u] \tag{A.131}$$

$$-6(R_l)^2 R_l'(R_l R_u''' + R_l' R_u'' - R_l'' R_u' - R_l''' R_u)$$

$$+[18R_l(R_l')^2 - 6(R_l)^2 R_l''](R_l R_u'' - R_l'' R_u]$$

$$+[18R_l R_l' R_l'' - 2(R_l)^2 R_l''' - 24(R_l)^3](R_l R_u' - R_l' R_u)$$

$$R_u^{iv}(\gamma) = 3\sqrt{(y')^2 + (z')^2}[y'y^v + 4(y''y^{iv} + z''z^{iv}) \tag{A.132}$$

$$+3([y''']^2 + [z''']^2) + z'z^v]$$

$$+\frac{12[y'y^{iv} + 3(y''y''' + z''z''') + z'z^{iv}](y'y'' + z'z'')}{\sqrt{(y')^2 + (z')^2}}$$

$$+\frac{9[y'y''' + (y'')^2 + (z'')^2 + z'z''']^2}{\sqrt{(y')^2 + (z')^2}}$$

$$-\frac{(y'y'' + z'z'')^2[y'y''' + (y'')^2 + (z'')^2 + z'z''']}{\sqrt[3]{(y')^2 + (z')^2}}$$

$$+\frac{9(y'y'' + z'z'')^4}{\sqrt[5]{(y')^2 + (z')^2}}$$

$$R_l^{iv}(\gamma) = \pm[y'z^{vi} + 3(y''z^v - z''y^v) \tag{A.133}$$

$$+2(y'''z^{iv} - z'''y^{iv}) - z'y^{vi}] \text{ if } y'z'' \gtrless z'y''$$

$$y^{vi}(\gamma) = (b - 15b'' + 15b^{iv})(D\cos\gamma - C\sin\gamma) \tag{A.134}$$

$$+(6b' - 20b''')(C\cos\gamma + D\sin\gamma)$$

$$+6b^v(C\cos\gamma + D\sin\gamma - B)$$

$$+b^{vi}(C\sin\gamma + D(1 - \cos\gamma) - B\gamma) \ , \text{ and}$$

314

$$z^{vi}(\gamma) = (b - 15b'')(F\cos\gamma - E\sin\gamma) \tag{A.135}$$

$$+(6b' - 20b''')(E\cos\gamma + F\sin\gamma)$$

$$+15b^{iv}\left(F\cos\gamma - E\sin\gamma - \frac{B^2}{2f_c}\right)$$

$$+6b^v\left(E\cos\gamma + F\sin\gamma - \frac{B(B\gamma + y_j)}{2f_c}\right)$$

$$+b^{vi}\left(E\sin\gamma + F(1 - \cos\gamma) + z_j - \frac{(B\gamma + y_j)^2}{4f_c}\right).$$

Consider now $b(\gamma)$ to be a fourth order blending function, so that $b(0) = 0$, $b'(0) = 0$, $b''(0) = 0$, $b'''(0) = 0$ and $b^{iv}(0) \neq 0$. One then finds that the following holds at the top junction:

$$y'(0) = B \tag{A.136}$$

$$y''(0) = 0 \tag{A.137}$$

$$y'''(0) = 0 \tag{A.138}$$

$$y^{iv}(0) = 0 \tag{A.139}$$

$$y^v(0) = 5b^{iv}(C - B) \tag{A.140}$$

$$y^{vi}(0) = 15b^{iv}D + 6b^v(C - B) \tag{A.141}$$

$$z'(0) = \frac{By_j}{2f_c} \tag{A.142}$$

$$z''(0) = \frac{B^2}{2f_c} \tag{A.143}$$

$$z'''(0) = 0 \tag{A.144}$$

$$z^{iv}(0) = 0 \tag{A.145}$$

$$z^v(0) = 5b^{iv}\left(E - \frac{By_j}{2f_c}\right), \text{ and} \tag{A.146}$$

$$z^{vi}(0) = 15b^{iv}\left(F - \frac{B^2}{2f_c}\right) + 6b^v\left(E - \frac{By_j}{2f_c}\right) \tag{A.147}$$

so that

$$R_l(0) = \frac{B^3}{2f_c} \tag{A.148}$$

$$R_l'(0) = 0 \tag{A.149}$$

$$R_l''(0) = 0 \tag{A.150}$$

$$R_l'''(0) = 0 \text{ , and} \tag{A.151}$$

$$R_l^{iv}(0) = -15Bb^{iv}\left(b_e\sqrt{1 + (y_j/2f_c)^2} + \frac{B^2}{2f_c}\right) \tag{A.152}$$

$$-15b^{iv}(C - B)\frac{B^2}{2f_c} \ .$$

It is then found that

$$\frac{d^4 R_c}{dy^4}(\gamma = 0) = \frac{R_l R_u^{iv} - R_l^{iv} R_u}{(R_l)^2 (y')^4} \tag{A.153}$$

where

$$R_u(0) = B^3 \sqrt[3]{1 + (y_j/2f_c)^2} \text{ , and} \tag{A.154}$$

$$R_u^{iv}(0) = \frac{9B^7}{16f_c^4\sqrt{1 + (y_j/2f_c)^2}} \tag{A.155}$$

$$-\frac{9B^7 y^2}{32f_c^6 \sqrt[3]{1 + (y_j/2f_c)^2}}$$

$$+\frac{9B^7 y^4}{256f_c^8 \sqrt[5]{1 + (y_j/2f_c)^2}}$$

$$+15B^2 b^{iv}\left(a_e[1 + (y_j/2f_c)^2] - B\sqrt[3]{1 + (y_j/2f_c)^2}\right) \ .$$

Combining the equations above with Equation (A.47), one finds that the following is true at the top junction:

$$\left(\frac{d^4 R_c}{dy^4}\right)^{blend} = \left(\frac{d^4 R_c}{dy^4}\right)^{parabola} + b^{iv}(0)\epsilon_4 \tag{A.156}$$

where

$$\epsilon_4 = \frac{60f_c \sqrt[7]{1 + (y_j/2f_c)^2}}{(x_m/\gamma_m)^4}\left(\frac{a_e}{(x_m/\gamma_m)} + \frac{f_c b_e \sqrt[3]{1 + (y_j/2f_c)^2}}{(x_m/\gamma_m)^2} - \frac{1}{2}\right) \ . \tag{A.157}$$

APPENDIX B

CLOSED FORM EXPRESSIONS FOR THE APERTURE INTEGRATION OVER A HALF PLANE IN FREE SPACE

In order to solve the problem described in Section 6.3, it is required to determine the scattered field resulting from the aperture integration performed over a planar aperture extending over the half plane $(-\infty \leq y \leq 0)$ in free space as shown in Figure 174. The two-dimensional transverse magnetic (TM) scattered field at a field point (x, y) is then given by Equation (6.77) as

$$E_z^{sa}(x, y) = -e^{j\pi/4} Z_0 \sqrt{\frac{k}{2\pi}} \int_{-\infty}^{0} H_y^{ap}(y') \frac{e^{-jk\rho}}{\sqrt{\rho}} \, dy' \qquad (B.1)$$

where y' is a point in the aperture, and

$$\rho = \sqrt{x^2 + (y' - y)^2} \; . \qquad (B.2)$$

Note that the angle (ϕ) which $\hat{\rho}$ makes with the $-y$-axis is given by

$$\phi = \arccos\left(\frac{y' - y}{\rho}\right) \qquad (B.3)$$

as shown in Figure 174. Consider an electric line source to be located at (x_s, y_s). The electric field incident upon the aperture from this source is given by

$$E_z^i(x = 0, y') = \frac{e^{-jk\rho'}}{\sqrt{\rho'}} \qquad (B.4)$$

where

$$\rho' = \sqrt{x_s^2 + (y' - y_s)^2} \qquad (B.5)$$

317
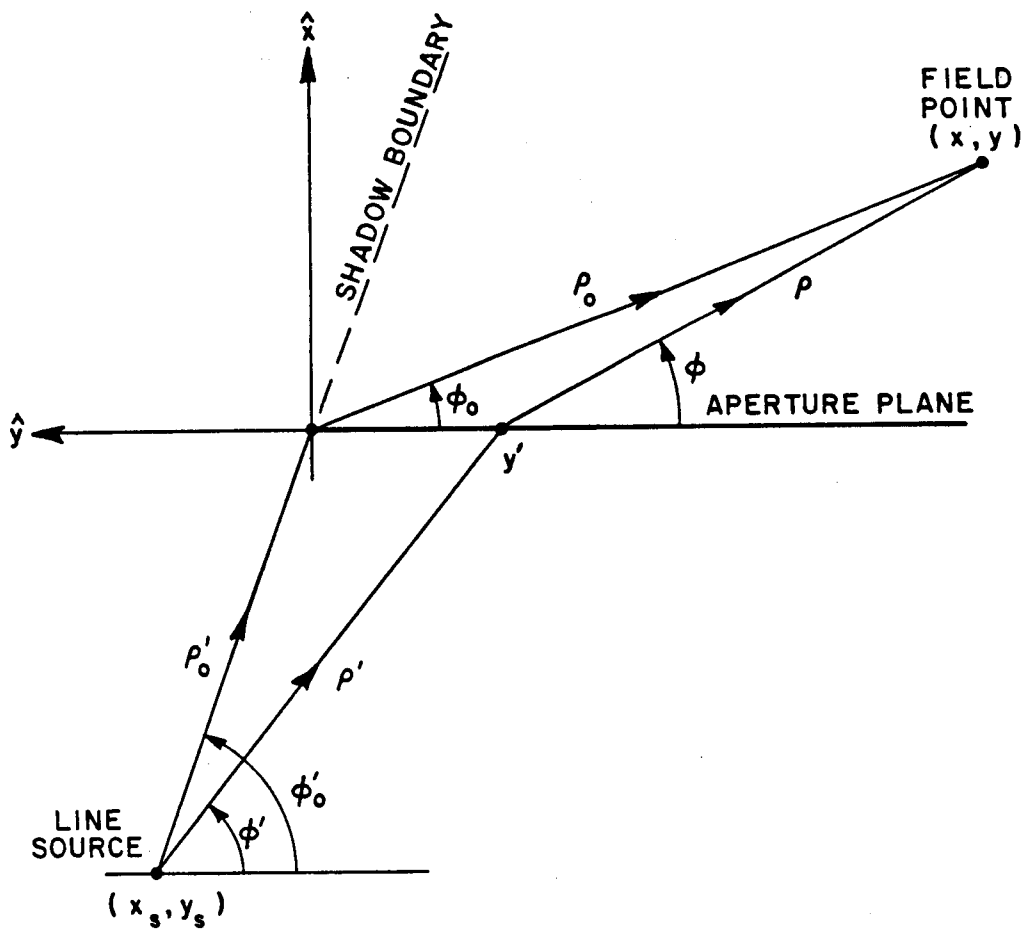
Figure 174: Aperture integration over a half plane in free space.

so that the tangential magnetic field in the aperture is given by

$$H_y^{ap}(y') = \frac{-\sin \phi' e^{-jk\rho'}}{Z_0 \sqrt{\rho'}} \qquad (B.6)$$

where

$$\phi' = \arccos \left(\frac{y_s - y'}{\rho'} \right) . \qquad (B.7)$$

The scattered field can thus be expressed as

$$E_z^{sa}(x,y) = e^{j\pi/4} \sqrt{\frac{k}{2\pi}} \int_{-\infty}^{0} \frac{\sin \phi' e^{-jk(\rho'+\rho)}}{\sqrt{\rho' \rho}} \, dy' . \qquad (B.8)$$

The integral in Equation (B.8) can be evaluated by the method of stationary phase as explained in Chapter 2, so that

$$E_z^{sa} \approx E_{zsp}^{sa} + E_{zep}^{sa} \qquad (B.9)$$

where E_{zsp}^{sa} is the contribution from the stationary point, and E_{zep}^{sa} is the contribution from the end point (at $y = 0$). The end point at $y = -\infty$ is too far away to have any effect.

Following the notation of Equations (2.79)–(2.83), one finds that

$$\Phi(y') = -(\rho' + \rho) \qquad (B.10)$$

or

$$\Phi(y') = -(\sqrt{x_s^2 + (y' - y_s)^2} + \sqrt{x^2 + (y' - y)^2}) . \qquad (B.11)$$

It follows that

$$\Phi'(y') = - \left(\frac{y' - y_s}{\rho'} + \frac{y' - y}{\rho'} \right) \qquad (B.12)$$

or

$$\Phi'(y') = \cos \phi' - \cos \phi . \qquad (B.13)$$

319
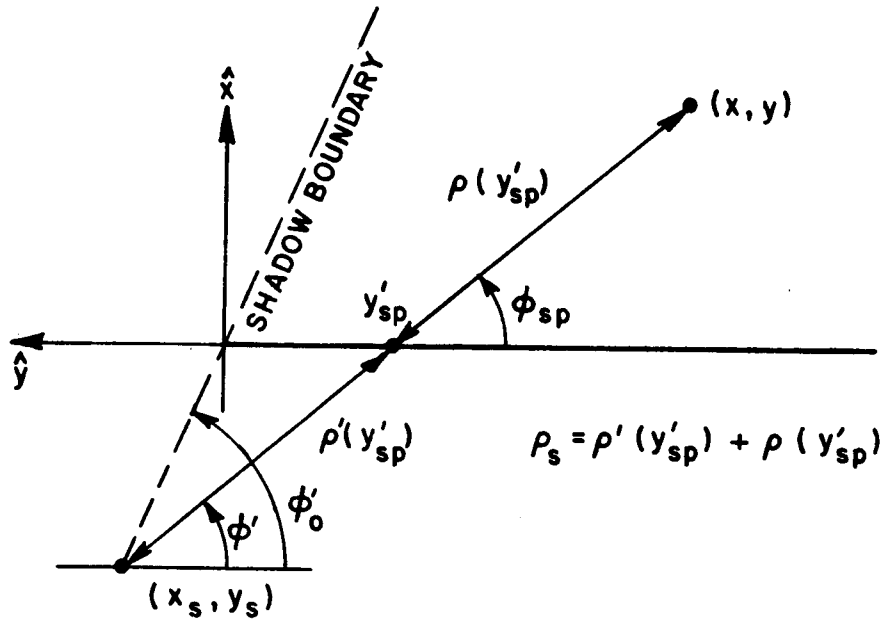
Figure 175: Stationary point in the aperture integration over a half plane in free space.

The stationary point (y'_{sp}) occurs where

$$\Phi(y'_{sp}) = 0 \qquad (B.14)$$

so that y'_{sp} is that point in the aperture where

$$\cos \phi' = \cos \phi_{sp} \qquad (B.15)$$

as shown in Figure 175.

Furthermore, one finds that

$$\Phi''(y'_{sp}) = -\sin^2 \phi' \left(\frac{\rho' + \rho}{\rho' \rho} \right) \qquad (B.16)$$

so that

$$| \Phi''(y'_{sp}) | = \sin^2 \phi' \left(\frac{\rho' + \rho}{\rho' \rho} \right) \text{ , and} \qquad (B.17)$$

$$\text{sgn}[\Phi''(y'_{sp})] = -1 \qquad (B.18)$$

where ρ and ρ' are interpreted as $\rho = \rho(y' = y'_{sp})$ and $\rho' = \rho'(y' = y'_{sp})$.

Substituting Equations (B.17) and (B.18) into Equation (2.79), one finds that the stationary point contribution to the scattered field is given by

$$E^{sa}_{zsp} = \frac{e^{-jk(\rho'+\rho)}}{\sqrt{\rho'+\rho}} \; .$$

(B.19)

Equation (B.19) can thus be expressed as

$$E^{sa}_{zsp}(x,y) = \begin{cases} \dfrac{e^{-jk\rho_s}}{\sqrt{\rho_s}} & 0 \le \phi' \le \phi'_0 \\[2mm] 0 & \text{otherwise} \end{cases}$$

(B.20)

where

$$\rho_s = \sqrt{(x-x_s)^2 + (y-y_s)^2} \; , \text{ and}$$

(B.21)

$$\phi'_0 = \arccos\left(\frac{y_s}{\rho_0}\right) \; .$$

(B.22)

This term represents the incident ray from the source at (x_s, y_s) to the field point at (x,y). Note that E^{sa}_{zsp} is equal to zero when the stationary point (y'_{sp}) is no longer in the aperture.

Consider now the end point contribution (E^{sa}_{zep}) due to the end point at $y = 0$. Substituting Equation (B.15) into Equations (B.13) and (2.83), one finds that the end point contribution can be expressed as

$$E^{sa}_{zep} = \frac{e^{-jk\rho'}}{\sqrt{\rho'}} D^a(\phi'_0, \phi_0)\frac{e^{-jk\rho}}{\sqrt{\rho}}$$

(B.23)

where

$$D^a(\phi'_0, \phi_0) = \frac{e^{-j\pi/4}\sin\phi'_0}{\sqrt{2\pi k}(\cos\phi'_0 - \cos\phi_0)}$$

(B.24)

$$\rho' = \sqrt{x_s^2 + y_s^2} \; , \text{ and}$$

(B.25)

$$\rho = \sqrt{x^2 + y^2} \; , \text{ and}$$

(B.26)

$$\phi_0 = \arccos\left(\frac{-y}{\rho_0}\right) \; .$$

(B.27)

321

Note that Equation (B.23) is cast in the form of a ray diffracted from the end point.

However, the diffraction coefficient (D^a) becomes singular at the shadow boundary; ie., where $\phi'_0 = \phi_0$. This singularity is similar to the one that occurs in Keller's GTD diffraction coefficients[16]. The discontinuity in the diffraction coefficients cause the total field (ie. incident plus diffracted fields) to be discontinuous at the shadow boundary. Koumyoumjian and Pathak developed the UTD[17] to correct this problem, and found that the total field becomes continuous when the diffraction coefficients are multiplied by a transition function (F). The coefficient in Equation (B.24) can now be heuristically multiplied by the same transition function, so that modified diffraction coefficient (D^{ep}) is given by

$$D^{ep}(\phi'_0, \phi_0, L) = \frac{e^{-j\pi/4}\sin\phi'_0}{\sqrt{2\pi k}(\cos\phi'_0 - \cos\phi_0)} F\left[\frac{kL}{2}\left(\frac{\cos\phi'_0 - \cos\phi_0}{\sin\phi_0}\right)^2\right] \qquad (B.28)$$

where the transition function is described in Section 2.2 and

$$L = \frac{\rho'_0 \, \rho_0}{\rho'_0 + \rho_0} \ . \qquad (B.29)$$

The end point contribition to the total scattered field can thus be expressed as

$$E^{sa}_{zep} = \frac{e^{-jk\rho'}}{\sqrt{\rho'}} D^{ep}(\phi'_0, \phi_0, L)\frac{e^{-jk\rho}}{\sqrt{\rho}} \ . \qquad (B.30)$$

The inclusion of the transition function causes the total field (E^{sa}_z) given in Equation (B.9) to be continuous.

REFERENCES

[1] W.H. Kummer and E.S. Gillespie, "Antenna Measurements–1978", Proc. IEEE, Vol 66, No 4, April 1978, pp. 483–507.

[2] P. Blacksmith Jr., R.E. Hyatt and R.B. Mack, "Introduction to Radar Cross-Section Measurements", Proc. IEEE, Vol 53, No 8, August 1965, pp. 901–918.

[3] H.C. Marlow *et. al.*, "The RAT SCAT Cross-Section Facility", Proc. IEEE, Vol 53, No 8, August 1965, pp. 946–954.

[4] E.F. Knott, J.F. Schaeffer and M.T. Tuley, *Radar Cross Section*, Artech House, 1985.

[5] W.H. Emerson, " Electromagnetic Wave Absorbers and Anechoic Chambers Through the Years", IEEE Trans. Antennas and Prop., Vol AP-21, No 4, July 1973, pp. 484–490.

[6] R.C. Johnson, "Antenna Range for Providing a Plane Wave for Antenna Measurements", U.S. Patent 3 302 205, January 31, 1967.

[7] E.K. Walton and J.D. Young, "The Ohio State University Compact Radar Cross-Section Measurement Range", IEEE Trans. Antennas and Prop., Vol AP-32, No 11, November 1984, pp. 1218–1223.

[8] R.C. Johnson, H.A. Ecker and R.A. Moore, " Compact Range Techniques and Measurements", IEEE Trans. Antennas and Prop., Vol AP-17, No 5, September 1969, pp. 568–576.

[9] *Measurement, Processing and Analysis of Radar Target Signatures*, Short Course Notes, The Ohio State University, September 10–13, 1985.

[10] D.W. Hess and R.C. Johnson, "Compact Ranges Provide Accurate Measurement of Radar Cross-Section", MSN, Vol 12, No 9, September 1982, pp. 150–160.

[11] R.F. Harrington, *Field Computation by Moment Methods*, Krieger, 1982.

[12] R.E. Collin, *Antennas and Radiowave Propagation*, McGraw-Hill, 1985.

[13] G.A. Deschamps, "Ray Techniques in Electromagnetics", Proc. IEEE, Vol 60, No 9, September 1972, pp. 1022–1035.

[14] R. Weinstock, *Calculus of Variations*, Dover, 1974.

[15] T.A. Milligan, *Modern Antenna Design*, McGraw-Hill, 1985.

[16] J.B. Keller, "Geometrical Theory of Diffraction", J. Opt. Soc. America, Vol 52, No 2, February 1962, pp. 116–130.

[17] R.G. Kouyoumjian and P.H. Pathak, "A Uniform Geometrical Theory of Diffraction for an Edge in a Perfectly Conducting Surface", Proc. IEEE, Vol 62, No 11, November 1974, pp. 1448–1461.

[18] W.D. Burnside, R.J. Marhefka and N. Wang, *Computer Programs, Subroutines and Functions for the Short Course on the Modern Geometrical Theory of Diffraction*, The Ohio State University.

[19] W.D. Burnside and R.J. Marhefka, "Applications of Edge Diffraction", Short Course Notes of *The Modern Geometrical Theory of Diffraction*, Vol 2, The Ohio State University, 1984.

[20] G.L. James, *Geometrical Theory of Diffraction for Electromagnetic Waves*, Peter Peregrinus Ltd, 1980.

[21] C.A. Mentzer, L. Peters Jr., and R.C. Rudduck, "Slope Diffraction and its Applications to Horns", IEEE Trans. Antennas and Prop., Vol AP-23, March 1975, pp. 153.

[22] R.F. Harrington, *Time Harmonic Electromagnetic Fields*, McGraw-Hill, 1961.

[23] W.L. Stutzman and G.A. Thiele, *Antenna Theory and Design*, John Wiley & Sons, 1981.

[24] P.I. Ufimtsev, "Method of Edge Waves in the Physical Theory of Diffraction", translated version, FTD-HC-23-259-71, August 1971.

[25] W.D. Gordon, "Far Field Approximation of the Kirchoff-Helmholtz Presentation of Scattered Fields", IEEE Trans. Antennas and Prop., Vol AP-23, No 5, July 1975, pp. 590–592.

[26] I.J. Gupta and W.D. Burnside, "A Correction to the Physical Optics Approximation", submitted to the IEEE Trans. Antennas and Prop.

[27] L.P. Felsen and N. Marcuvitz, *Radiation and Scattering of Waves*, Prentice-Hall, 1973.

[28] I.J. Gupta, C.W.I. Pistorius and W.D. Burnside, "An Efficient Method to Compute the End Point Contributions in PO Solutions", submitted to the IEEE Trans. Antennas and Prop.

[29] D.R. Rhodes, "On Minimum Range Radiation Patterns", Proc. IRE, Vol 42, September 1954, pp. 1408-1410.

[30] P.S. Hacker and H.E. Schrank, " Range Distance Requirements for Measuring Low and Ultralow Sidelobe Antenna Patterns", IEEE Trans. Antennas and Prop., Vol AP-30, No 5, September 1982, pp. 956-966.

[31] R.C. Hansen, "Measurement Distance Effects on Low Sidelobe Patterns", IEEE Trans. Antennas and Prop., Vol AP-32, No 6, June 1984, pp. 591-594.

[32] M.D. Rader and W.D. Burnside, *A Cassegrain Reflector System for Compact Range Applications*, Tech. Report 716148-14, The Ohio State University ElectroScience Laboratory, July 1986.

[33] R.C. Johnson, H.A. Ecker and J.S. Hollis, "Determination of Far-Field Antenna Patterns from Near-Field Measurements", Proc. IEEE, Vol 61, No 12, December 1973, pp. 1668-1694.

[34] R.C. Johnson, "Some Design Parameters for Point-Source Compact Ranges", IEEE Trans. Antennas and Prop., Vol AP-34, No 6, June 1986, pp. 845-847.

[35] W.D. Burnside and L. Peters Jr., "Target Illumination Requirements for Low RCS Target Measurements", Proc. 1985 AMTA Symposium, Melbourne, FL.

[36] J.D. Young, "Compact Range Reflector Design and Trade-offs", Short Course Notes of *Measurement, Processing and Analysis of Radar Target Signatures*, Vol 1, The Ohio State University, September 10-13, 1985.

[37] R.C. Johnson and D.W. Hess, "Performance of a Compact Antenna Range", Digest IEEE Int. Symp. Antennas and Prop., 1975.

[38] D.W. Hess, "Compact Range Reflector Design", Short Course Notes of *Measurement, Processing and Analysis of Radar Target Signatures*, Vol 1, The Ohio State University, September 10-13, 1985.

[39] D.W. Hess and F.G. Willwerth, "Compact Range Improvements and Performance at 30 GHz", Digest IEEE Int. Symp. Antennas and Prop., 1977.

[40] J. Vokurka, "Advanced Antenna Measurements", Proc. European Microwave Conference 1984, Leige, Belgium.

[41] W.D. Burnside, M.C. Gilreath and B. Kent, "A Rolled Edge Modification of Compact Range Reflectors", Proc. 1984 AMTA Symposium, San Diego, CA.

[42] W.D. Burnside, "Reflector Edge, Target Support and Feed Antenna for Compact Range", Short Course Notes of *Measurement, Processing and Analysis of Radar Target Signatures*, Vol 1, The Ohio State University, September 10-13, 1985.

[43] A.G. Repjar and D.P. Kremer, "Accurate Evaluation of a Millimeter Wave Compact Range Using Planar Near-Field Scanning", IEEE Trans. Antennas and Prop., Vol AP-30, No 3, May 1982, pp. 419–425.

[44] K.S. Kelleher, "Reflector Antennas", chapter in *Antenna Engineering Handbook* (2 ed.) (R.C. Johnson and H. Jasik edit.) McGraw-Hill, 1984.

[45] T.T. Chu, *First Order Uniform Theory of Diffraction Analysis of the Scattering by Smooth Structures*, Ph.D Dissertation, The Ohio State University, 1982.

[46] W.D. Burnside, A.K. Dominek and R. Barger, "Blended Surface Concept for a Compact Range Reflector", Proc. 1985 AMTA Symposium,Melbourne, FL.

[47] I.J. Gupta and W.D. Burnside, "Electromagnetic Performance Study of a New Compact Range Reflector", Tech. Report 718331-1, The Ohio State University ElectroScience Laboratory, June 1986.

[48] W.D. Burnside, R.C. Rudduck, I.J. Gupta and J. Clerici, "Electromagnetic Performance Study of Scientific-Atlanta's New Compact Range", Proc. 1986 AMTA Symposium, Ottawa, Ontario.

[49] W.D. Burnside, Personal communication, The Ohio State University Electro-Science Laboratory.

[50] S.H. Lee and R.C. Rudduck, "Aperture Integration and GTD Techniques Used in the NEC Reflector Antenna Code", IEEE Trans. Antennas and Prop., Vol AP-33, No 2, February 1985, pp. 189–194.

[51] I. Koffman, "Feed Polarization for Parallel Currents in Reflectors Generated by Conic Sections", IEEE Trans. Antennas and Prop., Vol AP-14, No 1, January 1966, pp. 37-40.

[52] T-S Chu and R.H. Turrin, "Depolarization Properties of Offset Reflector Antennas", IEEE Trans. Antennas and Prop., Vol AP-21, No 3, May 1973, pp. 339-345.

[53] J. Dijk et al, "The Polarization Losses of Offset Paraboloid Antennas", IEEE Trans. Antennas and Prop., Vol AP-22, No 4, July 1974, pp. 513-520.

[54] M.J. Gans and R.A. Semplak, "Some Far-Field Studies of an Offset Launcher", Bell Syst. Tech. J., Vol 54, No 7, September 1975, pp. 1319-1341.

[55] P.W. Hannan, "Microwave Antennas Derived from the Cassegrain Telescope", IRE Trans. Antennas and Prop., March 1961, pp. 140-158.

[56] W.A. Wong, "On the Equivalent Parabola Technique to Predict the Performance Characteristics of a Cassegrain System with an Offset Feed", IEEE Trans. Antennas and Prop., Vol AP-21, No 3, May 1973, pp. 335-339.

[57] A.W. Rudge and N.A. Adatia, "Offset-Parabolic-Antennas: A Review", Proc. IEEE, Vol 66, No 12, December 1978, pp. 1592-1618.

[58] C. Dragone, "Offset Multireflector Antennas with Perfect Pattern Symmetry and Polarization Discrimination", Bell Syst. Tech. J., Vol 57, No 7, September 1978, pp. 2663-2684.

[59] Y. Mizugutch, M. Akagawa and H. Yokoi, "Offset Dual Reflector Antenna", Digest IEEE Intl. Symp. Antennas and Prop., 1976.

[60] H. Tanaka and M. Mizusawa, "Elimination of Cross-Polarization in Offset Dual-Reflector Antennas", Elec. and Comm. in Japan, Vol 58-B, No 12, 1975, pp. 71-78.

[61] R.A. Shore, "A Simple Derivation of the Basic Design Equation for Offset Dual Reflector Antennas with Rotational Symmetry and Zero Cross Polarization", IEEE Trans. Antennas and Prop., Vol AP-33, No 1, January 1985, pp. 114-116.

[62] W.V.T. Rusch, Y. Rahmat-Samii and R.A. Shore, "The Equivalent Paraboloid of an Optimized Off-Set Cassegrain Antenna", Digest IEEE Intl. Symp. Antennas and Prop., 1986.

[63] N.A. Adatia, "Diffraction Effects in Dual Offset Cassegrain Antenna", Digest IEEE Intl. Symp. Antennas and Prop., 1978.

[64] G. Clerici, Personal communication, The Ohio State University ElectroScience Laboratory.

[65] B.T. DeWitt, *Analysis and Measurement of Electromagnetic Scattering by Piramidal and Wedge Absorbers*, Ph.D Dissertation, The Ohio State University, 1986.

[66] W.D. Burnside and R.W. Burgener, "High Frequency Scattering by a Thin Lossless Dielectric Slab", IEEE Trans. Antennas and Prop., Vol AP-31, No 1, January 1983, pp. 104–110.

[67] E.H. Newman, "TM and TE Scattering by a Dielectric/Ferrite Cylinder in the Presence of a Half Plane", IEEE Trans. Antennas and Prop., Vol AP-34, No 6, June 1986, pp. 804–813.

[68] J.A. Stratton, *Electromagnetic Theory*, McGraw-Hill, 1941.

[69] I.D. Faux and M.J. Pratt, *Computational Geometry for Design and Manufacture*, Ellis Horwood, 1979.